2018-01-01

Heterogeneous Integration Of Metallic, Semiconducting And Dielectric Two-Dimensional Layered Material Inks For Electronics And Sensing Device Platforms

Jay Amrish Desai
University of Texas at El Paso, jadesai@miners.utep.edu

HETEROGENEOUS INTEGRATION OF METALLIC, SEMICONDUCTING AND DIELECTRIC TWO-DIMENSIONAL LAYERED MATERIAL INKS FOR ELECTRONICS AND SENSING DEVICE PLATFORMS

JAY AMRISH DESAI

Doctoral Program in Materials Science and Engineering

APPROVED:

Anupama B. Kaul, Ph.D., Chair

Binata Joddar, Ph.D.

Stephen W. Stafford, Ph.D.

Cristian Botez, Ph.D.

Charles Ambler, Ph.D.
Dean of the Graduate School

HETEROGENEOUS INTEGRATION OF METALLIC, SEMICONDUCTING AND DIELECTRIC TWO-DIMENSIONAL LAYERED MATERIAL INKS FOR ELECTRONICS AND SENSING DEVICE PLATFORMS

by

JAY AMRISH DESAI, M.Tech.

DISSERTATION

Presented to the Faculty of the Graduate School of

The University of Texas at El Paso

in Partial Fulfillment

of the Requirements

for the Degree of

DOCTOR OF PHILOSOPHY

Department of Metallurgical, Materials and Biomedical Engineering

THE UNIVERSITY OF TEXAS AT EL PASO

August 2018

Acknowledgments

I would like to thank my advisor, Professor Anupama B. Kaul for providing the opportunity to join her research group, as one of the members of the Nanomaterials and Devices Lab (NDL) that she established upon her arrival to UTEP in September 2014. Without the fully supported Research Assistantship throughout my Ph.D. tenure provided by Prof. Kaul, this work would not have been possible. I value her guidance and constant support throughout my work, and in the review and significant edits, she made to my journal publications and this dissertation.

I would like to thank Dr. Theresa Maldonado for her assistance during the transition process to UNT. The use of the shared material characterization facilities at UTEP and UNT are greatly acknowledged. I would like to thank my dissertation committee members, Professor Binata Joddar and Professor Stephen W. Stafford from the Department of Metallurgical, Materials and Biomedical engineering and Professor Cristian Botez from the Department of Physics, for helping review this dissertation and providing their feedback on my research work. I also would like to thank Dr. Chandan Biswas, Dr. Nirmal Adhikari, and Dr. Misook Min for their help, support, and patience during my research.

I greatly appreciate the members of the NDL group for their support. I want to thank everybody in the group, Gustavo, Carlos, Jorge, Srishti, Ridwan, and Avra for always supporting me with their kind words, good sense of humor and making the group feel like a family.

Finally, I want to thank my family and friends for their support and understanding while I dedicated so much time to this work.

Abstract

In monolayers of two-dimensional (2-D) layered materials, the motion of electrons is confined to a 2-D plane yielding a "zero" effective thickness with regard to the electrons. These monolayers are commonly obtained by exfoliating membranes from the bulk crystal to overcome the weak interplanar Van der Waals bonding using the so-called top-down approach. The bottom-up approach is another avenue to realize these materials, where atoms and molecules coalesce together into increasingly larger assemblies for the realization of the bulk three-dimensional (3-D) crystal. The unique properties of many of these 2-D materials make them highly sought out candidates for advancing conventional electronics that is currently based on Silicon, in addition to flexible electronics, optoelectronics and sensing devices. Graphene was the first 2-D material to be isolated more than a decade ago using mechanical exfoliation. It is now being explored as an attractive material for interconnects and contacts for optoelectronic devices, given its ballistic electron transport, metal-like character and enhanced chemical and structural stability. In order to construct electronic devices, there is also a need to expand the suite of materials from metallic systems by exploring semiconducting and dielectric 2-D layered materials. In this regard, substantial interest has also been cast on tungsten disulfide (WS_2) which exhibits tunable semiconducting properties, where an indirect-to-direct band gap transition is observed in going from the bulk to monolayers. Another 2-D material of great interest is hexagonal boron nitride (h-BN) which finds its potential as an excellent dielectric for electronics and optoelectronics given its superb structural integrity devoid of trapped charges, its atomic super-flat surface morphology, and its high-temperature stability.

In this work, 2-D materials are obtained by chemical exfoliation which refers to the breaking of layered 3-D materials into single or few-layer nanosheets in suitable solvents. Inkjet-printing is used as a material-conserving deposition technique for printing graphene, WS_2, and h-BN nanosheets. Different avenues for formulating inks of nanomaterials, specifically graphene, WS_2, and h-BN, for electronic and optoelectronic devices using scalable, low-cost, additive manufacturing approaches have been explored and optimized. Inkjet-printed graphene/WS_2 based photodetector with rise and decay time of less than 50 ms, responsivity of up to ~ 0.86 A/W and detectivity up to ~ 10^{13} $cmHz^{-1/2}W^{-1}$ and graphene/h-BN based photosensitive capacitor with leakage current density as low as 0.072 $\mu A/mm^2$ and capacitance density as high as 24 $fF/\mu m^2$ are fabricated. Temperature-dependent Raman spectroscopy was performed to demonstrate the high-temperature stability of inkjet printed patterns. Optoelectronic properties of different materials and devices are studied using optical microscopy, scanning electron microscopy (SEM), UV-vis spectroscopy, current-voltage, current-time, capacitance-time and capacitance-frequency measurements.

Table of Contents

List of Figures

Chapter 1: Introduction

1.1 Introduction and production of 2-D materials

Since the first isolation of graphene in 2004 [1, 2], graphene and other two-dimensional (2-D) layered materials have shown an immense potential for applications in printed electronics [3], transparent electrodes [4], energy storage devices [5], and ultrafast transistors [6]. The term "two-dimensional materials" refers to a class of materials that exhibit zero effective thickness with respect to electrons. Since these materials are just one atomic layer thick, it restrains the motion of electrons along the length and breadth only.

These 2-D materials show properties that are different and significantly enhanced over their bulk counterparts. Some of the important 2-D materials of present interest (Graphene, $TaSe_2$, $MoSe_2$, $NbSe_2$, and Bi_2Se_3) with their unique properties are shown in Figures 1.1 and 1.2. Graphene is a sheet of monolayer of carbon atoms with a hexagonal honeycomb lattice structure exhibiting semi-metal like behavior. Tantalum diselenide ($TaSe_2$) is metallic transition metal dichalcogenide (TMD) with Se-Ta-Se tri-layer basic units. Molybdenum diselenide ($MoSe_2$) is a semiconducting TMD with molybdenum (Mo) layers sandwiched between two selenide (Se) layers. Niobium diselenide ($NbSe_2$) has shown its potential as superconducting TMD for applications requiring superconductivity. Bismuth selenide (Bi_2Se_3) marks its importance as a topological insulator belonging to the group of transition metal trichalcogenides. Thus, this new class of layered materials has gained a significant amount of attention in various electronics industries due to the range of properties (from superconducting to highly insulating) offered by them and are visioned as future materials for various device applications [7, 8].

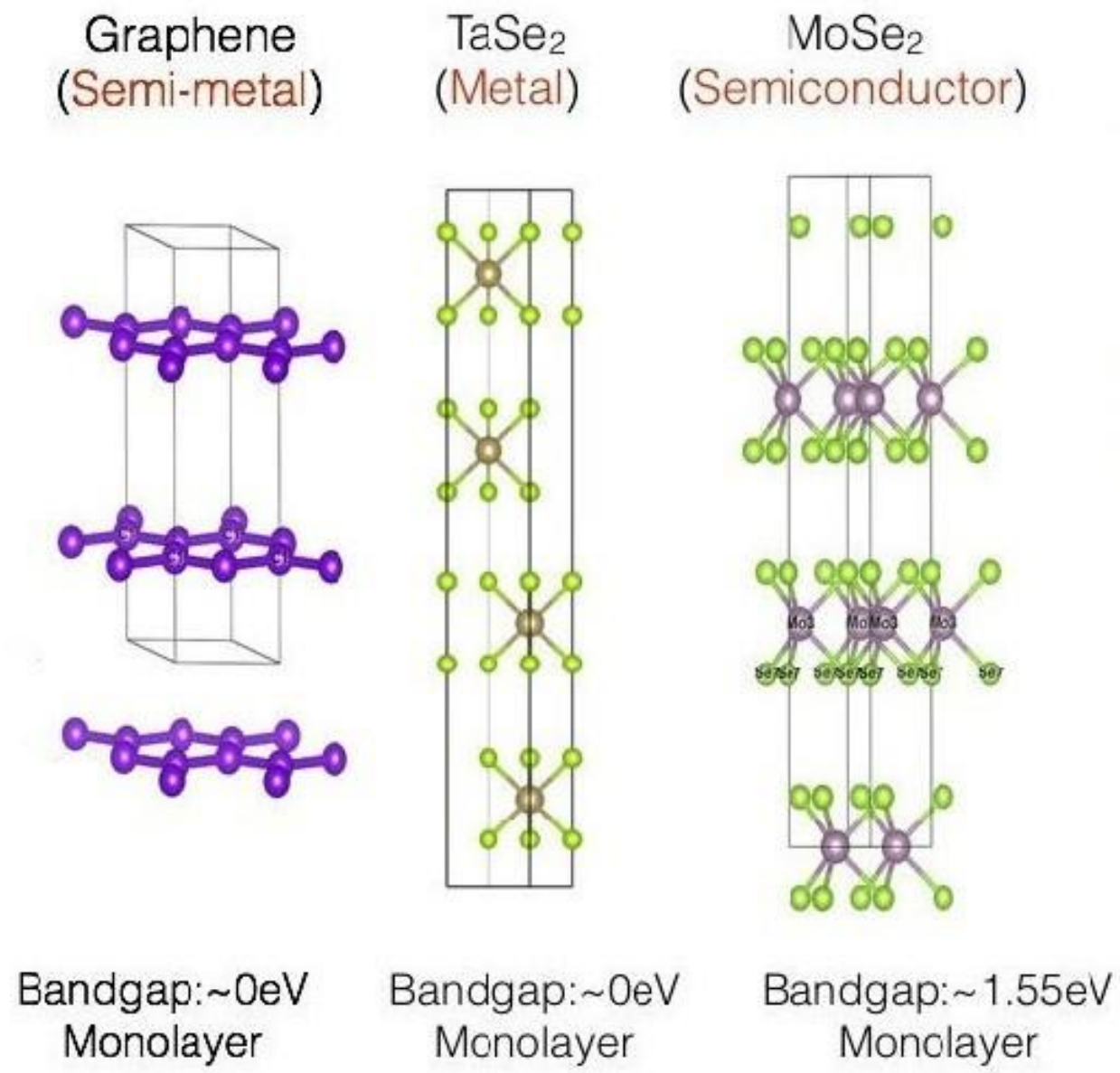

Figure 1.1: Atomic arrangement in graphene, $TaSe_2$ and $MoSe_2$.

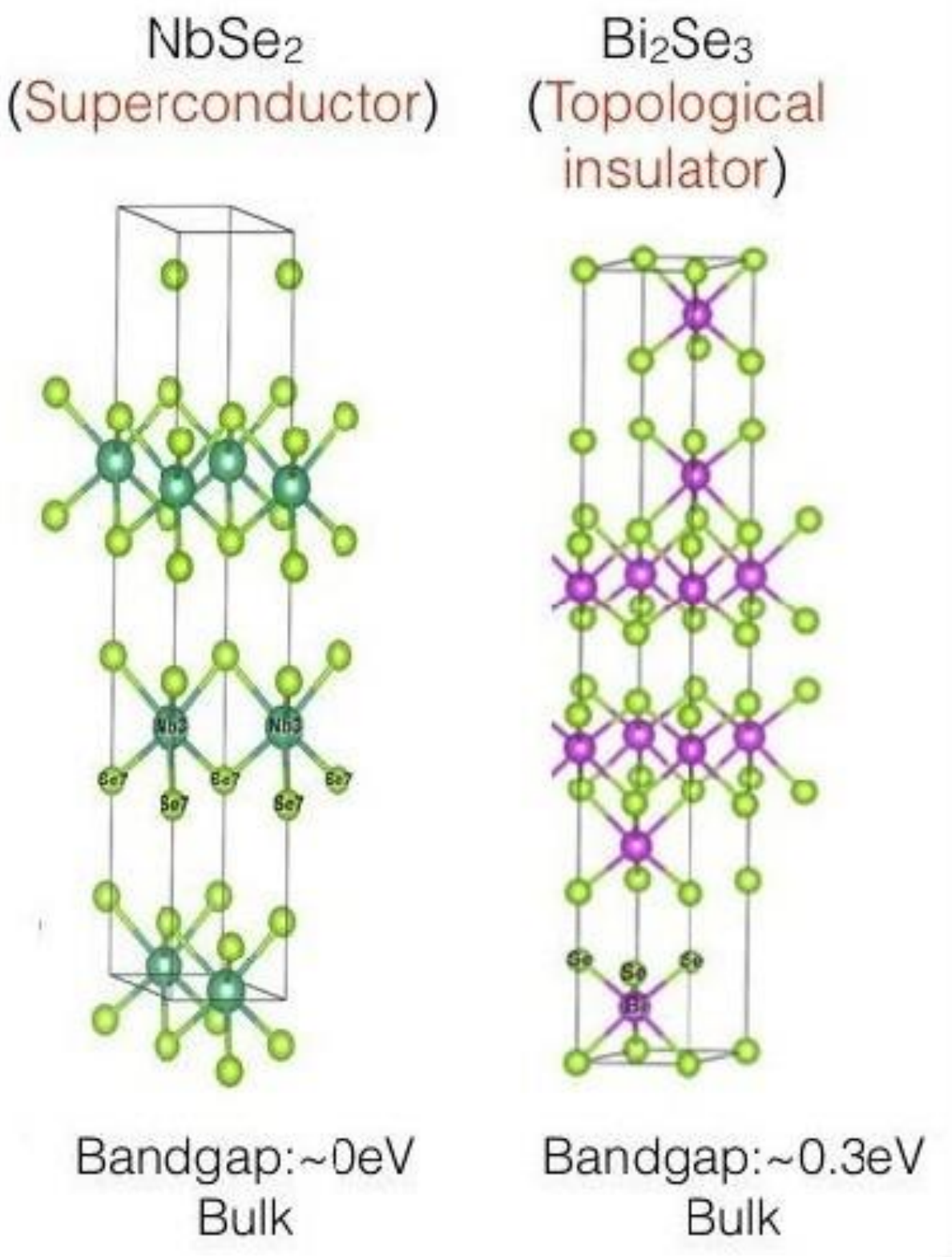

Figure 1.2: Atomic arrangement in $NbSe_2$ and Bi_2Se_3.

These 2-D nanosheets can be produced by either bottom-up approach or top-down approach. The bottom-up approach involves stacking of atoms or molecules to form 2-D nanosheets. Physical vapor deposition (PVD) [9, 10, 11, 12, 13, 14] and chemical vapor deposition (CVD) [15, 16, 17, 18, 19] are among the widely used methods in this category. In the PVD process, solid or liquid condensed phase is converted to a gaseous phase which is then transported and cooled to form solid of desired physical morphology. This is shown in Figure 1.3. Two common PVD processes are evaporation and sputtering, the schematic illustration of which is shown in Figure 1.4 and 1.5 respectively. In the CVD process, the wafer (substrate) is exposed to one or more volatile precursors, which react and/or decompose on the substrate surface to produce the desired deposit. Volatile by-products are also produced, which are removed by gas flow through the reaction chamber. Figure 1.6 shows a schematic illustration of a typical CVD process.

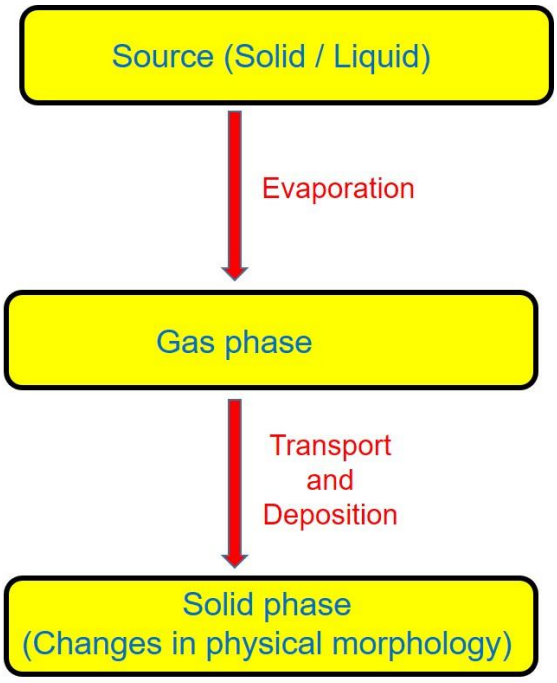

Figure 1.3: Phase change during the PVD process.

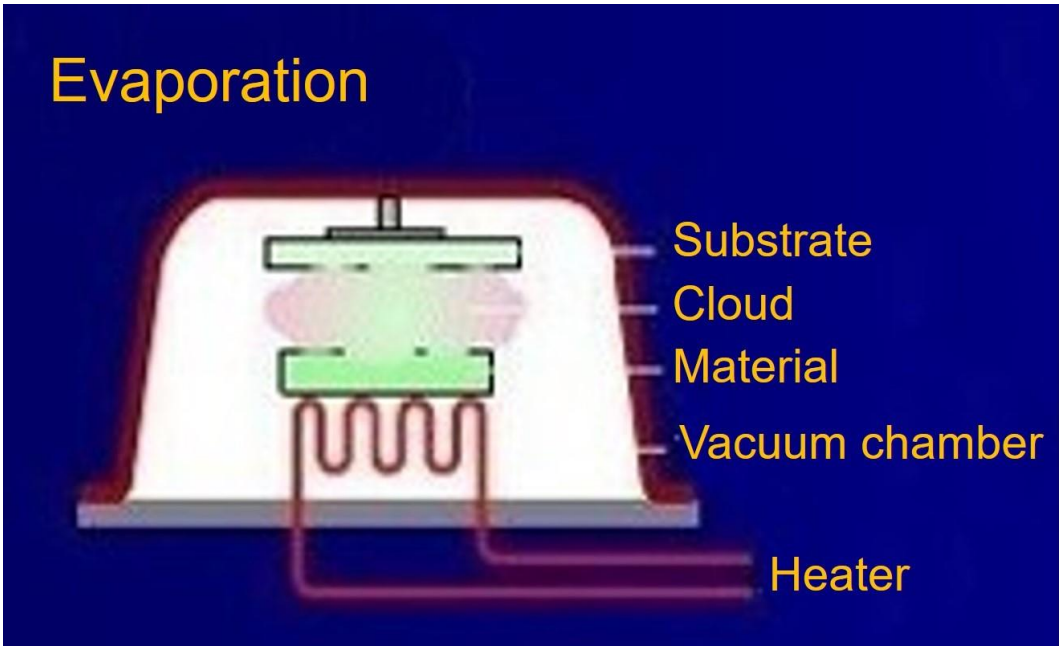

Figure 1.4: Evaporation process.

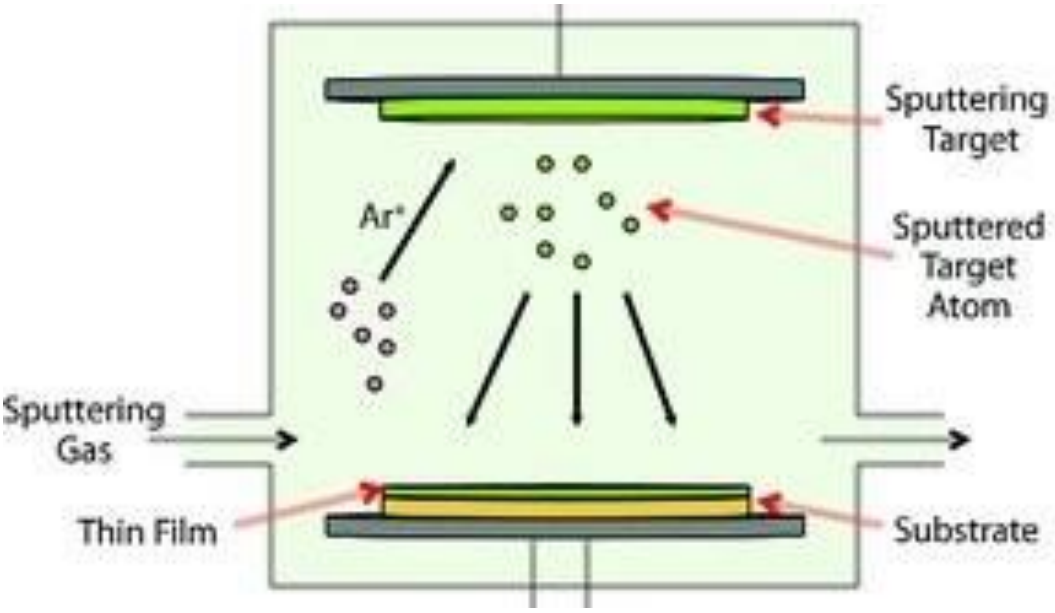

Figure 1.5: Sputtering process.

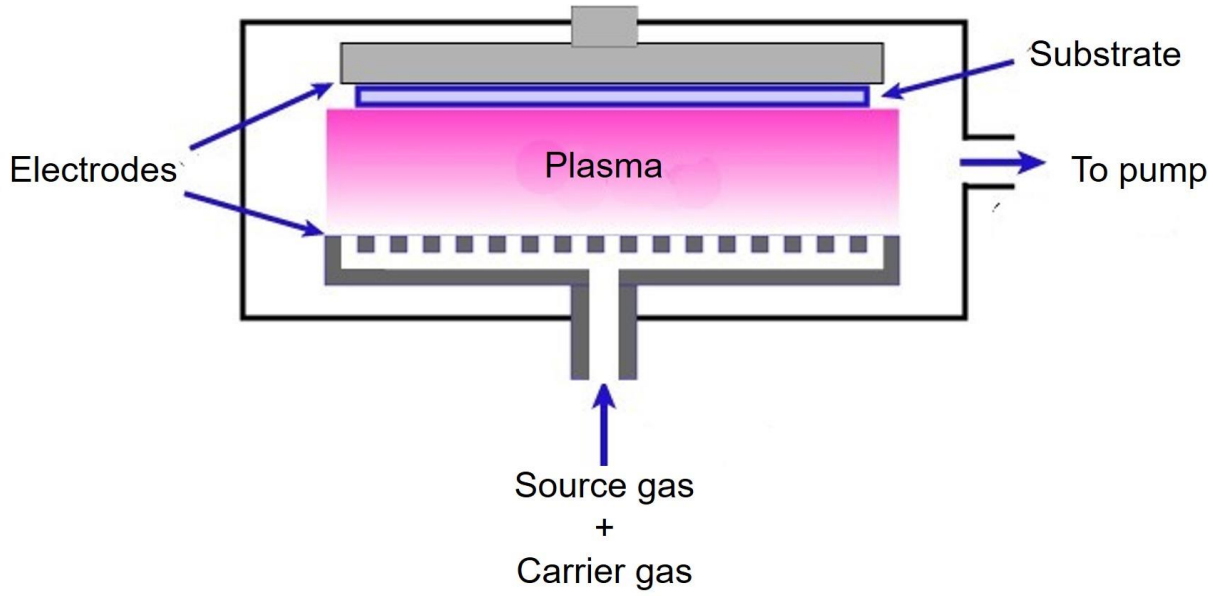

Figure 1.6: CVD process mechanism.

The top-down approach deals with removal of layers of bulk three-dimensional (3-D) precursor materials which have strong in-plane or intraplanar covalent bonding but weak out-of-plane or interplanar Van der Waals bonding. Exfoliation of these 3-D layered materials can lead to rupture or breakage of Van der Waals bonds producing thin atomic or molecular 2-D nanosheets. Mechanical [20, 21, 22, 23, 24] and chemical exfoliation [25, 26, 27, 28, 29] are two widely used top-down approaches for 2-D materials production. In the mechanical exfoliation method, atomically thin nanosheets are separated from bulk crystal using adhesive tape by repeated peeling of multi-layers into various platelets of few-layer nanosheets. This is shown in Figure 1.7. Chemical exfoliation refers to breakage of bulk 3-D materials into 2-D nanosheets in a suitable solvent which is demonstrated in Figure 1.8.

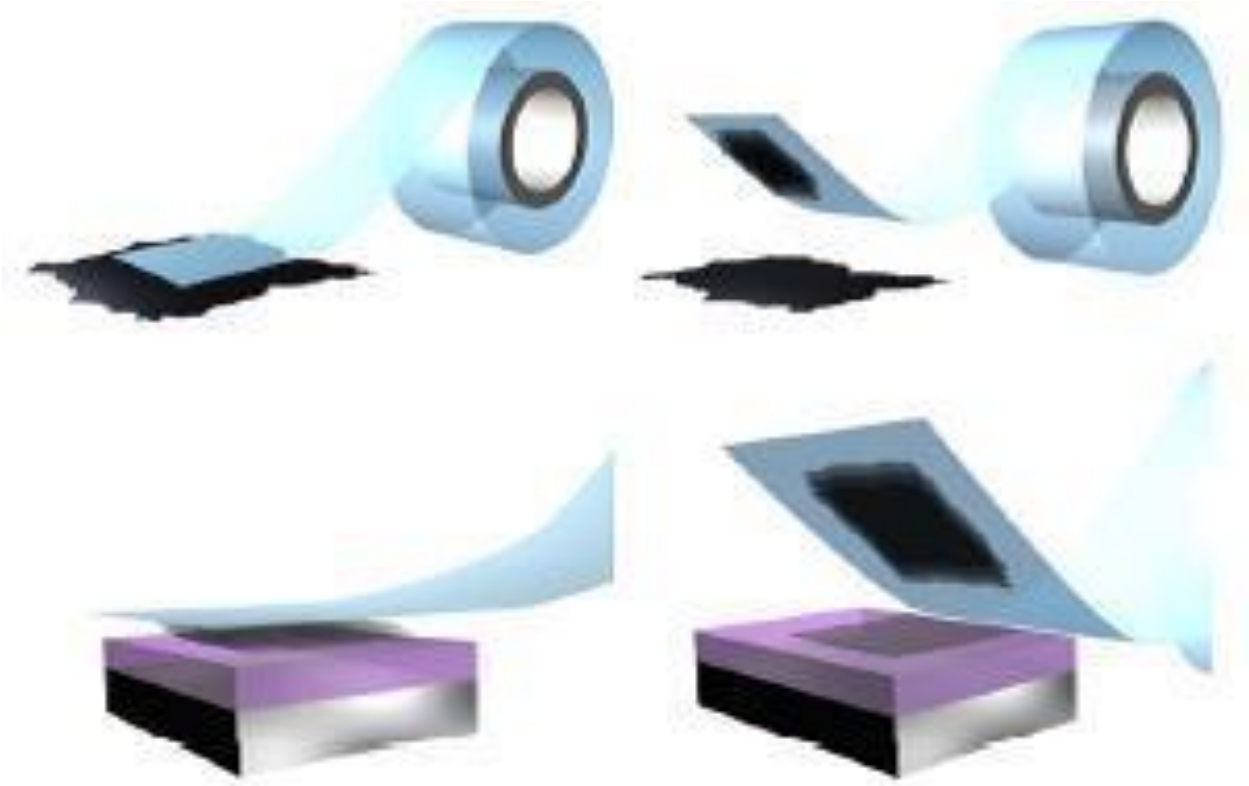

Figure 1.7: Mechanical exfoliation method.

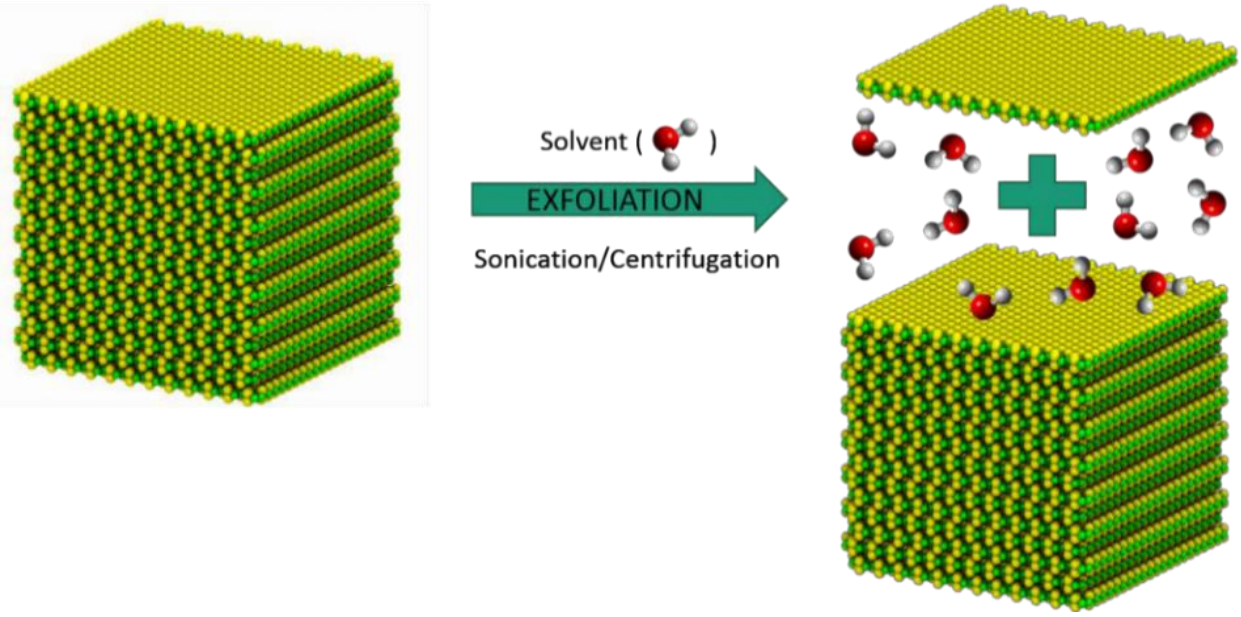

Figure 1.8: Chemical exfoliation process.

1.2 Chemical exfoliation methods

Chemical or liquid-phase exfoliation offers several advantages over other methods of obtaining 2-D materials. It is relatively low-cost, material conserving and time-saving method which can be done even at room temperatures and facilitates the production of large quantities of 2-D nanosheets [30]. Oxidation and subsequent dispersions into suitable solvents, ion intercalation, ion-exchange and sonication assisted exfoliation are common techniques involving liquid-phase exfoliation [31, 32, 33]. Sonication-assisted exfoliation refers to exposing the layered material to ultrasonic waves in an appropriate solvent and is relatively simple among all the common chemical exfoliation techniques. Ultrasonic waves generate cavitation bubbles that collapse into high energy jets, breaking up the layered crystallites to produce exfoliated nanosheets.

Two types of sonication-assisted exfoliation methods are used for 2-D materials fabrication- Bath sonication and tip sonication. Bath sonication usually has very low power resulting in lower production rates of dispersed nanosheets. Tip sonication on another hand has very high power and energy is imparted to the dispersed media directly as the ultrasonic tip is positioned in dispersion media resulting in higher nanosheets production rates i.e. more exfoliation in a shorter time. The photographs demonstrating bath and tip sonication are shown in Figure 1.9 and Figure 1.10. Other methods of liquid exfoliation include magnetic stirring and shear mixing. Magnetic stirring refers to using a magnetic field to spin stir bar immersed in a liquid, thus stirring it. The energy provided by stirring breaks the 3-D layered materials into 2-D nanosheets. Shear mixing refers to exfoliation technique by using a shear force such that one area of fluid travels with different velocity relative to the adjacent area. The photographs demonstrating magnetic stirring and shear mixing process are shown in Figure 1.11 and Figure 1.12.

Figure 1.9: Photograph of bath sonication process.

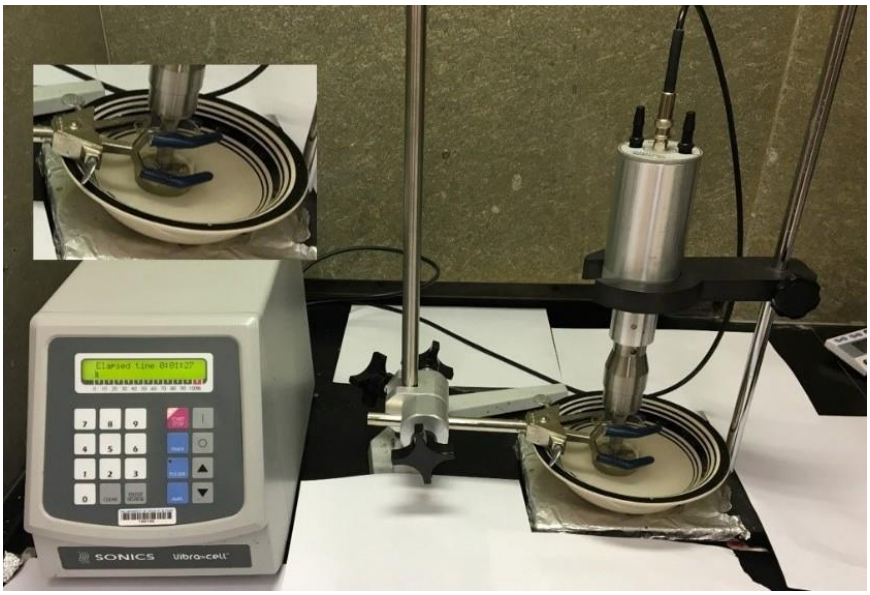

Figure 1.10: Photograph of tip sonication process.

Figure 1.11: Photograph of the magnetic stirring process.

Figure 1.12: Photograph of the shear mixing process.

1.3 Inkjet printing

Inkjet printing is a material-conserving deposition technique used for liquid-phase materials for printing patterns with good dimensional accuracy [34, 35, 36]. The Dimatix Materials Printer has found its application as a production tool that utilizes the ink jetting technology in new manufacturing and fabrication processes. Figure 1.13 shows the Dimatix Materials Printer and its components. Main components include a print carriage for moving the cartridge to desired locations, cartridge holder to hold the cartridge, drop watcher to check the flow of ink through each nozzle before printing and platen where the substrate on which printing patterns is desired is kept. An appropriate amount of electric field is applied that generates mechanical strain which allows the flow of ink (printable liquid) from cartridge to substrate. e.g. silicon (Si), silicon dioxide (SiO_2), kapton, glass, etc. This effect of generating mechanical strain by applying an electric field is called the piezoelectric effect. Drops are formed by propagating a pressure pulse in a fluid held in the chamber behind the printing nozzle. If the pulse exceeds some threshold at the nozzle, a drop is ejected. In absence of pressure pulse, the liquid is held in place by surface tension at the nozzle. This is shown in Figure 1.14. Dispensing and precise positioning of very small volumes of fluid (1-100 picolitres) can be facilitated which transforms into solid after impact on the substrate.

For uniform and unhindered flow of ink, viscosity, the property of the fluid which opposes the relative motion between its two surfaces, should be low enough to allow refill of channel and surface tension, the inward force at the surface of the liquid, must be high enough to hold ink in the nozzle without dripping. Resolution and accuracy of printed patterns is a function of the interaction between individual drops and substrate. The flow of ink depends on inertia, drop velocity, density, viscosity and surface tension of the ink [37, 38, 39]. Present challenges with ink preparation involves ensuring proper flow of ink, obtaining high concentration of dispersed 2-D

materials, preventing aggregation, suppressing coffee-ring effects, obtaining viscosity of about 10-12 cP, preventing clogging of nozzles, reducing spreading of the ink, promoting adsorption onto the substrate, and optimizing resolution by trade-off between drop size and speed [40, 41, 42, 43, 44].

Good solvents for exfoliation like *N*-methyl 2-pyrrolidone (NMP), dimethylacetamide (DMA), dimethylformamide (DMF), isopropyl alcohol (IPA) and cyclohexanone have viscosity significantly less than 12 cP. To obtain a viscosity of about 12 cP that is ideal for inkjet printing either highly viscous solvent, e.g. terpineol, in an appropriate amount can be added to the exfoliating solvent, use surfactants like ethyl cellulose (EC) that are comparatively stable or combination of both in appropriate amounts can be used. The increase in viscosity of five common solvents with the addition of EC is shown in Figure 1.15 [45].

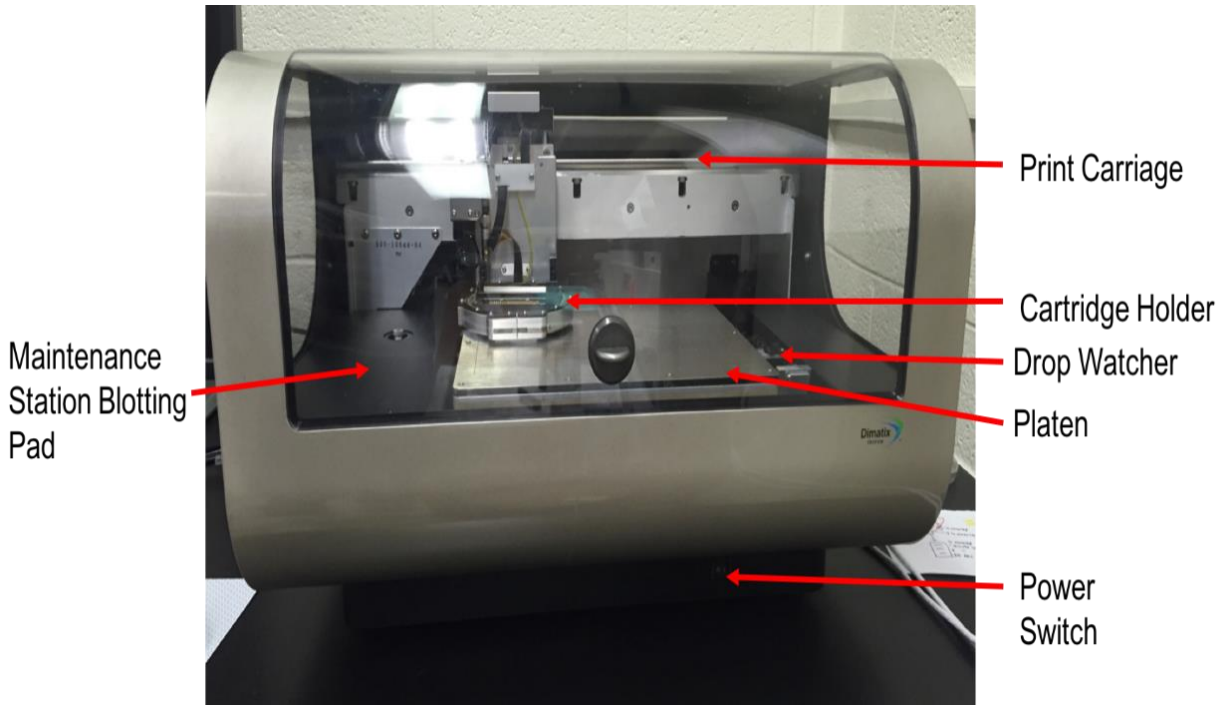

Figure 1.13: Photograph of Dimatix Materials Printer showing its major components.

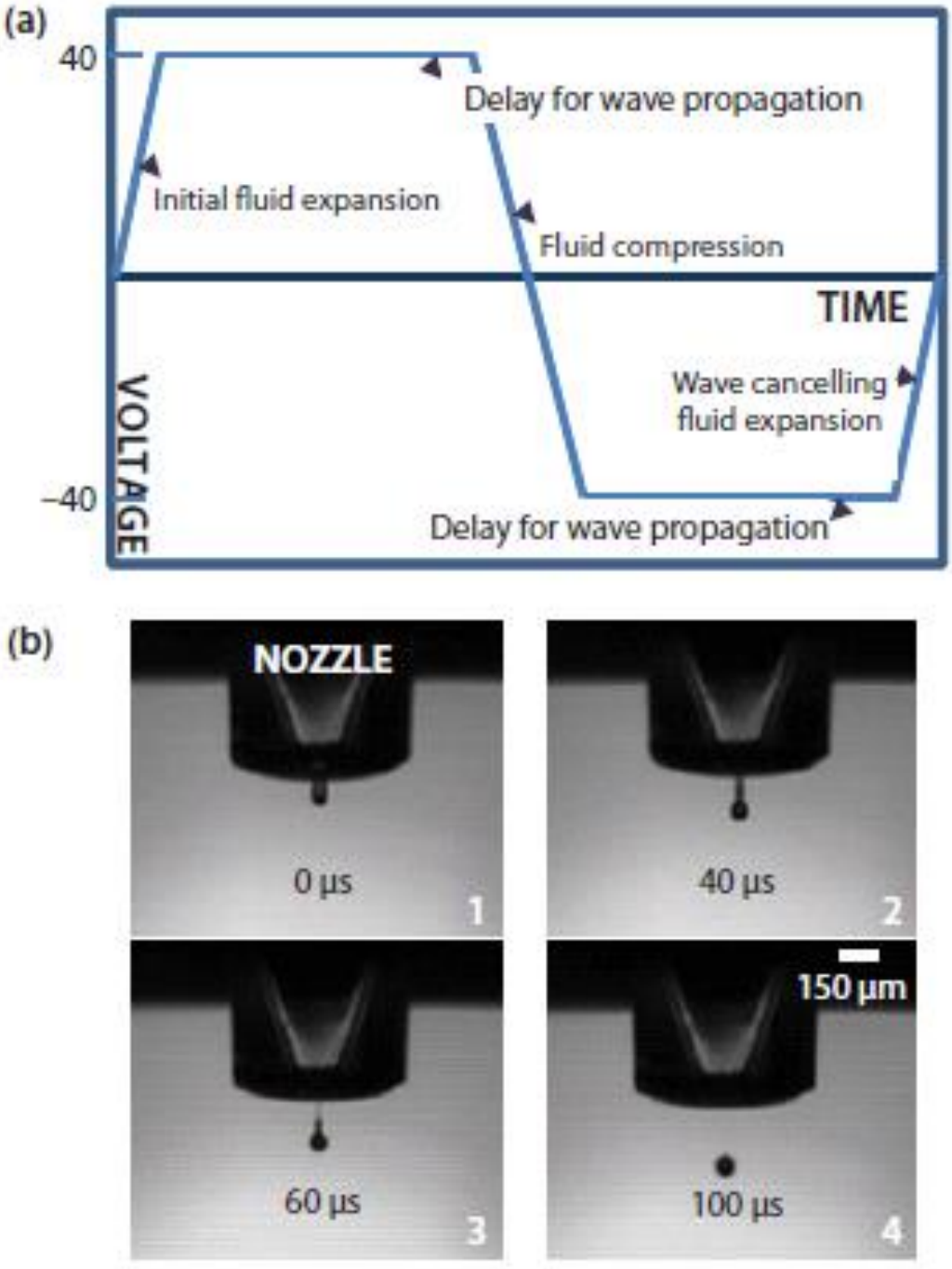

Figure 1.14: (a) Schematic showing waveform generated in the inkjet printer and (b) Drop formation mechanism.

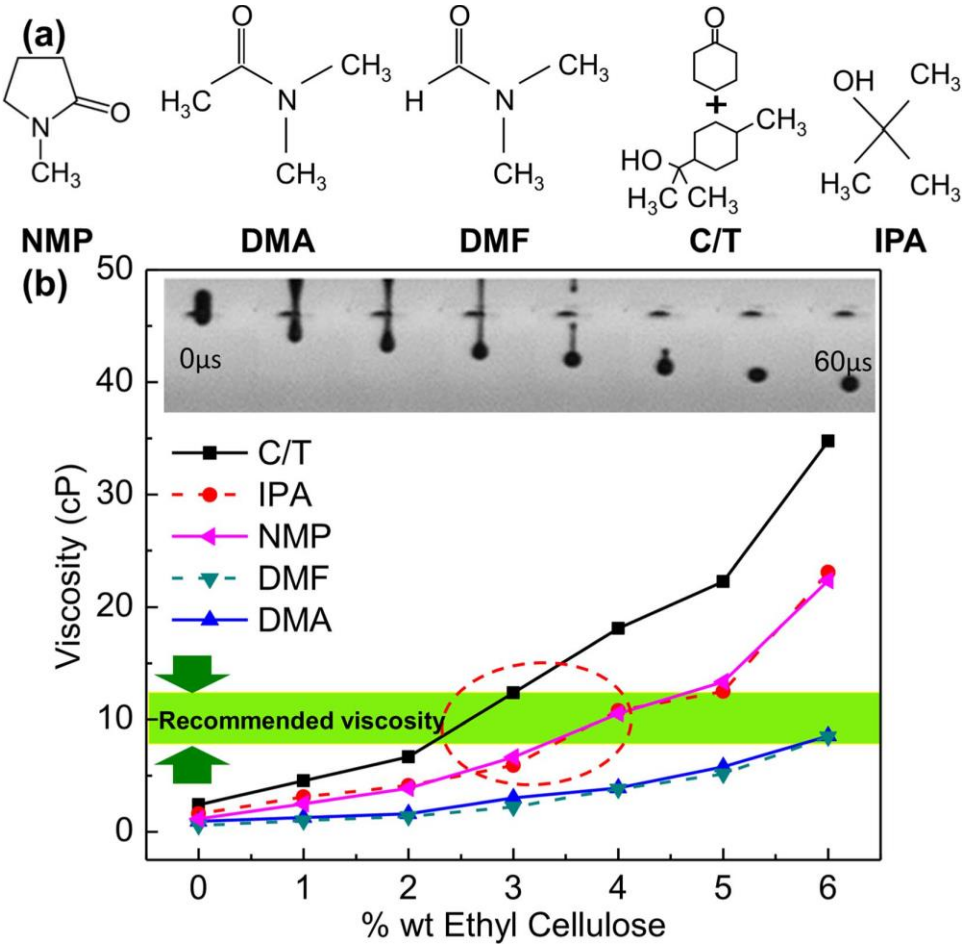

Figure 1.15: (a) Molecular structure of some of the common solvents and (b) Effect of ethyl cellulose on the viscosity of different solvents [45].

1.4 Graphene

In 2004, Novosolev et al. exfoliated graphite with thin transparent adhesive tape into single atomic layers of graphene having a honeycomb structure. Graphene is the first and thinnest 2-D material known since its discovery in 2004. It comprises of the 2-D hexagonal lattice of carbon atoms and has shown a variety of interesting optical and electronic properties due to its linear dispersion relation near the K point of the Brillouin zone and zero effective rest mass of its charge carriers. The top-view and side-view of graphene nanosheets are shown in Figure 1.16 [30]. Each carbon atom in graphene possesses three electrons that are bounded with nearest neighbor atom electrons creating chemical bonds. The fourth electron is delocalized on the whole graphene layer, which allows conduction of electric current. Graphene is different from conventional metal (e.g. gold) electrodes as it has a finite density of states from the Dirac cones of valence and conduction bands. There is no band gap unlike insulators and at the same time, there are no partially filled bands, unlike metals. It is also stable and chemically inert. It has a finite density of states which enables tuning of its Fermi level for low contact resistance or barrier-free contact with the semiconductor. The above-mentioned properties make graphene a potential candidate to serve as a conductive contact in optoelectronics applications [46, 47, 48, 49, 50].

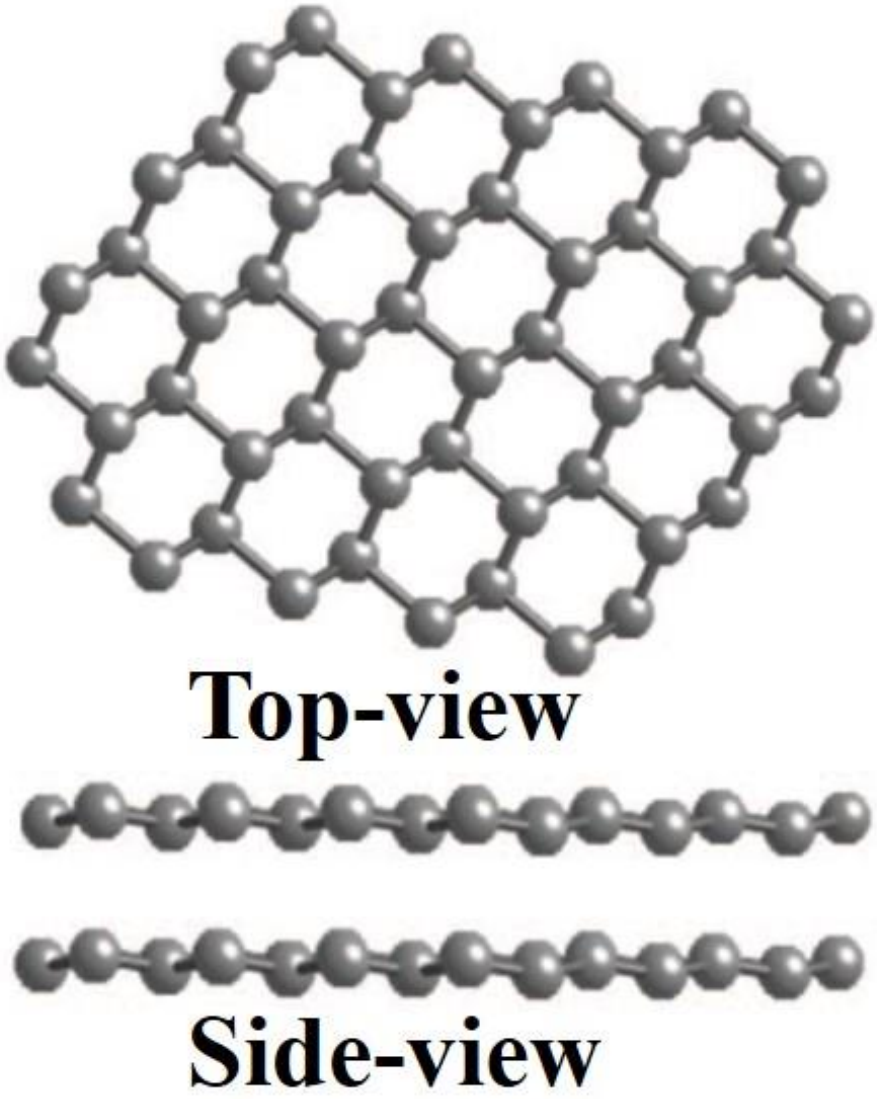

Figure 1.16: Top-view and side-view of graphene. Each sphere represents one carbon atom.

1.5 Tungsten disulfide (WS_2)

Various layered materials have been subjected to extensive research studies of which transition metal dichalcogenides (TMDCs) have shown great interest among researchers due to its wide range of electronic [51], optical [52], mechanical [53], chemical and thermal properties [54]. They are a class of materials with formula MX_2 where M is transition metal element (e.g. Mo, W, Ti, V, and Nb) and X is chalcogen (S, Se or Te). They have layered structures in the form of X-M-X where two planes of chalcogen atoms are separated by a plane of metal atoms [55]. In popular semiconducting TMDCs like molybdenum disulfide (MoS_2) and tungsten disulfide (WS_2), indirect-to-direct band gap transition is observed when the bulk layered material is exfoliated to its monolayer form [56, 57, 58, 59]. They possess sizeable band gaps of around 1-2 eV which marks their importance as future materials in the electronics industry [60]. In its bulk state, WS_2 has an indirect bandgap of approximately 1.4 eV but converts to a direct bandgap of 2.1 eV when thinned to its monolayer form [61]. It exhibits strong light-matter interaction, reasonable valence and conduction bandwidth, high absorption coefficients, long-term stability, non-toxicity, large exciton binding energy and sensitivity to interlayer interactions [62]. These properties of WS_2 nanosheets makes them attractive for various optoelectronic applications [63, 64, 65], especially for photodetector applications. Schematic of atomic arrangement of tungsten and sulfur atom in monolayer and bilayer WS_2 is shown in Figure 1.17.

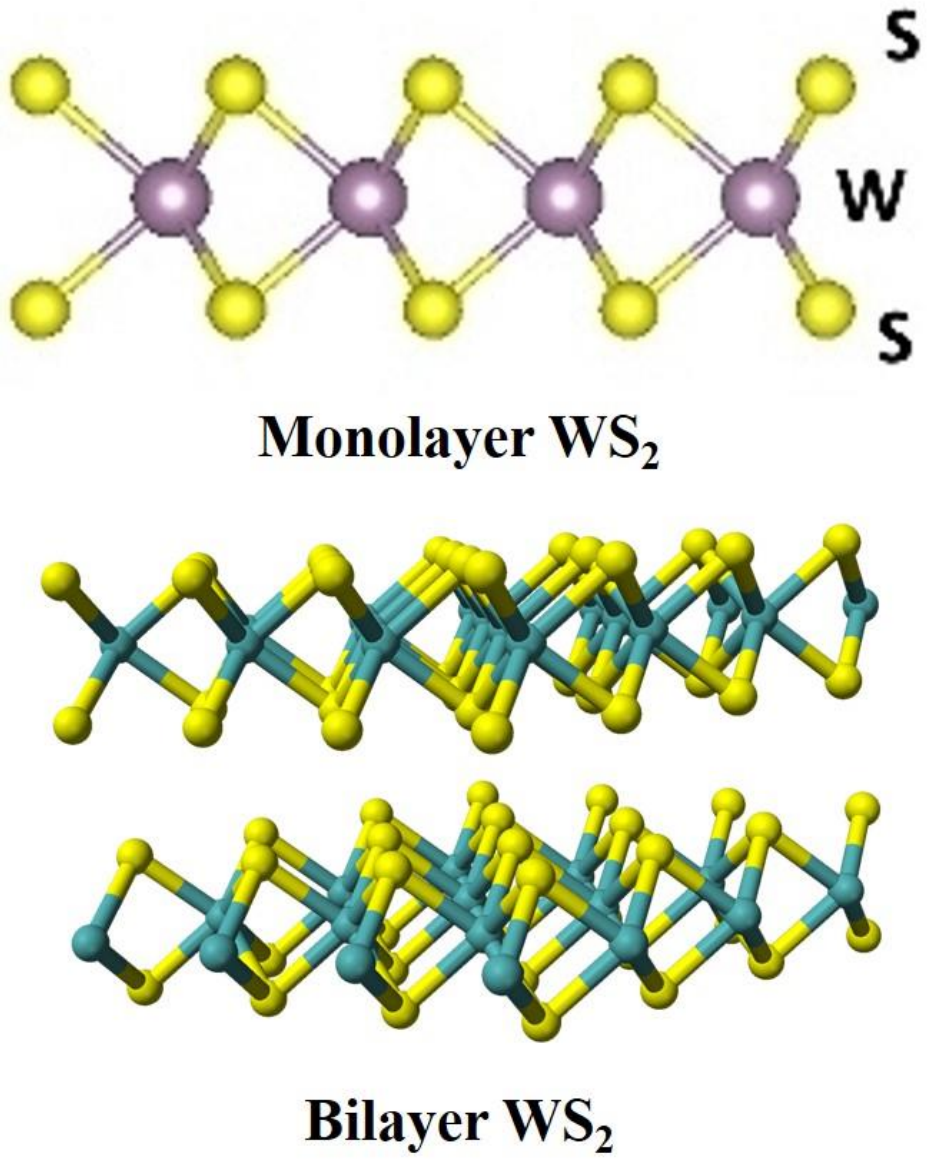

Figure 1.17: Schematic showing the atomic arrangement of tungsten and sulfur atoms in monolayer and bilayer WS_2.

1.6 Hexagonal boron nitride (h-BN)

Hexagonal boron nitride (h-BN) is another material of great interest as it finds application as an insulator for 2-D devices and has also emerged as a strong contender to replace silicon dioxide (SiO_2) dielectric since the latter exhibits limited carrier mobility due to scattering from charged surface states, impurities and surface roughness. Interesting properties of h-BN include high mechanical hardness and resilience, the absence of dangling bonds and trapped charges and atomic flatness. It exhibits strong covalent bonding between boron and nitrogen atoms within each layer and weak Van der Waals force binding layers together. Top-view and side-view of h-BN are shown in Figure 1.18 [30]. It also exhibits wide direct band gap of around 5.2 to 5.9 eV and small lattice mismatch (approximately 1.7%) with graphene [66]. These properties make h-BN suitable for applications as transparent membrane [67], encapsulating material [68], tunneling barrier [69], dielectric substrate [70] and the dielectric layer in capacitive structures especially for graphene-based electronics [71].

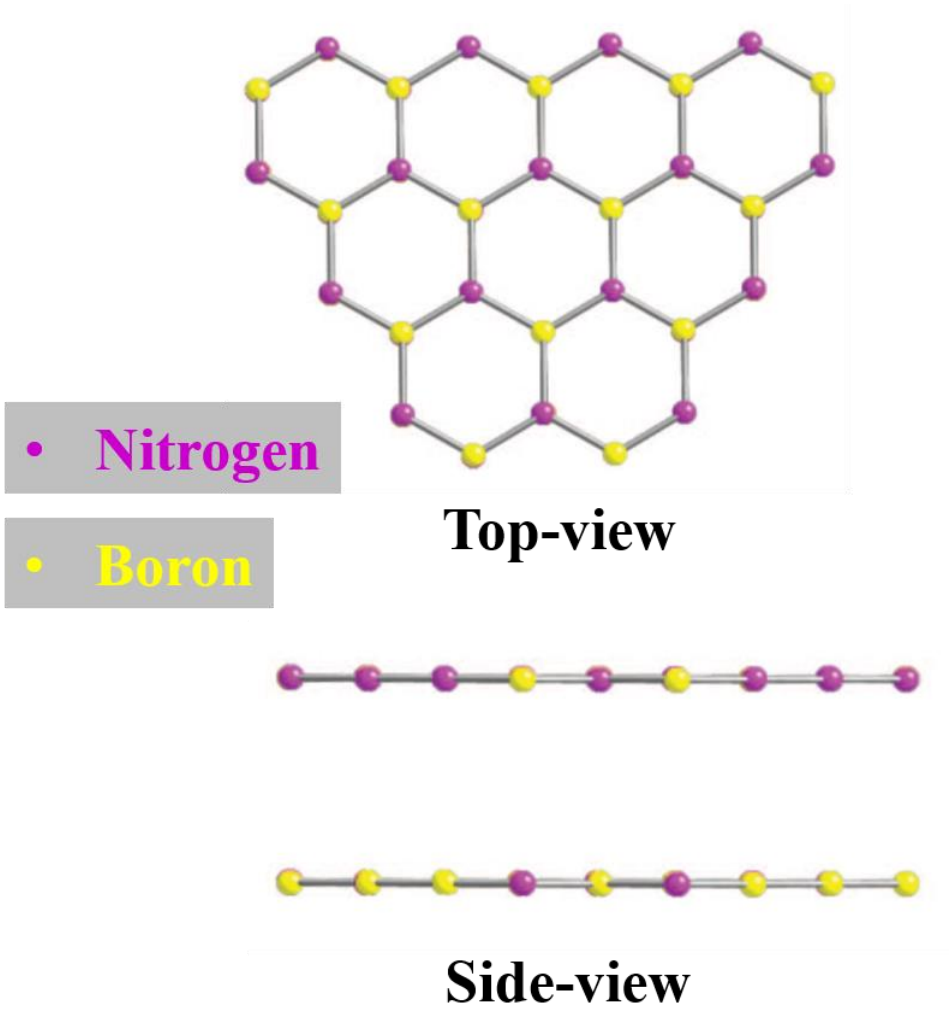

Figure 1.18: Top-view and side-view of h-BN.

1.7 Characterization techniques

1.7.1 Scanning Electron Microscopy (SEM)

Scanning electron microscopy (SEM) is the electron microscopy technique used to obtain images and various signals from the sample by scanning the surface with a focused beam of high-energy electrons. It can be employed to reveal different and diverse information such as morphology (texture), chemical composition, crystalline structure and orientation of the sample. These signals include secondary electrons, backscattered electrons, and characteristic X-rays. In this work, Hitachi S4800 is used to observe the morphology of different 2-D materials. The photograph of the instrument is shown in Figure 1.19.

Figure 1.19: Horiba S4800 Scanning electron microscope.

1.7.2 Ultraviolet-visible (UV-Vis) Spectroscopy

The UV-Vis spectroscopy refers to absorption or reflectance spectroscopy performed in the ultraviolet (10 nm to 400 nm wavelength) -visible (400 nm to 700 nm) spectral region. It is used to measure the absorption or reflectance of the radiation from the material under analysis. The wavelength of light, the material can absorb depends on the ease with which it can excite the electrons. The UV-Vis spectroscopy can be used to determine the concentration of the particles in a solution. Higher the absorbance more is the concentration of absorbing particles in the solution. The absorbance spectra can also be used to determine the band-gap of semiconducting or insulating particles/ material present in the solution. In the present work, a spectrophotometer Cary 5000, was used to measure the quality and concentration of different 2-D materials. The photograph of the instrument is shown in Figure 1.20.

Figure 1.20: CARY 5000 Spectrophotometer.

1.7.3 Raman Spectroscopy and Photoluminescence

Raman spectroscopy is a spectroscopic technique used to observe and analyze different vibrational, rotational and other low-frequency modes in the sample. It relies on Raman or inelastic scattering of monochromatic light, usually a laser when it is made to fall on the sample. The laser light interacts with different molecular vibrations in the sample leading to an increase or decrease in its energy. This shift in energy gives information about different modes present in the system affecting its structural and thermal properties. The present work utilizes Horiba LabRAM HR Evolution to obtain and analyze raman spectra of different samples. The photograph of equipment is shown in Figure 1.21. The equipment was also used to study photoluminescence (PL) spectra of different materials. Photoluminescence (PL) refers to emission of light from a material after absorption of photons. This spectrum is useful to determine the band-gap of the material and in determining the effectiveness of exfoliation techniques use to exfoliate different 2-D materials.

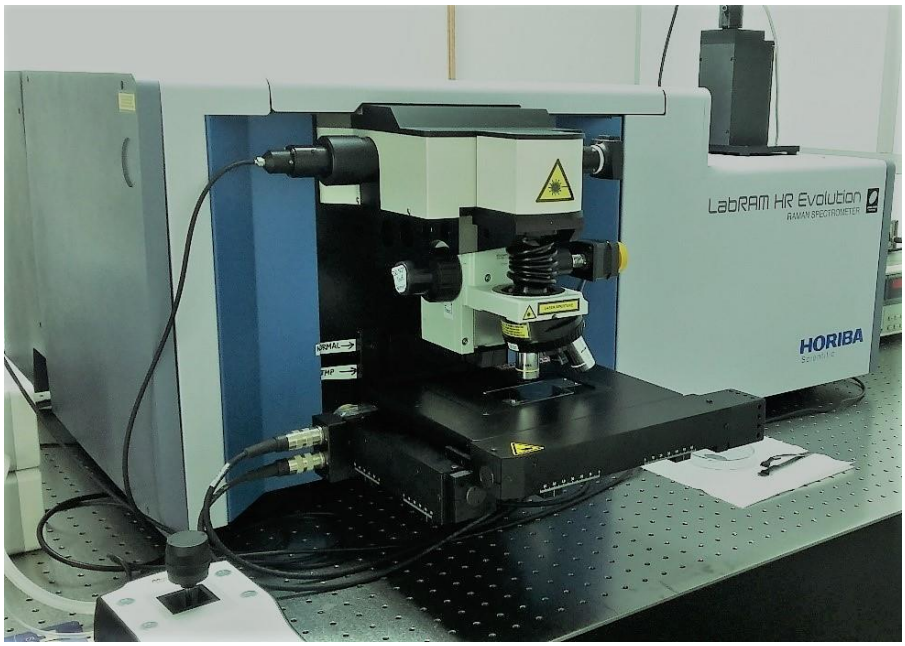

Figure 1.21: Horiba LabRAM HR Evolution.

1.7.4 Probe Station

Electrical characterization performed in the present work was done using the micromanipulator 450PM-B probe stage equipped with an HP precision semiconductor parameter analyzer 4156A and Lakeshore CRX-4K cryogenic probe station. Current-voltage, capacitance-voltage, capacitance-frequency and current-time response were some of the key measurements that were performed and are reported in this work. Various parameters like response time, decay time, responsivity, detectivity, on/off ratio, photocurrent, dark current, capacitance density and leakage current density were derived using the above measurements to study photodetector and photosensitive capacitor performance and analyze graphene/WS_2 and graphene/h-BN interface behavior.

Chapter 2: Inkjet-printed graphene as interconnect for photodetectors

The present work demonstrates two simple, but highly efficient methods for transferring graphitic nanocarbons onto various substrates. The first approach utilizes the viscoelastic stamping process to yield an effective approach for transferring graphene platelets with high crystallinity and minimal residue onto substrates using mechanical exfoliation. The second approach uses liquid-phase exfoliation, where N-methyl 2-pyrrolidone (NMP) and 4 weight% EC solution was used for chemical exfoliation to yield a scalable approach to produce printed graphene films with high electronic transport properties over large areas. A comparative analysis of the two techniques was conducted and how each of these processes affects the respective properties of the graphene on an arbitrary substrate. This comparison is important because certain applications require high-quality, defect-free graphene which can be best produced by mechanical exfoliation as chances of defect generation are minimal. In other applications, the role of defects is not as critical to the device operation, such as in flexible electronics, and the important criteria are the ease of large-area scalability and low-cost production approaches; chemically exfoliated graphene is the preferred route in this scenario. Thus, both mechanical and chemical exfoliation methods have their respective roles to play for the roadmap of applications arising from graphene, and each technique needs to be optimized to serve the desired purpose. As a follow-on from the inkjet printed conductive graphene, we then demonstrate the role of this ink as an interconnect with tungsten disulfide (WS_2), another 2D layered material with semiconducting properties. The graphene/WS_2 based photodetector prototype devices were constructed using inkjet printing which validates the use of the graphene inks as highly conductive contacts and as interconnects in a broad range of applications.

2.1 Materials and methods

For mechanical exfoliation study through viscoelastic stamping method, a piece of the crystal of HOPG (Figure 2.1(b)) from SPI Supplies Grade SPI-1, 10x10x1 mm in dimensions was taken and placed gently on the residue-free blue medium tack tape from Semiconductor Equipment Corp. Another piece of tape was taken and gently laid on the first tape to ensure adequate adhesion and was pulled apart. This step was repeated 4 times using multiple tapes for the successful isolation of graphene. During exfoliation, it is important to keep good tension on the tape. Viscoelastic stamping was then prepared using the PDMS-based gel pad and platelets were transferred to the desired electrode area.

For chemical exfoliation study, 6 mg/ ml (0.06 grams) of graphite powder obtained from breaking graphite rod (Sigma Aldrich #496553) was taken in a glass vial and 10 ml NMP was added to it. The solution was sonicated in Branson 2800 bath sonicator for 24 hours. Ethyl cellulose (4 weight% or 0.4 grams) was then added to the solution and sonicated again in a bath sonicator for 6 hours. The net graphene concentration in final ink was 13.04%. This was the final ink. Ethyl cellulose (EC) was added primarily to obtain a viscosity of about 10 cP which is ideal for inkjet printing. Exactly 4 weight% of ethyl cellulose increases the viscosity of NMP from 1.16 cP to 10.51 cP which is ideal for inkjet printing [45]. It also prevents particle agglomeration and improves suspension stability. DMP-2800 series Fujifilm Dimatix Materials Printer with a print head consisting of 16 inkjet nozzles was used to print various patterns in this work. Drop spacing of 20 μm, the cartridge temperature of 40 °C and a platen temperature of 60 °C was used during all of the printing work. Annealing of all the inkjet-printed patterns was done at 250 ºC for 2 hours immediately after inkjet printing. Viscosity was measured using Brookfield DV-E viscometer at

100 rpm. WS_2 ink for photodetector device was made using the same concentration of WS_2 powder (Sigma Aldrich #243639) and similar technique used in graphene ink preparation.

2.2 Mechanical and chemical exfoliation of graphene

In this work, the properties of mechanically and chemically exfoliated graphene were compared. Figure 2.1 shows a schematic representation of graphene produced by both approaches, where the arrangement of carbon atoms in graphene is shown in Figure 2.1(a). The starting materials for obtaining graphene by mechanical and chemical exfoliation are highly oriented pyrolytic graphite (HOPG) (Figure 2.1(b-i)) and bulk graphite powder (Figure 2.1(c-i)). The schematic of mechanical exfoliation showing separation of graphene nanosheets from HOPG bulk material and their transfer onto silicon dioxide SiO_2/Si substrates is shown in Figure 2.1(b-ii). The viscoelastic stamping method was used to transfer 2-D platelets of graphene onto a specified region to yield residue-free, mechanically exfoliated graphene. Figure 2.1(b-iii) represents graphene platelets on top of sputtered molybdenum electrodes which served as contacts to gauge the electronic transport properties of the HOPG graphene that are discussed later in this paper. In order to produce the dispersions for chemical exfoliation, 6 mg/ml of graphite powder was mixed with 10 ml NMP and sonicated for 24 hours. This was followed by the addition of 4 weight% EC to the solution and sonication was then conducted for 6 hours to yield the final ink dispersion, which is seen in the vial of Figure 2.1(c-ii). The amount of this ink used to print various patterns using the Fujifilm Dimatix inkjet printer was 3 ml. Inkjet-printed lines of 5 mm length and varying width (0.1, 0.2, 0.3, 0.4, 0.6, 0.8 and 1 mm from top to bottom) are shown in Figure 2.1(c-iii).

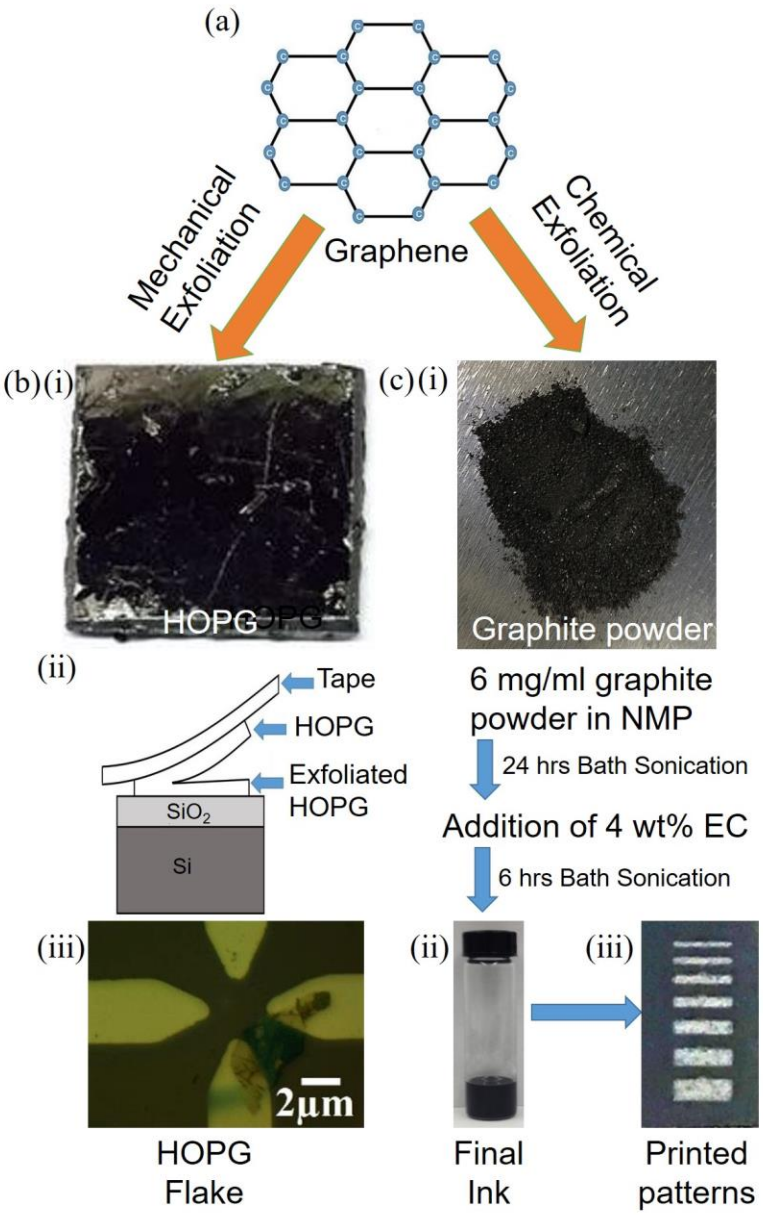

Figure 2.1: (a) Schematic model of carbon atoms arrangement in graphene. (b): (i) Photograph of HOPG bulk crystal; (ii) Schematic of mechanical exfoliation process; (iii) HOPG platelets on molybdenum electrodes. (c): (i) Photograph of graphite powder and schematic of chemical exfoliation process; (ii) Optical images of the nanodispersed graphene ink solution contained in the glass vial; (iii) Photograph of inkjet-printed patterns onto arbitrary substrates with different line widths ranging from 0.1, 0.2, 0.3, 0.4, 0.6, 0.8 and 1 mm from top to bottom.

2.3 Optical characterization of HOPG and IPGF

Mechanical exfoliation of HOPG was performed using the conventional scotch-tape approach and this was then compared to platelets generated using the viscoelastic stamping method. The conventional scotch tape approach is not ideal as it leaves residues which is illustrated in Figure 2.2(a) and (b). The exfoliated platelets also tended to be thicker with a smaller, fragmented platelet area of ~ 105 μm^2 as shown in Figure 2.2(b), as viewed using an optical microscope. The residues seen here on the substrate are a hindrance to the ensuing device applications of such poor-quality materials [72]. Our adapted viscoelastic stamping method [73] for mechanical exfoliation left a residue-free substrate surface with a larger platelet size (Figure 2.2(c) and (d)) which is a typical areal size of ~ 140 μm^2 wide platelets. Therefore, it can be concluded that the viscoelastic stamping approach was significantly superior compared to the conventional scotch tape exfoliation method, where the former yielded higher quality, larger area, and residue-free graphene platelets.

On the other hand, for the chemical exfoliation of 2-D graphene, an appropriate ink dispersion needs to be formed first. To characterize the effectiveness of the dispersion, optical absorption spectroscopy was used, as shown by the image in Figure 2.3(a), which is the optical absorbance spectrum for chemically exfoliated graphene inks that were bath sonicated for 6 and 24 hours. This spectrum was obtained in the visible regime from the 400 -700 nm wavelength range. The higher absorbance values for the 24 hours bath-sonicated graphene inks are noted here, in contrast to the 6 hours sonication case, indicating a high and uniform concentration of graphene dispersed in NMP/EC solution, compared to the 6 hours case which exhibited a lower optical absorption in this spectral range. Figure 2.3(b) represents absorbance and good uniform dispersibility of EC and graphene in NMP. In inkjet printing, it is important to obtain uniformly

dispersed inks with no precipitates to avoid nozzle clogging and ensure a uniform ink flow. Figure 2.4(a) depicts a square 1 mm x 1 mm pattern that was printed using increasing numbers of printing passes that ranged from 1, 5, 10, 20, 30, 40 and 50 passes, using our graphene ink. Figure 2.4(b) is the magnified image of the square pattern (1 mm length and 1 mm in width) with 50 printing passes. Uniform printed patterns were observed with increasing number of passes. Uniformity was observed only after a minimum of 10 printing passes was used. This is due to the fact that a continuous channel of graphene particles must be first formed in order to obtain a conduction path for charge carriers. Moreover, the coffee ring effect was also not evident in our printed patterns [74].

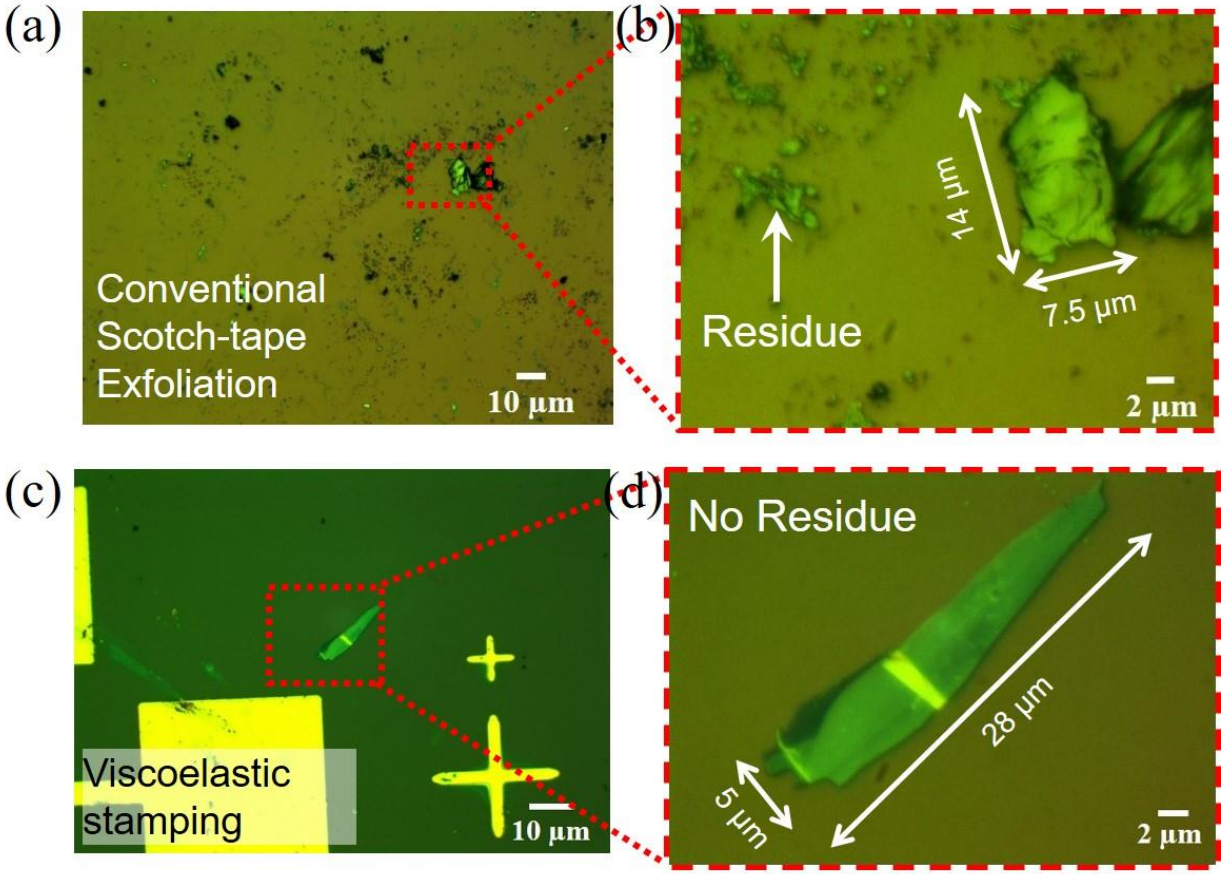

Figure 2.2: (a) Optical image of conventional scotch-tape exfoliated graphene platelets. (b) Zoomed image of representative platelets in (a). (c) Optical image of mechanically exfoliated graphene platelets using viscoelastic stamping method. (d) Zoomed image of representative platelets in (c).

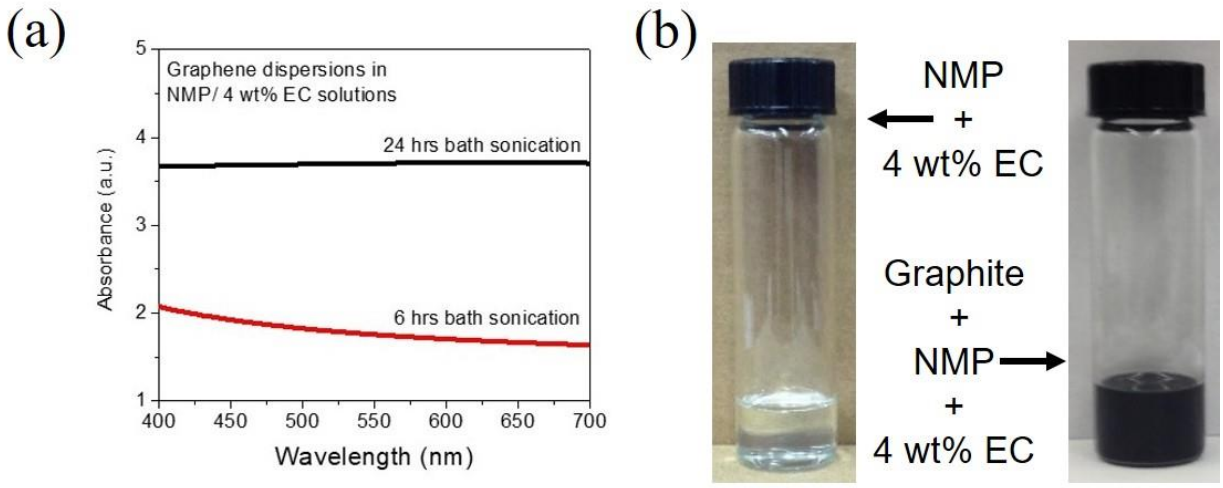

Figure 2.3: (a) Optical absorbance as a function of wavelength in the visible range (400-700 nm) for graphene-based ink dispersions for 24 hours of sonication showing a higher optical absorption compared to the 6 hours case. (b) Glass vials showing good uniform dispersibility and absorbance of EC and graphene in NMP.

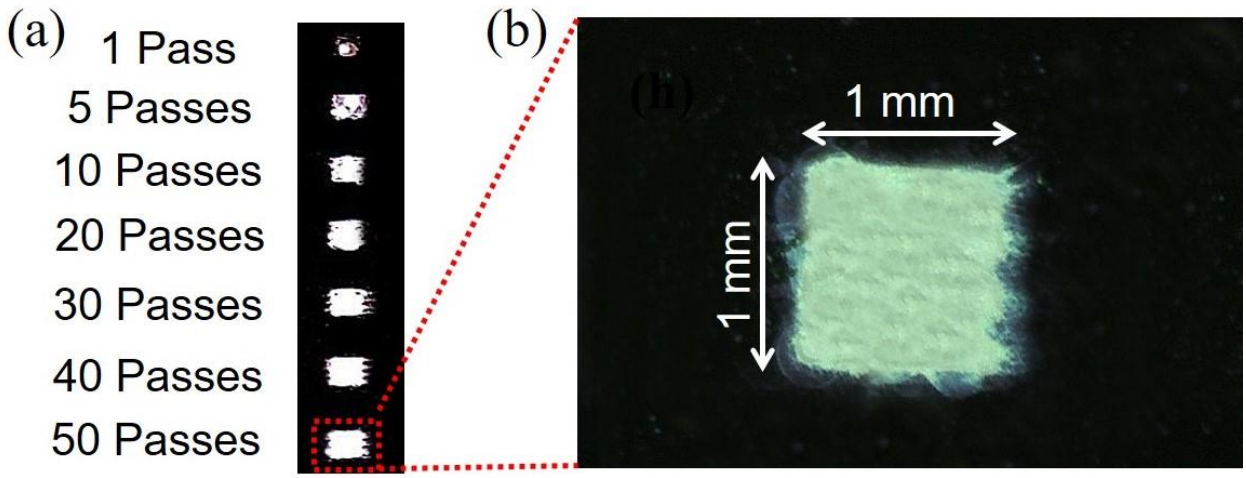

Figure 2.4: (a) Photograph of printed 1 mm square patterns with different number of printing passes. (b) Zoomed image of the trace in (a) for 50 passes, showing large area uniformity.

2.4 Temperature-dependent raman spectroscopy of HOPG and IPGF

Raman spectra of both mechanically exfoliated HOPG platelets and chemically exfoliated inkjet-printed graphene films (IPGFs) were obtained as a function of temperatures using a Linkam Thermal Cell in the Horiba Raman microscope. A typical Raman spectrum of single-layer graphene films comprises of the D-band (at ~ 1350 cm^{-1}), G-band (at ~1580 cm^{-1}) and a 2D or G'-band (at ~2700 cm^{-1}). The D-band is due to the presence of in-plane A_{1g} zone-edge mode [75] and is used to study the distribution of defects in graphene films by comparing the D/G ratio of the Raman spectra [76]. The presence of defects gives rise to two other features at ~ 1350 cm^{-1} as already mentioned for the D-band and at ~ 1615 cm^{-1} (D'-band). The D'-band appears just as a small shoulder from the G-band as a result of single phonon intravalley scattering process and is relatively small in intensity compared to the D-band [77]. The G-band is the result of in-plane vibrations occurring as a result of C-C bond stretching in graphitic materials. The G'-band is caused by second-order phonon processes involving various in-plane vibrations. The intensity ratio of G'-band to G-band can also be used to predict the number of layers present in graphene.

Figure 2.5 represents the normalized (relative to the G-band) Raman shift spectra of the mechanically exfoliated HOPG platelets and chemically exfoliated IPGF patterns measured at room temperature. The D-band peak was non-existent in the HOPG sample due to its highly crystalline, defect-free nature. In comparison, IPGF patterns showed a well-defined D-band at ~ 1348 cm^{-1} due likely to the defects generated during the sonication-induced exfoliation process [72]. Not surprisingly, the G-band was observed both in HOPG platelets and IPGF patterns near 1580 cm^{-1}. A comparatively broader G' band was observed in IPGF patterns (at ~ 2700 cm^{-1}) with respect to HOPG platelets (at ~ 2720 cm^{-1}). The small red-shift in the G'-band of IPGF patterns compared to HOPG platelets may have resulted from the thicker printed graphene layers.

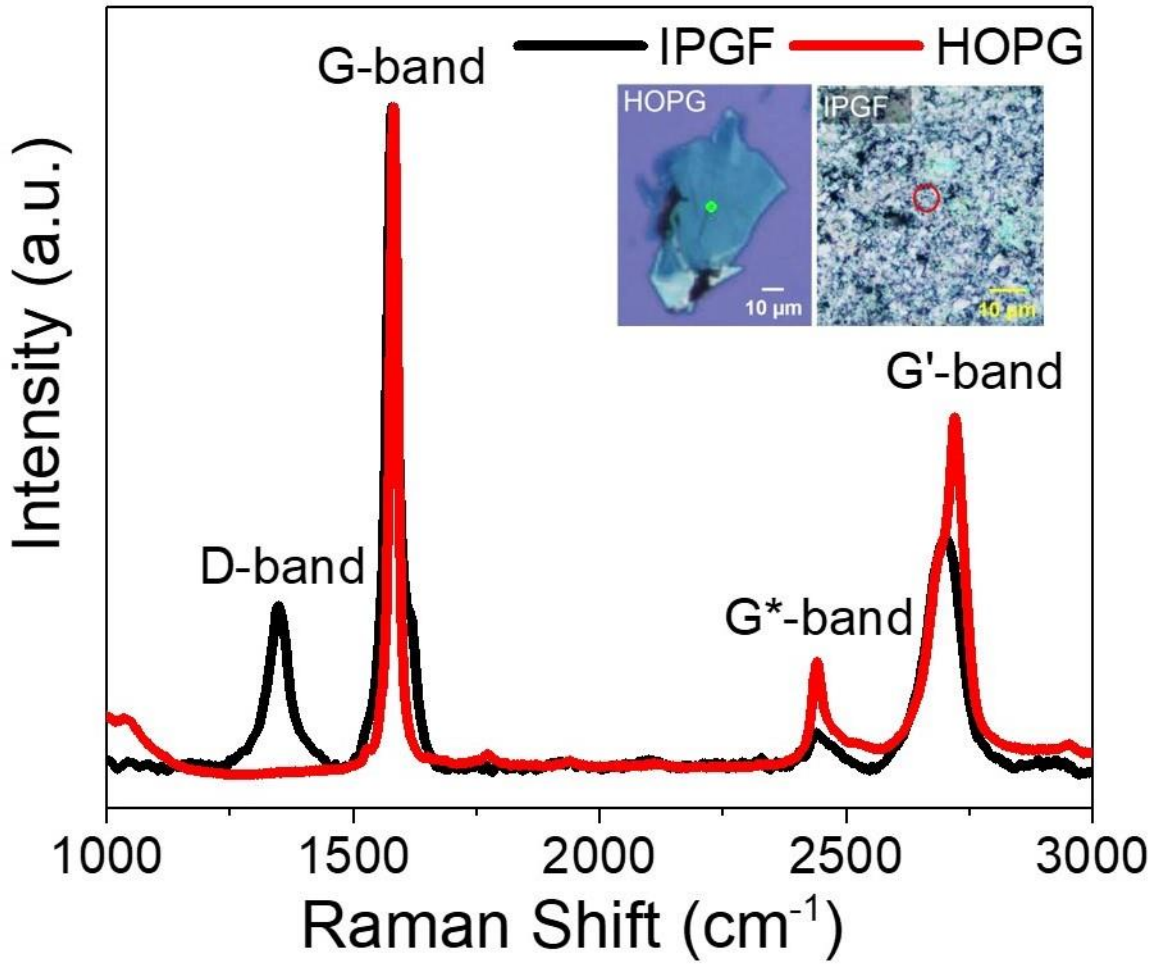

Figure 2.5: Raman spectra of IPGF patterns and HOPG platelets at room temperature.

Temperature-dependent (from room temperature (RT) to 600 °C) Raman spectra of HOPG platelets and IPGF patterns are compared in Figure 2.6. The D-band intensity decreased with a rise in temperature for IPGF patterns, which may be attributed to annealing effects that may have resulted in a reduction in defect densities. Small red-shifts in G-band and relatively higher red-shifts in G'-band were observed with increasing temperatures. These red-shifts are caused by elongation of the C-C bond owing to thermal expansion resulting in the anharmonic coupling of phonon modes. G-band peak position was red-shifted in HOPG sample from ~ 1580 cm^{-1} at room temperature to ~ 1566 cm^{-1} at 600 °C (Figure 2.7). In comparison, the G-band peak shift in IPGF patterns was observed at ~ 1577 cm^{-1} at room temperature and red-shifted towards 1563 cm^{-1} at 600 °C. Moreover, a red-shift in the D'-band was also observed from ~ 1617 cm^{-1} at room temperature to 1603 cm^{-1} at 600 °C.

The previous investigation demonstrated that electron-phonon coupling plays an important role in the temperature dependence of the G-band and D'-band shifts [78]. Figure 2.8 represents the peak shift in the G'-band of HOPG platelets and IPGF patterns at different measurement temperatures. Room temperature Raman measurement exhibited G'-band in the HOPG platelets at ~ 2720 cm^{-1}. However, it shifted to 2693 cm^{-1} at 600 °C. Similarly, the G'-band was also shifted from 2701 cm^{-1} at room temperature to 2684 cm^{-1} at 600 °C in IPGF patterns. It was observed in the previous investigation that the G'-band was more sensitive to changes in the electronic band structure that were induced by temperature induced strain [79]. On the contrary, the G-mode is related to the optical phonon which is substantially sensitive to the carrier density instead of temperature-induced strain [80, 81]. Similar peak position shift (around 14 cm^{-1} as can be seen in Figure 3(c)) in the G-band was observed due to the temperature increment (from room temperature to 600 °C), both for HOPG and IPGF samples. However, the G'-band peak shift with increasing

temperature was much higher in the HOPG sample (~ 28 cm^{-1}) compared to IPGF (~ 19 cm^{-1}) sample (Figure 2.8). These results suggest the higher sensitivity of the G'-band peak position shift is likely due to the higher crystallinity in the HOPG platelets compared to the IPGF patterns. The defect ratio (D/G) of IPGF patterns was ~ 0.26 and the full-width-half-maximum (FWHM) of the G-band was 26.4 cm^{-1}. On the other hand, the FWHM of the G-band of mechanically exfoliated HOPG platelets was ~ 18.6 cm^{-1}, which suggests that our inkjet-printed graphene is comprised of a significant fraction of crystalline graphene platelets with minimal defects.

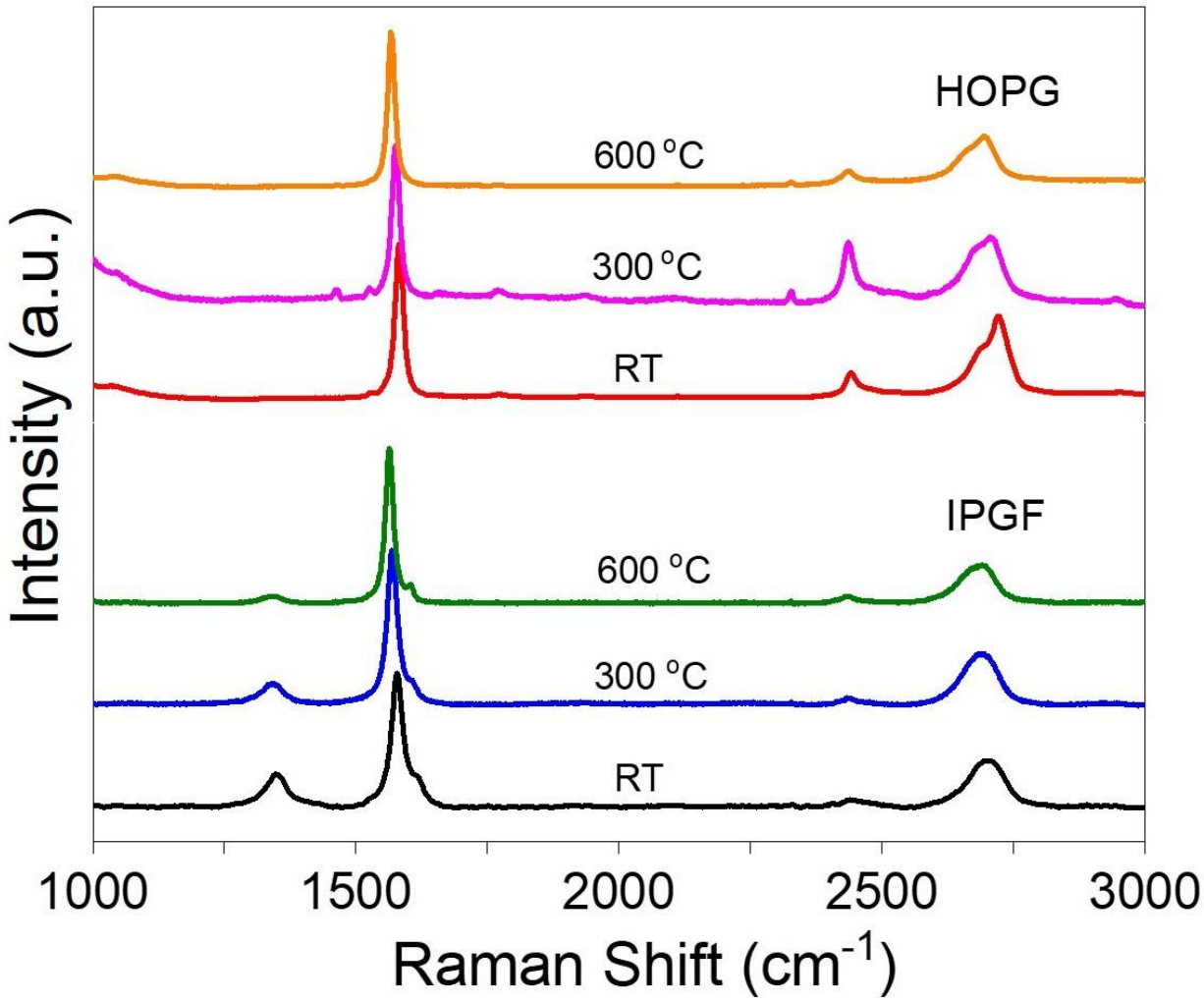

Figure 2.6: Raman spectra of IPGF patterns and HOPG platelets at different temperatures.

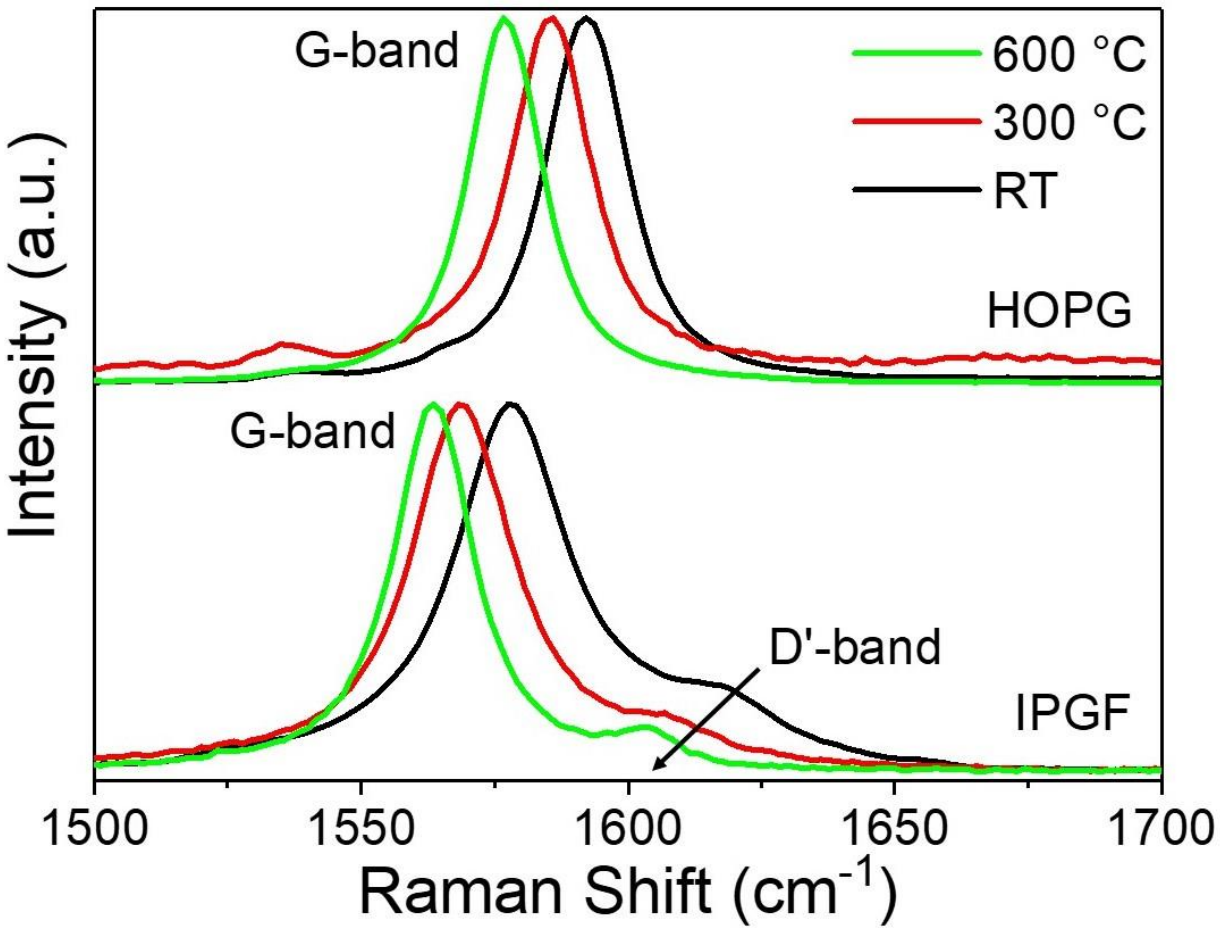

Figure 2.7: Variation of G-band with temperature in IPGF patterns and HOPG platelets.

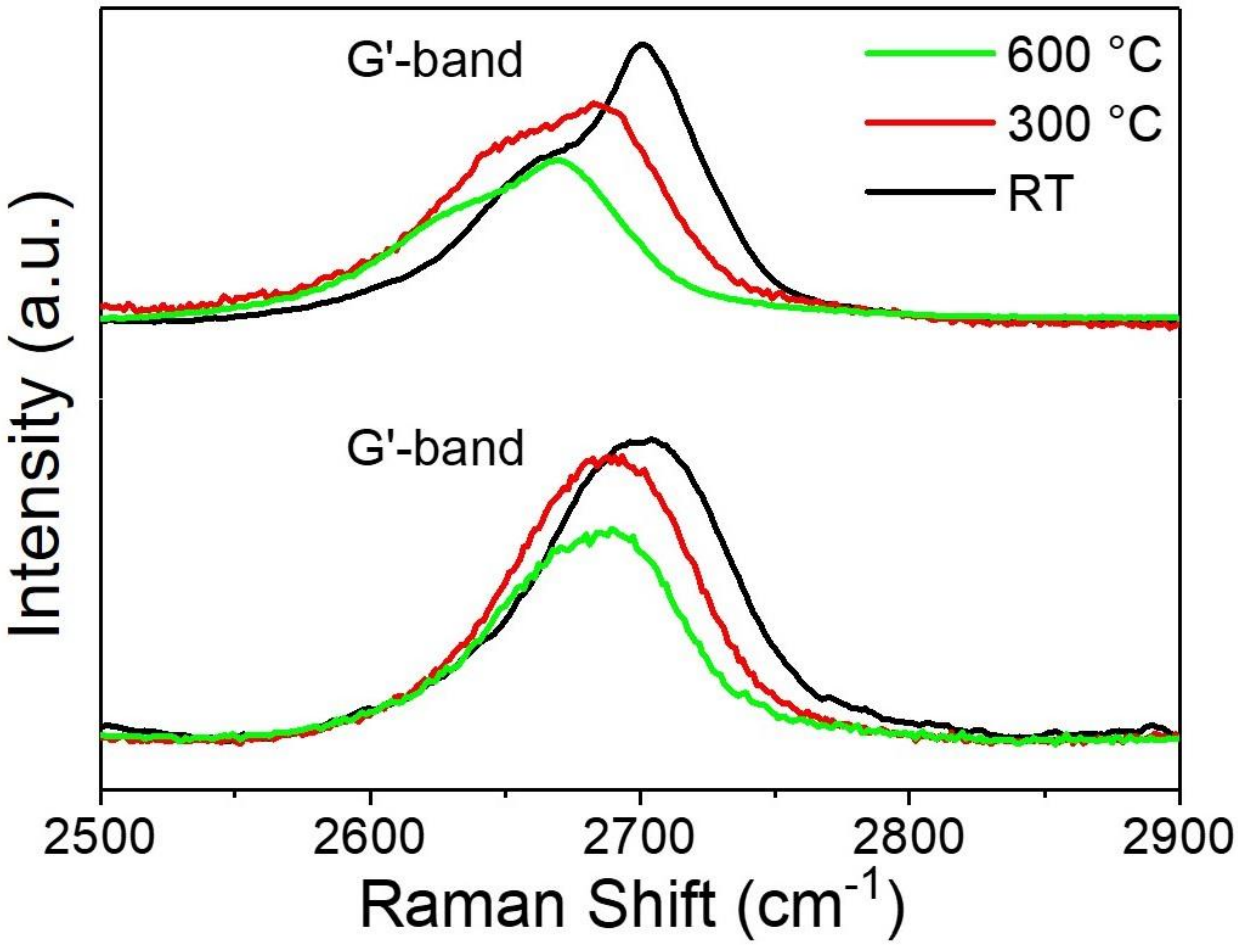

Figure 2.8: Variation of G'-band with temperature in IPGF patterns and HOPG platelets.

2.5 Electronic transport of HOPG and IPGF

In order to investigate the electronic transport properties of both IPGF patterns and HOPG platelets, their electrical properties were measured in terms of current, resistance and power dissipation. In the case of IPGF, 1 mm^2 films were printed with varying printing passes (10, 20, 30, 40 and 50 passes). Figure 2.9(a) represents the variation of current with voltage for HOPG platelets. Figure 2.9(b) shows the variation of current with voltage for IPGF patterns. The resistance obtained from the HOPG platelets measurement was ~ 885 Ω, whereas the resistance obtained from IPGF patterns with 50 passes was ~ 297 Ω which was significantly lower than the HOPG platelets. The thickness of the 1 mm square IPGF patterns were measured using the Bruker DektakXT Stylus Profiler. The thickness increased from ~ 505.37 nm for 10 printing passes to ~ 1667.88 nm for 50 printing passes. The resistivity values ranged from 0.44 mΩ-m to 0.56 mΩ-m with an average value of ~ 0.51 mΩ-m. Figure 2.10(a) and (b) represent the variation of power with voltage for both HOPG platelets and IPGF patterns. It can be seen that even with larger probe separation distances and a number of passes as low as 10 passes, our chemically exfoliated inkjet-printed graphene films showed power comparable to mechanically exfoliated HOPG platelets, i.e. 1.03 mW and 1.13 mW, respectively. With an increasing number of passes, the power dissipation in the IPGF patterns increased significantly compared to the HOPG platelets. Figure 2.11 and Figure 2.12 provide a comparative analysis for resistance and power of HOPG platelets and IPGF patterns with varying number of passes. Electrical transport of inkjet-printed graphene patterns showed high currents (up to 3.35 mA at 1 V), high powers (up to 3.35 mW at 1 V) and low resistance (down to 297 Ω) values as compared to previously reported work for inkjet-printed graphene [45, 82, 83]. This suggests the presence of a continuous network of graphene platelets with a high mass fraction to yield electrically conducting IPGF graphene films. Higher power and

lower resistance may be obtained by increasing the number of passes even further beyond 50 passes. However, the present study also aims to minimize the number of passes to efficiently save time and promote productivity from a practical standpoint toward a manufacturing platform.

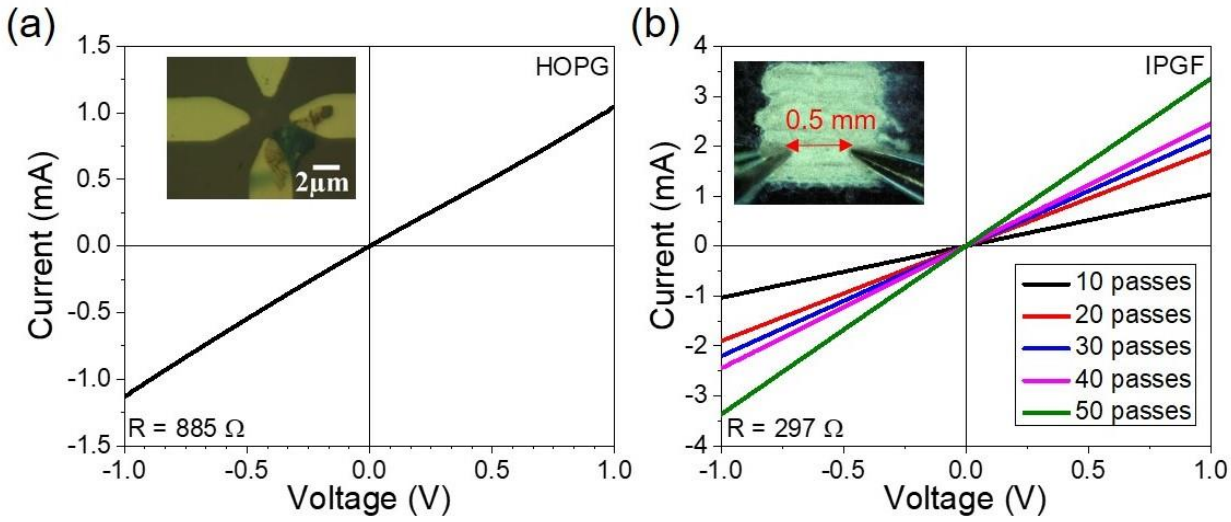

Figure 2.9: Current as a function of voltage for (a) HOPG platelets and (b) IPGF patterns.

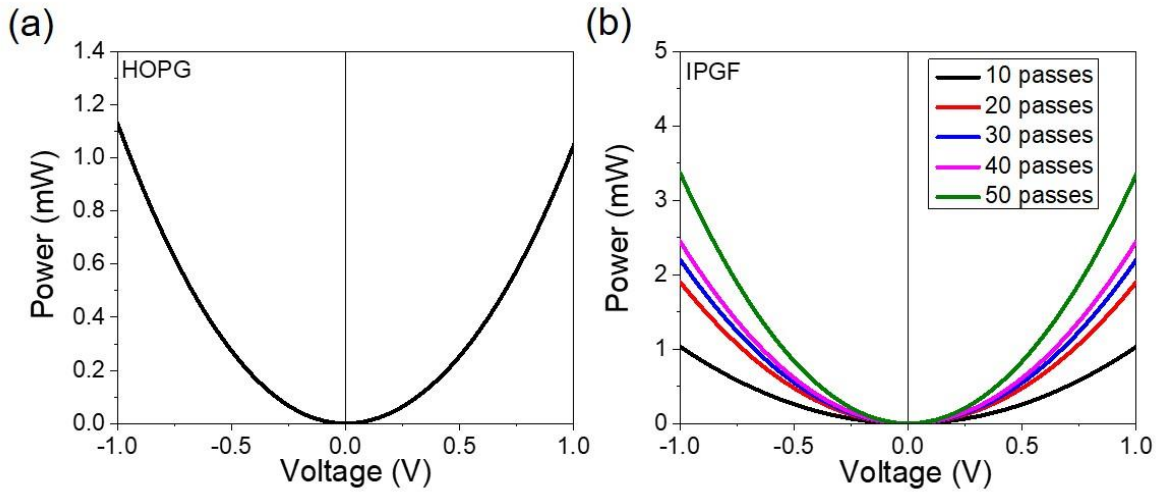

Figure 2.10: Variation of power with voltage for (a) HOPG platelets (b) IPGF patterns.

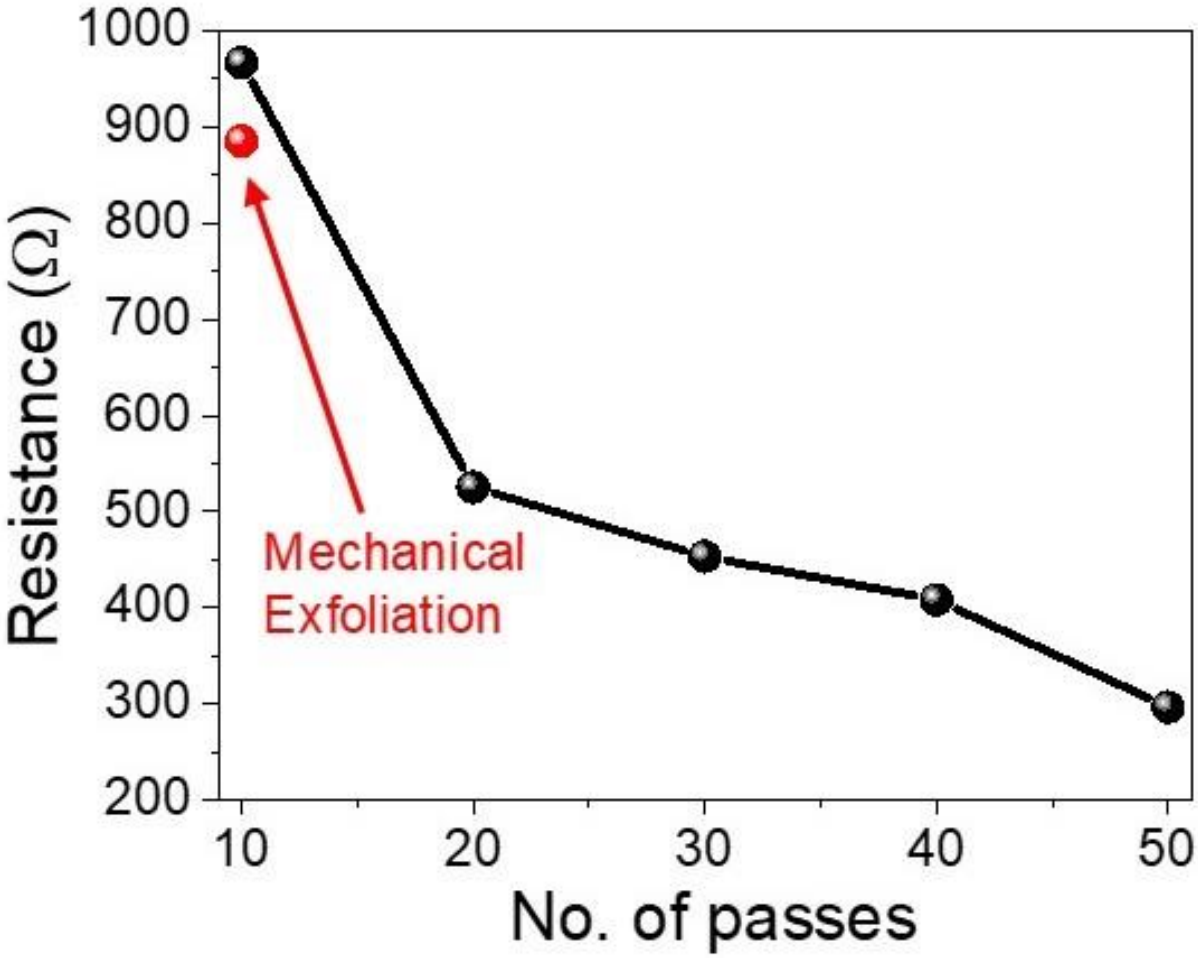

Figure 2.11: Variation of resistance with number of printing passes.

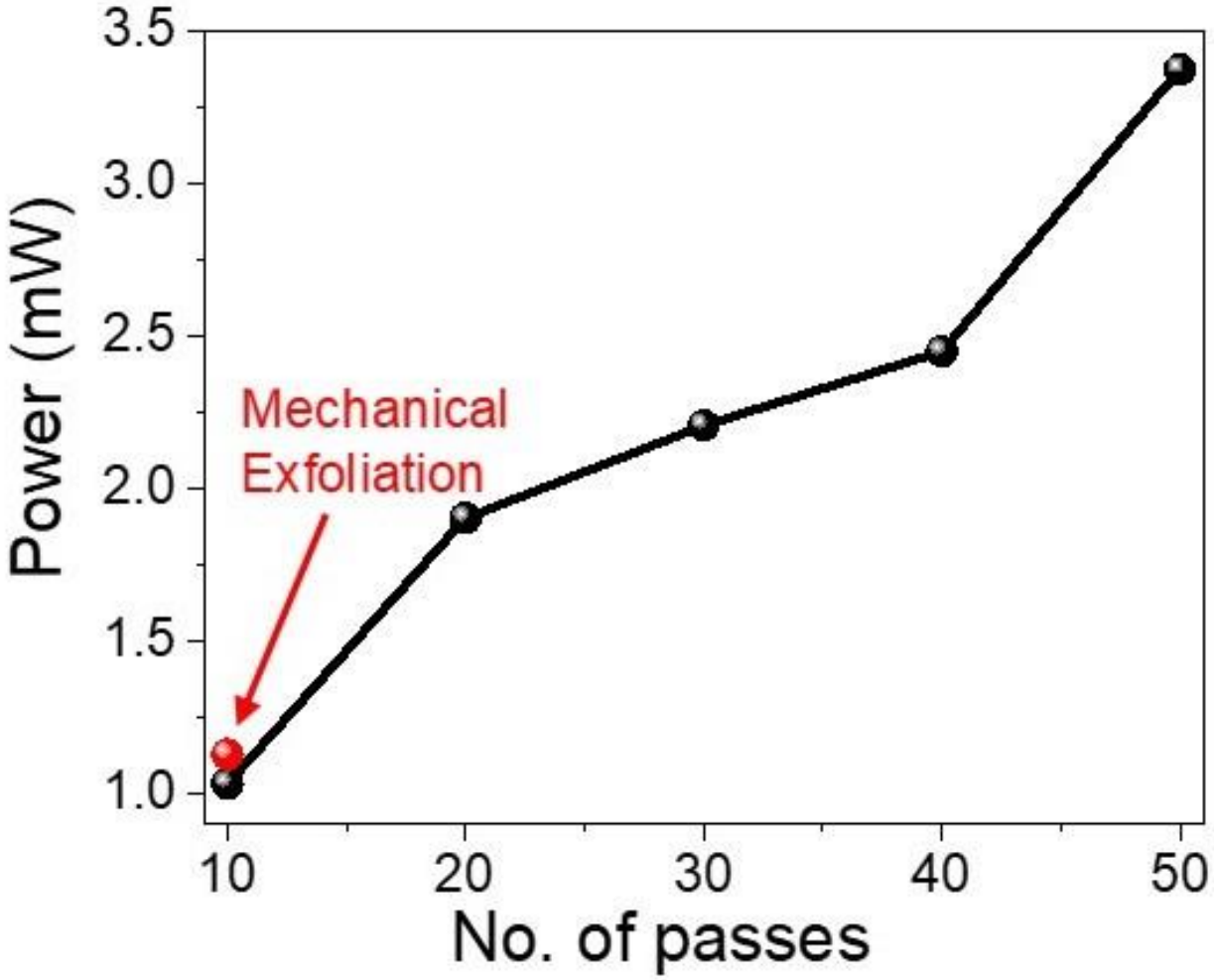

Figure 2.12: Variation of power with printing passes.

2.6 Length-dependent electronic properties of IPGF

A geometrical scaling study of our printed graphene lines was also conducted. Line patterns with 1 mm width but with increasing lengths (1, 2, 3, 4 and 5 mm) were printed with 50 passes to gauge the scalability of electronic transport properties of inkjet-printed features. Scalability refers to accurately printing patterns of large dimensions, and though up to 5 mm was used in this study, this by no means represents an upper limit for what is possible with inkjet printing where roll-to-roll processes are commonly used in printed and flexible electronics. Figure 2.13 shows an optical image of the printed graphene films with varying lengths on SiO_2/Si substrates. Figure 2.14 represents the variation of current with voltage and length in IPGF patterns. It can be observed that the change in current values is appreciable when the probe separation distance increases from 1 mm to 3 mm but not significantly altered after 3 mm. This suggests that after 3 mm length, current values will not significantly decrease when the number of passes is kept constant. Figure 2.15 shows the increase in resistance of printed graphene films with increasing length. Linear resistivity (slope of resistance versus length plot) of 281.98 Ω/mm was obtained for printed graphene films with increasing linear scaling. Figure 2.16 illustrates the variation in power with voltage with varying line length of the printed graphene patterns. The highest power value was observed in printed graphene pattern with 1 mm length and sequentially decreased with increasing pattern length (Figure 2.16). However, comparable current, resistance, and power values were observed at 5 mm line length compared to mechanically exfoliated HOPG platelets. The good carrier conduction in the IPGF patterns can be attributed to graphene nanomembranes which are continuously distributed over large areas without any visible signs of clustering or aggregation as is evident from the optical and SEM micrographs in Figure 2.17 and Figure 2.18, respectively.

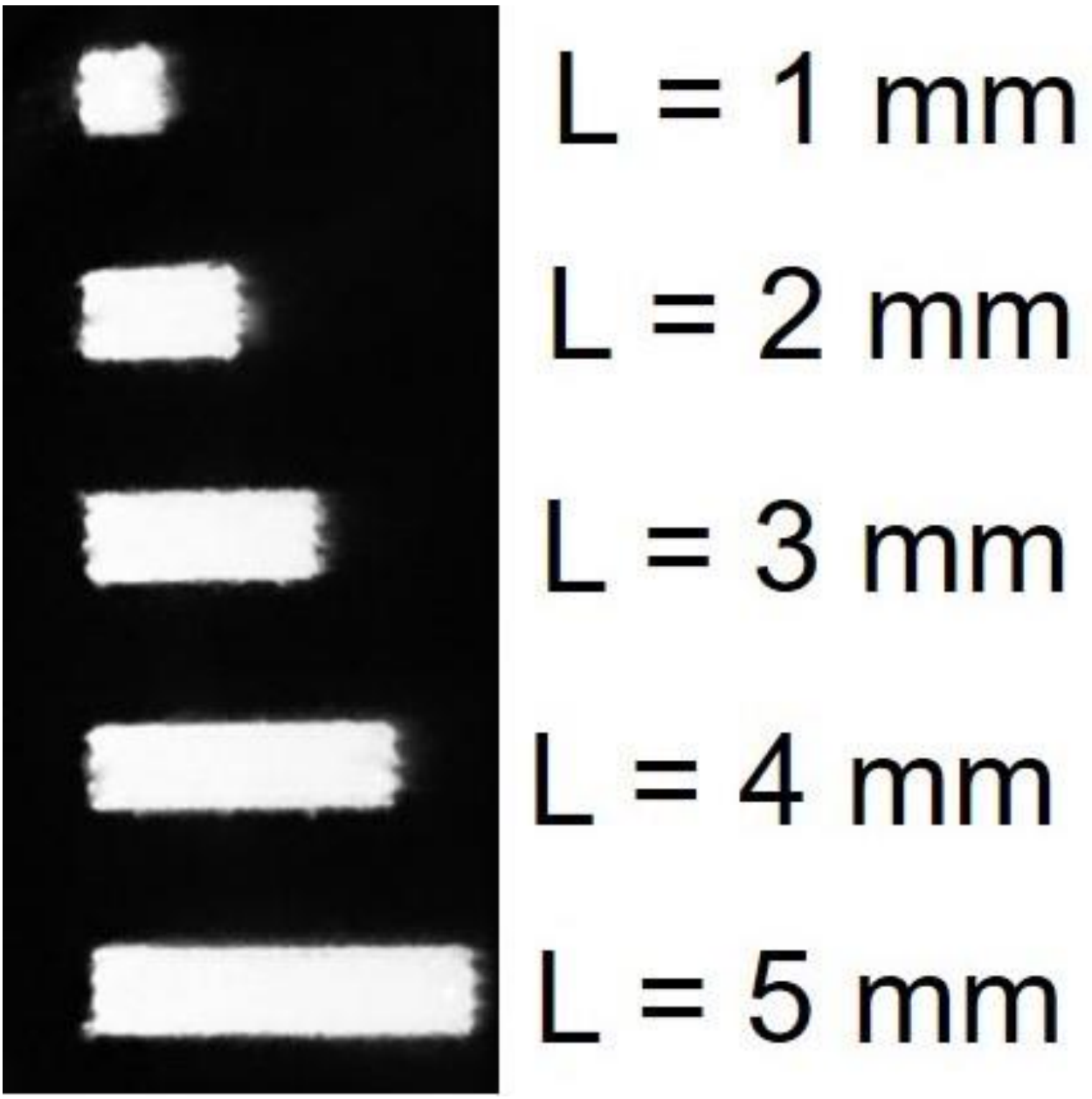

Figure 2.13: Photograph of graphene printed lines with varying length, L (1, 2, 3, 4 and 5 mm).

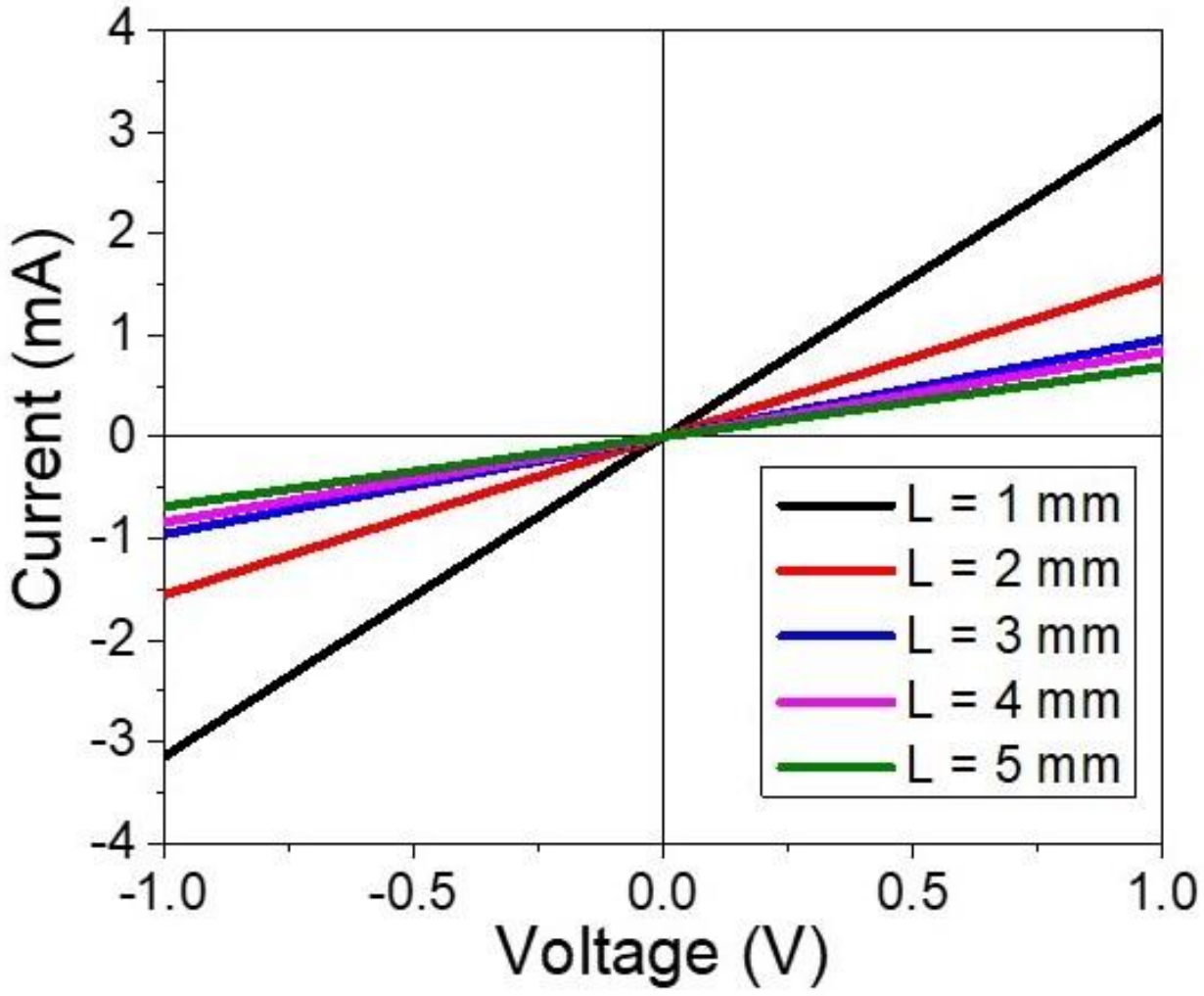

Figure 2.14: Variation of current with voltage and line length for graphene patterns.

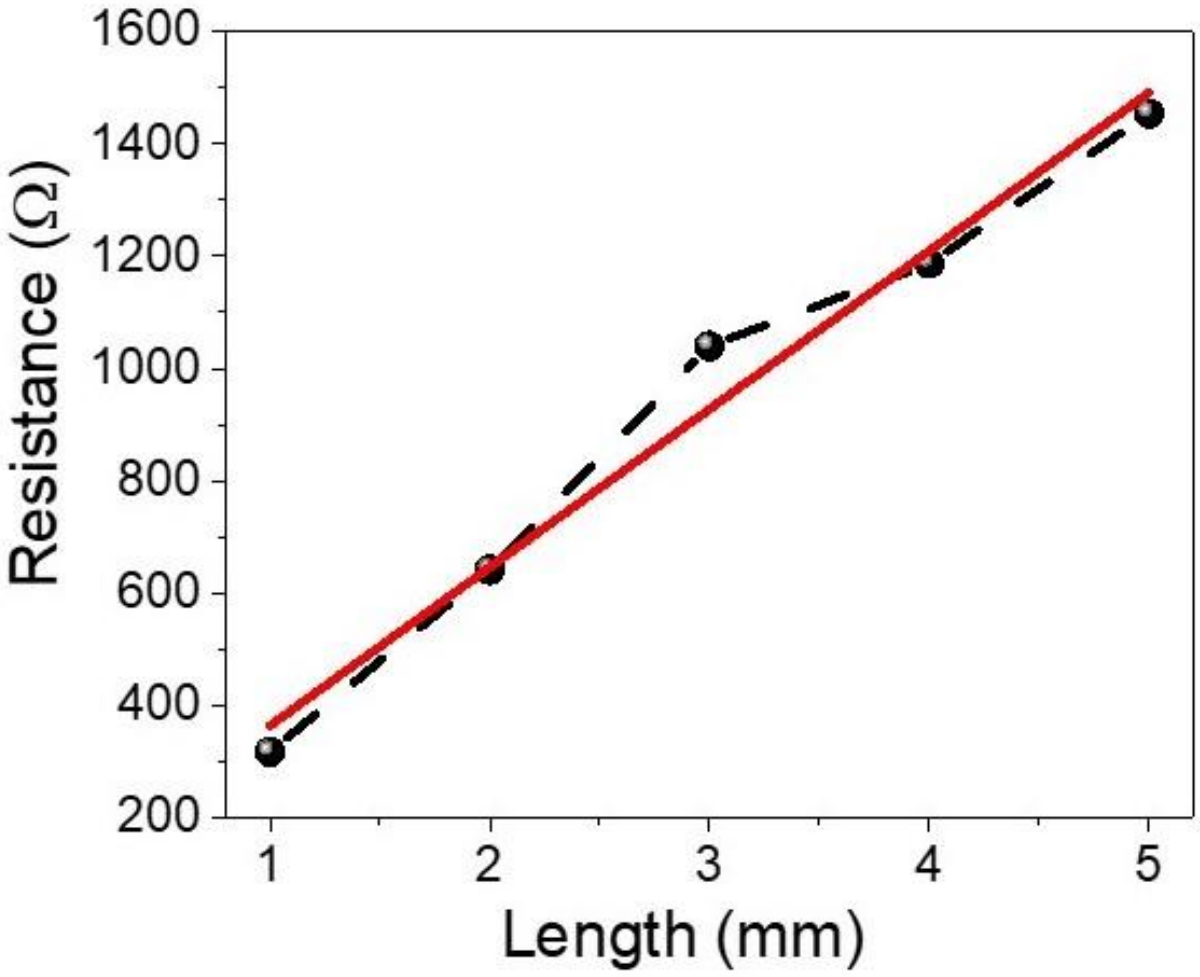

Figure 2.15: Resistance as a function of length for graphene printed patterns.

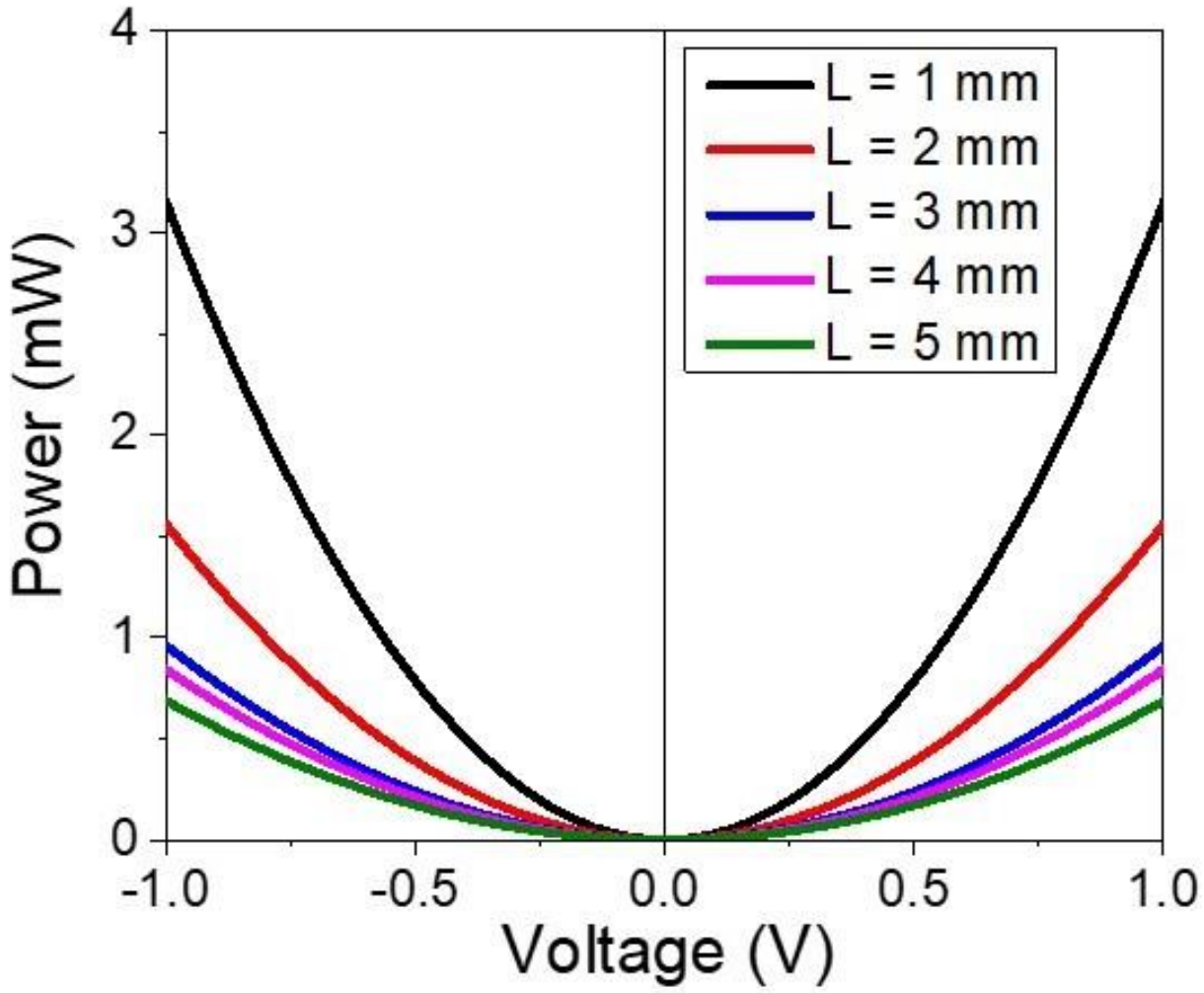

Figure 2.16: Variation of power with length for graphene printed patterns.

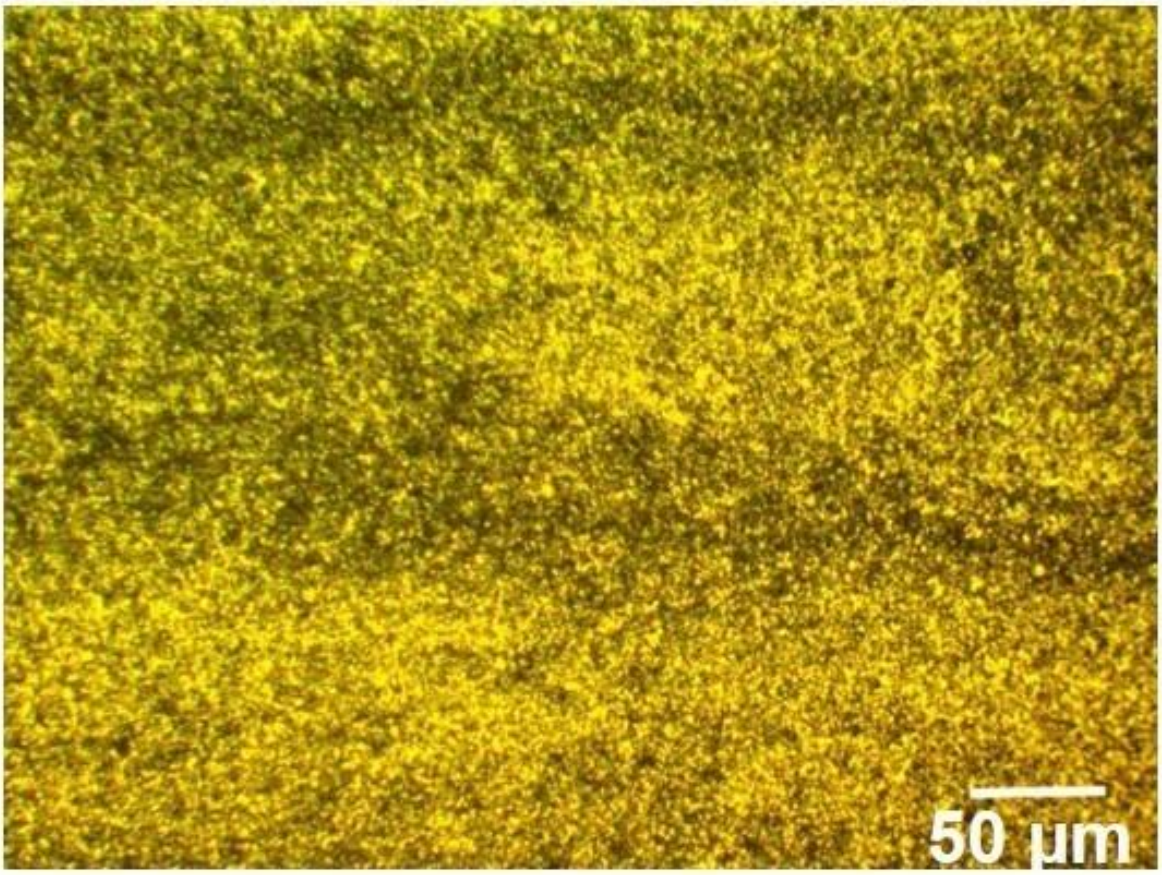

Figure 2.17: Optical micrograph of the center of inkjet-printed graphene films, showing large-area uniformity.

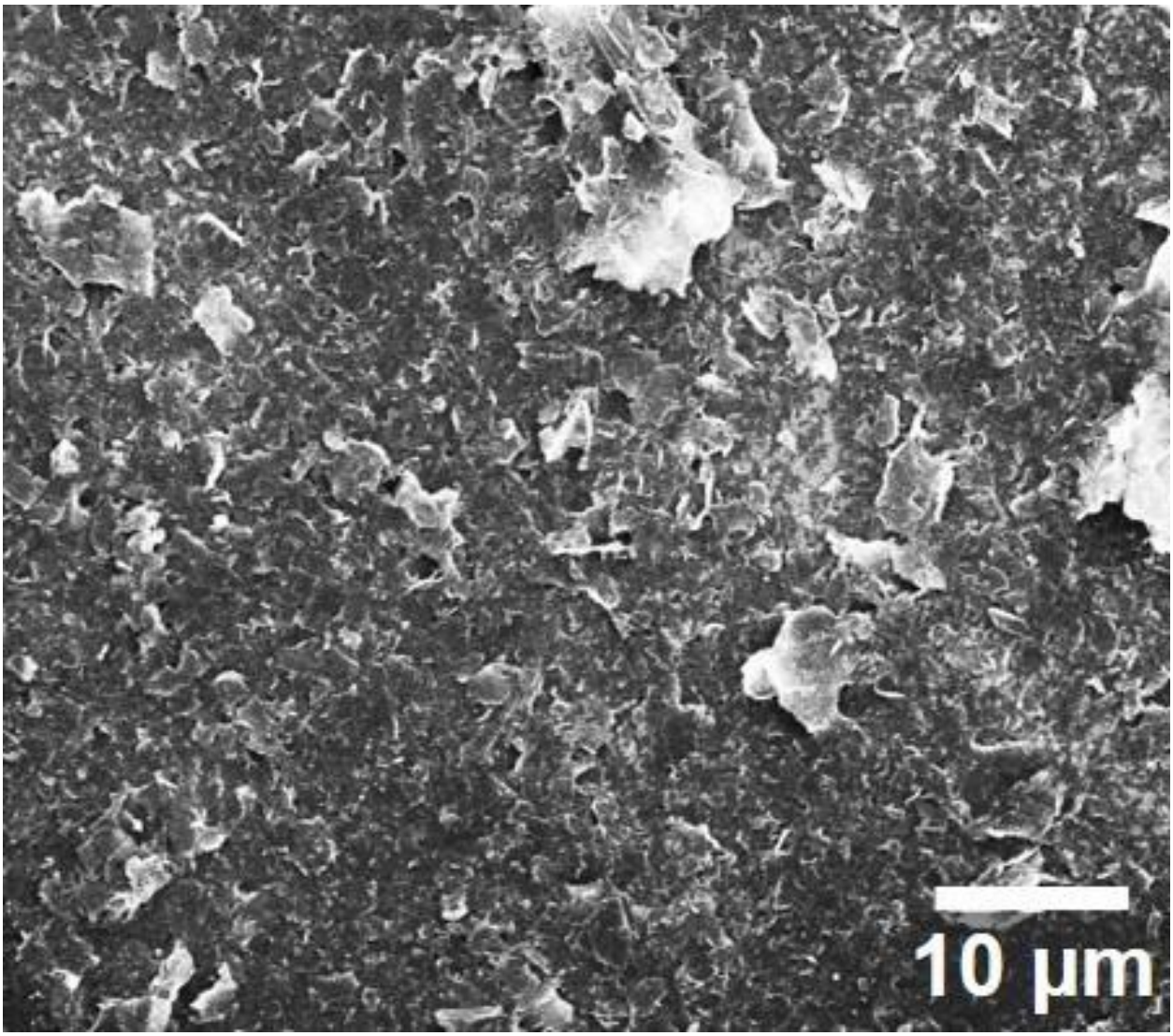

Figure 2.18: SEM image of inkjet-printed graphene films over large areas depicting a continuous network of graphene on the substrate.

2.7 Conducting graphene contacts for photodetectors

To demonstrate the application of our graphene inks as conducting contacts, graphene/WS_2 photodetector was fabricated by first printing two 3 mm square graphene patterns with 30 printing passes and 1 mm spacing in between. This was followed by annealing at 250 °C for 2 hours. The WS_2 inks were then prepared using a similar procedure as used to formulate the graphene inks. The channel of WS_2 with length and width ranging from 2 mm and 1 mm, respectively, was then printed using 30 printing passes followed by annealing at 250 °C for 2 hours. Figure 2.19 shows the photoresponse of inkjet-printed graphene/WS_2 based photodetector up to 20 seconds with 0.5 seconds of laser pulse time when a stream of radiation pulses was applied to the active area of the device. The inkjet-printed device is shown in the inset of Figure 2.19. Figure 2.20 depicts a magnified region of a single laser on/off pulse. From this, the rise time and decay time of ~ 4.53 ms and 4.81 ms were observed, as shown in Figure 2.21 and Figure 2.22, respectively. Thus, it is clear that the graphene-based inks serve as an adequate interconnect for printed electronics applications, where its integration with a semiconducting WS_2-based ink served as a prototype demonstration of high-performance, high-speed photodetector devices.

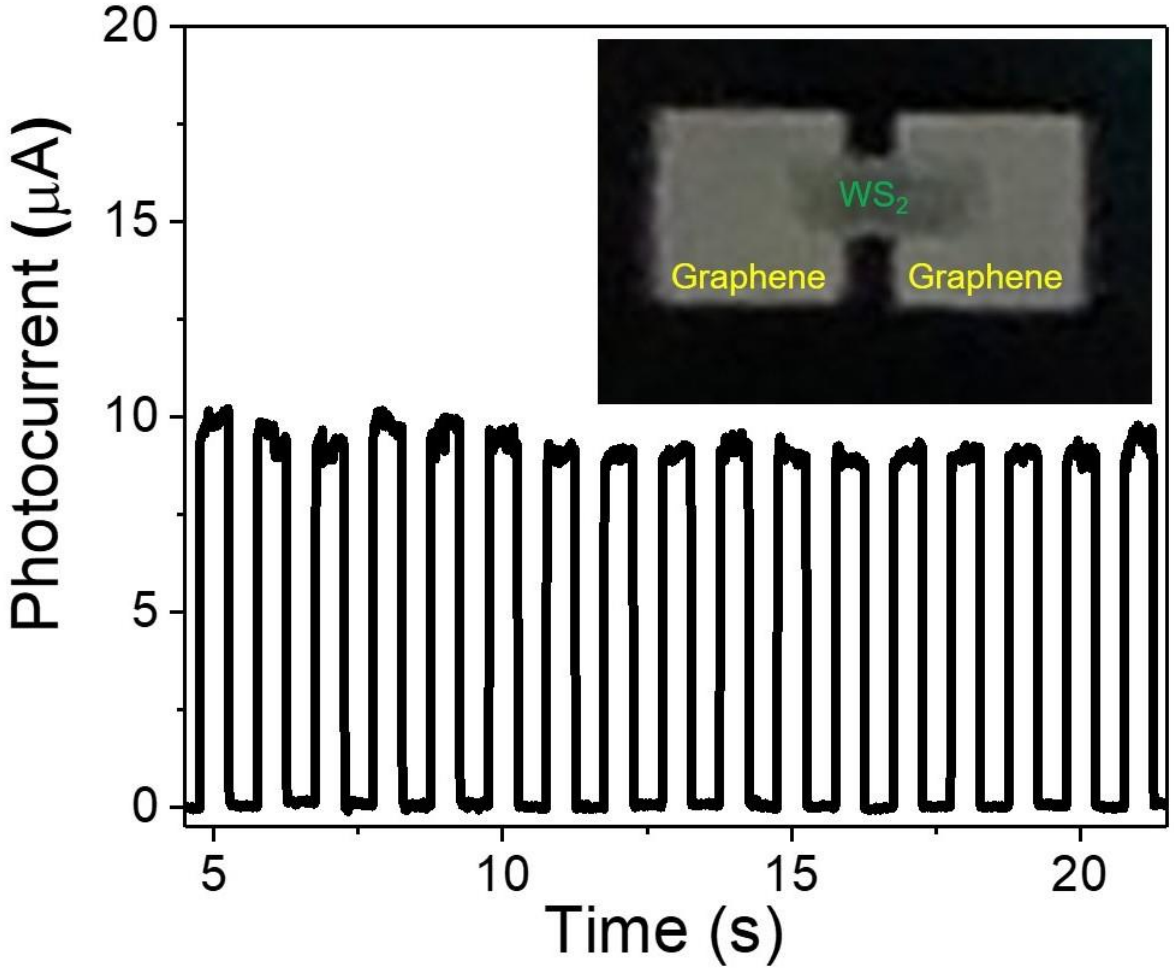

Figure 2.19: (a) Photoresponse of inkjet-printed graphene/WS_2 based photodetector up to 20 seconds. Inset: photograph of inkjet printed graphene/WS_2 based photodetector.

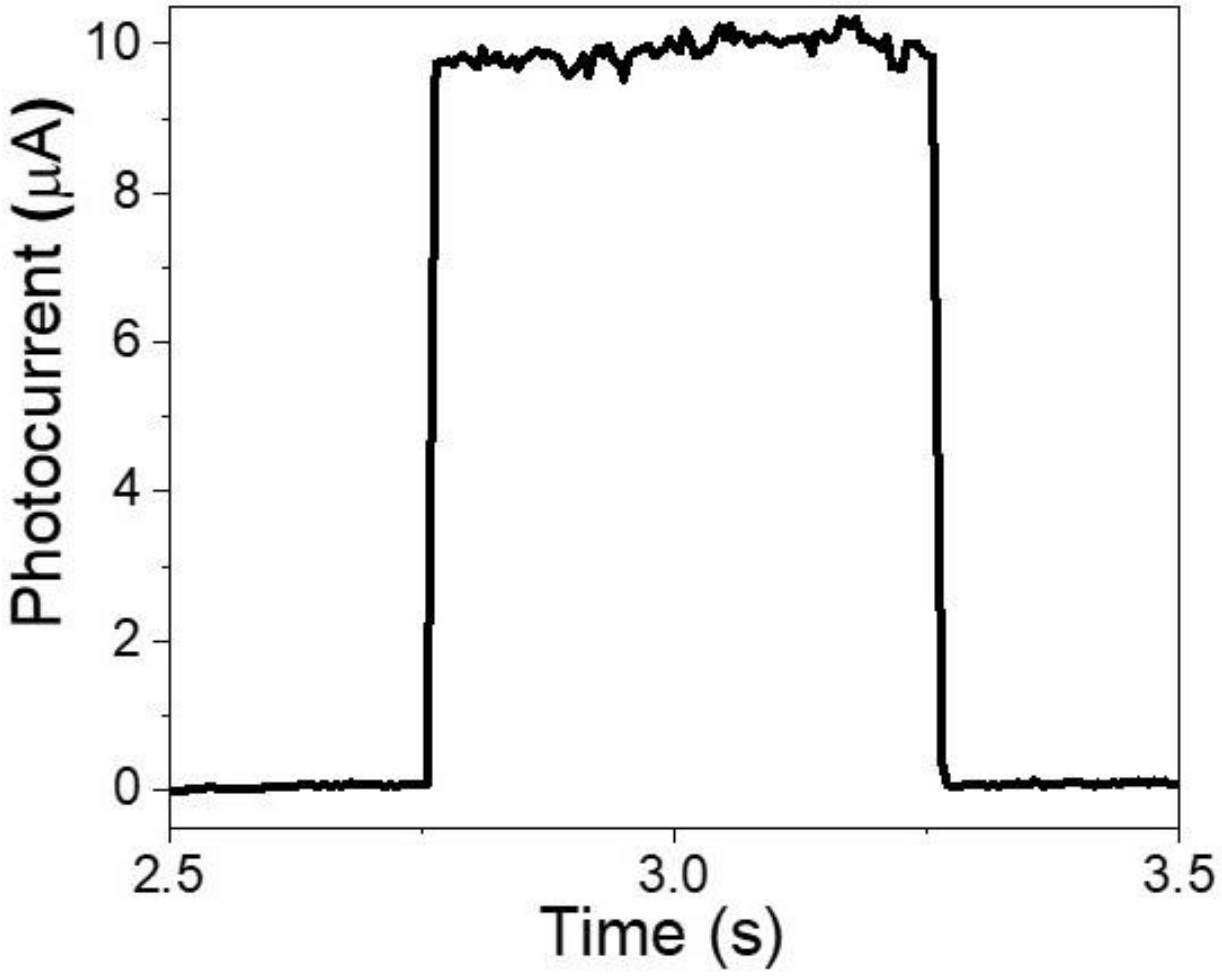

Figure 2.20: Variation of photocurrent with time for a single laser on/off cycle.

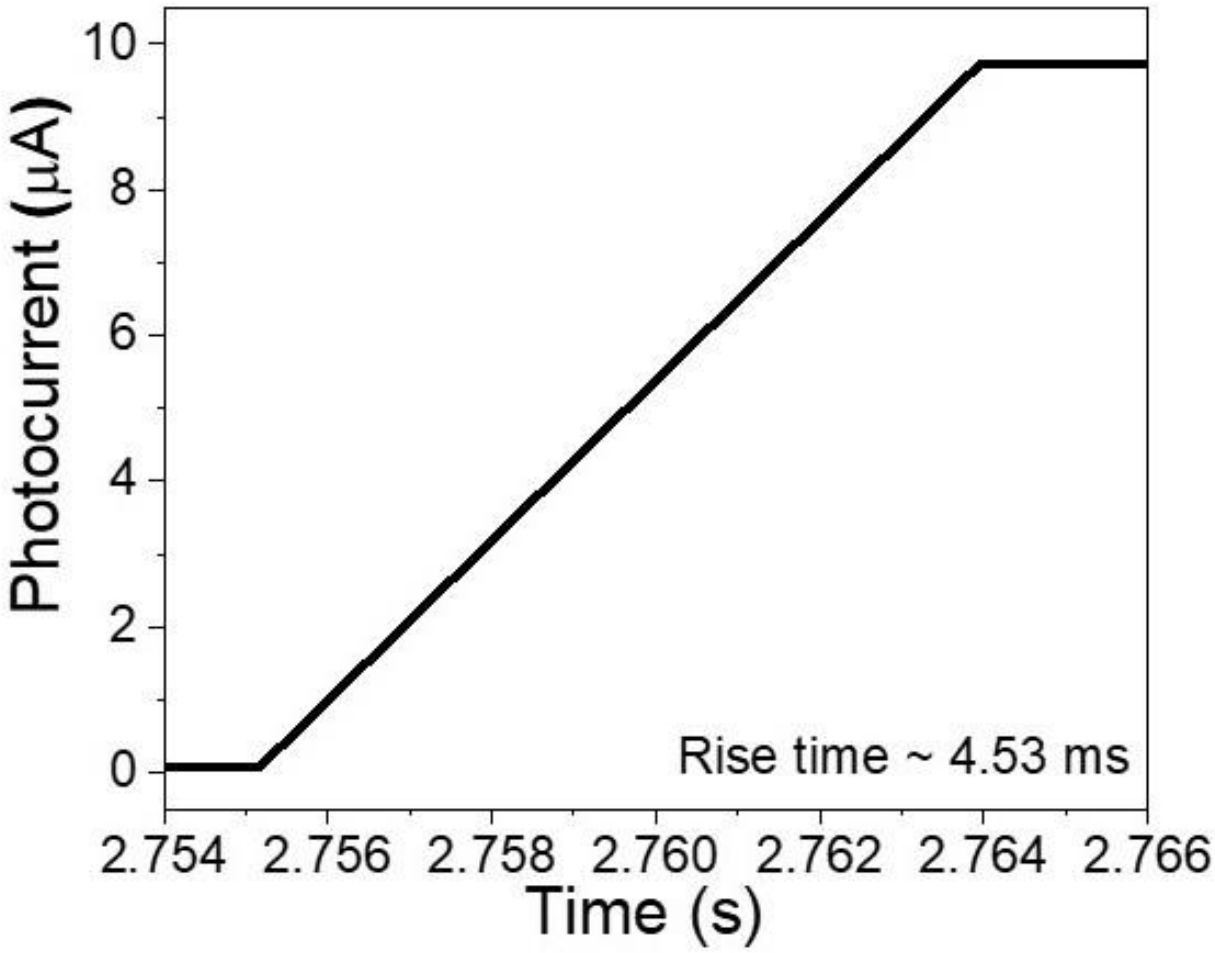

Figure 2.21: Photocurrent-time graph showing rise time of 4.53 ms.

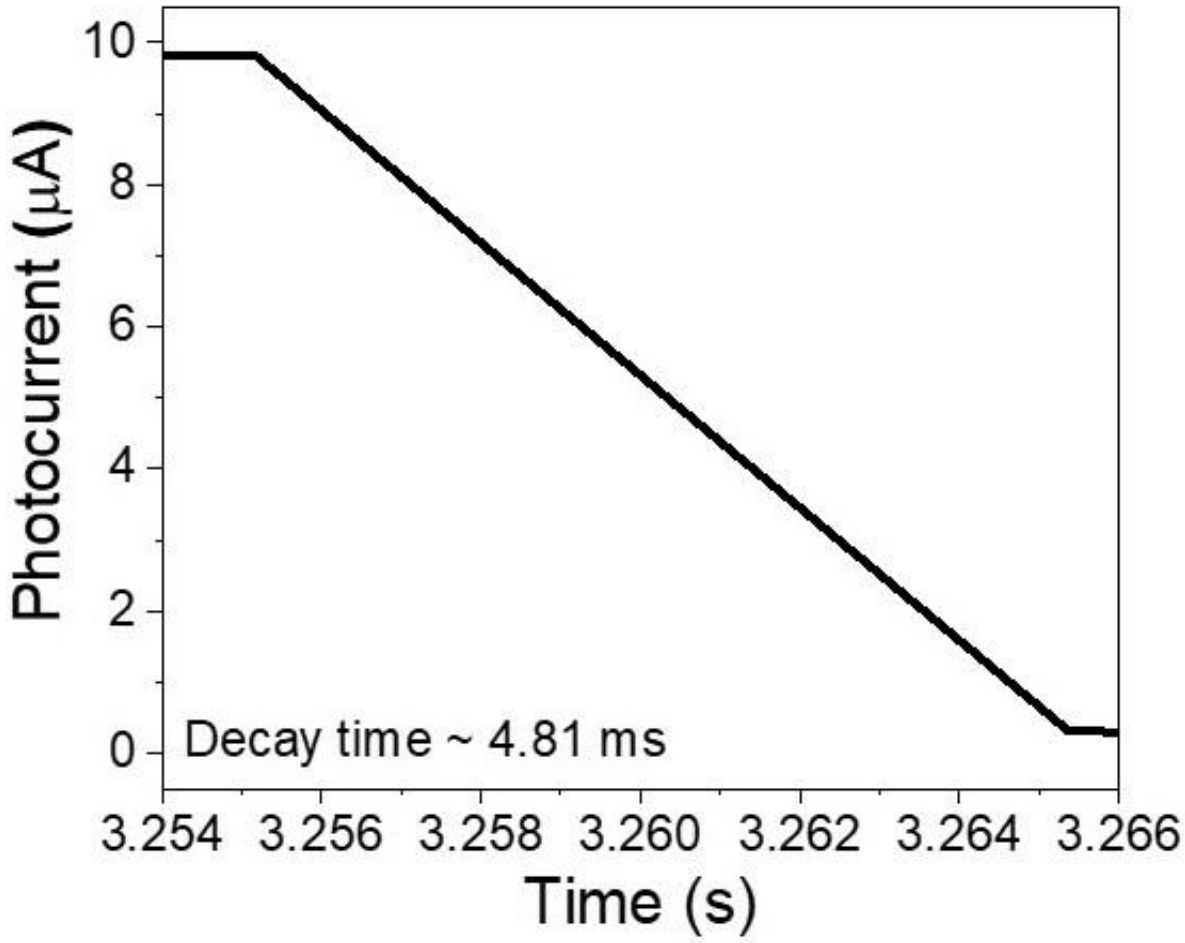

Figure 2.22: Photocurrent-time graph showing decay time of 4.81 ms.

Chapter 3: Inkjet printing of liquid-exfoliated, highly conducting graphene/PEDOT: PSS nanosheets for organic electronics

Surfactants used to achieve desired viscosity for inkjet printing can be divided into two categories- conductive and non-conductive. Both promote stabilization of dispersed 2-D nanosheets [84, 85, 86], however, use of conducting polymer like PEDOT: PSS (poly(3,4 ethylenedioxythiophene) poly(styrenesulfonate)), as a surfactant helps in enhancing electrical conductivity in applications where high electrical conductivity is desired [87, 88]. Graphene/PEDOT: PSS inks have found applications in gas, electrochemical and biochemical sensing [89, 90, 91]. This work utilizes the conductive property of PEDOT: PSS polymer surfactant to demonstrate good electronic transport properties of graphene/PEDOT: PSS inkjet printed films and promotes inkjet printing as a scalable approach to yield printed features with the desired high electrical transport properties.

3.1 Materials and methods

Graphite powder in the amount of ~ 15 mg/ml was obtained by breaking graphite rod (Sigma Aldrich #496553) and placed in a glass vial and 10 ml NMP (Sigma Aldrich #270458) was then added. The solution was sonicated in a Branson 2800 bath sonicator for 48 hours. 0.25 weight% PEDOT: PSS was then added to the solution and magnetic stirred for 1 hour at 100 rpm. This was our final conductive ink. Ink preparation procedure is shown in Figure 3.1. PEDOT: PSS used in the present study was 1.1 weight% PEDOT: PSS in water solution (Sigma Aldrich #739332).

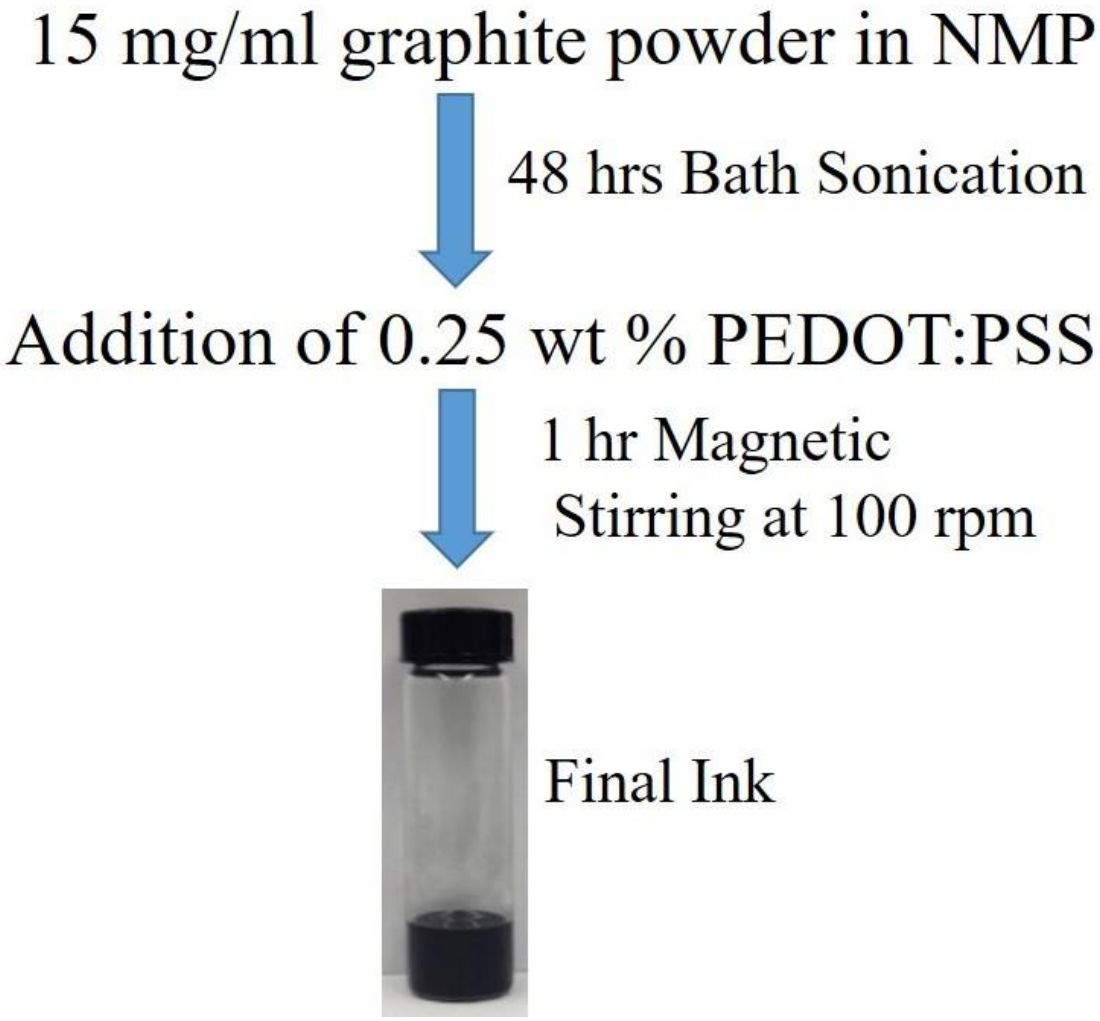

Figure 3.1: Schematic representation of ink preparation procedure.

PEDOT: PSS was added primarily to obtain a viscosity of about 12 cP which is ideal for inkjet printing. It also prevents particle agglomeration and improves suspension stability. Graphene/PEDOT: PSS ink was characterized by optical absorption spectroscopy using CARY 5000 spectrophotometer. DMP-2800 series Fujifilm Dimatix Materials Printer with a printhead consisting of 16 inkjet nozzles was used to print various patterns in this work. Annealing of printed patterns was done at 250^0C for 2 hours to remove solvents. Cartridge temperature of 30^0C and platen temperature of 60^0C was used during all the printing work.

3.2 Optical characterization of graphene/PEDOT: PSS inks

Optical absorption study was conducted to observe the effectiveness of the exfoliation and dispersion, where the absorption measurements of the graphene/PEDOT: PSS solutions was conducted in the visible range (400-700 nm). NMP was used as the reference sample. High values of optical absorbance were found indicating good uniform dispersibility and high concentration of graphene and PEDOT: PSS in NMP as shown in Figure 3.2. These high values of absorbance are attributed to nanodispersions of graphene and PEDOT: PSS particles which were confirmed by optical micrograph of annealed graphene/PEDOT: PSS printed line as shown in Figure 3.3.

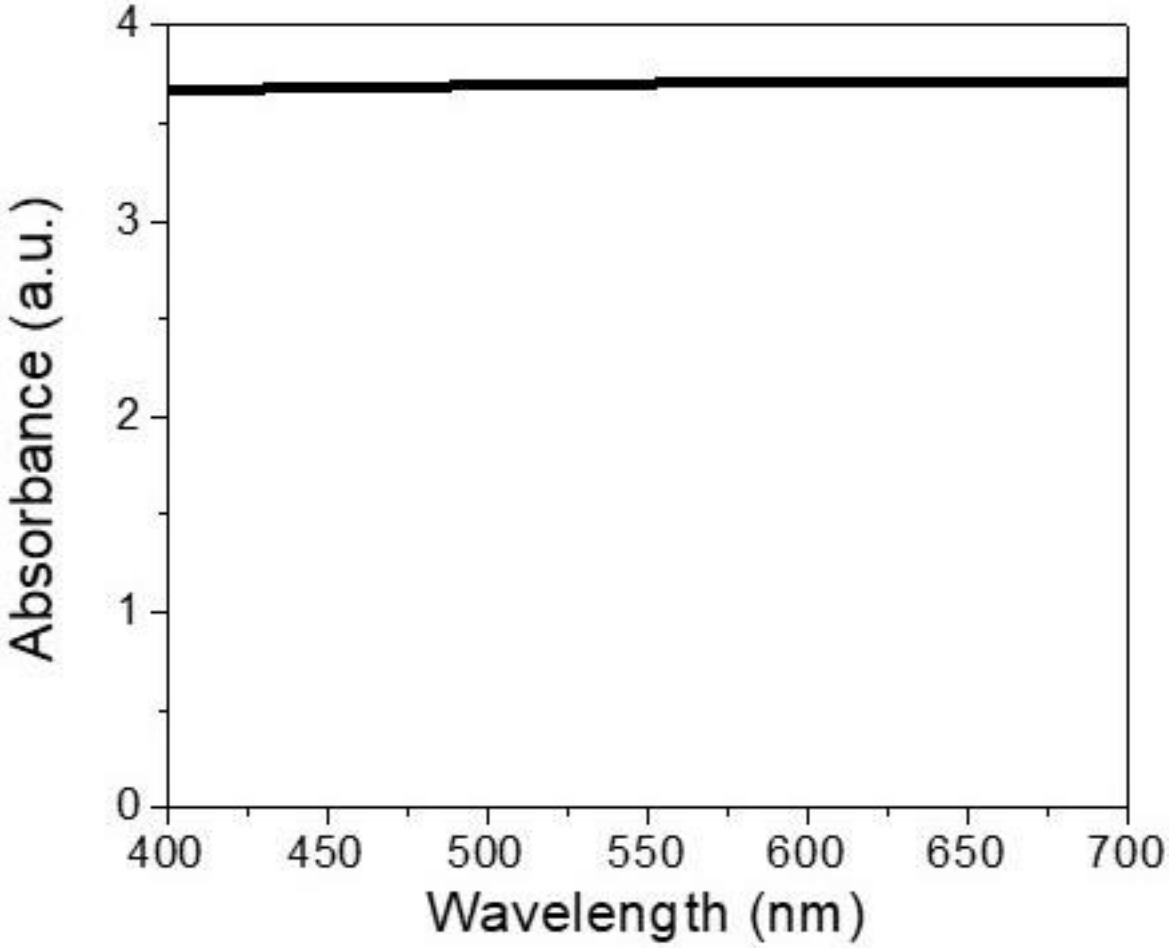

Figure 3.2: Optical absorption spectra of graphene in NMP sonicated for 48 hours.

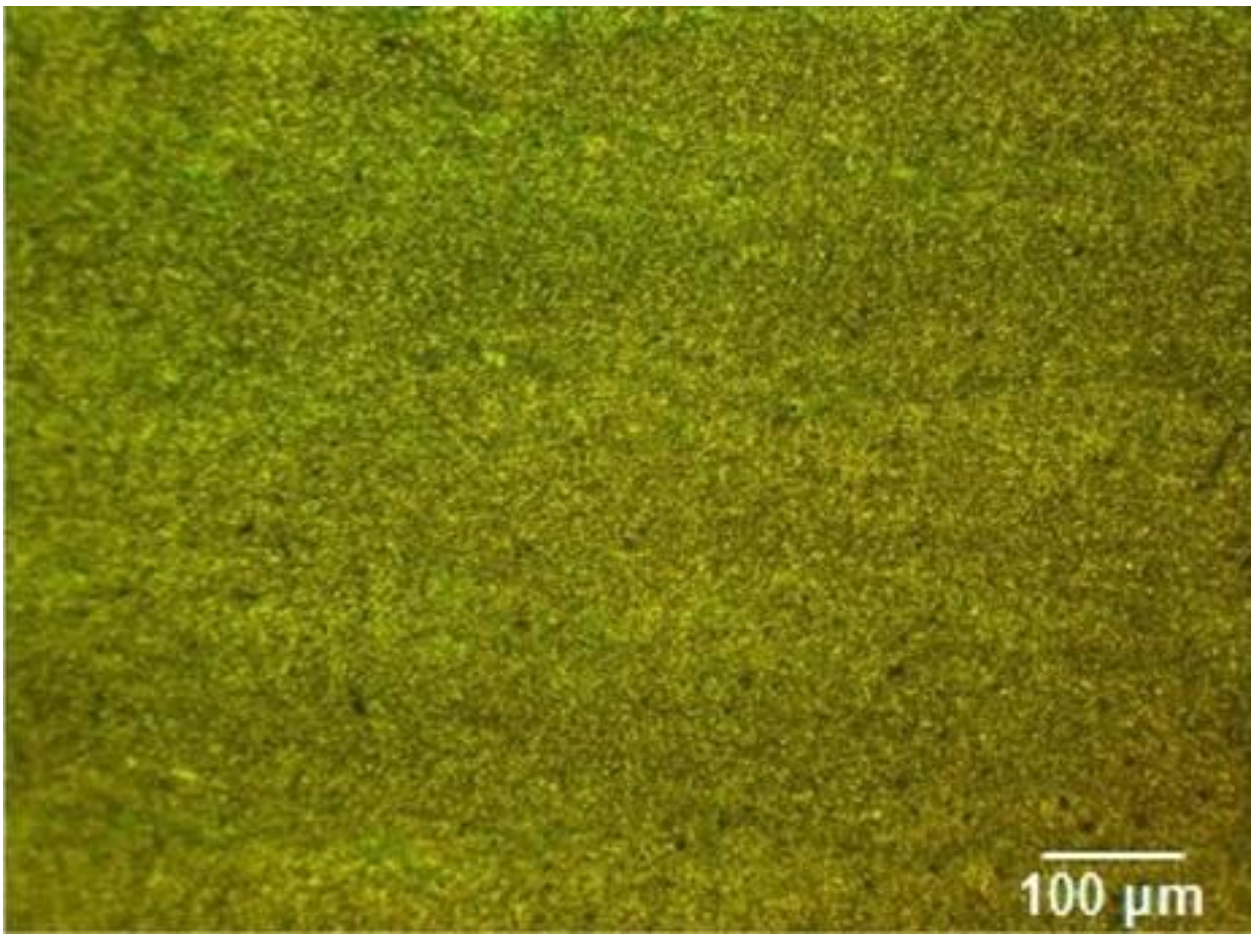

Figure 3.3: Optical micrograph showing graphene/PEDOT: PSS nanosheets.

3.3 Raman spectroscopy of graphene/PEDOT: PSS inks

Raman spectra of annealed printed PEDOT: PSS showed a strong peak at about 1436 cm^{-1} which is ascribed to C=C stretching [92, 93, 94, 95] as shown in Figure 3.4. Raman spectra of annealed printed graphene/PEDOT: PSS showed D-band, G-band, G^{*}-band and G'-band of graphene and PEDOT: PSS peak at about 1436 cm^{-1} indicating uniform mixing of graphene and PEDOT: PSS nanoparticles as shown in Figure 3.5. No other significant peaks were observed as NMP solvent was removed completely by annealing at a temperature of 250 ^{o}C for 2 hours which is well above its boiling point.

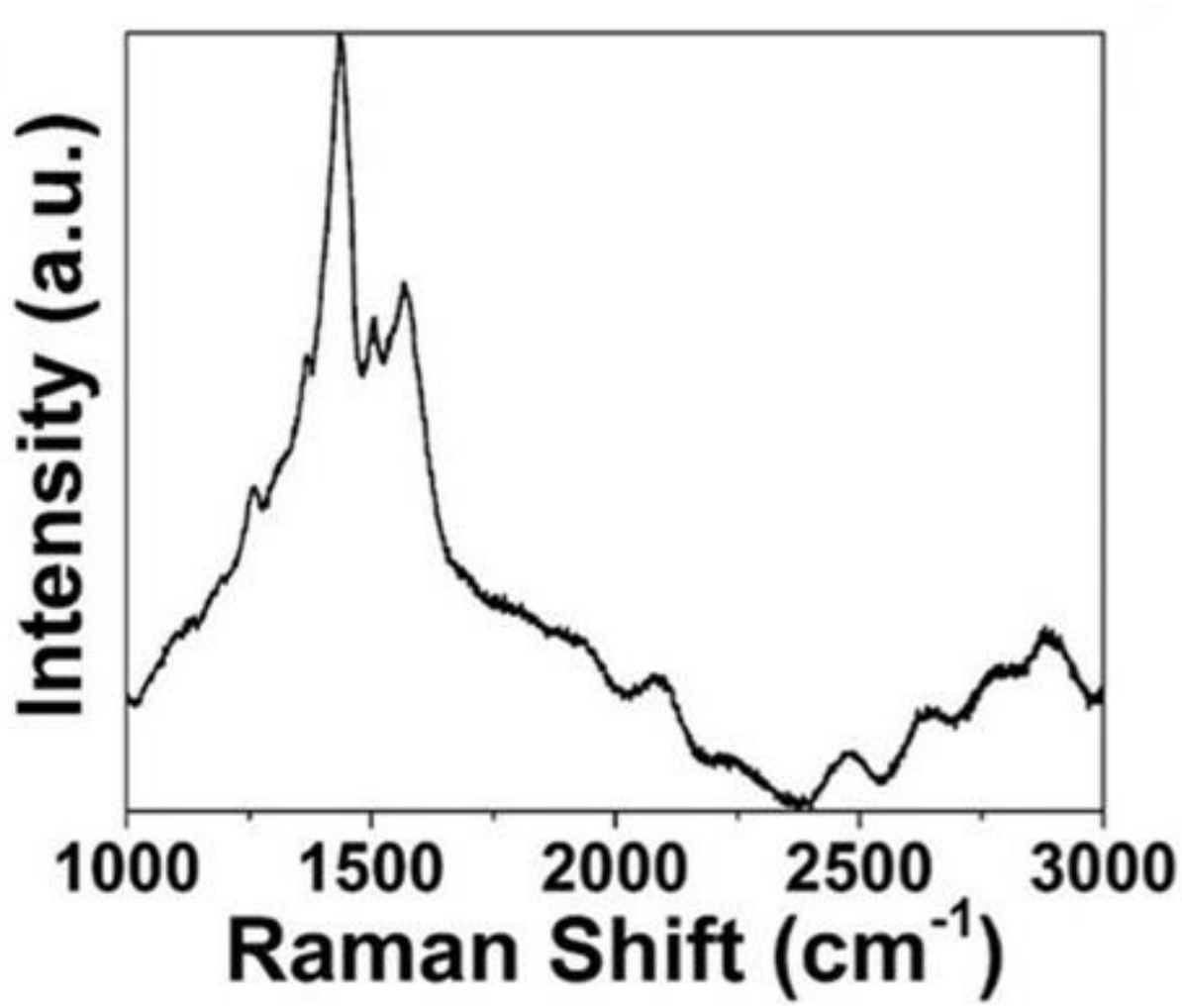

Figure 3.4. Raman spectra of annealed printed PEDOT: PSS patterns.

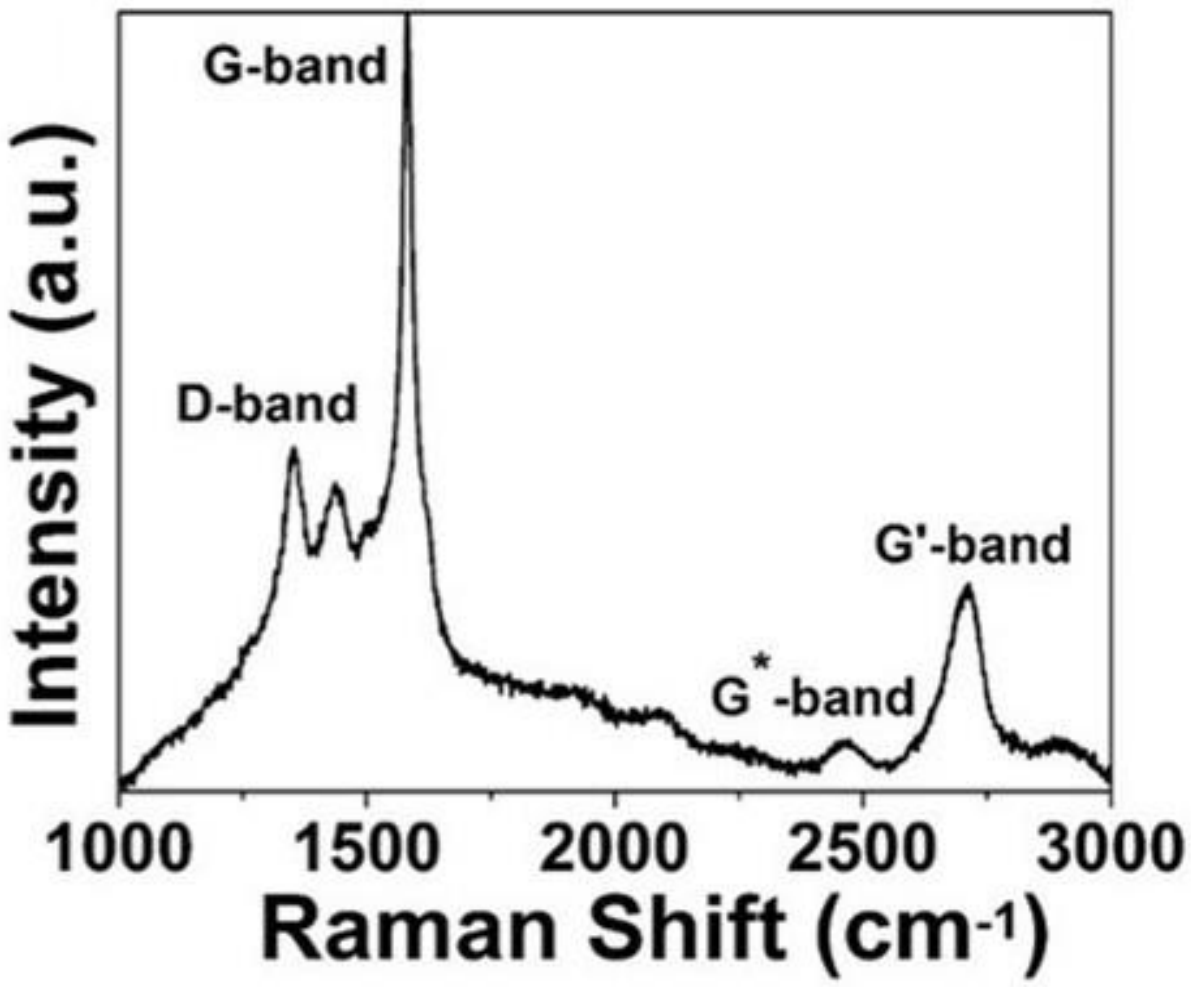

Figure 3.5: Raman spectra of annealed printed graphene/PEDOT: PSS patterns.

3.4 Inkjet printing of PEDOT: PSS and graphene/ PEDOT: PSS inks

Lines of 5 mm length and 1 mm width were printed first with 2.5 weight% PEDOT: PSS in NMP [Figure 3.6] and then with graphene/2.5 weight% PEDOT: PSS in NMP [Figure 3.7] followed by annealing at 250^0C for 2 hours to remove NMP solvent. Good resolution and uniform printability was observed during printing of both inks. This was done to study and compare the optical and electrical behavior of PEDOT: PSS in NMP inks with and without graphene. Lines of different lengths (1, 5, 10, 15, 20 and 25 mm) with 50 number of printing passes [Figure 3.8] were printed to show good dimensional accuracy and scalability of inkjet printing process.

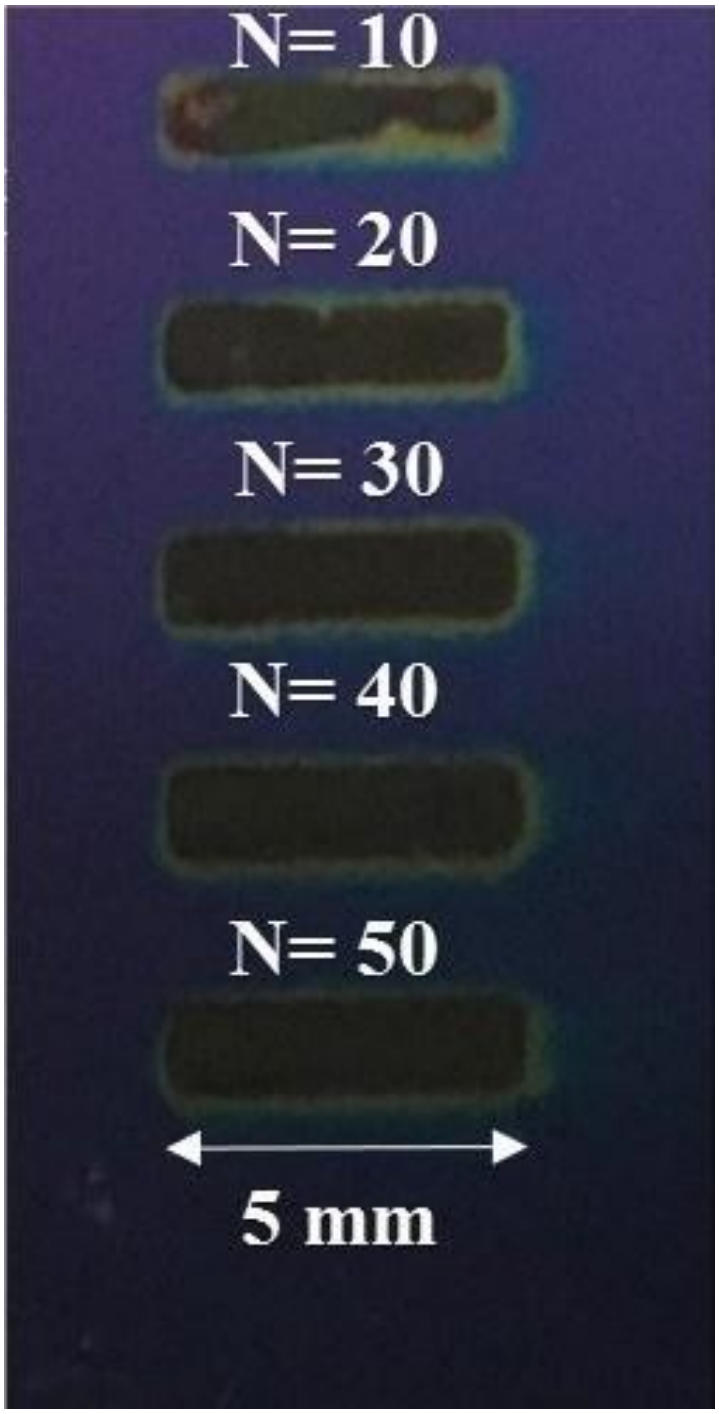

Figure 3.6: 5 mm length and 1 mm width line patterns of annealed PEDOT: PSS with different number of passes (N= 10, 20, 30, 40 and 50).

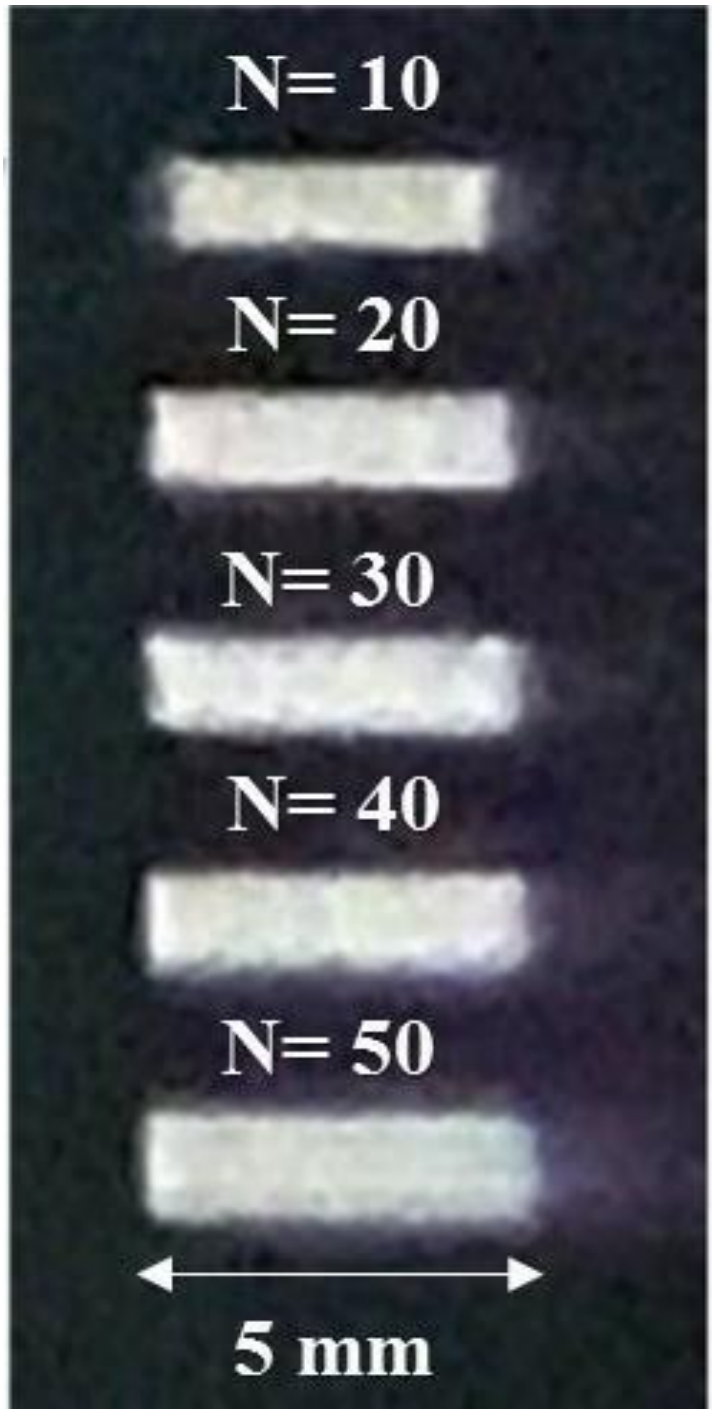

Figure 3.7: 5 mm length and 1 mm width line patterns of annealed graphene/ PEDOT:PSS with different number of passes (N= 10, 20, 30, 40 and 50).

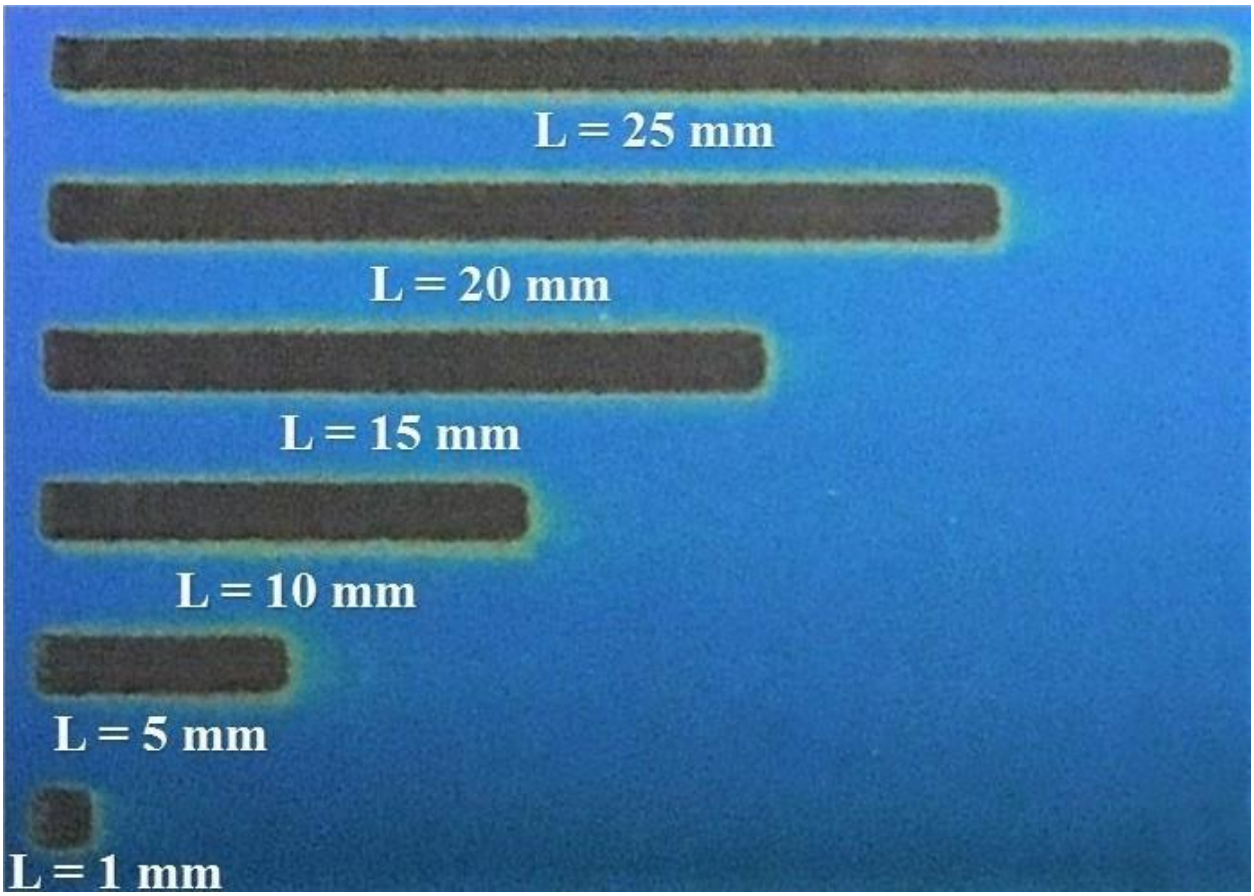

Figure 3.8: Printed lines with 50 number of passes of annealed graphene/PEDOT: PSS of varying lengths (L = 1, 5, 10, 15, 20 and 25 mm).

3.5 Electrical characterization of PEDOT: PSS and graphene/ PEDOT: PSS inks

Electrical measurements of annealed printed patterns were carried out to compare the electrical behavior of graphene/PEDOT: PSS and only PEDOT: PSS printed films. Figure 3.9 demonstrates that 0.25 weight% PEDOT: PSS is not conductive by itself even up to 50 number of printing passes. Graphene/PEDOT: PSS annealed printed patterns showed good conductivity up to 0.7 mA with 50 number of printing passes at 5 mm length scale or probe separation distance [Figure 3.10].

The response of current was inversely proportional to length. Values of the current increased with decreasing lengths [Figure 3.11]. It can be observed that high values of current (around 0.2 mA) can be obtained even at length scales of 25 mm which is significantly higher in the electronics industry. The resistance of printed graphene/PEDOT: PSS annealed films showed inverse proportionality with number of printing passes and direct proportionality with length of printed patterns. It decreased with increasing number of passes when length was kept constant at 5 mm [Figure 3.12] and increased with line length when number of printing passes was constant at 50 [Figure 3.13]. Resistances as low as 1.36 kΩ and 6.49 kΩ at lengths of 5 mm and 25 mm was achieved with just 50 number of printing passes. Higher electrical conductivity can be achieved by either increasing number of printing passes, decreasing pattern lengths or using higher initial graphite concentration.

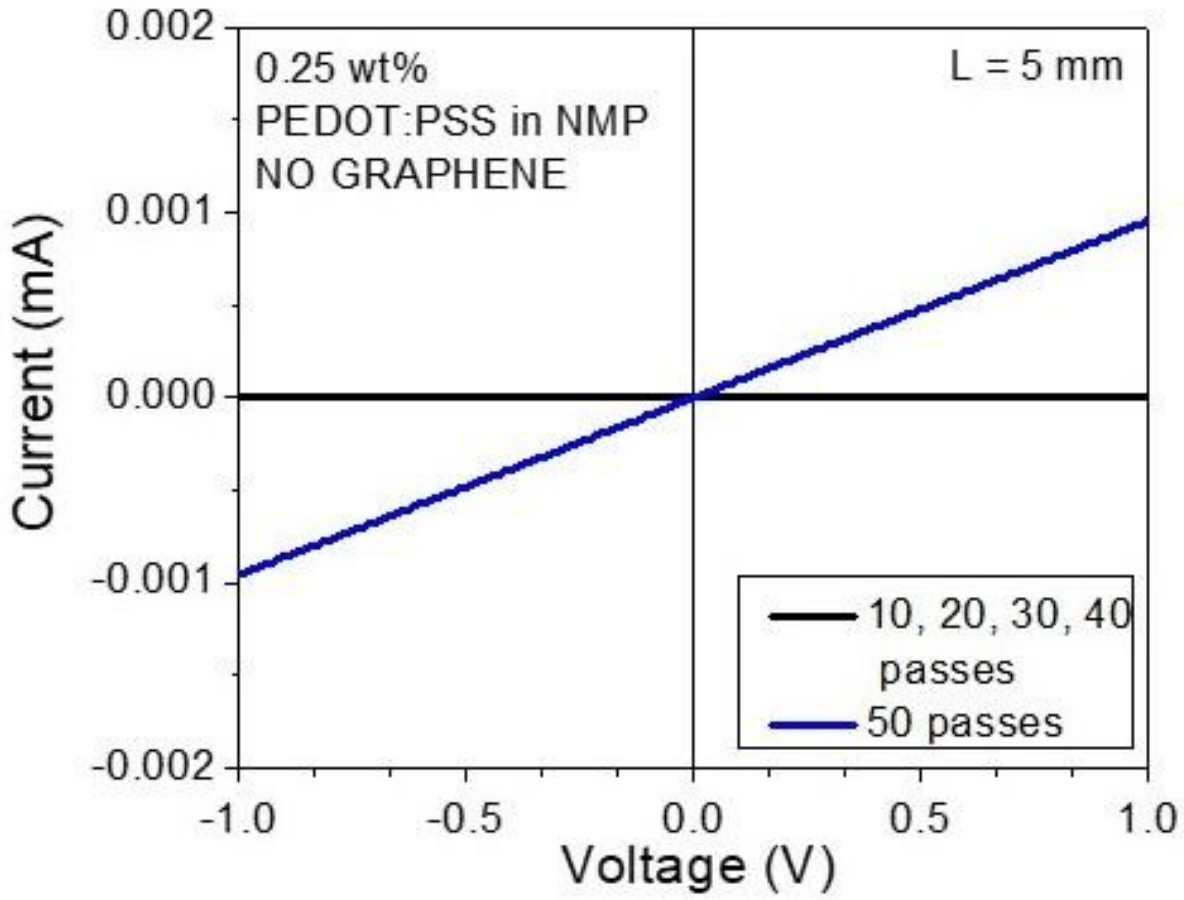

Figure 3.9: Variation of current with voltage for PEDOT: PSS at 5 mm length.

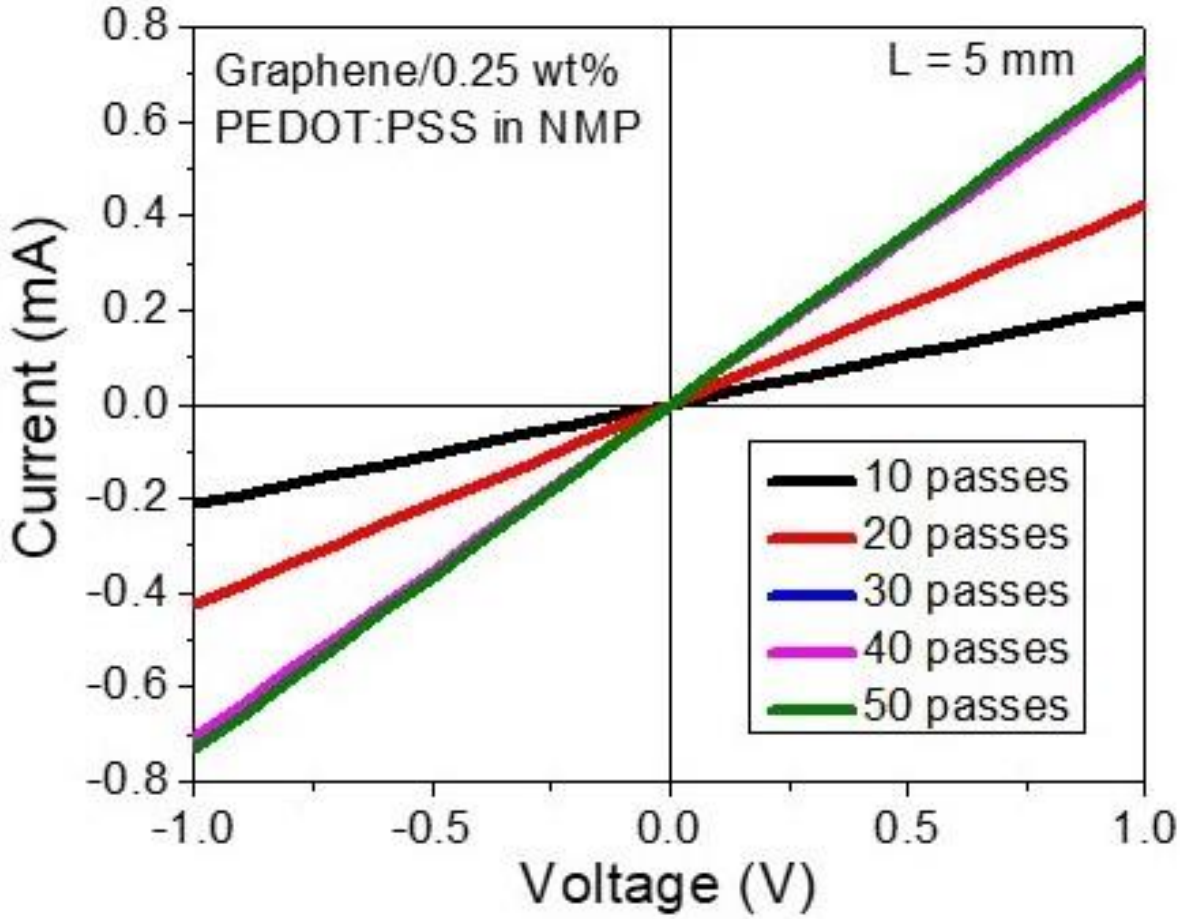

Figure 3.10: Variation of current with voltage for graphene/ PEDOT: PSS at 5 mm length.

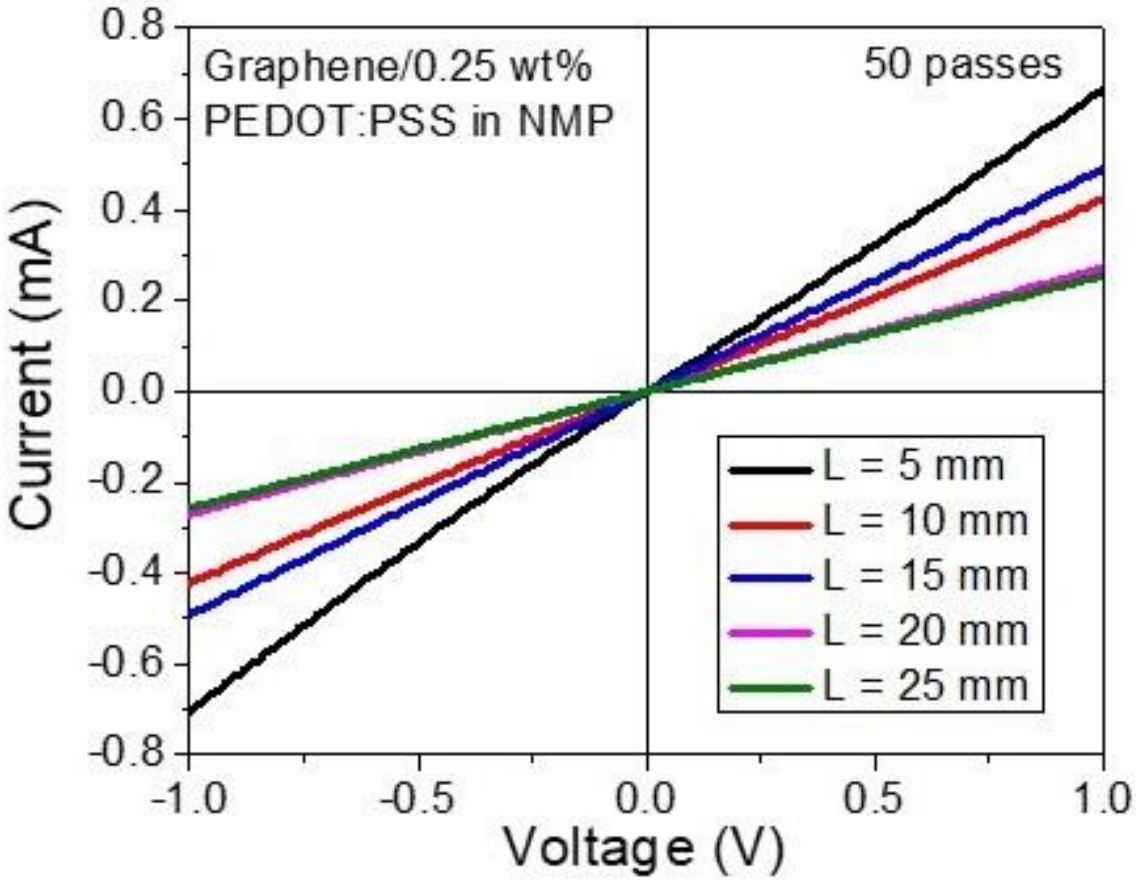

Figure 3.11: Variation of current with voltage for graphene/ PEDOT:PSS at varying lengths (5,10,15,20,25 mm).

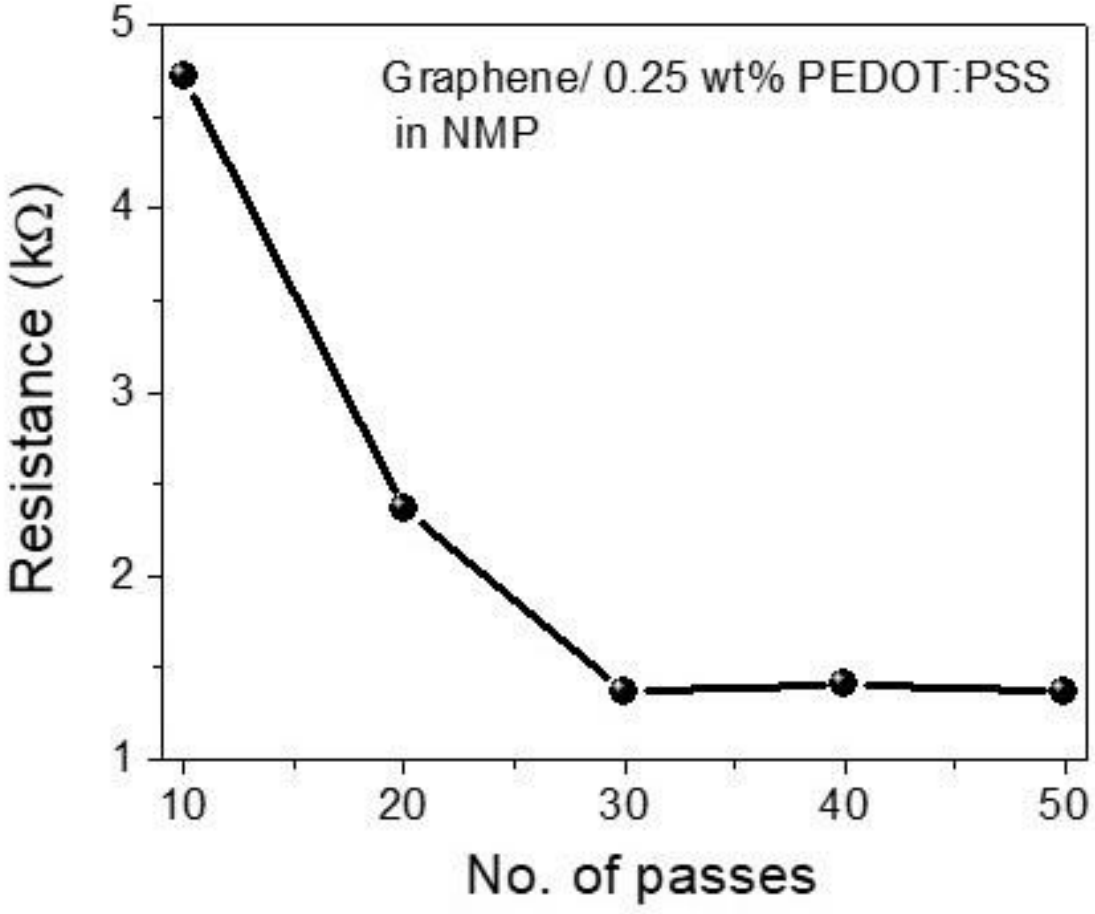

Figure 3.12: Variation of resistance with number of printing passes.

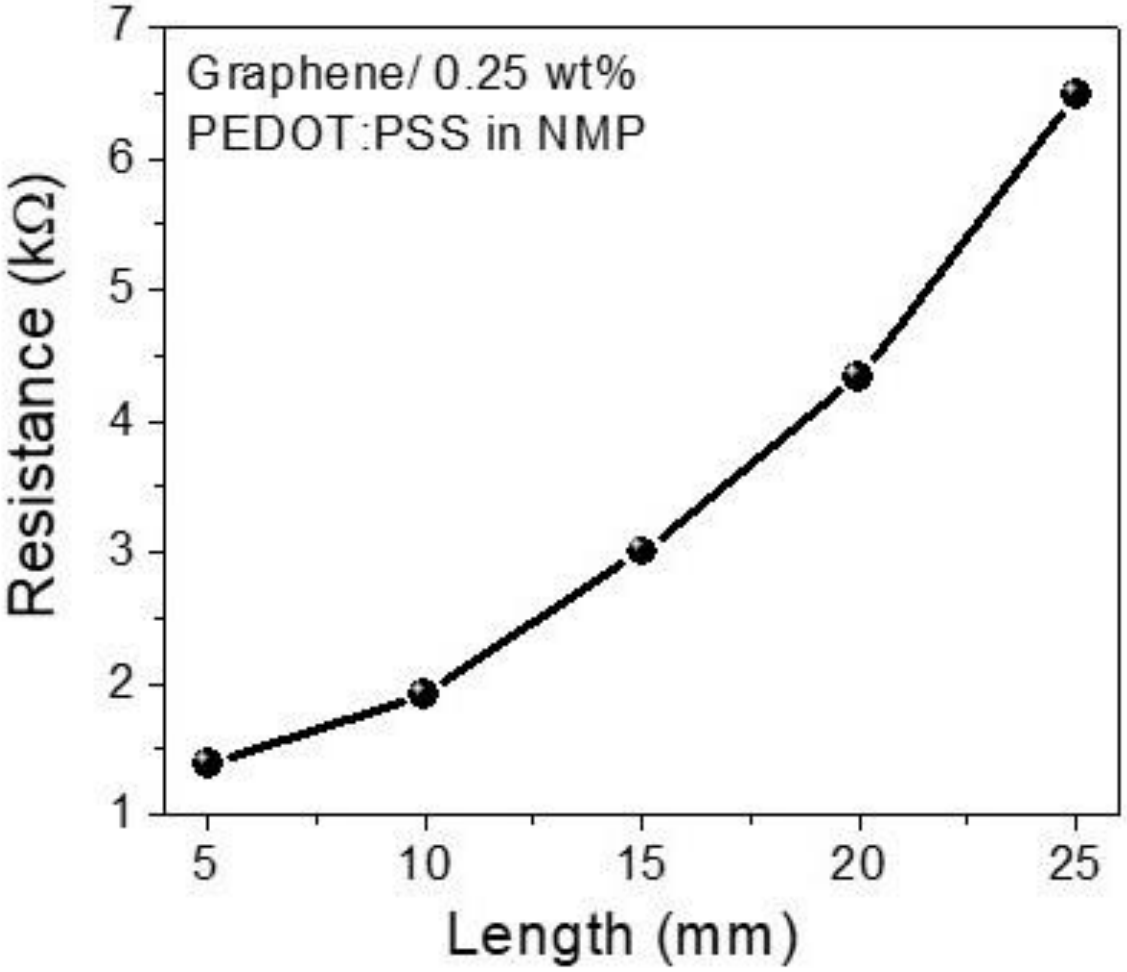

Figure 3.13: Variation of resistance with printing pattern length.

Chapter 4: High power exfoliation of tungsten disulfide for photodetector applications

One of the major potential applications of exfoliated WS_2 nanosheets can be as an active semiconducting channel in photodetection devices. Photodetectors are used in wide range of applications from imaging to optical communications as they convert light into electrical signals [96, 97, 98, 99, 100, 101, 102, 103], which reach the quantum limit in certain cases through cryogenic cooling. Due to their transparency, WS_2 nanosheets exhibit strong light-matter interaction, flexibility and ease of processing can be used to overcome limitations associated with the conventional choice of semiconducting channel (Si, InGaAs, etc) and produce bendable and transparent photodetection devices with high absorption efficiencies in a wide range enabling faster detection [104, 105]. Conventional semiconductors used in photodetectors are usually opaque, lack effective light absorption and are brittle in nature which limits their use to rigid substrates only.

There is no reported work yet on high power (significantly higher than 110 watts) exfoliation methods which can be done even at room temperature. In the present work, various high-power exfoliation methods (magnetic stirring, shear mixing, and horn-tip sonication) have been explored to optimize the best possible combination for enhanced semiconducting properties of WS_2. The work also reports graphene/WS_2 based photodetector where WS_2 is used as a semiconducting channel and graphene due to its finite density of states from Dirac cones of valence and conduction bands, chemical inertness, and high stability is used as a highly conducting contact. Inkjet printing has been employed as a material-conserving technique for precise deposition of graphene and WS_2 nanosheets. It is a modern production tool which enables the flow of ink (printable liquid) from the cartridge to the substrate. The liquid undergoes some drying after impact on substrate depending on platen temperature used. Various optoelectronic measurements including Raman and photoluminescence spectroscopy, photocurrent response, capacitance-voltage and capacitance-frequency measurements have been performed on the all inkjet-printed device to understand device properties and graphene-WS_2 interactions.

4.1 Materials and methods

Cyclohexanone (70%) /terpineol (30%) solution (C/T) mixtures were prepared in glass vials. Ethyl cellulose (2.5 weight%) was then added to the solution and bath sonicated for 2 hours to ensure complete dissolution of ethyl cellulose (EC) in C/T solution mixture. This particular combination of cyclohexanone, terpineol and ethyl cellulose (C/T/EC) was used because it has a viscosity of about 12 cP which is ideal for inkjet printing.WS_2 powder in a concentration of 30 mg/ml is used for all experiments.

For magnetic stirring, the WS_2 powder was taken in two separate glass vials and 5 ml of C/T/EC solution mixture was added to them. A magnetic stir bar was then put in both glass vials. One vial was magnetic stirred at 100 rpm (MS (Low), lowest to stir the entire liquid) and another vial was stirred at 1500 rpm (MS (High), highest limit of the equipment) for 24 hours to ensure complete breakage of all the Van der Waals bonds.

For shear mixing, the WS_2 powder was taken in two separate glass beakers and 50 ml of C/T/EC solution mixture was added to them. This was the minimum amount of solution required for using our shear mixer. Lowest speed of 2500 rpm (SM (Low)) and highest speed of 6000 rpm (SM (High)) for 5 hours was used for shear mixing. These parameters were decided to achieve uniform mixing while avoiding overheating or long hours of operation.

For horn-tip sonication, the WS_2 powder was taken in two separate glass beakers and 20 ml of C/T/EC solution mixture was added to them. This was the minimum amount of solution required for horn-tip sonication. Power amplitude of minimum 20% (HT (Low)) and maximum of 40% (HT (High)) was used for 3 hours. Pulse on time of 30 seconds and pulse off time of 30 seconds was used increasing total sonication time to 6 hours. The parameters for sonication was also chosen such that it can be performed at room temperature without heating of samples thus removing the need for ice bath or chiller.

Extreme parameters are used for all three methods of chemical/ liquid-phase exfoliation to optimize the best approach of producing semiconducting WS_2 nanosheets that are stable for at least one month. One drop of each sample was cast on Si/SiO_2 wafer using a plastic pipette. Annealing was performed at 250 ^oC for 2 hours to ensure complete removal of the solvent.DMP-2800 series Fujifilm Dimatix Materials Printer consisting of 16 inkjet nozzles was used to print

graphene/WS_2/graphene photodetector in this work. Cartridge temperature of 40 °C and a platen temperature of 60 °C was used during all the printing work.

4.2 High power exfoliation methods for WS_2

As noted, the three techniques used to disperse WS_2 in chemical dispersions are magnetic stirring, shear mixing and horn-tip sonication. These techniques are illustrated in Figure 1 which shows the various mechanisms and parameters, used in producing single-to-few layer WS_2 nanosheets. The first technique, Magnetic stirring, refers to using a magnetic field to create fluidic shear forces that are generated as a bar magnetic is spun in the liquid to generate the stirring and exfoliation mechanism. The details of the magnetic stirring mechanism is illustrated in Figure 4.1(a). The magnetic stirrer moves the fluid in a clockwise direction when a value for the stirring rpm (revolutions per minute) is given as input. When a vial containing magnetic stirrer and liquid is placed above hot plate stirrer the magnetic stirrer also starts to move in a clockwise direction at same rpm. The energy provided by stirring breaks the 3D layered materials into 2D nanosheets. In the second technique, shear mixing, exfoliation results when a shear force is produced such that one area/layer of fluid travels with a different velocity relative to the adjacent area/layer. Figure 4.1(b) demonstrates the mechanism of shear mixing used in the current work. High-speed rotation of the rotor blades in a clockwise direction results in shearing of nanosheets. In the third technique, exfoliation by horn-tip sonication refers to the case of exposing the layered material to ultrasonic waves in an appropriate solvent by inducing vibrations of horn-tip. This is shown in Figure 4.1(c). Ultrasonic waves generate cavitation bubbles that collapse into high energy jets, breaking up the layered crystallites to produce exfoliated nanosheets. Figure 4.1(d) summarizes the various parameters used for magnetic stirring, shear mixing, and horn-tip sonication. In the present work, MS (Low) and MS (High) refers to magnetic stirring conditions at 100 and 1500 rpm for 24 hours,

respectively. The shear mixing conditions at 2500 rpm and 6000 rpm for 5 hours is referred as SM (Low) and SM (High) whereas the horn-tip sonication at 20% and 40% power amplitude is denoted as HT (Low) and HT (High).

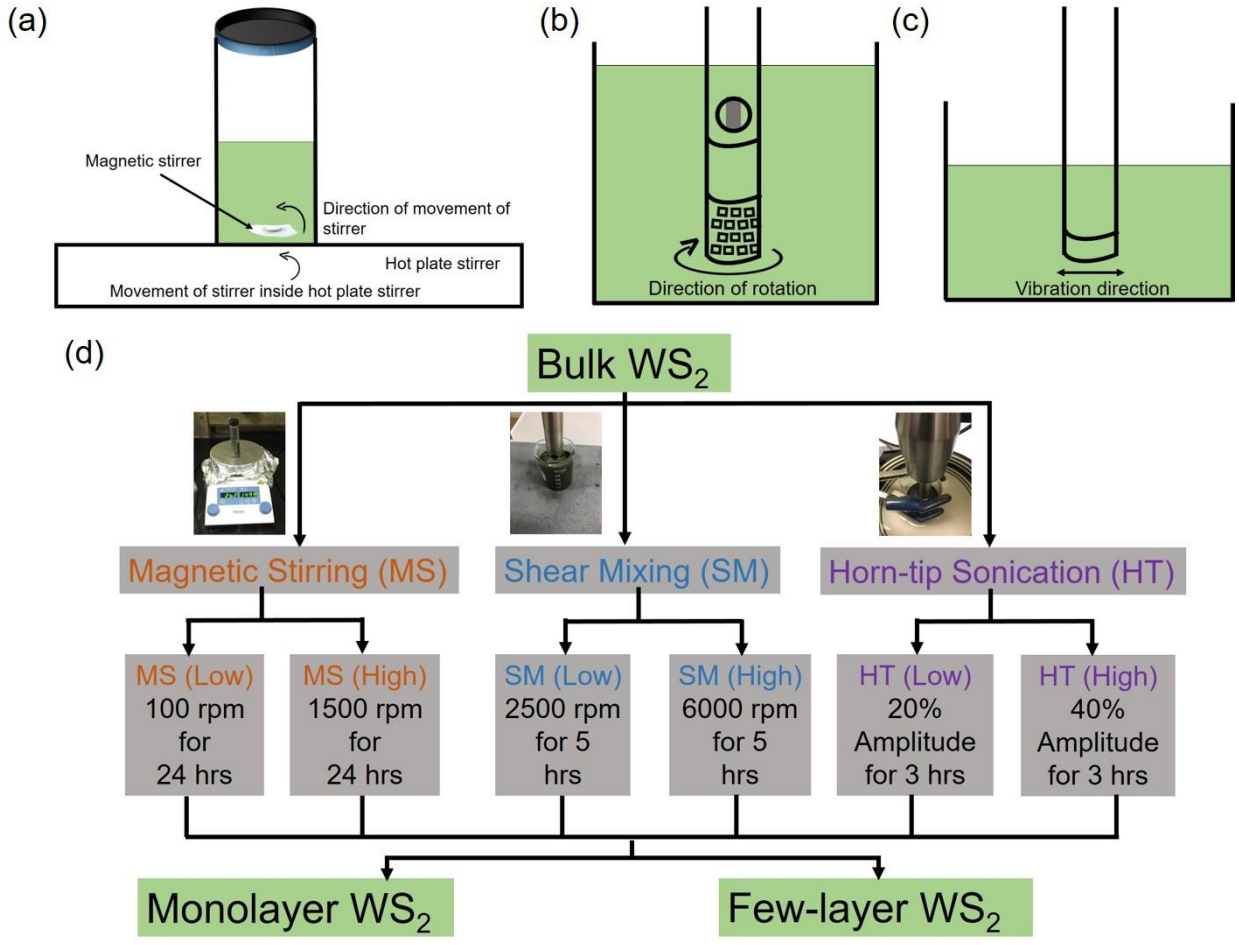

Figure 4.1: (a-c) Mechanism of (a) Magnetic stirring, (b) shear mixing and (c) horn-tip sonication. (d) Schematic illustration of different parameters and techniques used for WS_2 ink preparation.

4.3 Electrical and optical characterization of drop-casted samples

Figure 4.2 demonstrates the current-voltage (I-V) relationship for drop-casted annealed MS (Low) and MS (High) samples. Figure 4.3 shows the current-voltage (I-V) relationship for drop-casted annealed SM (Low) and SM (High) samples. Figure 4.4 displays the current-voltage (I-V) relationship for drop-casted HT (Low) and HT (High) samples. It can be observed that higher values of current are obtained at a higher speed of magnetic stirring and shear mixing and at a higher amplitude of sonication when the time is kept constant since net power applied to the solution is greater, leading to higher exfoliation rates. Raman and photoluminescence spectroscopy were used to explain this behavior. In WS_2, there are two primary Raman active modes. A_{1g} mode due to out-of-plane vibrations involving only sulfur atoms which occur at ~ 418.8 cm^{-1} and 2LA(M) mode at about 352.4 cm^{-1} due to the in-plane displacement of tungsten and sulfur atoms. The intensity ratio, $I_{2LA(M)}/ I_{A1g}$, can be used to approximate the number of layers present. The intensity ratio of 2.2 or higher is a signature of the presence of monolayers whereas intensity ratio of 0.47 or less indicates the presence of WS_2 in its bulk form [106, 107, 108]. Intensity ratio in between 0.47 and 2.2 may be indicative of the presence of few-layer WS_2. Figure 4.5 shows Raman spectra of MS (Low) and MS (High) samples. Intensity ratios of MS (Low) and MS (High) sample were found to be 3.826 and 1.171 indicating presence of monolayer and few-layer WS_2 respectively. Figure 4.6 displays Raman spectra of SM (Low) and SM (High) samples. Intensity ratios of SM (Low) and SM (High) samples were found to be 1.159 and 0.923, respectively indicating the presence of few-layer WS_2. Figure 4.7 shows Raman spectra of HT (Low) and HT (High) samples. Intensity ratios of HT (Low) and HT (High) samples were found to be 2.104 and 1.229 respectively indicating the presence of few-layer WS_2.

Photoluminescence (PL) refers to emission of light from a material after absorption of photons. Figure 4.8 shows the PL spectra of MS (Low) and MS (High) samples displaying a single peak. However, the PL peak of MS (High) sample (FWHM ~ 90.39 nm) is broader and is blue-shifted by ~ 4.47 nm from the PL peak of MS (Low) (FWHM ~ 87.22 nm) sample. Figure 4.9 shows the PL spectra of SM (Low) and SM (High) samples displaying a single peak. However, PL peak of SM (High) sample (FWHM ~ 144.38 nm) is broader and is blue-shifted by ~ 39.6 nm from the PL peak of SM (Low) (FWHM ~ 43.63 nm) sample. Figure 4.10 shows the PL spectra of HT (Low) and HT (High) samples. PL spectra of HT (High) sample showed strong single peak (FWHM ~ 142.62 nm) whereas PL spectra of HT (Low) sample does not indicate any dominant PL peak and its highest point was ~ 146. 9 nm from the PL peak of HT (High sample).

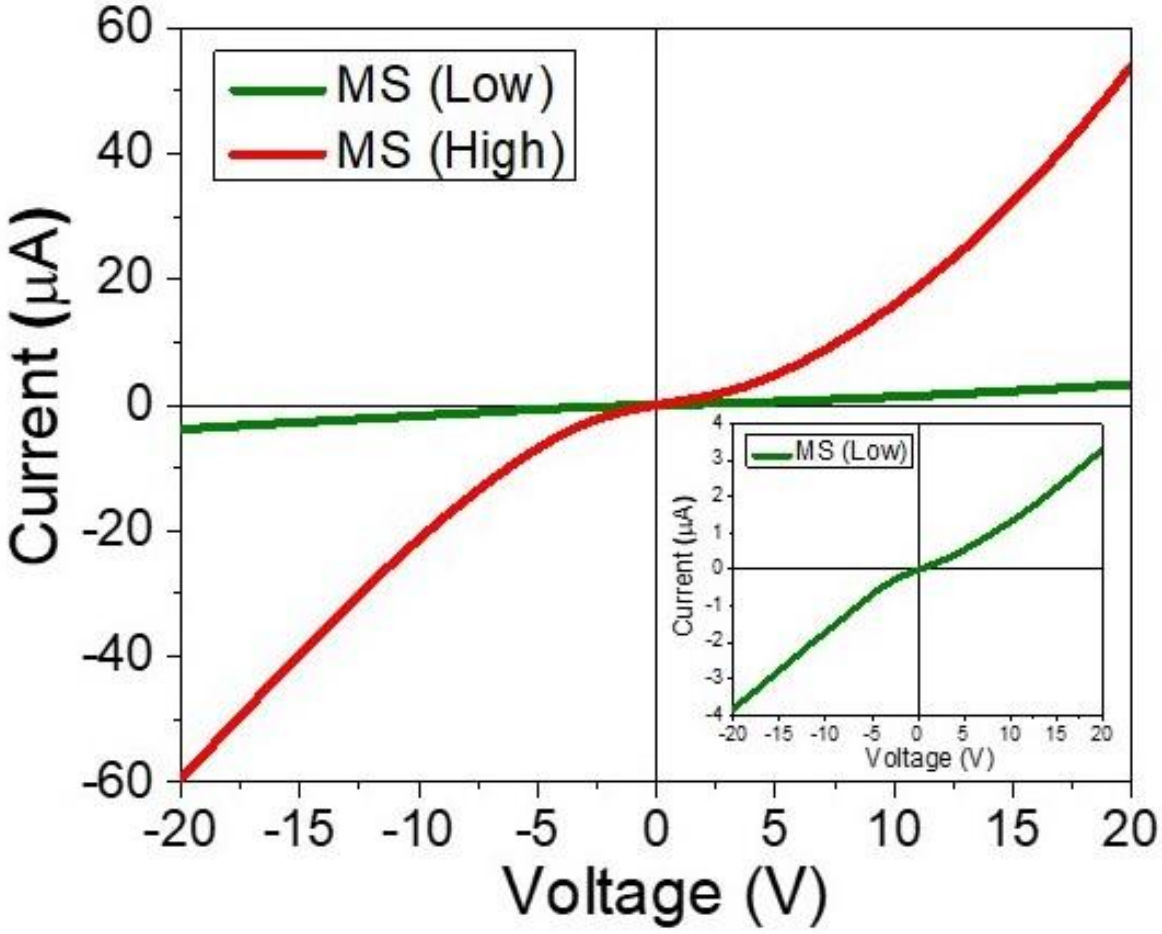

Figure 4.2: Current-voltage measurements of drop-casted and annealed MS (Low) and MS (High) samples.

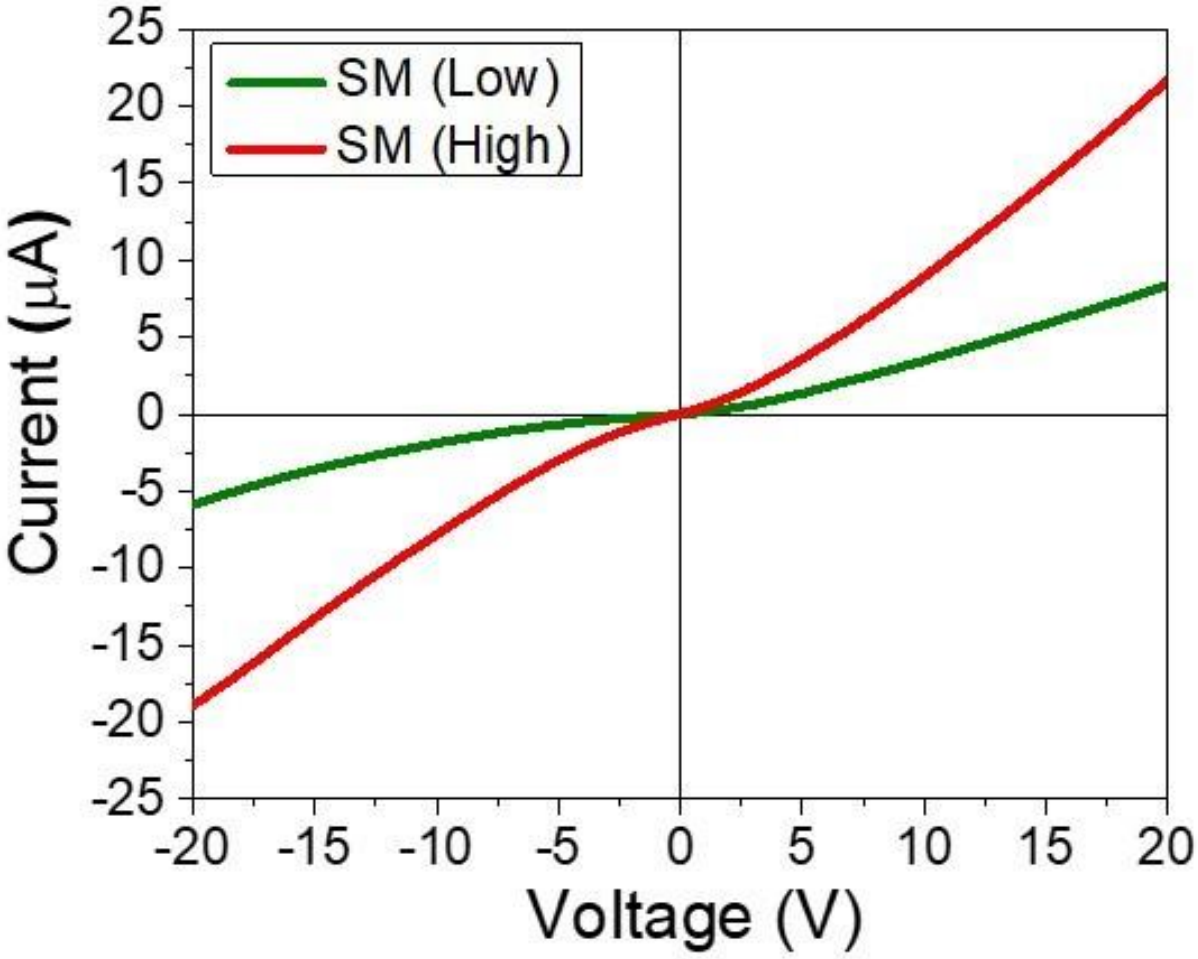

Figure 4.3: Current-voltage measurements of drop-casted and annealed SM (Low) and SM (High) samples.

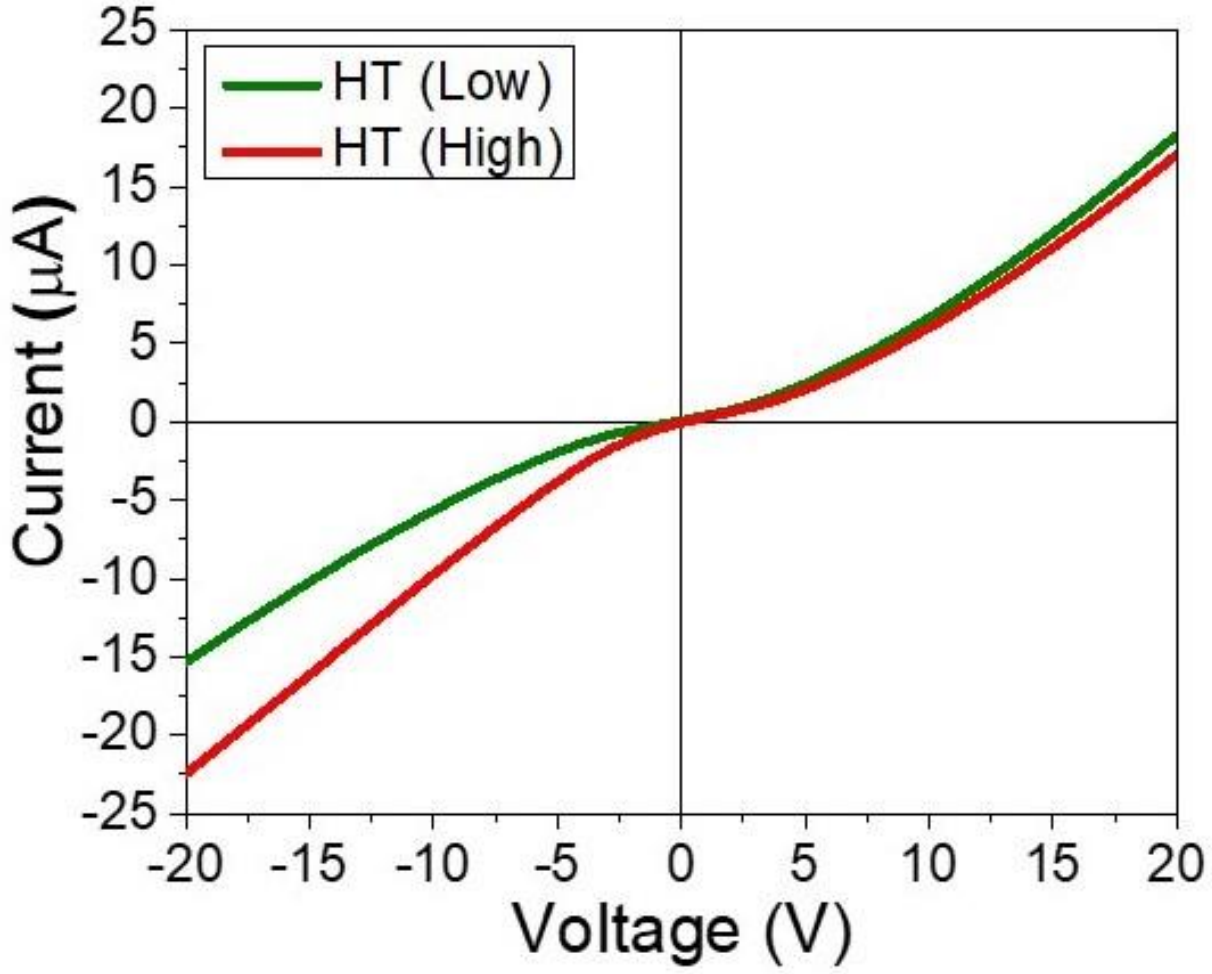

Figure 4.4: Current-voltage measurements of drop-casted and annealed HT (Low) and HT (High) samples.

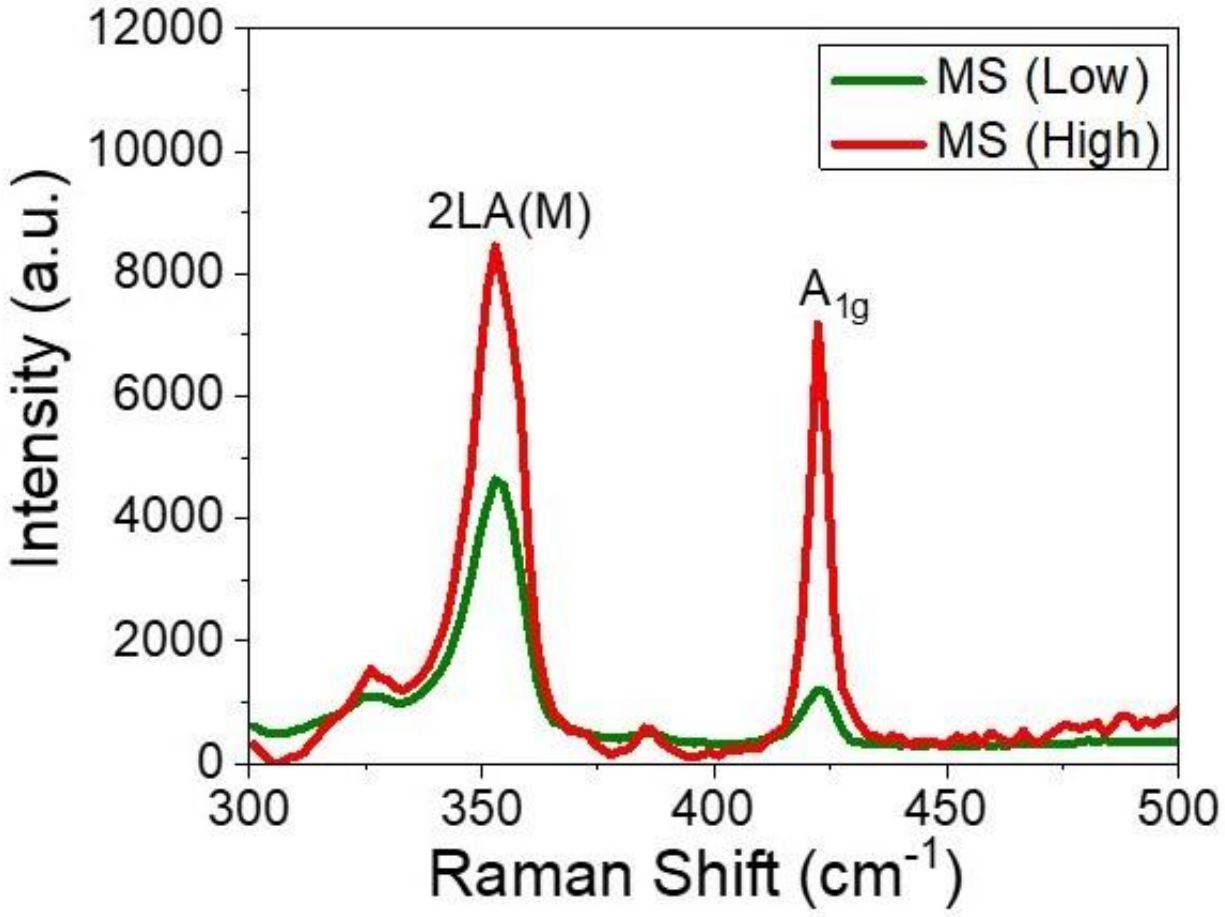

Figure 4.5: Raman spectra of drop-casted and annealed MS (Low) and MS (High) samples.

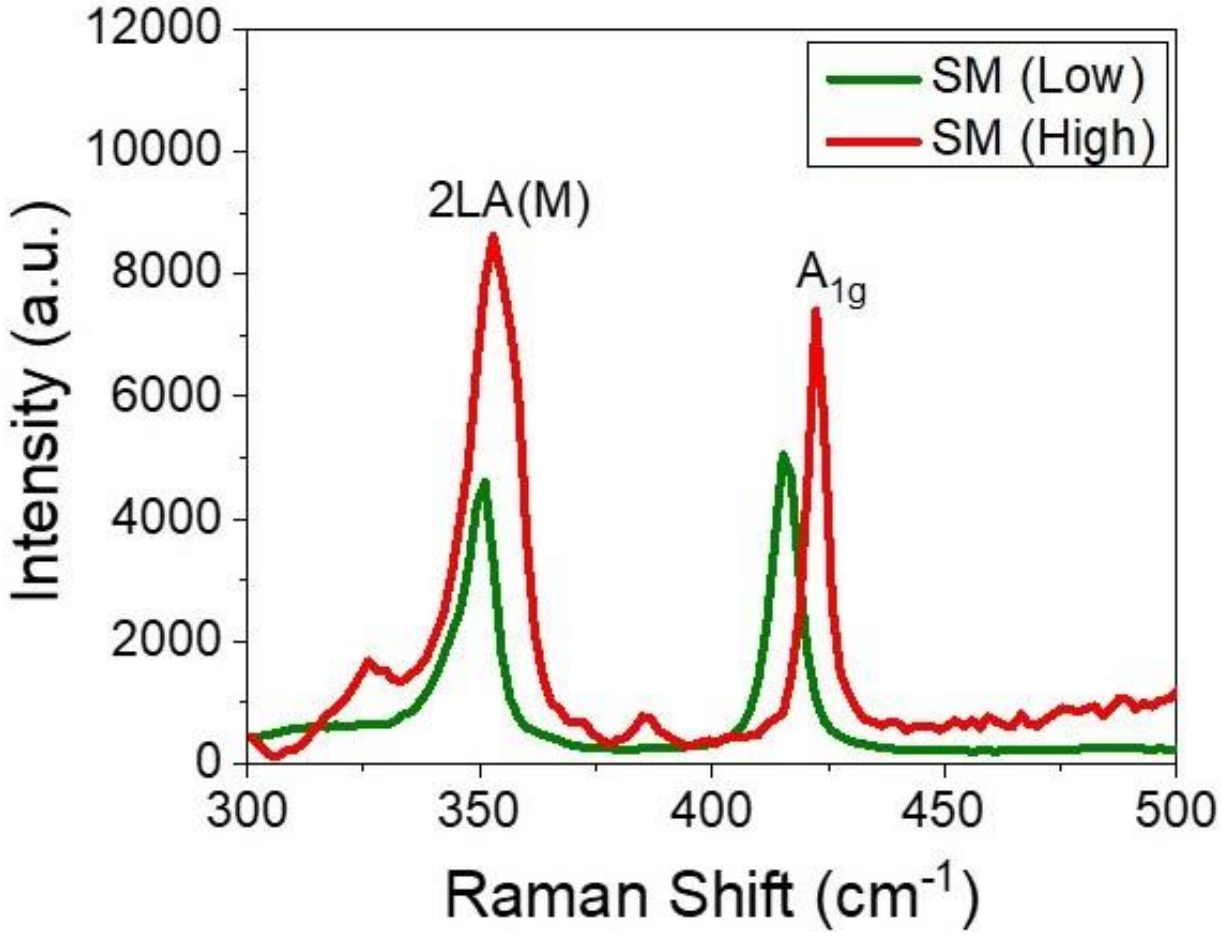

Figure 4.6: Raman spectra of drop-casted and annealed SM (Low) and SM (High) samples.

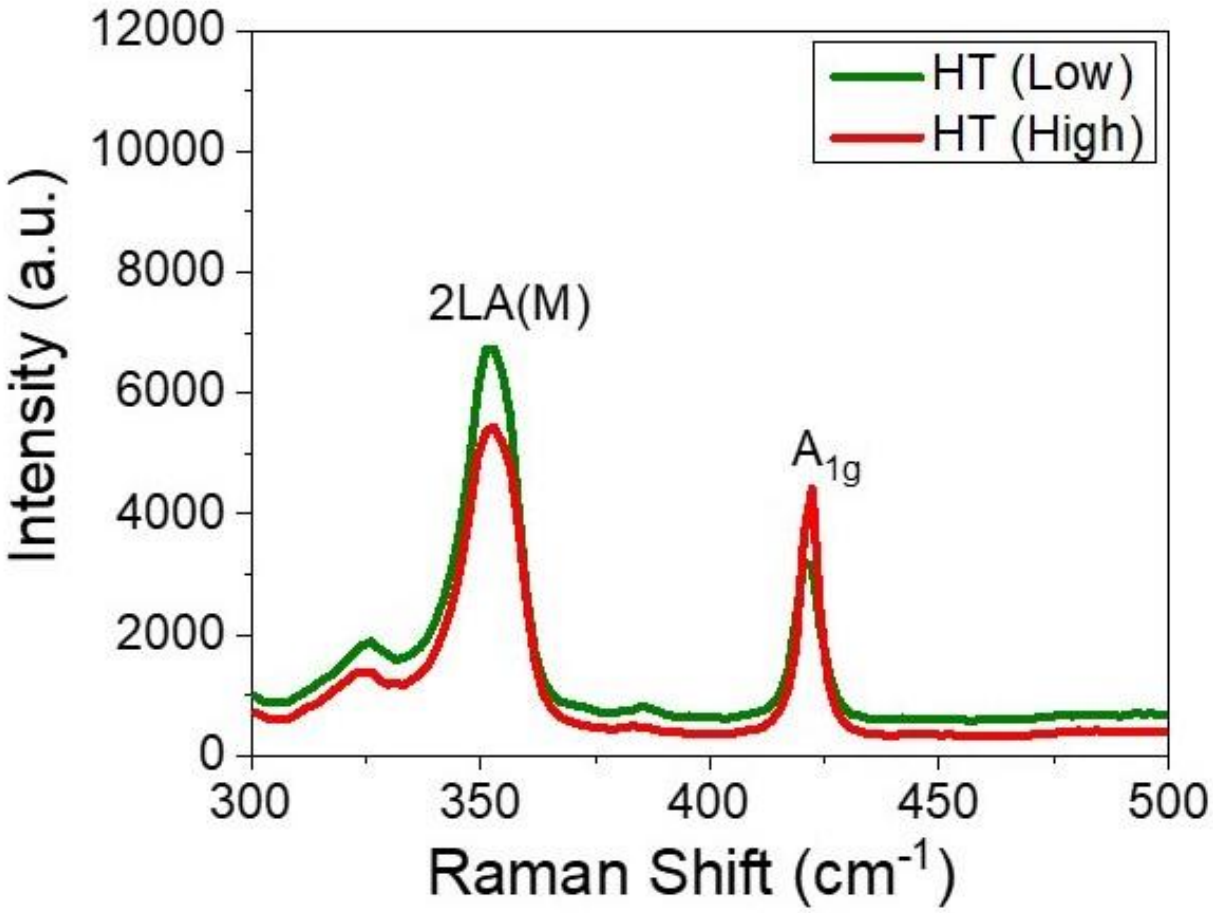

Figure 4.7: Raman spectra of drop-casted and annealed HT (Low) and HT (High) samples.

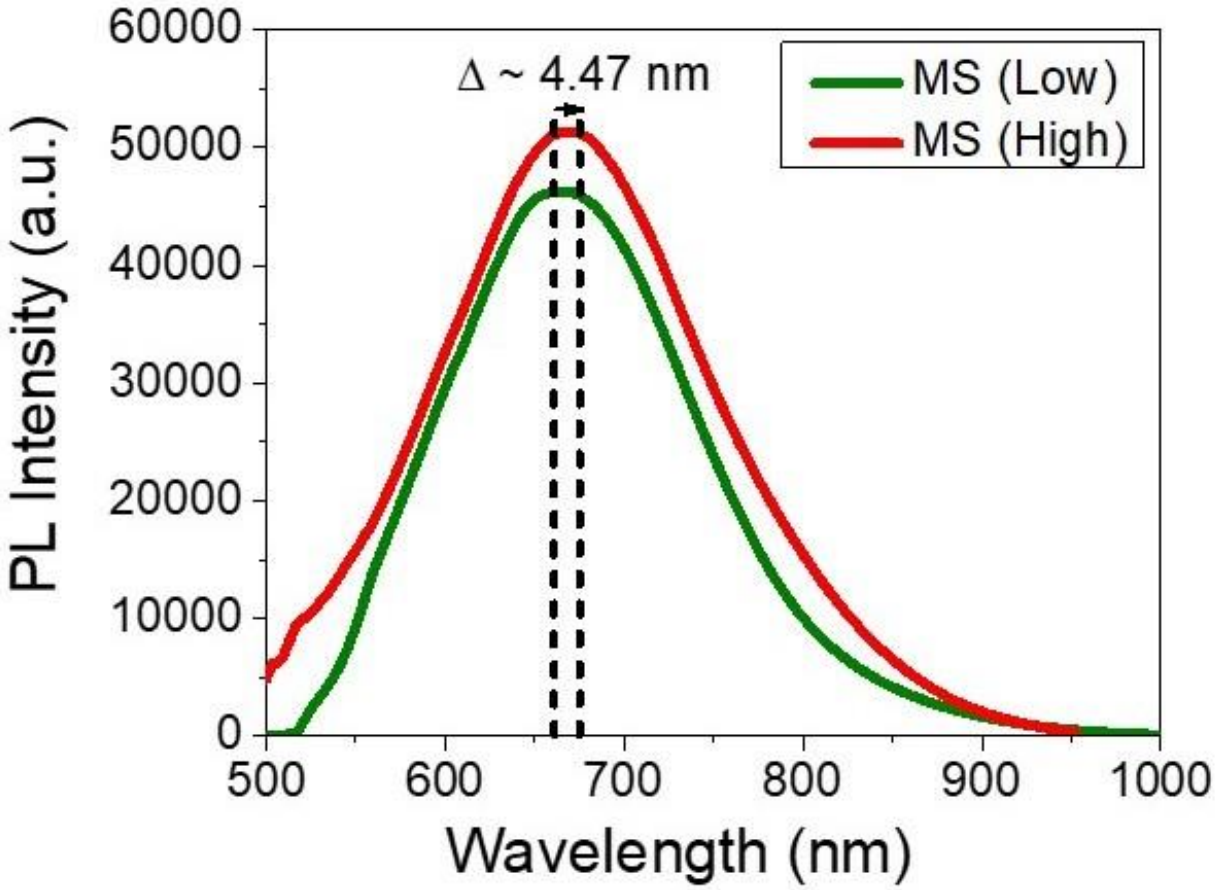

Figure 4.8: Photoluminescence spectra of MS (Low) and MS (High) samples.

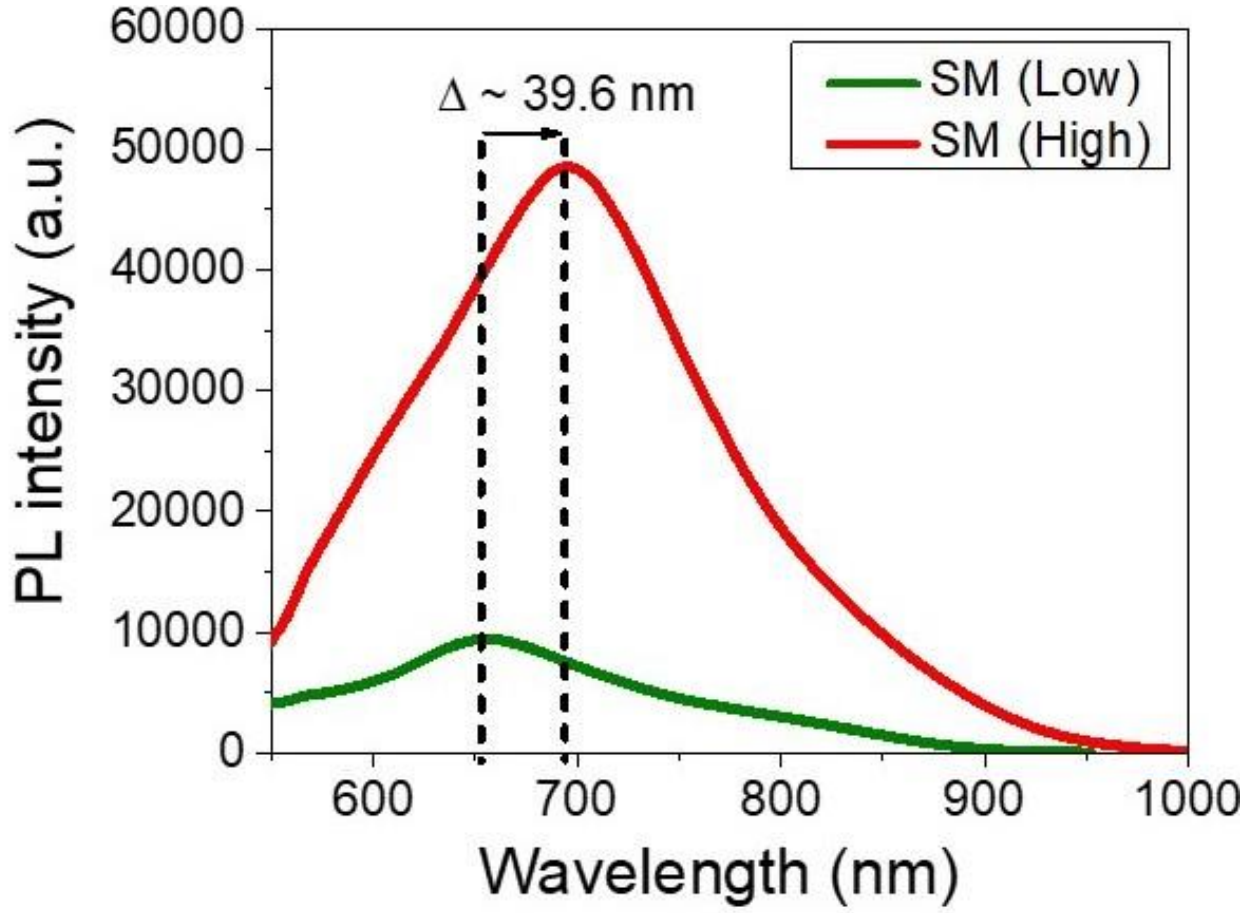

Figure 4.9: Photoluminescence spectra of SM (Low) and SM (High) samples.

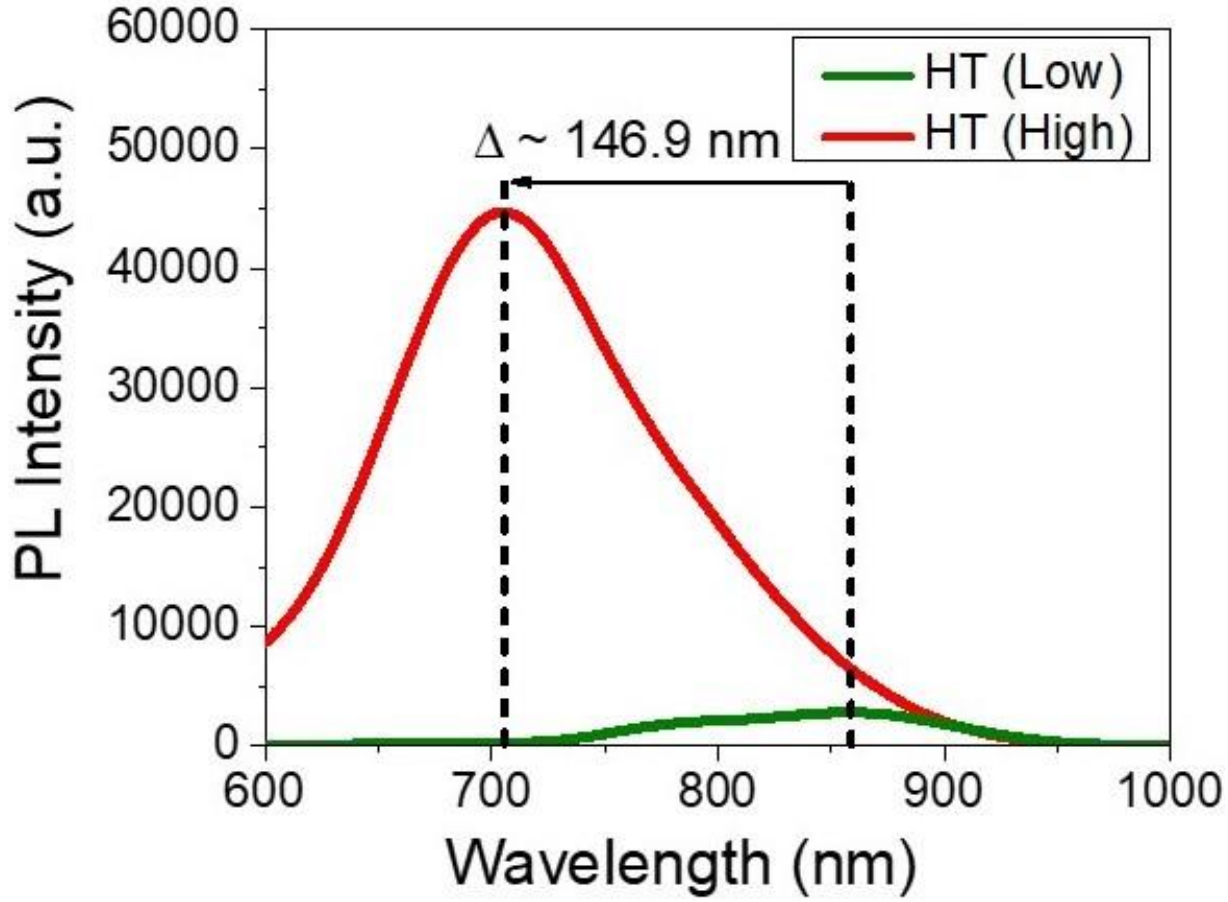

Figure 4.10: Photoluminescence spectra of HT (Low) and HT (High) samples.

The higher electrical conductivity of MS (High), SM (High), and HT (High) samples may be due to the lower resistance offered by few-layer WS_2 nanosheets as they have extra channels for carrier transport [109, 110]. However, MS (Low) and MS (High) samples were unstable and WS_2 nanosheets precipitated at the bottom of the vial in less than 12 hours. On the other hand, SM (Low), SM (High), HT (Low) and HT (High) samples were stable for at least 1 month indicating good stability. The photographs of solutions just after the experiment and 12 hours after the experiment is shown in Figure 4.11 and Figure 4.12 respectively. However, HT (High) sample showed higher conductivity than the former three samples. Thus, horn-tip sonication was used as the approach of choice for inkjet printing our photodetector devices in the subsequent work.

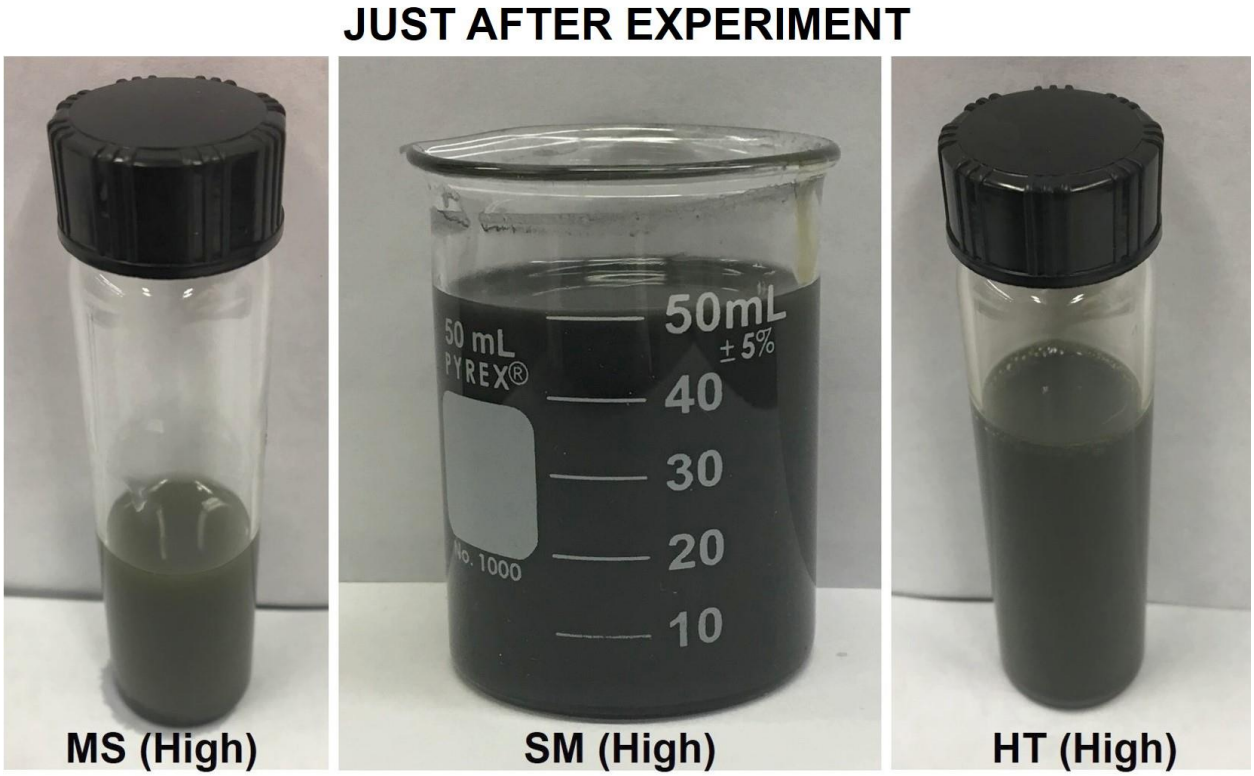

Figure 4.11: The photographs of solutions just after the experiment.

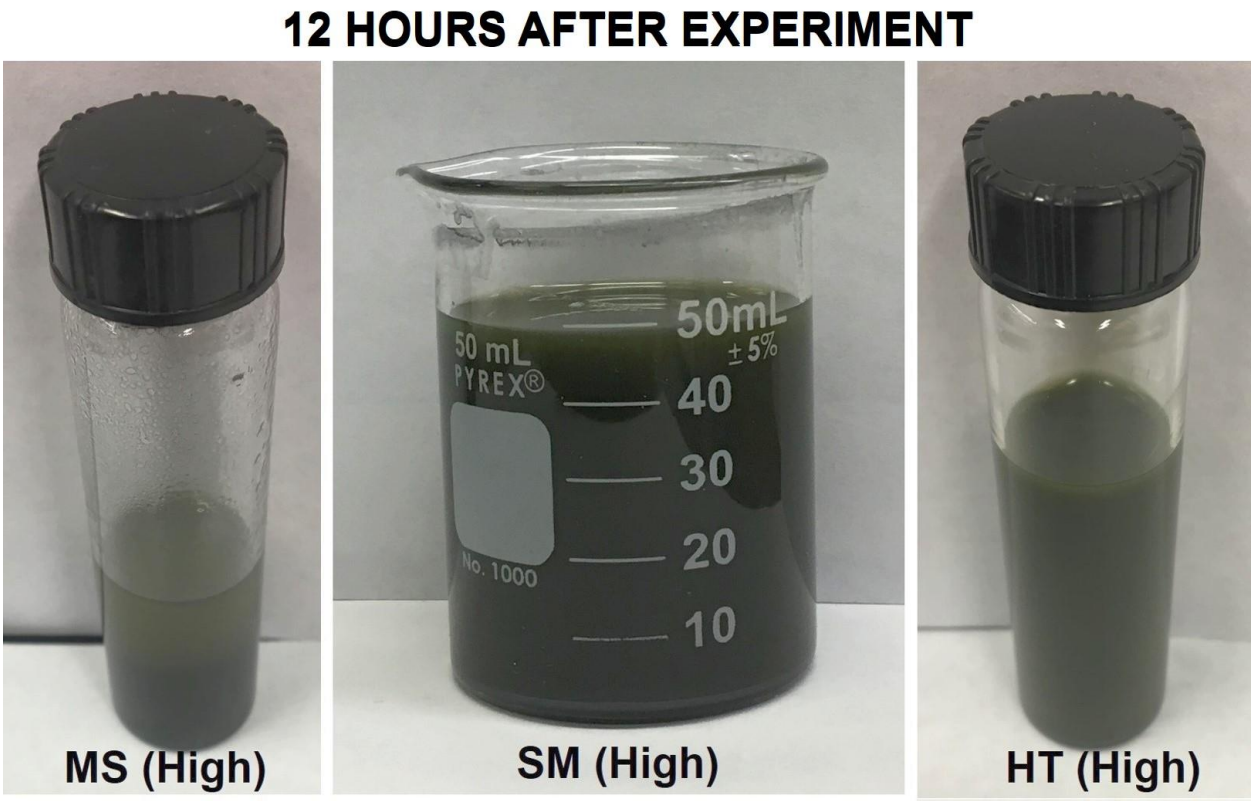

Figure 4.12: The photographs of solutions just after the experiment and 12 hours after the experiment

4.4 Inkjet printing of graphene/ WS_2 based photodetector

Horn-tip sonication with 40% power amplitude for 3 hours duration was used to make graphene and WS_2 inks. The line pattern of 1 mm (width) and 0.8 mm (length) were printed with 40 number of passes with WS_2 inks followed by annealing at 250^{o}C for 2 hours. Two 3 mm graphene pads were then printed such that effective WS_2 channel length was 0.6 mm followed by annealing at 250^{o}C for 2 hours. This is shown in the inset of Figure 4.13. Figure 4.13 illustrates typical dark current-voltage relationship for graphene/WS_2/ graphene photodetector device. Figure

4.14 demonstrates the same current-voltage graph plotted in log scale to show the dark current value (0.1342 µA) at 0V which is used for further calculations.

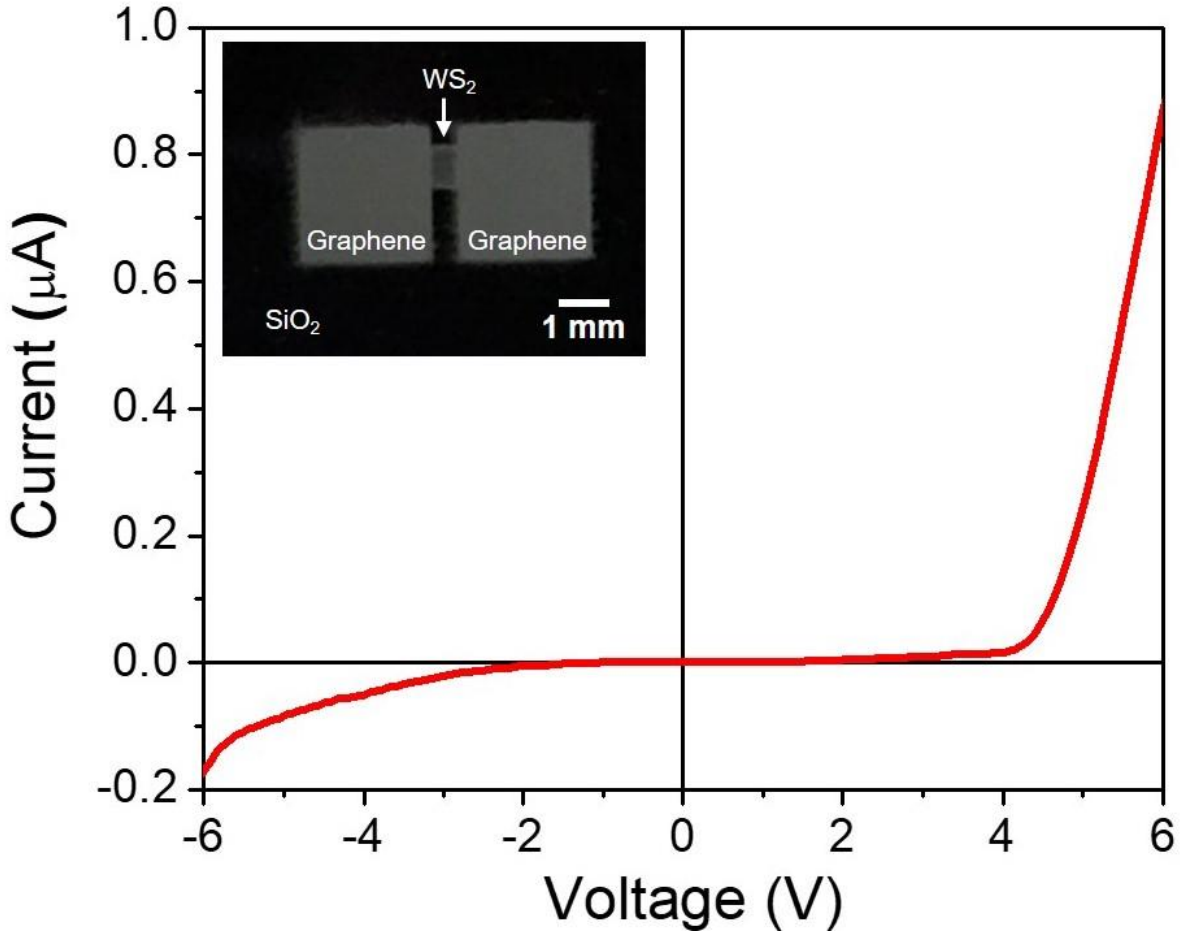

Figure 4.13: Dark current measurement of graphene/WS_2 based inkjet printed photodetector (Inset: Photograph of inkjet printed graphene/WS_2/graphene photodetector).

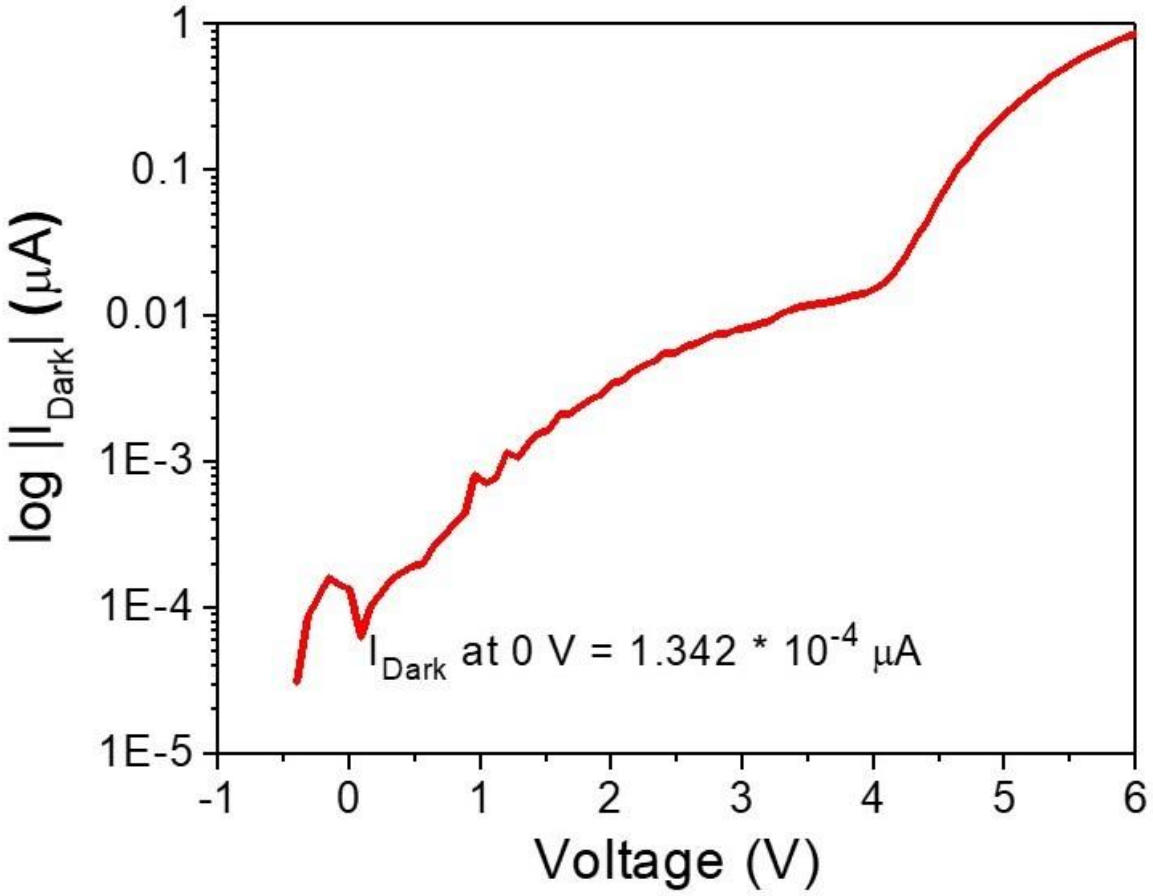

Figure 4.14: Dark current-voltage measurement in log scale to show dark current value at 0V used for responsivity and detectivity calculations.

4.5 Photocurrent measurement of graphene/ WS_2 based photodetector

Figure 4.15 shows the photodetection measurement setup. It consists of an arbitrary waveform generator which generates electrical waveforms and provides input to the laser source. Laser source then emits light of wavelength 660 nm through the process of optical amplification. The laser light is then made to drop on the device under test (DUT) which is kept in a probe station. When laser interacts with the semiconducting WS_2 channel, enhanced electrical conductivity is obtained due to extra free carriers generated by photon absorption. This can be confirmed by current-time measurements using semiconductor device analyzer and laser on and off cycle. Laser power in this work was varied by changing the input voltage from 1V to 5V which led to a change in laser power from 2.29 mW/cm^2 to 12.13 mW/cm^2. A linear relation was observed between laser power and input voltage. This is shown in Figure 4.16. Figure 4.17 shows the time response of graphene/WS_2 based photodetector with varying laser power.

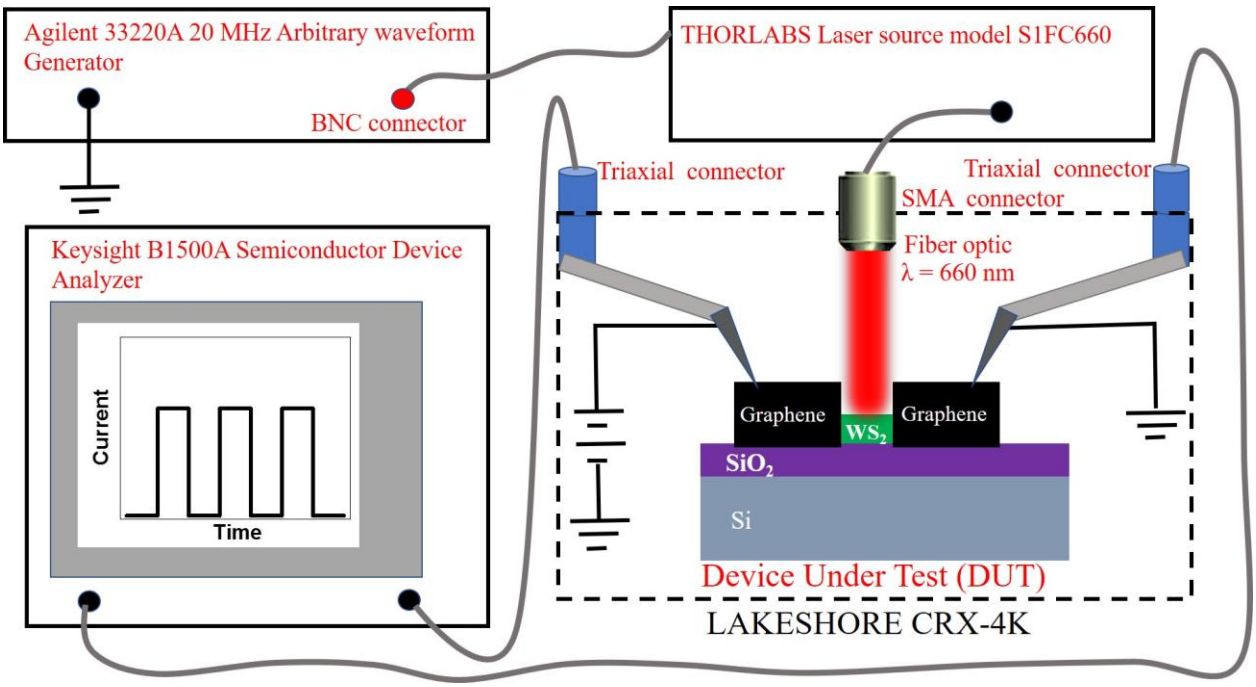

Figure 4.15: Instrument setup for photodetection measurement.

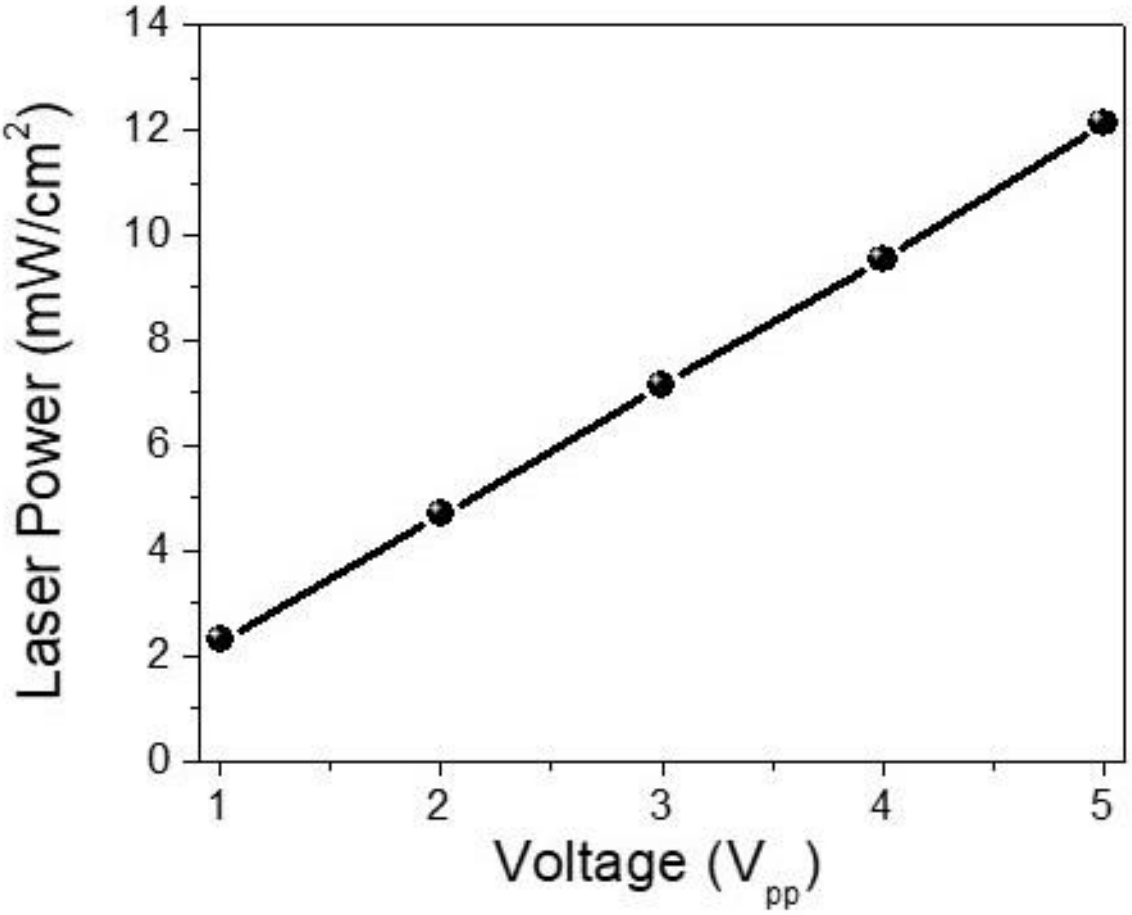

Figure 4.16: Variation of laser power with an applied voltage.

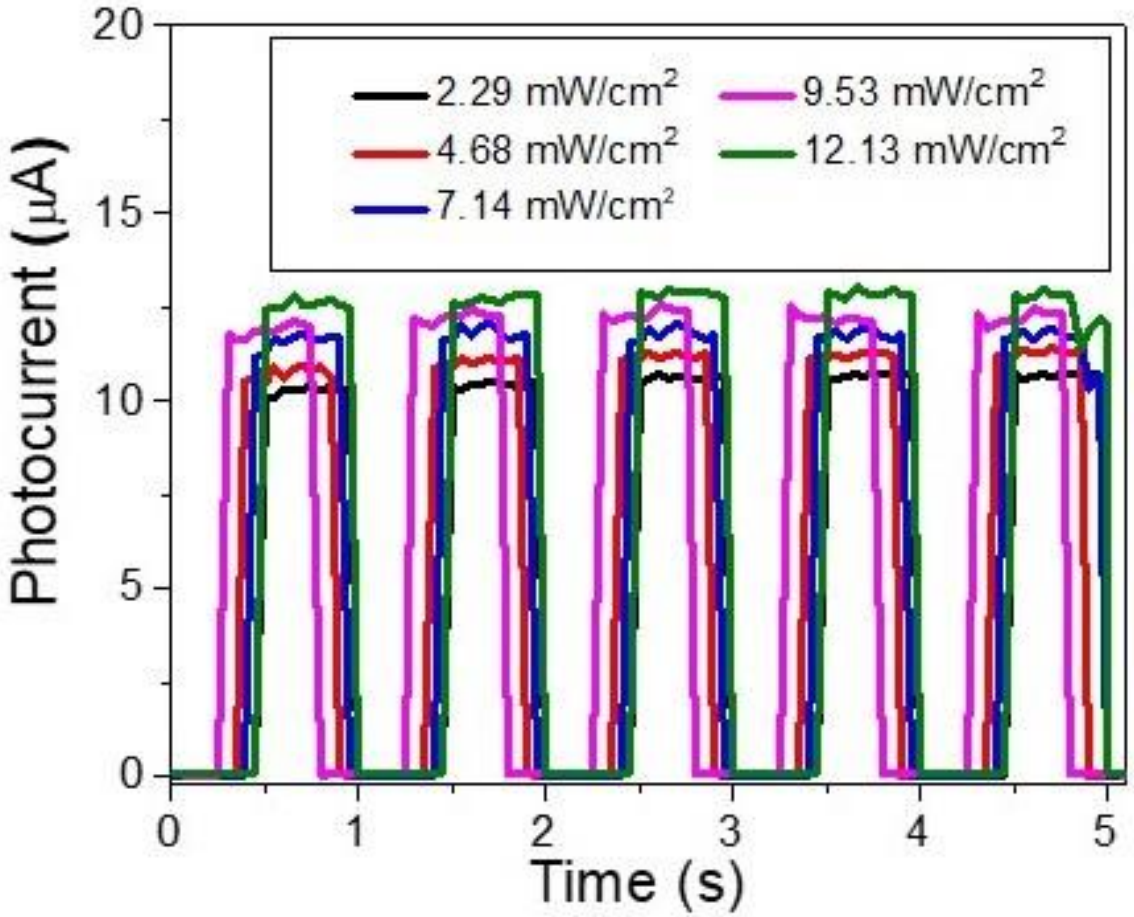

Figure 4.17: Photoresponse of graphene/WS_2 based photodetector at various laser power.

4.6 Photodetector parameter study for graphene/ WS_2 based photodetector

The amount of photocurrent, decay and rise time, on/off ratio, responsivity, and detectivity are key figures-of-merit for the photodetector. The photocurrent is the current induced when the light of appropriate wavelength is made to fall on the semiconducting substrate. Decay time is the time required by the photodetector to reach 10% of maximum photocurrent value when the laser is switched off from it's on the state. Rise time is the time required by the photodetector to reach 90% of maximum photocurrent value when the laser is switched on from its off state. On/off ratio refers to the ratio of the on-state current and off-state current in a photodetector. Responsivity (R) is a measure of the device's electrical response to incident light and can be calculated using equation 1[111],

$$R = \frac{I_p - I_d}{P_{laser}} \tag{1}$$

where I_p is the photocurrent, I_d is the dark current and P_{laser} is the laser power.

Detectivity (D) is the measure of the photodetector's sensitivity to incident light and can be calculated using equation 2,

$$D = \sqrt{\frac{A}{2eI_d}}R \tag{2}$$

where A is te effective channel area in cm^2 and e is the elementary charge of $1.6* 10^{-19}$ C.

Responsivity and detectivity are key device parameters used to evaluate the photodetector's performance. Zhang *et al.* [62] reported Ti/Au/WS_2 based photodetector with the rise and decay time less than 0.245 and 0.358 ms, on/off ratio and spectral responsivity as high as 336 and 3.14 A/W. Tan *et al.* [109] fabricated graphene/WS_2 based photodetector synthesized by chemical

vapor deposition with responsivity up to 3.5 A/W and detectivity up to 9.9 * 10^{10} $cmHz^{-1/2}W^{-1}$. However, there is no reported work on graphene/WS_2 based all inkjet-printed photodetector so far.

In this work, different figures-of-merit for all inkjet printed photodetector is reported. Figure 4.18 and Figure 4.19 shows the decay time and rise time of less than 50 ms when the laser power of 12.13 mW/cm^2 was used for current-time measurements. Figure 4.20 shows a variation of photocurrent with laser power. Photocurrent increases with laser power as a number of photons having energy higher than band gap increases which lead to higher number of electron-hole pair generation. It also increases with laser power as shown in Figure 4.20 due to higher photocurrent generation. Figure 4.21 shows a variation of responsivity and detectivity with laser power. Effective semiconducting channel area (A) of 0.006 cm^2 (0.06 cm length by 0.1 cm width), dark current value of ~ 0.1342 µA and photocurrent values of 11.83, 12.43, 13.25, 13.62 and 14.15 µA which corresponded to 2.29, 4.68, 7.14, 9.53 and 12.13 mW/ cm^2 were used for responsivity and detectivity calculations. Graphene/WS_2 based photodetector showed high photoresponsivity in the range of 0.86 A/W to 0.19 A/W. High detectivity in the range from 10^{13} $cmHz^{-1/2}W^{-1}$ to 2.29*10^{12} $cmHz^{-1/2}W^{-1}$ was also observed. Both responsivity and detectivity are inversely related to laser power.

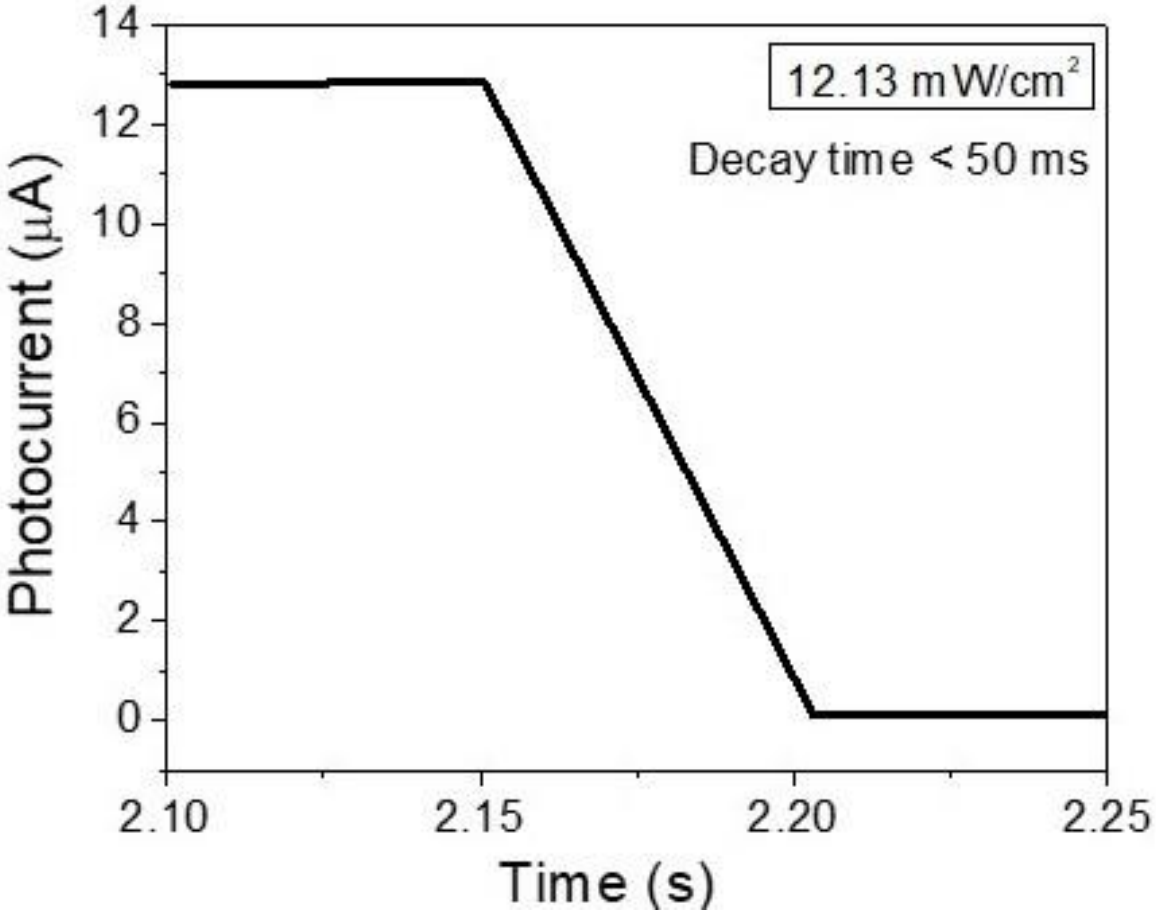

Figure 4.18: Photocurrent- time graphs at 5V to show decay time.

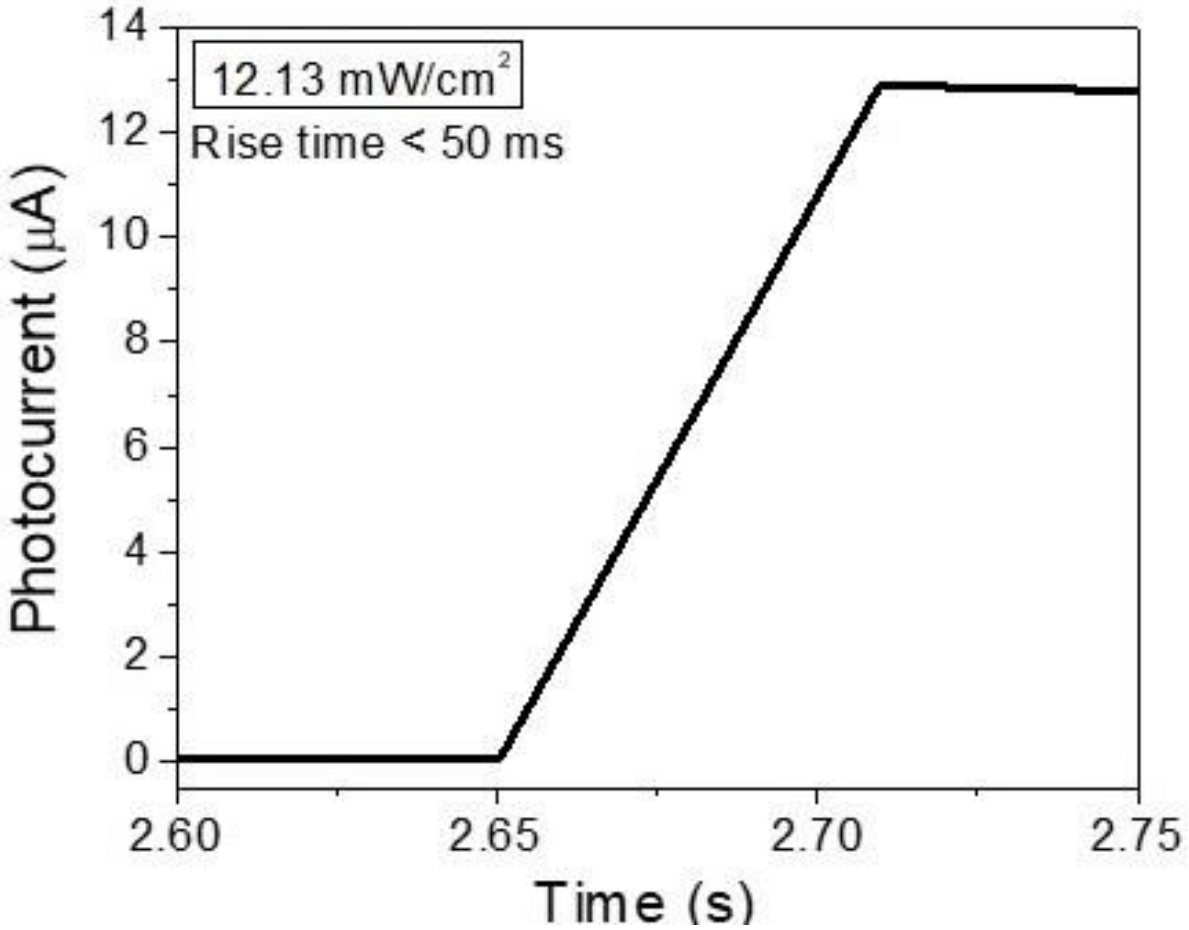

Figure 4.19: Photocurrent- time graphs at 5V to show rise time.

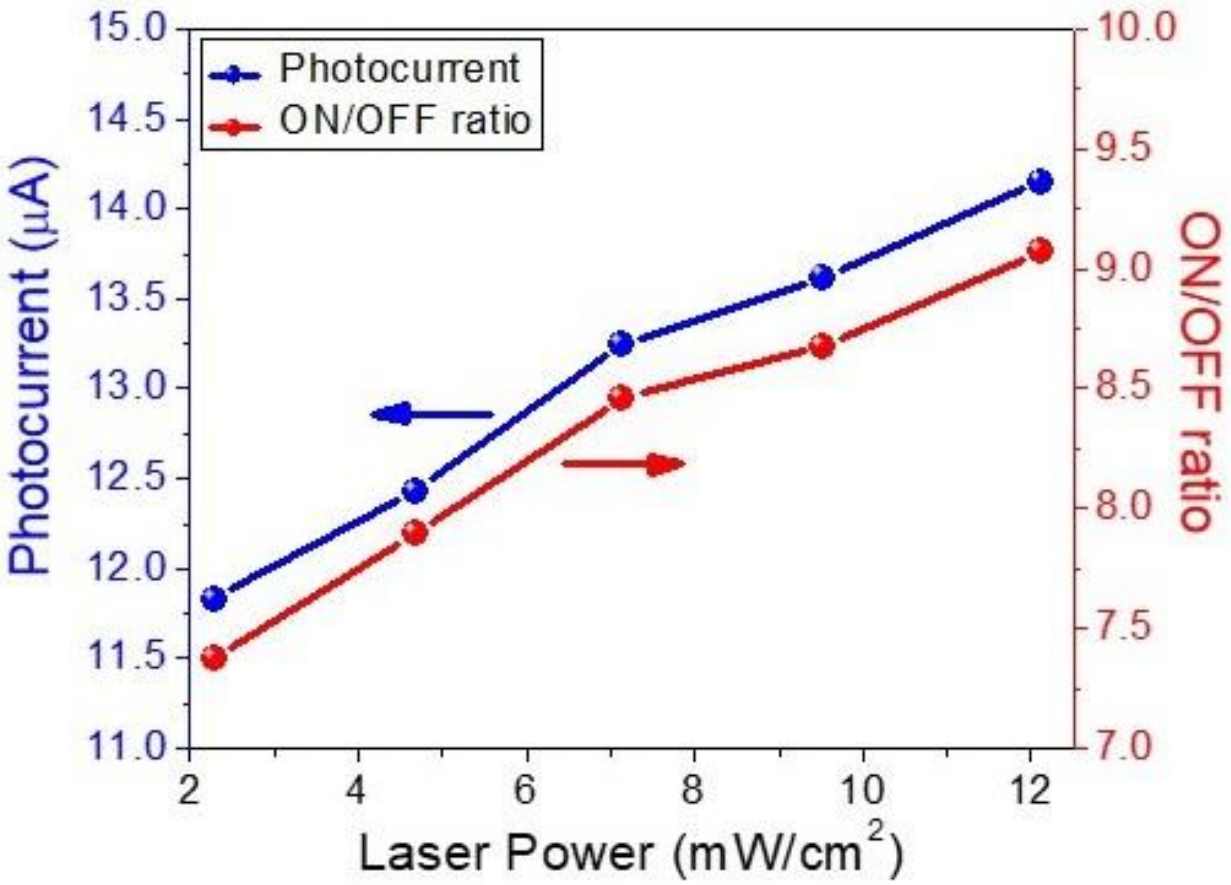

Figure 4.20: Variation of photocurrent and on/off ratio with applied laser power.

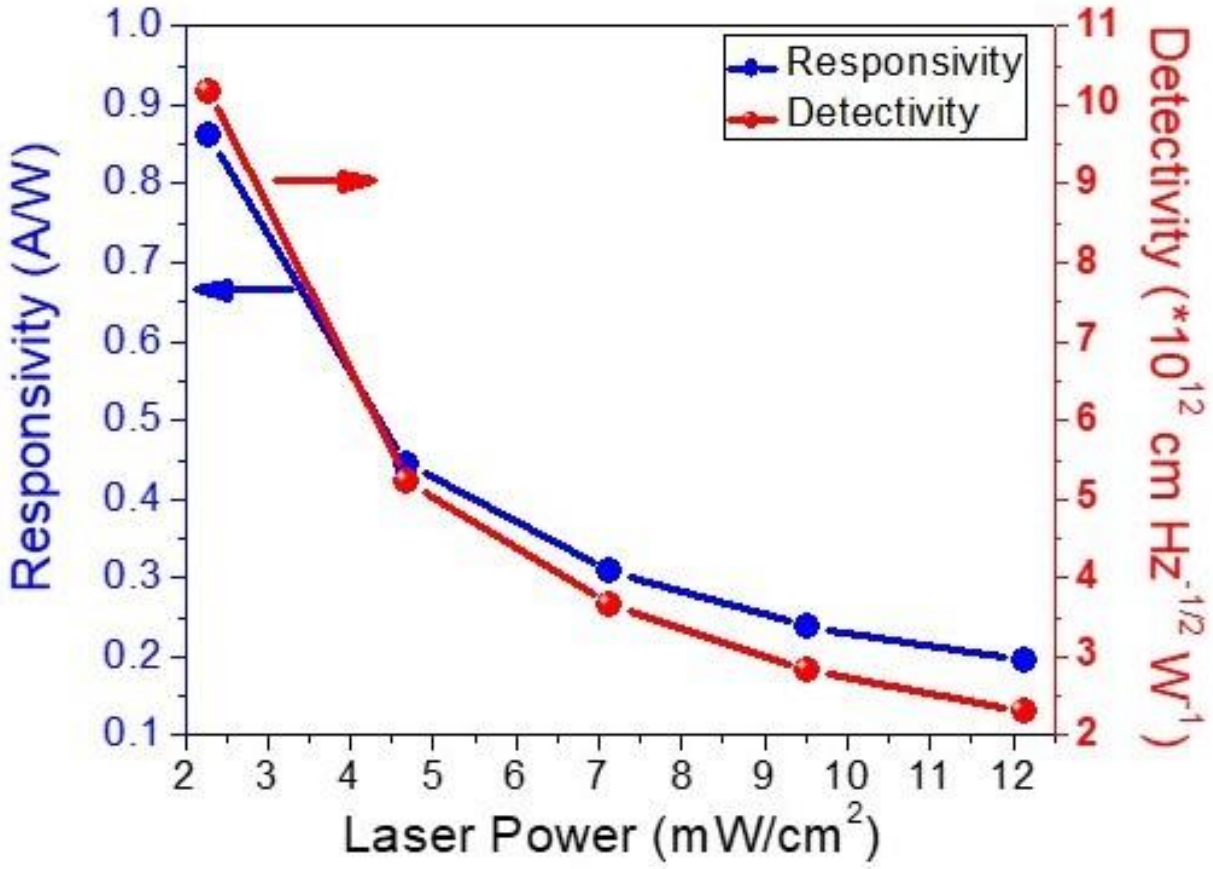

Figure 4.21: Responsivity and detectivity as a function of laser power.

4.7 Graphene/WS_2 interface analysis using capacitance measurements

Capacitance-voltage measurements were also conducted to study the nature of graphene (semi-metal) and WS_2 (semiconductor) interface. Figure 4.22 shows a schematic of front-view of graphene/WS_2/graphene photodetector. Graphene-WS_2 junction appears to form Schottky barrier thus behaving like a Schottky diode. Therefore, two Schottky diodes are in series with each other. Figure 4.23 shows capacitance at different frequencies as a function of bias voltage. The initial increase in capacitance with bias voltage can be attributed to the formation of a Schottky barrier against electron flow at the graphene/WS_2 interface. Capacitance remains constant up to certain bias voltage and then decreases. This decrease in capacitance can be attributed to removal or reduction of the Schottky barrier at WS_2/graphene interface. The value of capacitance is dependent on the filling and refilling of trap states by electrons [112, 113]. When frequency applied is significantly low, a higher value of capacitance is observed because of extra capacitance offered by interface trapped states. Capacitance decreases with an increase in frequencies from 20 kHz to 100 kHz which may be due to a decrease in Schottky barrier height. No significant change in capacitance was observed at frequencies of 200 kHz and higher indicating absence of barrier against electron flow. The decrease in capacitance with frequency can be attributed to the fact that lesser number of electrons get trapped in interface states and after a certain amount of applied frequency, their contribution to capacitance formation is nearly negligible. Highest capacitance value measured at 20 kHz and zero bias voltage was 324.88 pF whereas lowest capacitance value measured at 3000 kHz frequency and zero bias voltage was 2.81 pF. Figure 4.24 shows capacitance at different frequencies as a function of positive bias voltage. This behavior is typical of semiconductor (WS_2)-semi-metal (graphene) interface. Capacitance-voltage measurements help in predicting the formation of the depletion region and predicting the charging and discharging of

capacitance [114, 115]. Capacitance-frequency measurements were also performed to investigate the effect of frequency on capacitance formation as shown in Figure 4.25. It can be observed that there is a sharp decrease in capacitance value from nearly 315.75 pF at 25.76 kHz to 23.79 pF at 480 kHz frequency indicating a strong effect of frequency on capacitance built-up at graphene/WS_2 interface.

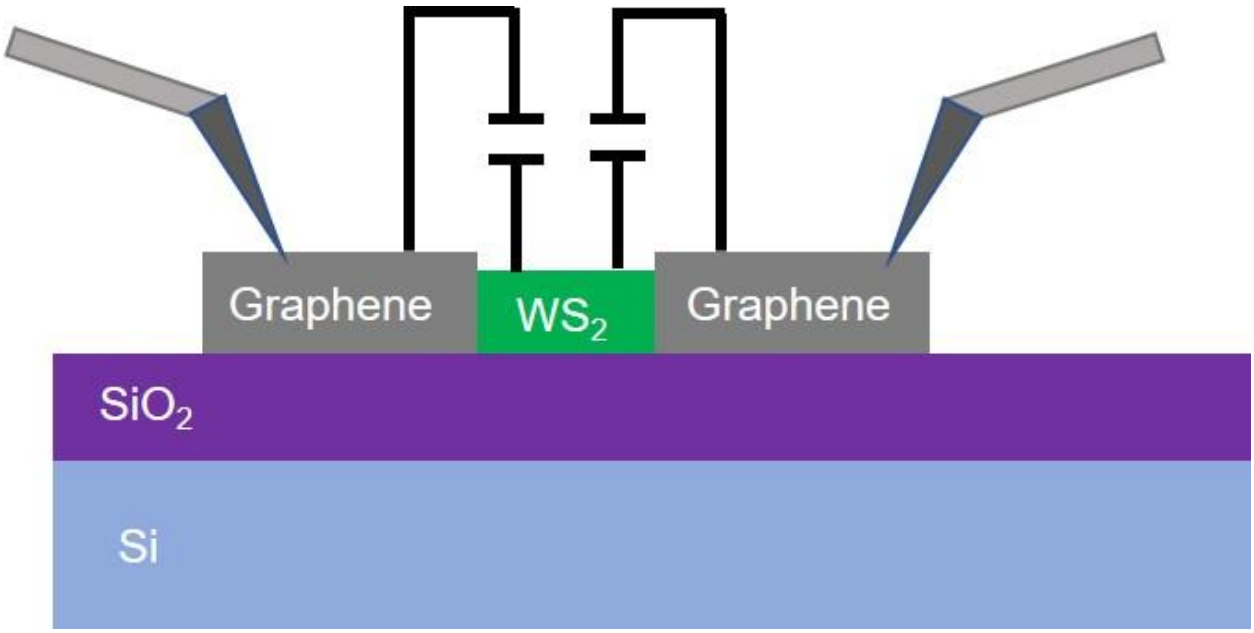

Figure 4.22: Front-view of the graphene-WS_2-graphene photodetector.

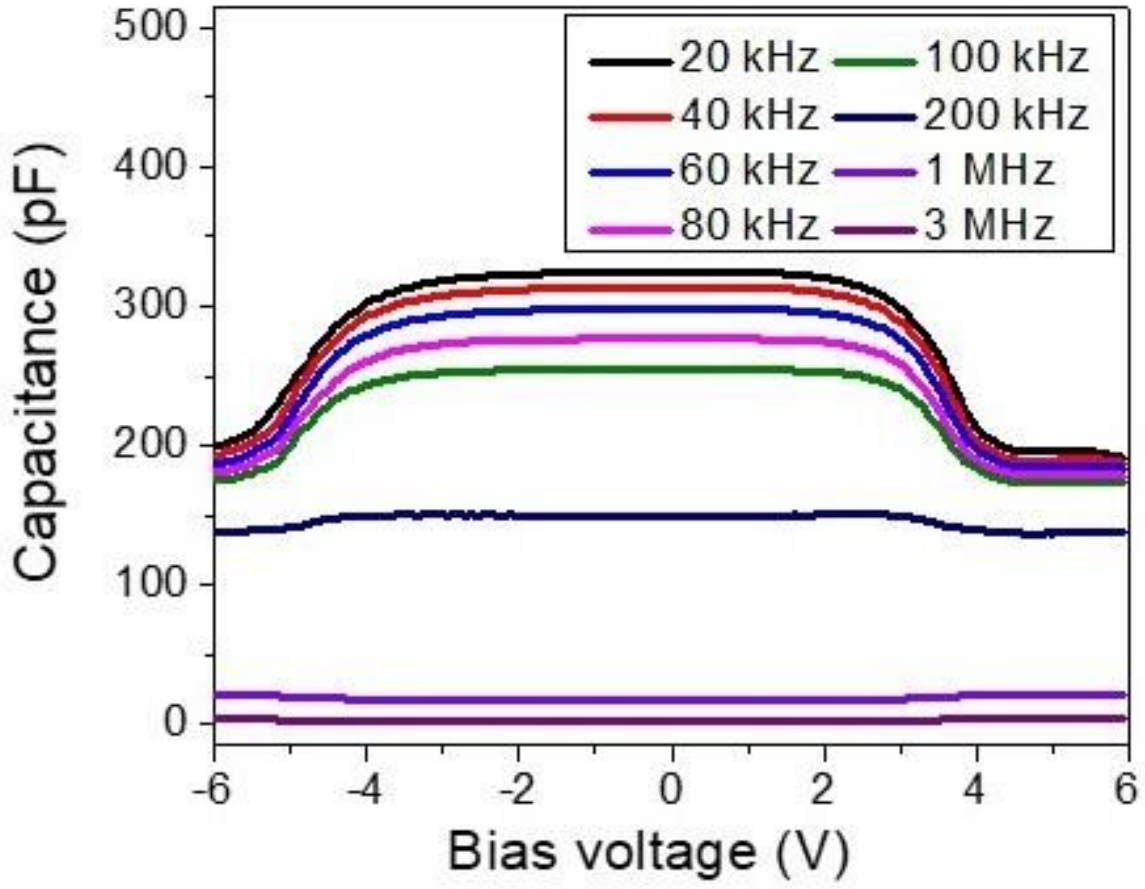

Figure 4.23: Capacitance at different frequencies as a function of bias voltage.

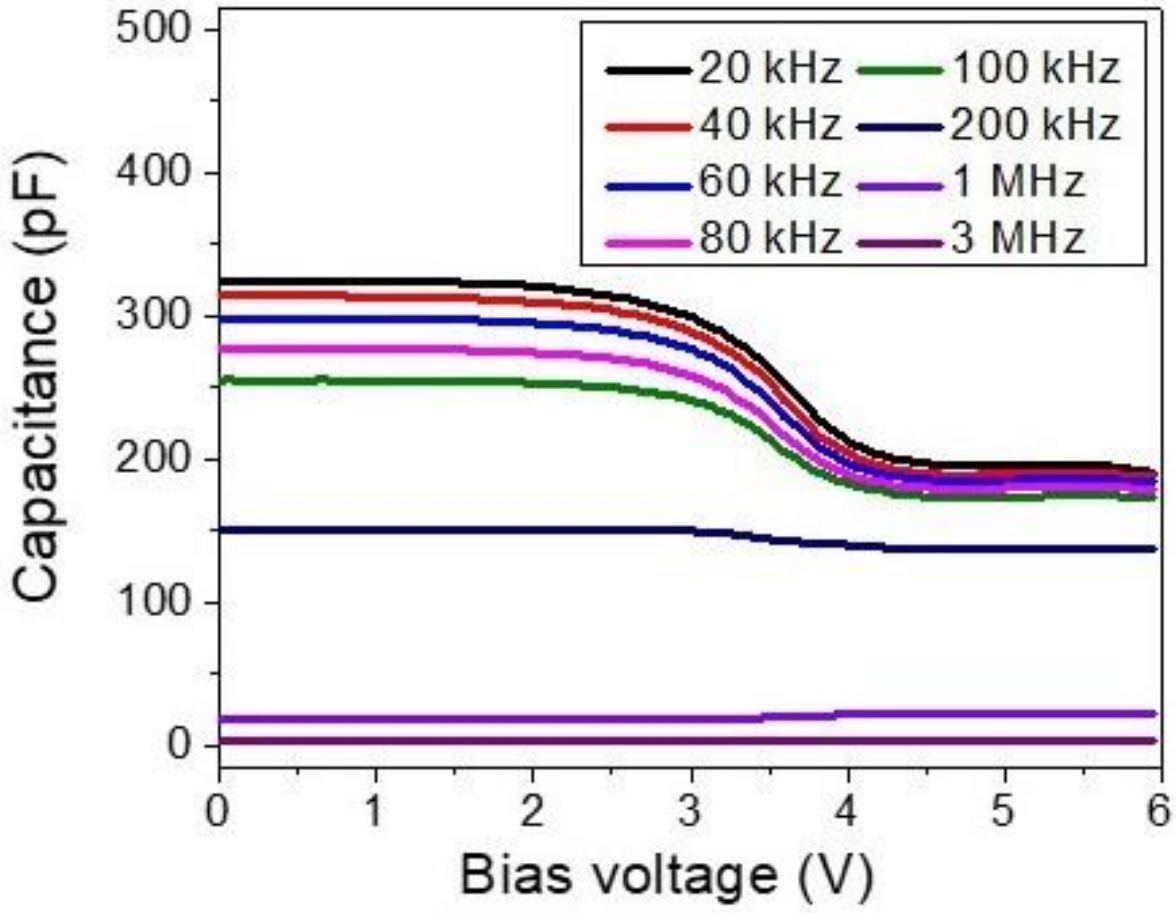

Figure 4.24: Capacitance at different frequencies as a function of positive bias voltage.

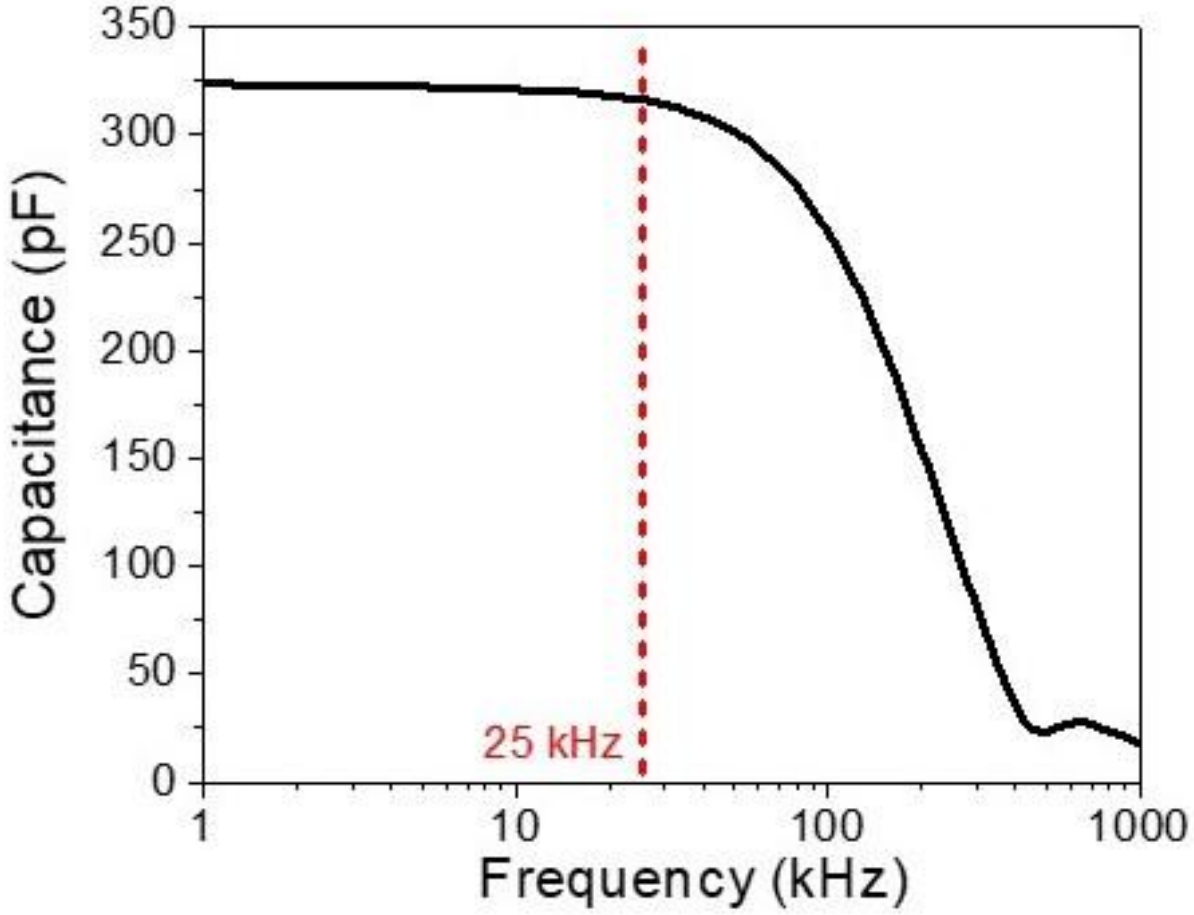

Figure 4.25: Capacitance versus frequency graph showing a sharp decrease in capacitance at approximately 25 kHz frequency.

Chapter 5: Hexagonal boron nitride nanosheets for photosensitive capacitor applications

Interesting properties and various synthesis routes to produce 2-D h-BN nanosheets have opened up different avenues for its use as dielectric especially for charge storage in capacitors which are devices used to store an electric charge. Capacitors in applied electronics are used for power supply smoothing [116, 117], audio frequency coupling [118], RF coupling [119] and decoupling [120] and tuning circuits [121, 122] depending on the conductive layer/ electrodes used, dielectric present in-between them and measured capacitance.

Lee *et al.* [123] fabricated metal/h-BN/metal capacitor with a breakdown electric field of over 4 MV/cm. Wu *et al.* [124] reported parallel plate capacitor with an h-BN dielectric having high breakdown field strength of approximately 9.0 MV/cm and specific capacitance of up to 6.8 μF/ cm^2 using low-pressure chemical vapor deposition (LP-CVD) process. Coleman *et al.* [125] reported graphene/ boron nitride capacitive heterostructure using a combination of inkjet printing and spray coating deposition techniques with areal capacitance ranging from 0.24 to 1.1 nF/cm^2 with limiting the dielectric thickness of 1.65 μm.

However, there are no reports to date on graphene/h-BN based all inkjet printed capacitors. The present work aims to explore the thickness-dependent optoelectronic properties of h-BN nanosheets with increasing number of passes through the help of Raman spectroscopy, UV-vis spectroscopy, leakage current density and capacitance density measurements. The work also intends to explore the effect of temperature on Raman peaks of h-BN printed patterns with different thickness and to study the effect of LED illumination, temperature, and frequency on capacitance density of all inkjet-printed graphene/h-BN based capacitor.

5.1 Materials and methods

A mixture of 70% cyclohexanone and 30% terpineol (C/T) was prepared in glass vials with total volume of solution amounting to 20 ml. Ethyl cellulose (EC) surfactant was then added to increase the viscosity of the solution and promote stability. The mixture was bath sonicated for 2 hours to promote complete and uniform mixing of EC in C/T solution mixture. This combination also has a viscosity of approximately 12 cP which is ideal for inkjet printing [45]. The h-BN powder in a concentration of 30 mg/ml or 0.6 grams was then taken in a 50 ml beaker and 20 ml of C/T/EC solution was added to it. Horn-tip sonication at 40% power amplitude and magnetic stirring at 500 rpm for 3 hours was then employed for ink preparation. Fujifilm Dimatix Materials Printer consisting of 16 inkjet nozzles was used to print graphene and h-BN inks for different patterns and devices in this work. Cartridge temperature of 40 ˚C and a platen temperature of 60 °C was used during all the printing work. The height measurements for AFM studies were performed for the areas of 5 μm x 5 μm with the scanning speed of 0.85 Hz.

5.2 Optical characterization of h-BN

Figure 5.1 shows the working mechanism of the unique ink preparation setup comprising of horn-tip sonicator and hot plate with magnetic stirrer employed in the present work. The photograph of actual setup is shown as its inset. Both horn-tip sonication and magnetic stirring have been used either as a medium of exfoliation or medium for uniform mixing. Horn-tip exfoliation is a very good and effective high power means of exfoliation, but the degree of exfoliation varies from being the highest in the vicinity of the probe tip to lowest at the bottom of the vial resulting in the very large amount of unexfoliated particles at the bottom. A very slow magnetic stirring at the bottom of the beaker can resolve this issue. The horn-tip vibrates and

generates energy for exfoliation of layered material whereas the slow magnetic stirring does not allow particles to settle down in form of precipitates. The thickness of inkjet printed h-BN on SiO_2/Si substrate with a different number of printing passes is shown in Figure 5.2. Its inset comprises of a photograph of actual printed patterns. It can be observed that the optical contrast of h-BN printed structures varies from translucent to opaque with a different number of printing passes due to increase in thickness. It has been reported that h-BN in its monolayer form is highly transparent [126, 127, 128, 129, 130]. However, obtaining monolayer h-BN with inkjet printing remains a challenge.

Figure 5.3 represents Raman spectra of h-BN with different printing passes. No change in Raman peak position and no significant change in full-width at half-maximum (FWHM) was observed which may be due to the presence of few-layer h-BN even in a printed structure with 1 pass. It can be observed that the intensity of Raman spectra increases with increase in number of passes. This can be attributed to higher interlayer interactions in thicker h-BN patterns [131]. The absorbance of h-BN as a function of wavelength is shown in Figure 5.4. Absorption peaks for 1, 5, 10, 20 and 30 passes were observed at approximately 252, 275, 279, 282 and 287 nm corresponding to 4.92, 4.51, 4.44, 4.39 and 4.32 eV band gap. This is in accordance with reported literature indicating a reduction in band gap with thickness. No peaks at 307 or 365 nm were observed indicative of no optical transitions and redistribution of h-BN's electron-hole density between Van-Hove singularities [132, 133].

Figure 5.5, Figure 5.6 and Figure 5.7 show the atomic force microscopy (AFM) images of the inkjet printed *h*-BN patterns on SiO_2 substrates with 1, 5 and 10 passes respectively. AFM images of the inkjet printed *h*-BN patterns showed the same value roughness depending on the number of printing passes which indicates that the roughness does not change even if the number of printing

passes increases. The 1, 5 and 10 passes inkjet printed samples showed a root mean squared (RMS) roughness of 78.7 nm, 72.0 and 74.2 nm, respectively.

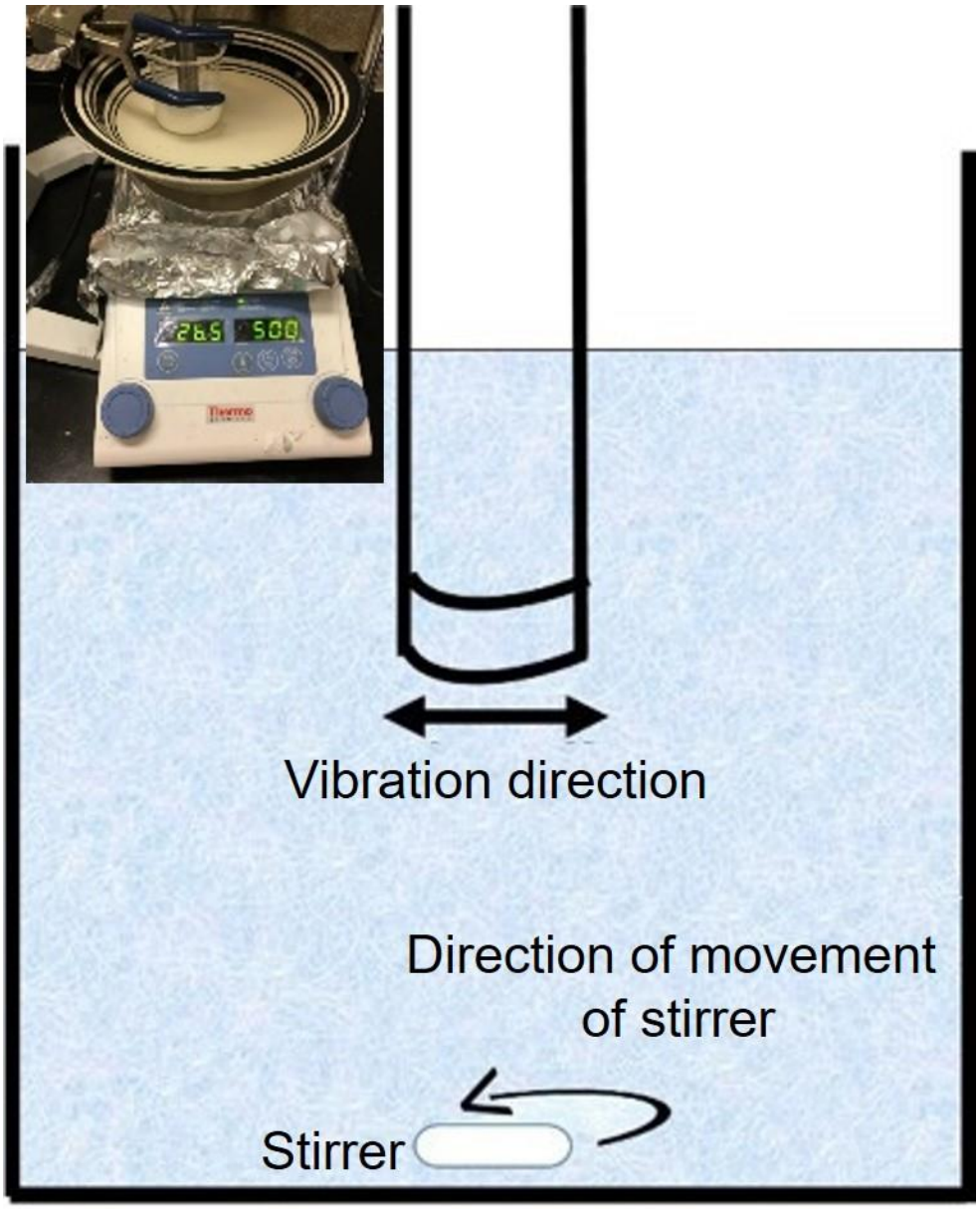

Figure 5.1: Schematic of working mechanism involved in ink preparation. Inset: Photograph of actual setup.

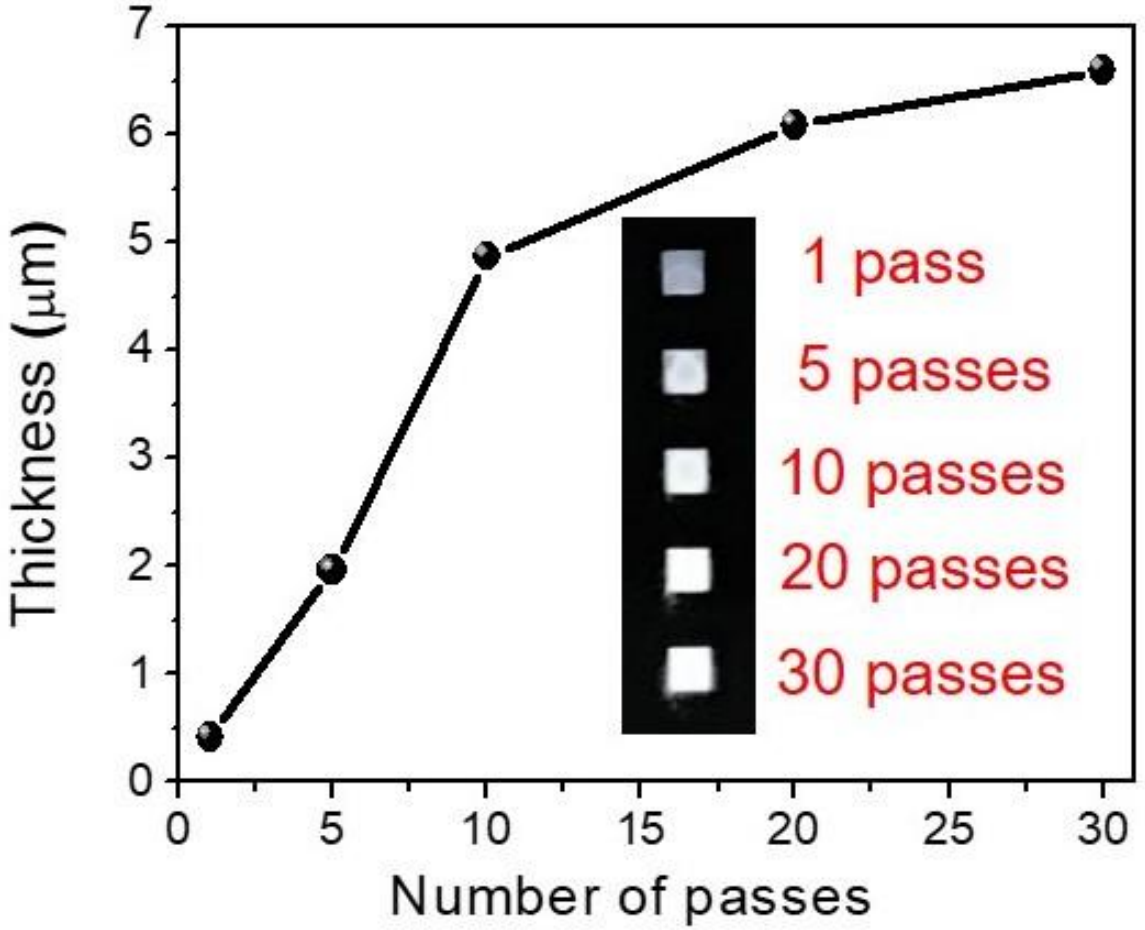

Figure 5.2: Thickness dependence on number of inkjet printing passes. Inset: 2 mm square inkjet printed h-BN patterns with 1, 5, 10, 20 and 30 number of printing passes.

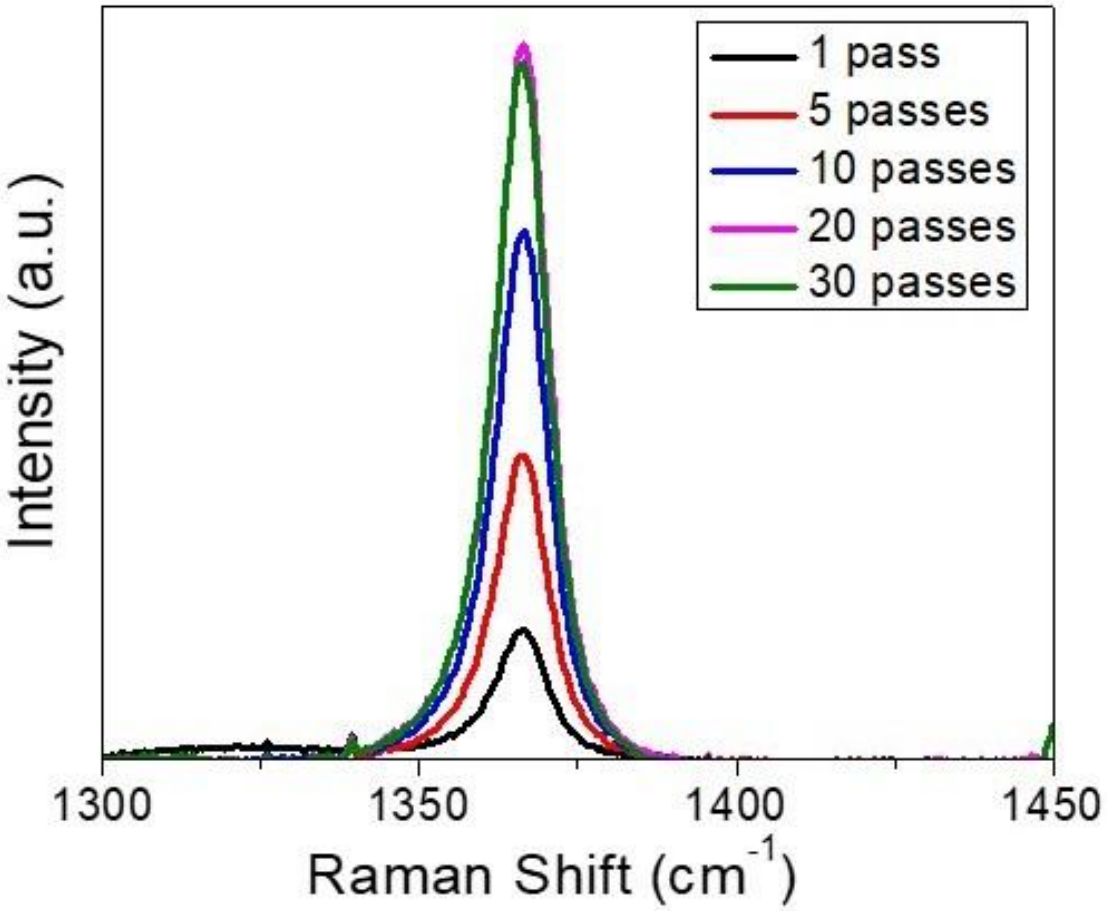

Figure 5.3: Raman spectra of inkjet h-BN films with different printing passes.

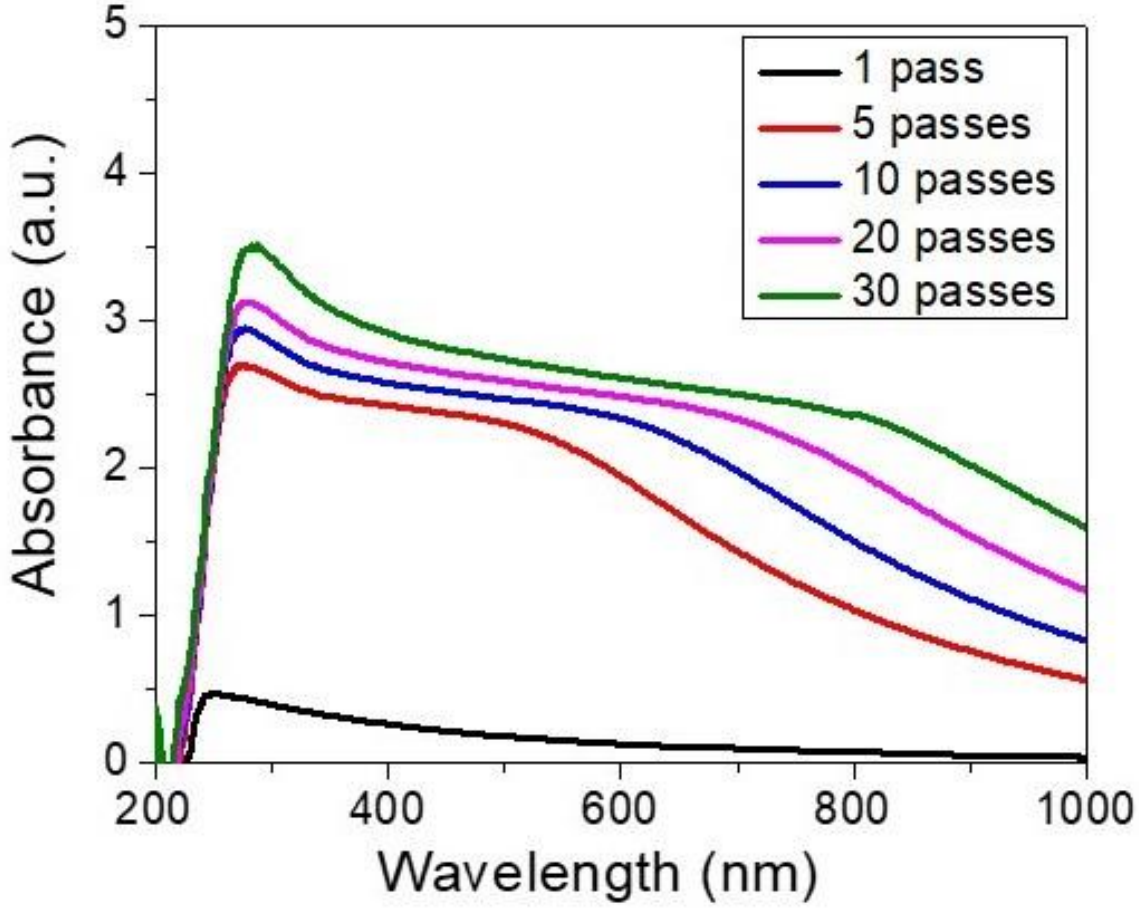

Figure 5.4: Absorption spectra of h-BN printed films.

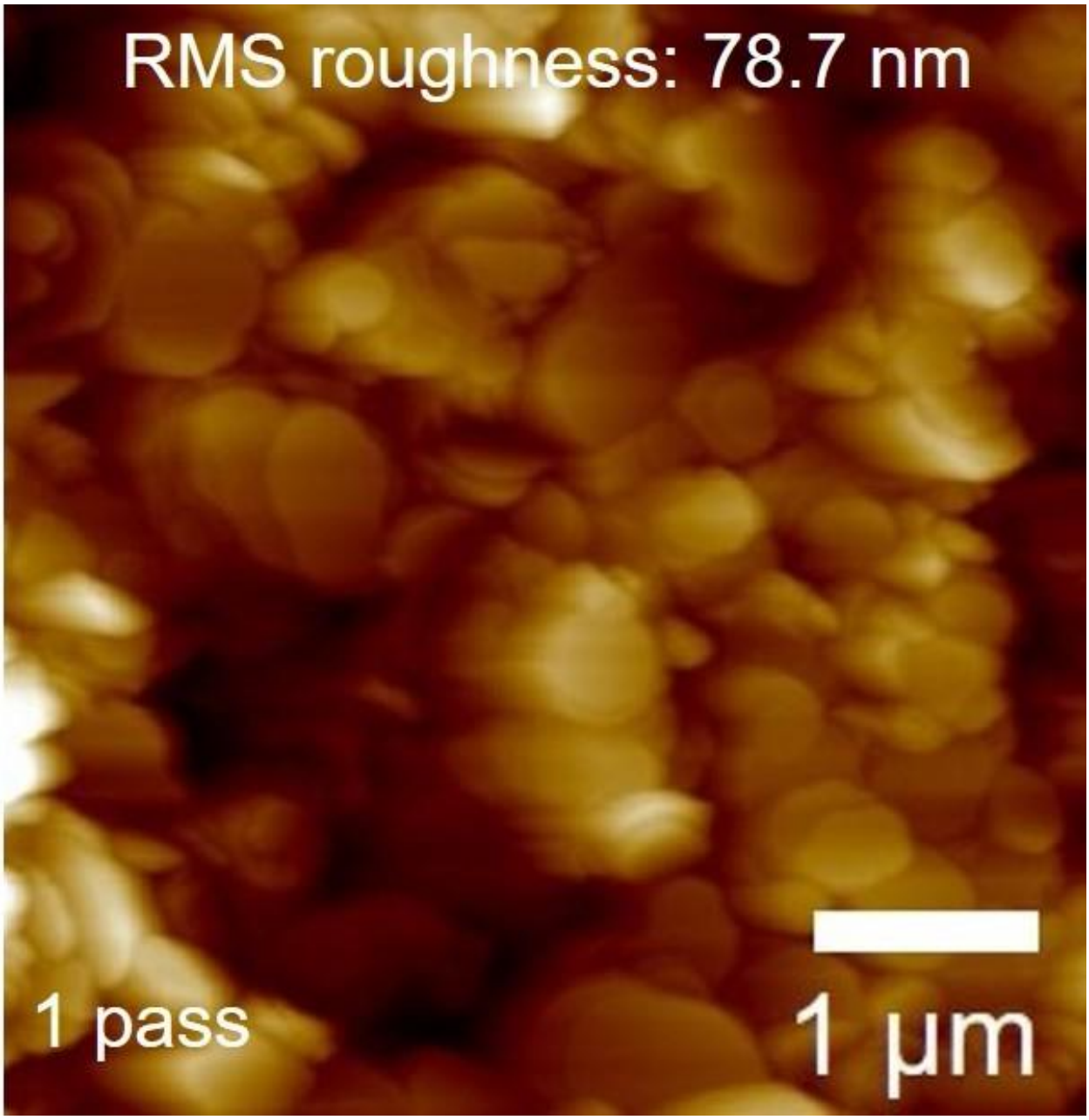

Figure 5.5: AFM image of the inkjet printed *h*-BN pattern on SiO_2 substrates with 1 pass.

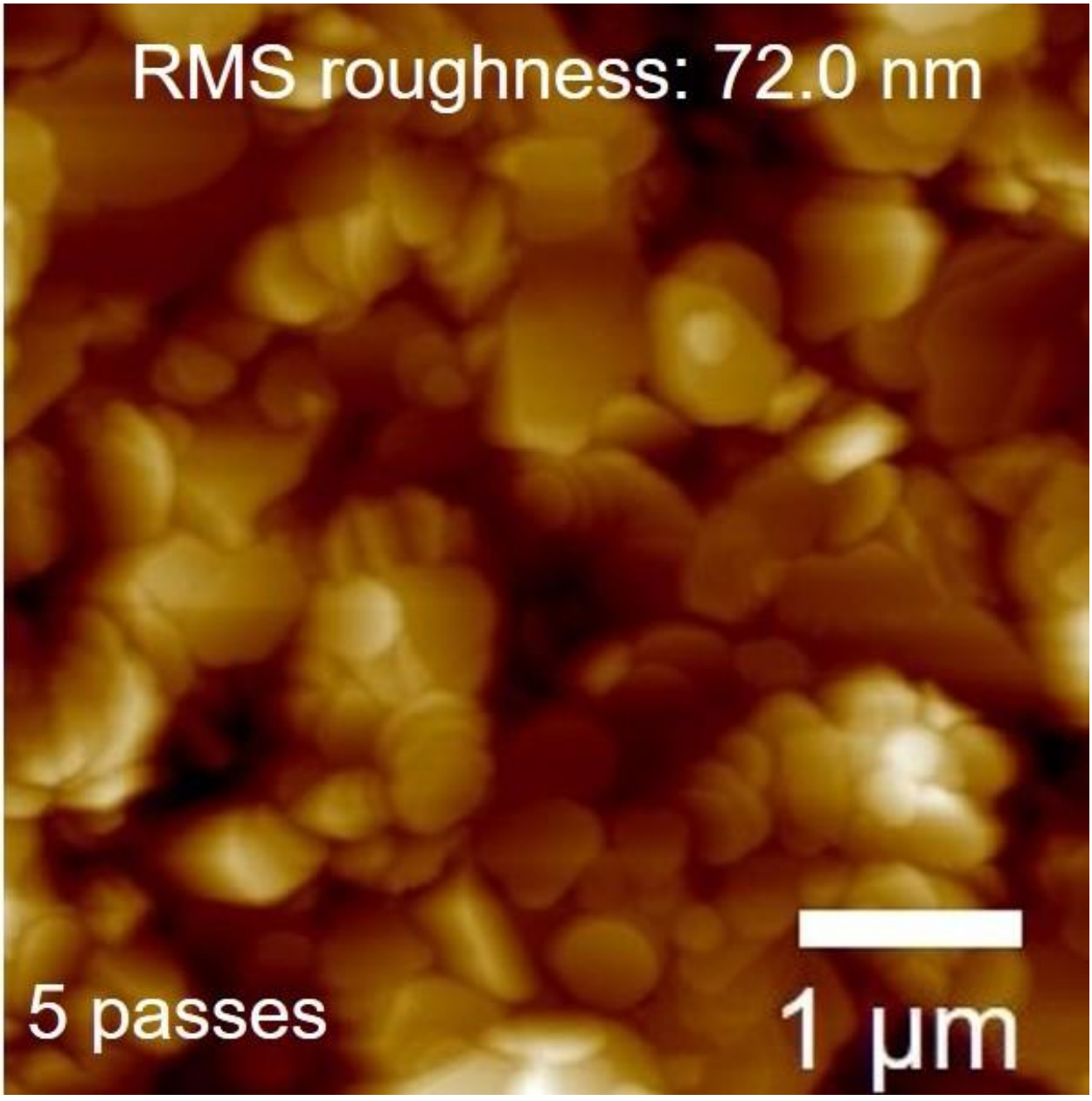

Figure 5.6: AFM image of the inkjet printed *h*-BN pattern on SiO_2 substrates with 5 passes.

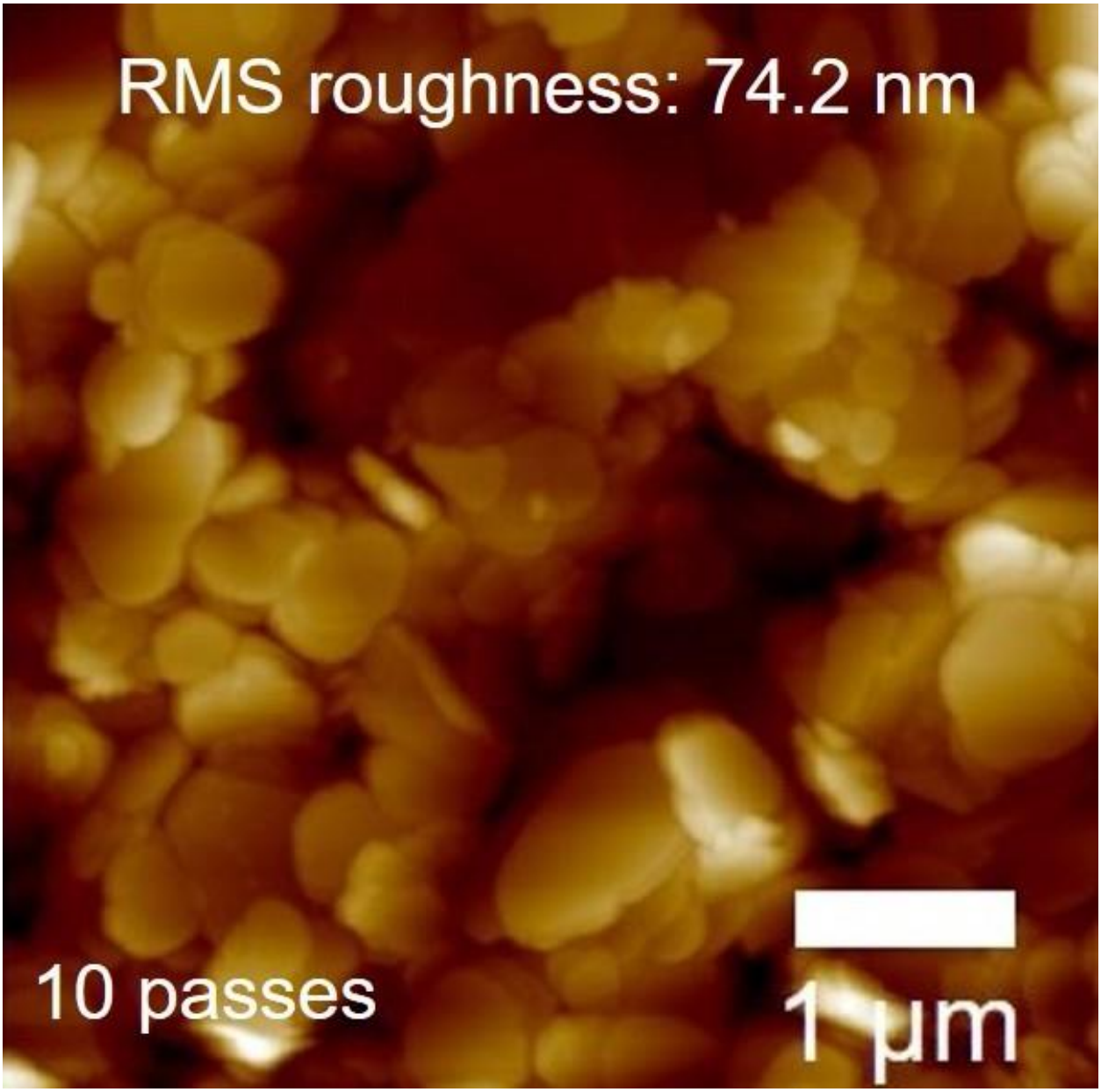

Figure 5.7: AFM image of the inkjet printed *h*-BN pattern on SiO_2 substrates with 10 passes.

5.2 Temperature-dependent raman spectroscopy of printed h-BN films

Figure 5.8 and Figure 5.9 shows temperature-dependent Raman spectra of inkjet printed h-BN patterns with 20 and 30 passes respectively. Raman spectra of h-BN typically comprise of the just single peak at around 1366 cm^{-1} corresponding to the E_{2g} phonon vibration mode [132]. E_{2g} band position red shifts to approximately 19 cm^{-1} from 1366.34 cm^{-1} at room temperature (298 K) to 1347.29 cm^{-1} at 873 K for h-BN inkjet printed pattern with 20 passes. The relatively smaller E_{2g} band position red shift of approximately 16 cm^{-1} was observed from 1365.89 cm^{-1} at room temperature to 1349.69 cm^{-1} at 873 K suggesting higher temperature stability of thicker h-BN printed films. The red shift with temperature is attributed to B-N bond strength change [134]. To study the temperature effect further, the first order temperature coefficient (χ) which is the slope of the linear fit of E_{2g} mode frequency shift (ω_{E2g}) versus temperature curve was obtained and is shown in Figure 5.10 for 20 and 30 printing passes respectively. It was found to be -0.033 cm^{-1}/K and -0.028 cm^{-1}/K for 20 and 30 printing passes respectively suggesting higher temperature stability for 30 passes as mentioned above. The reported first order temperature coefficients of 1-layer, 2-layer and 9-layer h-BN nanosheets synthesized using low-power chemical vapor deposition (LPCVD) are – 0.0341, – 0.0315 and – 0.0378 cm^{-1}/K, respectively. The present work also reports a lower temperature coefficient for h-BN films than previous reports [134].

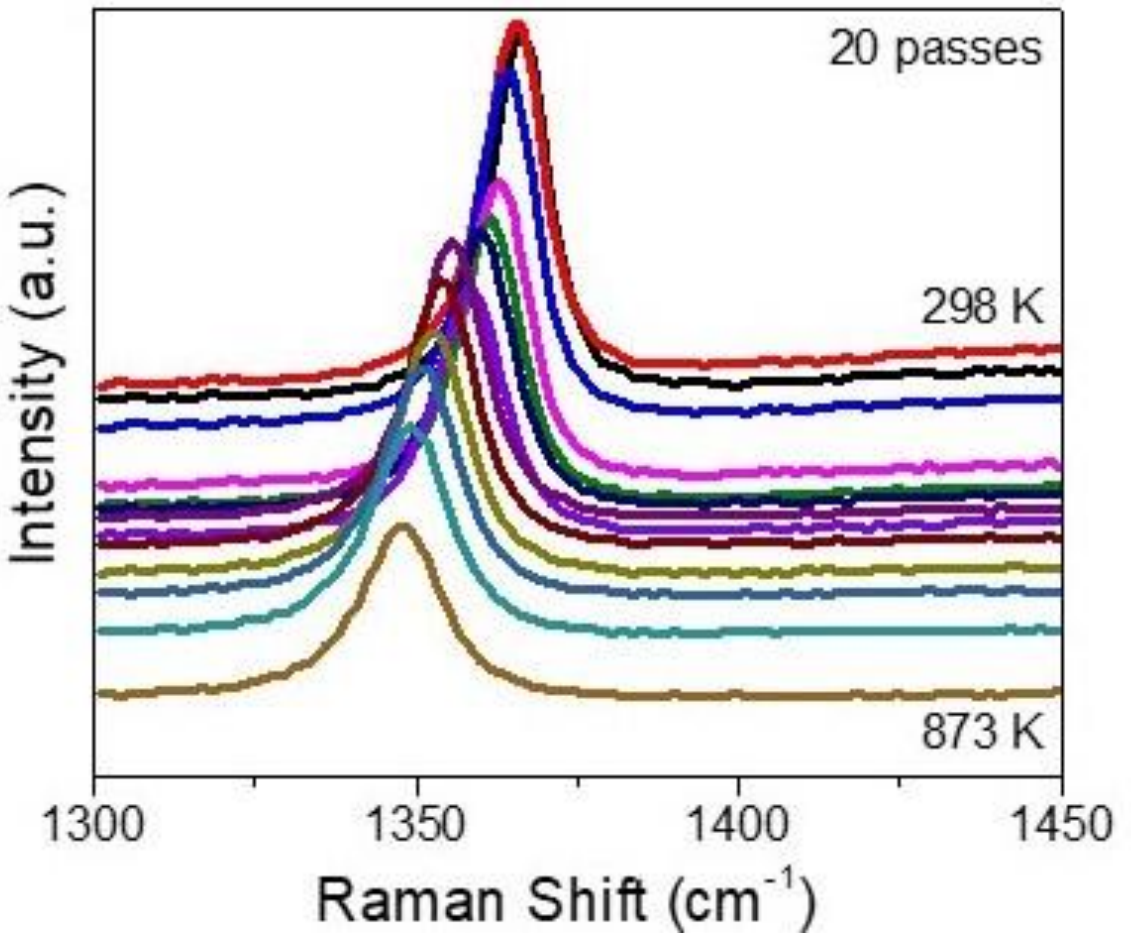

Figure 5.8: Raman spectra of 2 mm square h-BN inkjet printed pattern with 20 passes at different temperatures.

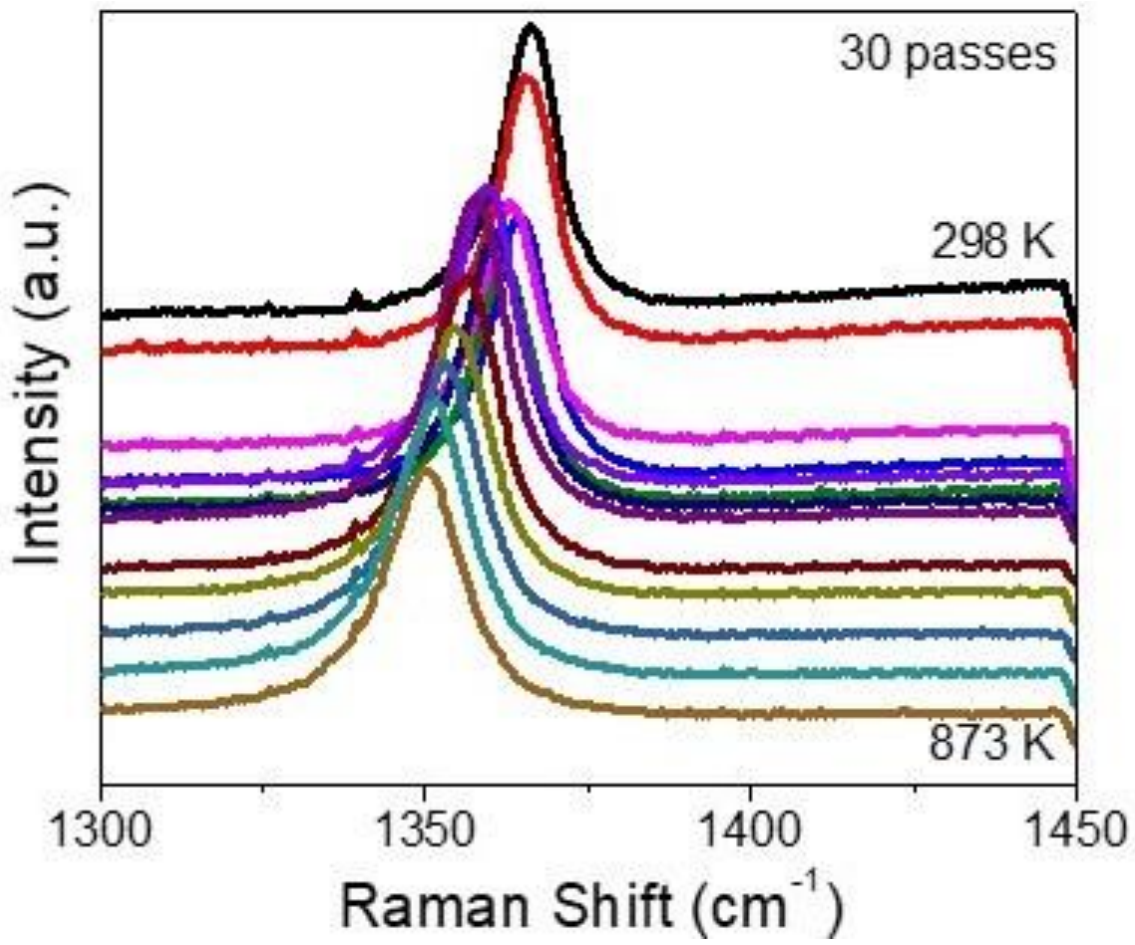

Figure 5.9: Raman spectra of 2 mm square h-BN inkjet printed pattern with 30 passes at different temperatures.

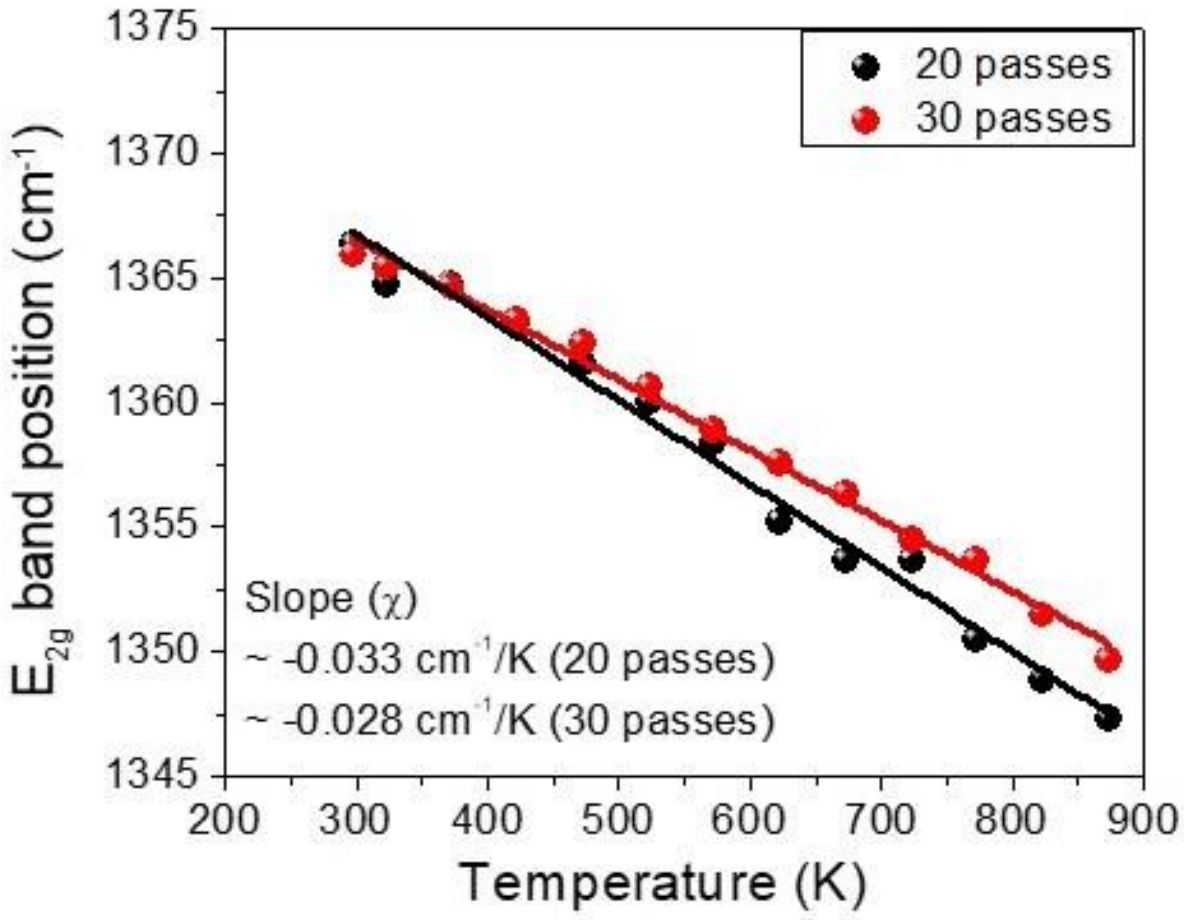

Figure 5.10: Linear fit showing the extracted first order temperature coefficient (χ) of -0.033 cm^{-1}/K and -0.028 cm^{-1}/K for 20 and 30 passes of printed h-BN.

5.3 Effect of number of printing passes on current density and capacitance density

Leakage current density and capacitance density are two important figures-of-merit used to compare the performance of capacitors with different geometries. Leakage current density is the current flowing through the capacitor per unit area whereas capacitance density refers to capacitance per unit area of a capacitor. Figure 5.11 and Figure 5.12 shows the variation of leakage current density with voltage of graphene/ h-BN based capacitor with 20 and 30 number of h-BN printing passes having a thickness of 6.083 and 6.596 µm. Their inset shows the actual capacitor with 1 and 20 number of printing passes. Graphene 5 mm by 3 mm with 30 number of printing passes was printed first followed by annealing at 350 ^{o}C for 3 hours. This was followed by 5 mm by 3 mm h-BN printing with 20 and 30 number of printing passes and annealing at 450 ^{o}C for 2 hours. Graphene 7 mm by 1 mm with 30 number of printing passes was printed then followed by annealing at 350 ^{o}C for 3 hours. The high conductivity of the only graphene is shown in Figure 5.11 inset to validate that top and bottom graphene are not in contact. The current density was lowest (0.072 µA/mm^2 at 40 V) for 30 number of printing passes due to thicker h-BN dielectric presence.

Capacitance density-voltage measurements were performed at different frequencies on both the devices at room temperature as shown in Figure 5.13 and Figure 5.14 respectively. Higher values of capacitance density (~ 24 fF/µm^2 at -25 V for 1kHz frequency) were observed for a capacitor with 20 number of h-BN printing passes owing to the lower thickness and thus lower area. The capacitance-voltage measurement technique is widely used for characterizing semiconductor and dielectric materials and devices. The applied voltage is varied, and capacitance values are obtained. Capacitance density is then derived by dividing capacitance by area and plotted with respect to voltage. In the metal-insulator-metal type of capacitors, metal-insulator

junction behaves as depletion region which does not have to conduct electrons or holes but may contain ionized donors or electrically active traps which promotes the flow of leakage current in the capacitor. Initial capacitance values in the capacitance-voltage measurement of inkjet printed graphene/h-BN based capacitor decreases with frequency. This can be attributed to the reduction of the barrier at the graphene/h-BN interface. At lower frequencies, a higher value of initial capacitance is obtained because of interface trapped states. When the applied voltage is small, the valence band edge is driven far from the Fermi level resulting in low carrier density. This explains the drop-in capacitance at lower voltages. However, at higher frequencies, lower value of initial capacitance and a lower drop in capacitance at low voltages is observed due to the inability of interface trapped charges to retain a charge. Figure 5.15 shows drop in initial capacitance density (from ~ 24 fF/μm^2 at 1 kHz to ~ 10.4 fF/μm^2 at 1 MHz) as a function of frequency at -25 V for 20 passes respectively. Figure 5.16 shows drop in initial capacitance density (from ~ 22.7 fF/μm^2 at 1 kHz to ~ 10.3 fF/μm^2 at 1 MHz) as a function of frequency at -25 V for 30 passes respectively.

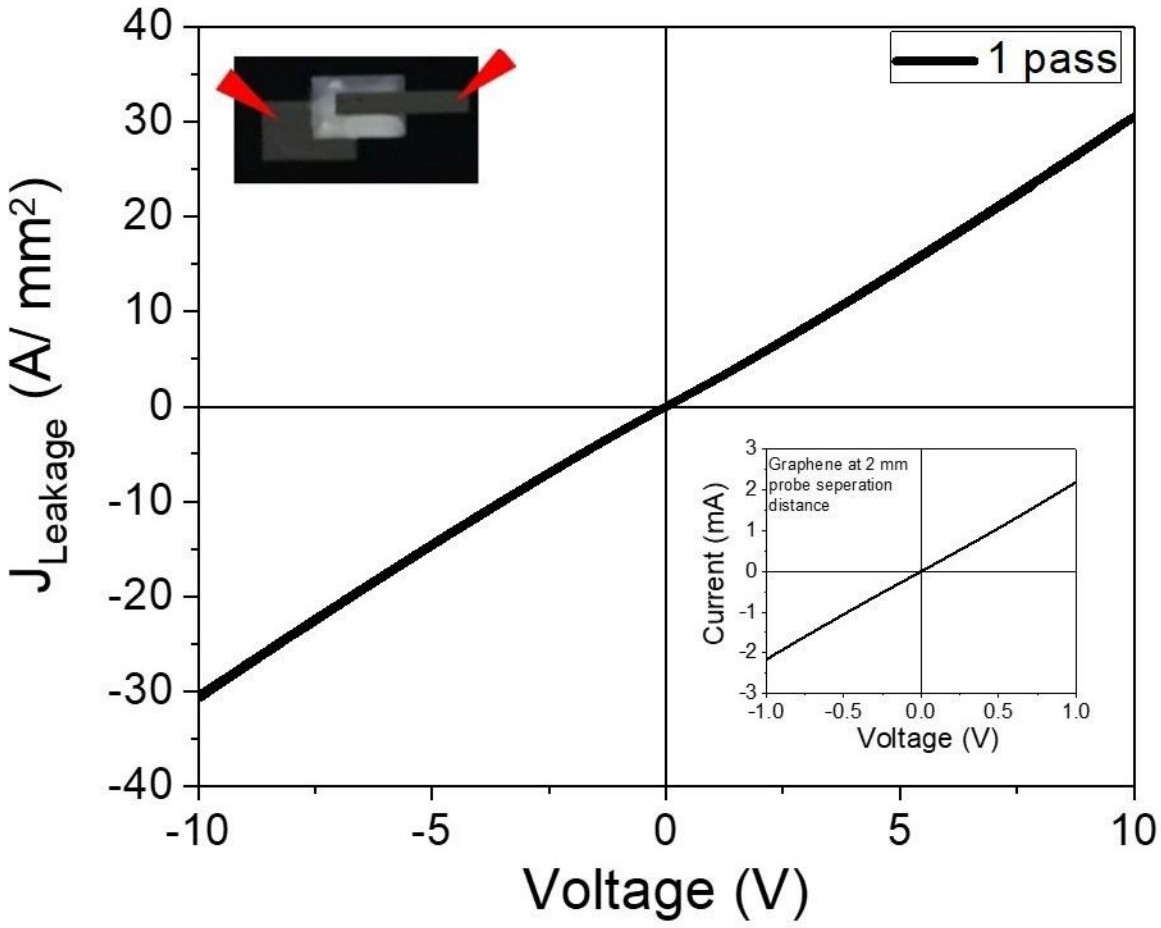

Figure 5.11: Leakage current density variation with voltage for a graphene-h-BN-graphene capacitor with 1 h-BN printing pass (Inset: Inkjet-printed graphene-h-BN-graphene capacitor with 1 h-BN pass).

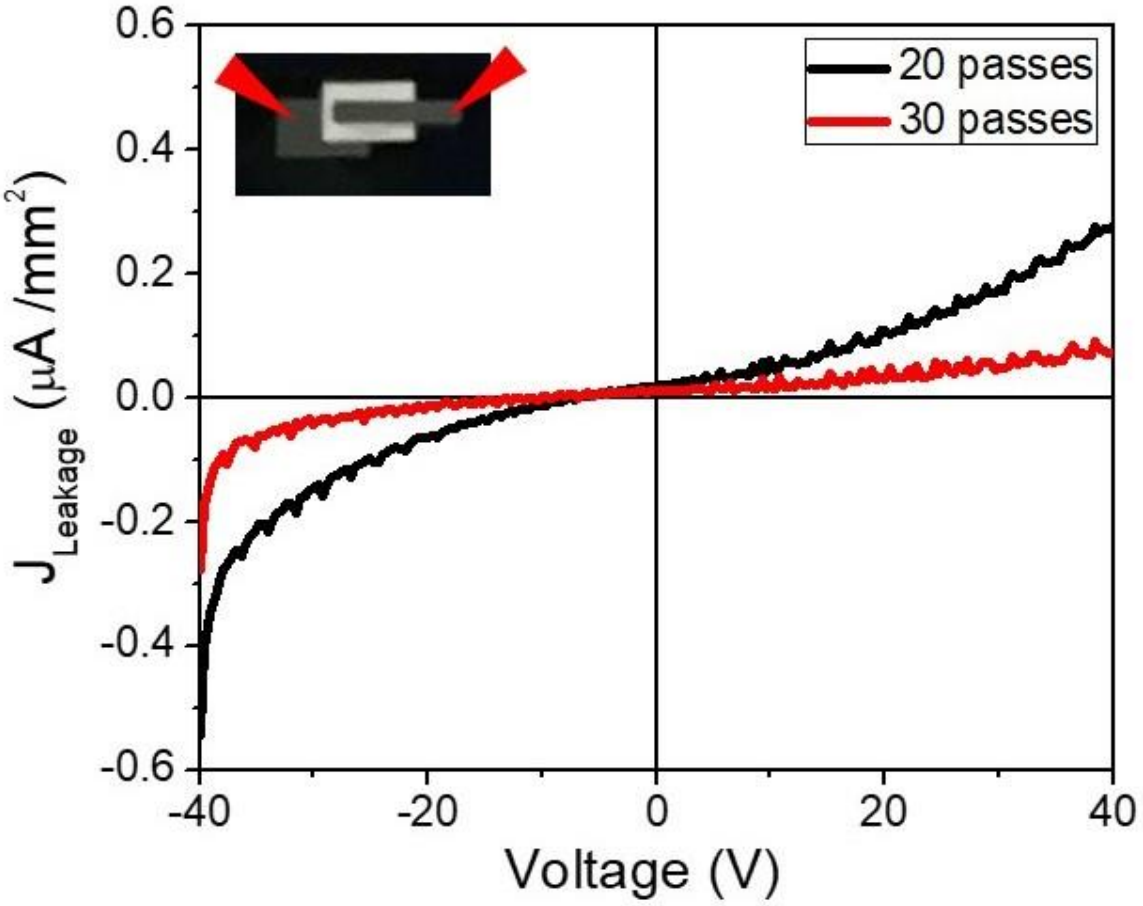

Figure 5.12: Leakage current density variation with voltage for a graphene-h-BN-graphene capacitor with 20 and 30 h-BN printing passes (Inset: Inkjet-printed graphene-h-BN-graphene capacitor with 20 h-BN passes).

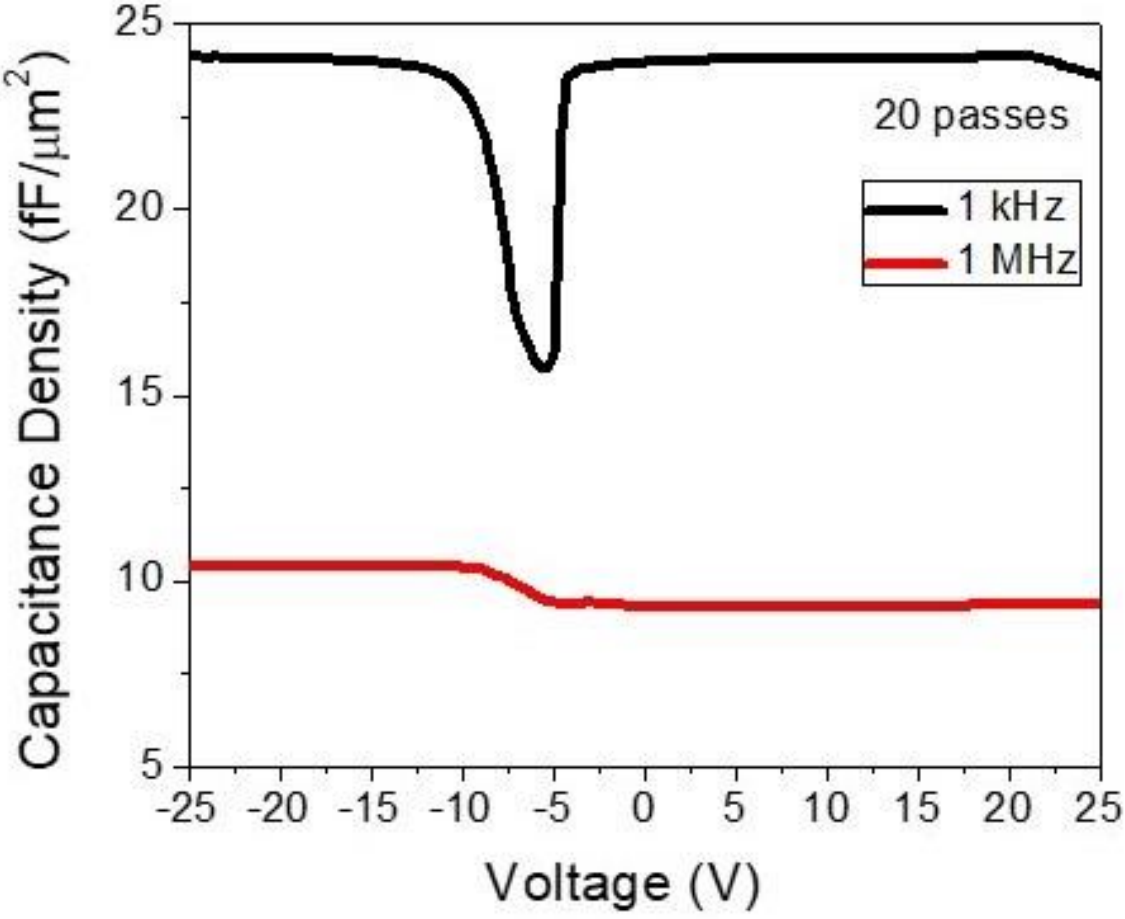

Figure 5.13: Variation of capacitance density with the voltage at 1 kHz and 1 MHz for 20 number of h-BN printing passes.

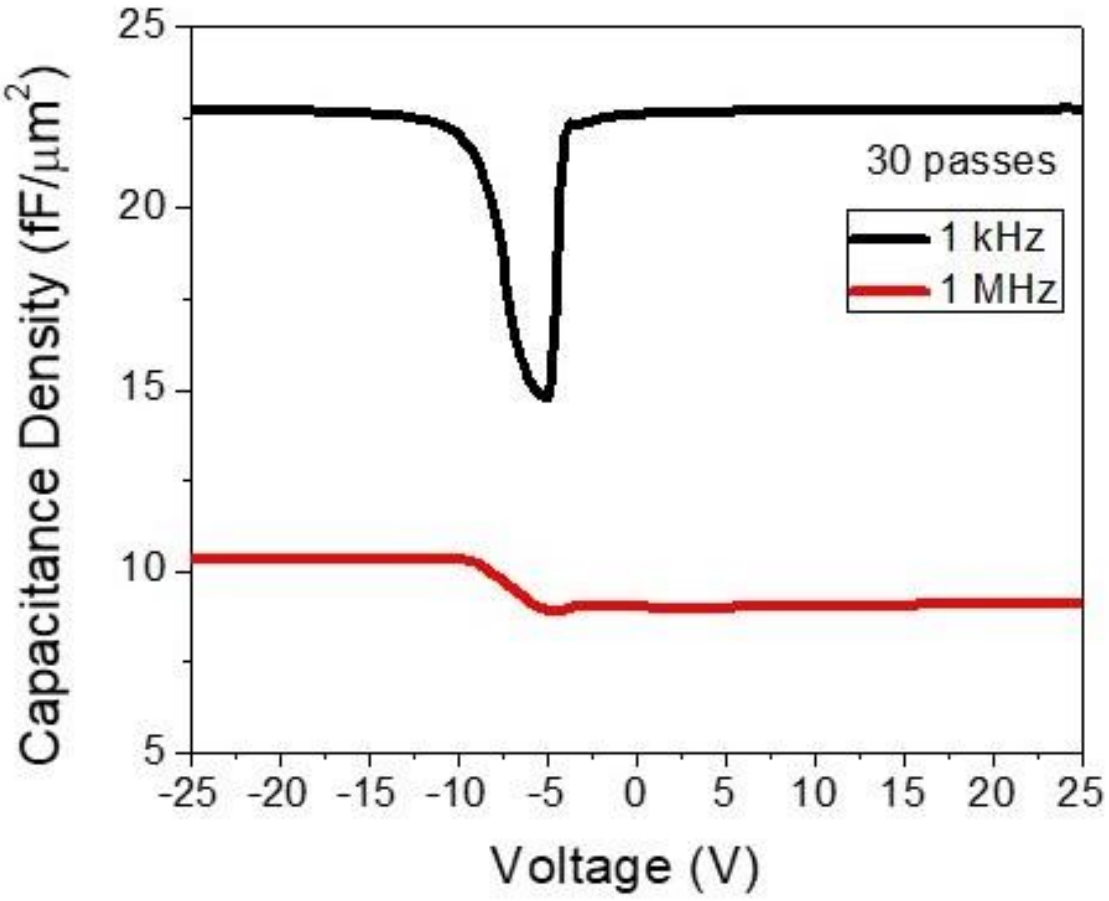

Figure 5.14: Variation of capacitance density with the voltage at 1 kHz and 1 MHz for 30 number of h-BN printing passes.

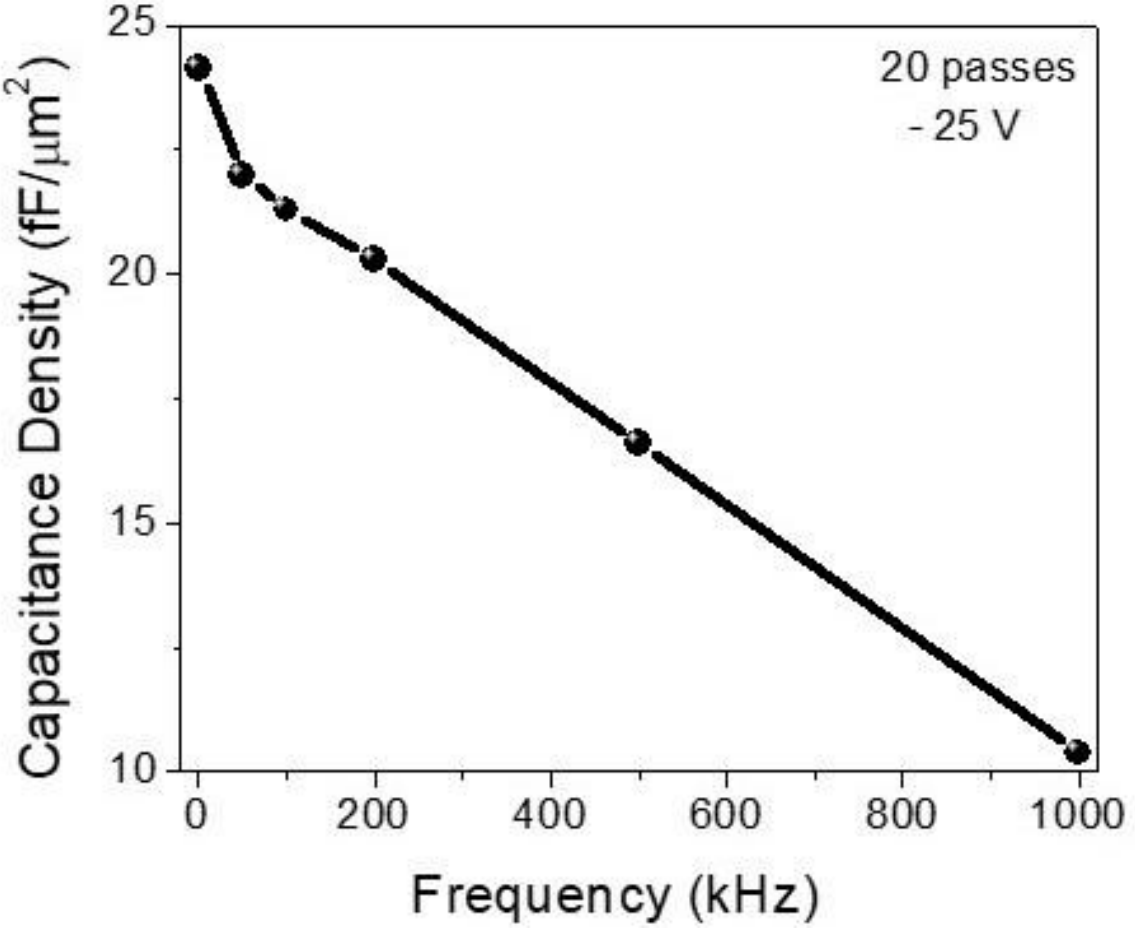

Figure 5.15: Drop in initial capacitance as a function of frequency at -25 V for 20 passes.

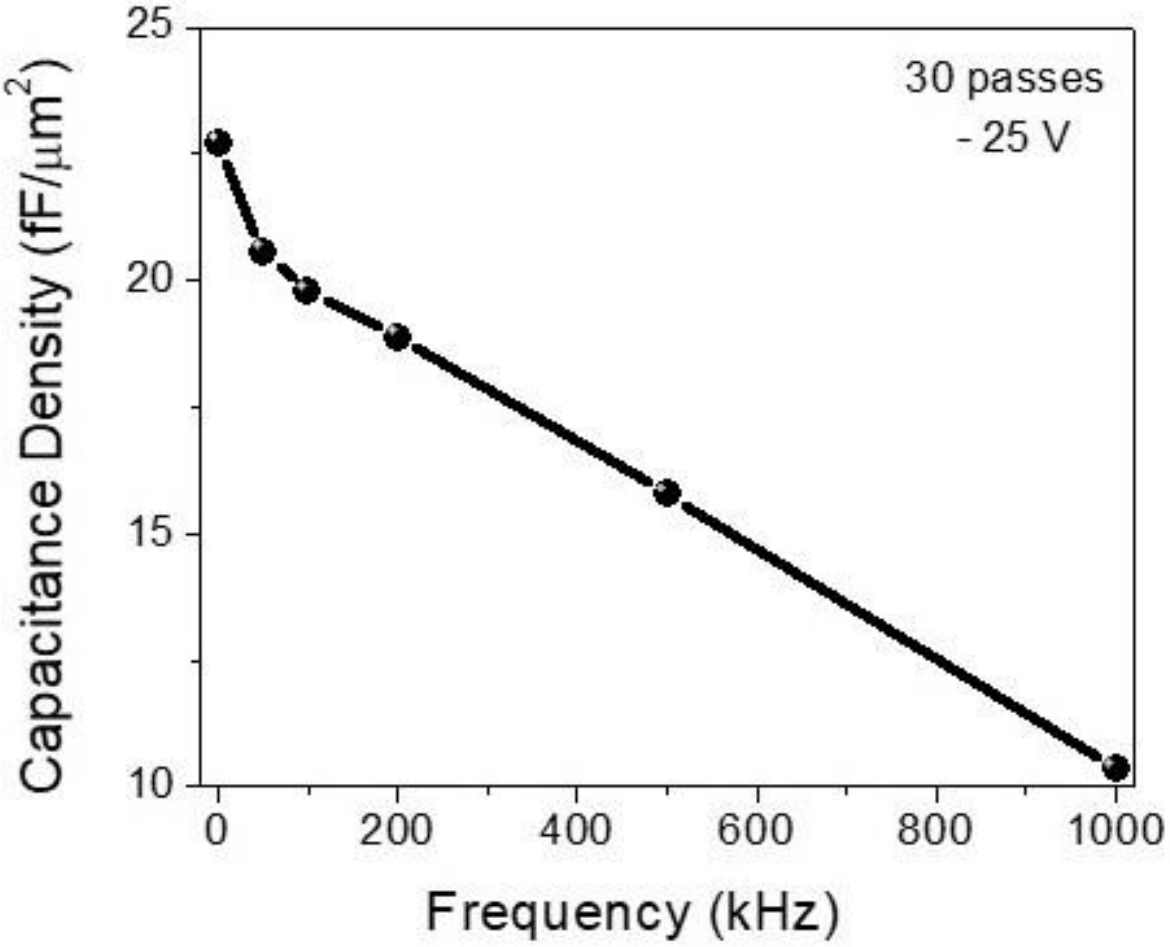

Figure 5.16: Drop in initial capacitance as a function of frequency at -25 V for 30 passes.

5.4 Effect of temperature and LED illumination on capacitance density

The effect of temperature and LED illumination on capacitance density of graphene/h-BN based capacitor with 30 number of printing passes was also studied. Figure 5.17 and Figure 5.18 shows the variation of capacitance density with the voltage at 1 kHz frequency and at 6 K and 350 K temperature respectively with (Light) and without (Dark) LED illumination. Figure 5.19 and Figure 5.20 shows the variation of capacitance density with the voltage at 1 MHz frequency and at 6 K and 350 K temperature respectively with (Light) and without (Dark) LED illumination. It can be observed that both temperature and LED illumination reduces the drop in capacitance at lower voltages. This can be attributed to the fact that both temperature and LED illumination drive the valence band edge closer to Fermi level which results in relatively higher carrier density even at lower applied voltages. Thus, lower drop in capacitance values indicating the photosensitive and temperature-sensitive behavior of the all inkjet-printed graphene/h-BN based capacitor.

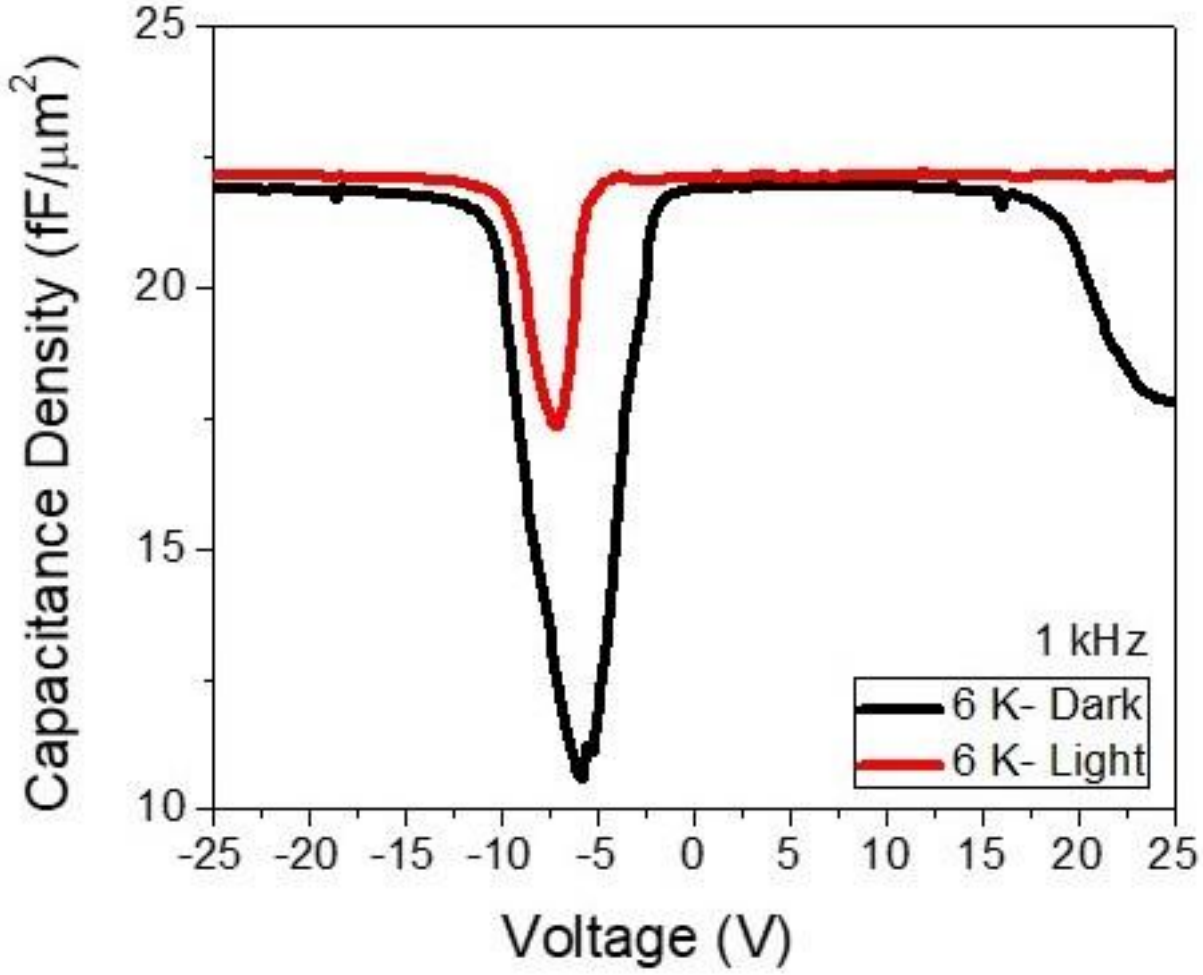

Figure 5.17: Variation of capacitance with voltage in dark and with LED illumination (Light) at 1 kHz at 6 K temperature.

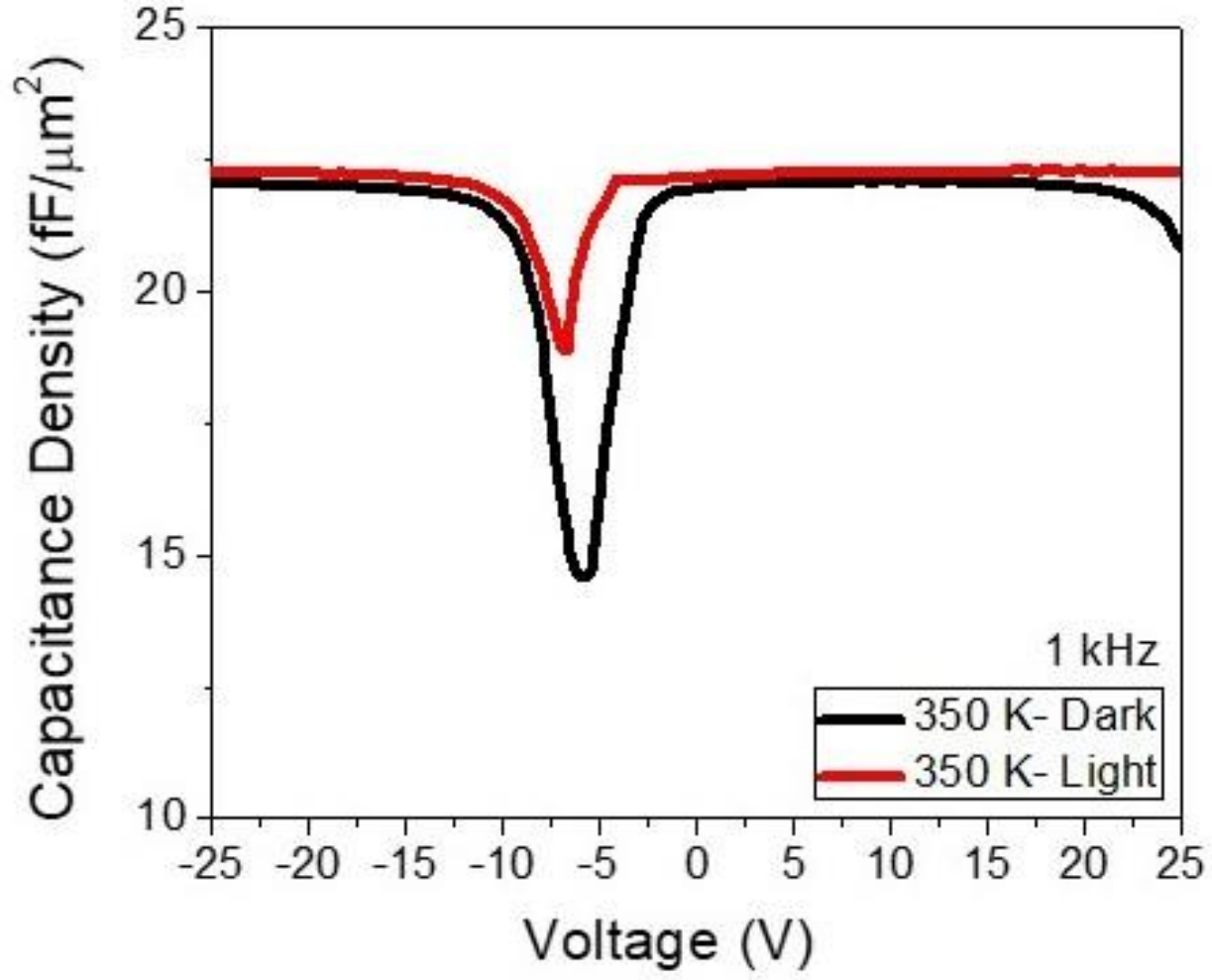

Figure 5.18: Variation of capacitance with voltage in dark and with LED illumination (Light) at 1 kHz at 350 K temperature.

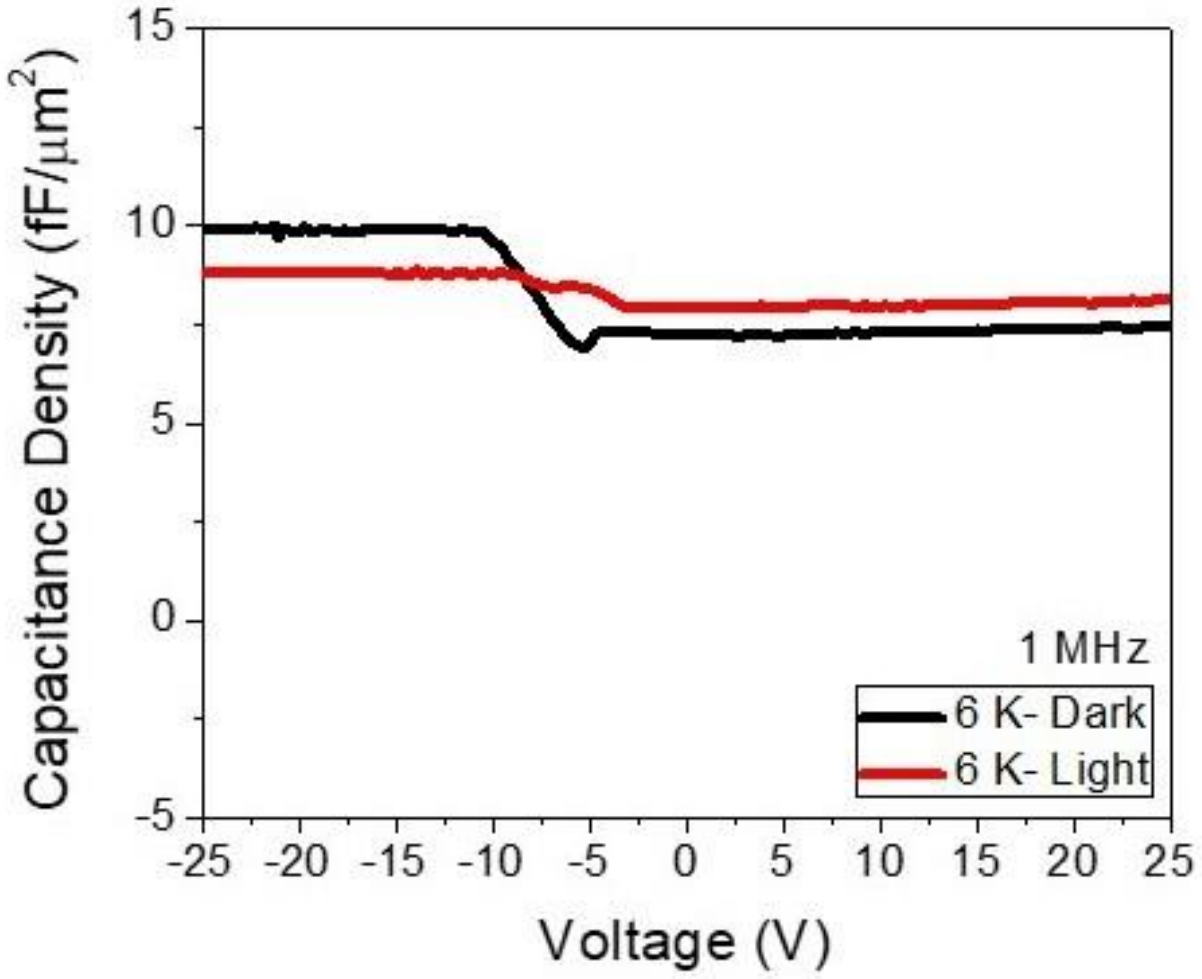

Figure 5.19: Variation of capacitance with voltage in dark and with LED illumination (Light) at 1 MHz at 6 K temperature.

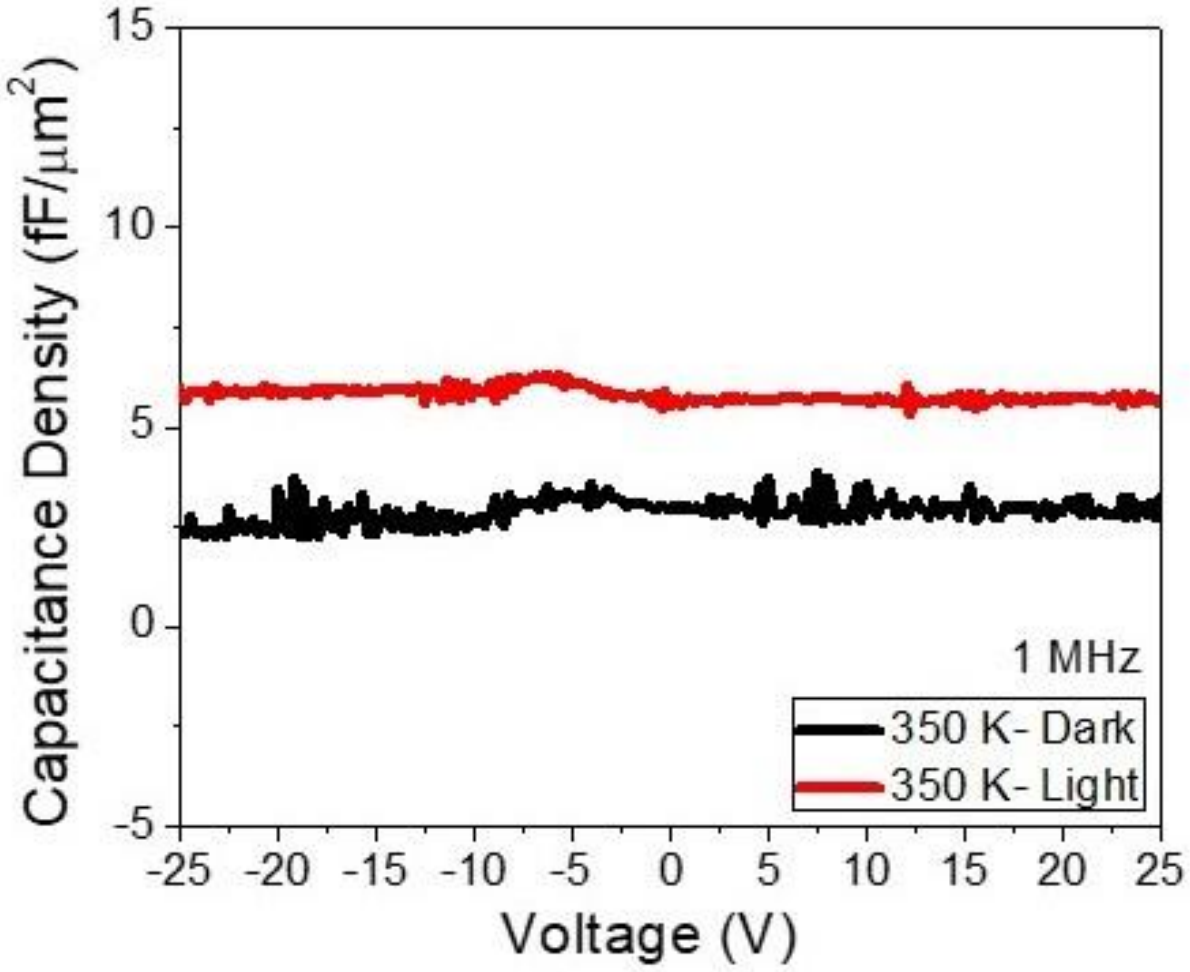

Figure 5.20: Variation of capacitance with voltage in dark and with LED illumination (Light) at 1 MHz at 350 K temperature.

Chapter 6: Different dielectrics for microstrip antenna and coupled transmission line applications

In this work, SiO_2 and h-BN substrates have been investigated for their potential use as dielectric material for graphene-based micro strip antenna and coupled transmission line fabrication [135, 136, 137]. A microstrip patch antenna is essentially a metallic strip mounted on a dielectric substrate. It finds its application in GPS, mobile satellite communications, and remote sensing applications. Coupled transmission lines find their application where the transfer of power is desired from one line to other.

6.1 Materials and methods

The ink preparation procedure for h-BN and graphene inks in the present study is similar to the one described in section 5.1. A mixture of 70% cyclohexanone and 30% terpineol (C/T) was prepared in glass vials with total volume of solution amounting to 20 ml. Ethyl cellulose (EC) surfactant was then added to increase the viscosity of the solution and promote stability. The mixture was bath sonicated for 2 hours to promote complete and uniform mixing of EC in C/T solution mixture. The h-BN/graphite powder in a concentration of 30 mg/ml or 0.6 grams was then taken in a 50 ml beaker and 20 ml of C/T/EC solution was added to it. Horn-tip sonication at 40% power amplitude and magnetic stirring at 500 rpm for 3 hours was then employed for ink preparation. Fujifilm Dimatix Materials Printer consisting of 16 inkjet nozzles was used to print graphene and h-BN inks for different patterns and devices in this work. Cartridge temperature of 40 $^{\circ}$C and a platen temperature of 60 °C was used during all the printing work. All inkjet printed samples were subjected to vacuum annealing at 250 °C for 24 hours to ensure maximum surfactant and solution removal.

6.2 Inkjet printing of graphene on SiO_2 and h-BN/SiO_2 substrates

Inkjet printed graphene lines of length 5 mm and at 1, 2 and 3 mm separation distance on SiO_2 substrate is shown in Figure 6.1. Inkjet printed graphene lines of length 5 mm and at 1,2 and 3 mm separation distance on h-BN/ SiO_2 substrate is shown in Figure 6.2.

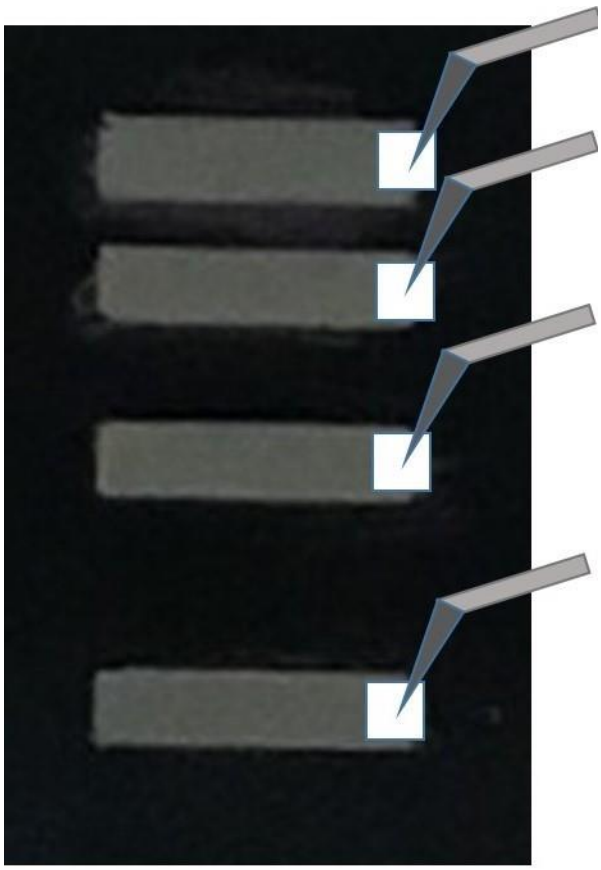

Figure 6.1: 5 mm graphene lines on SiO_2 substrate.

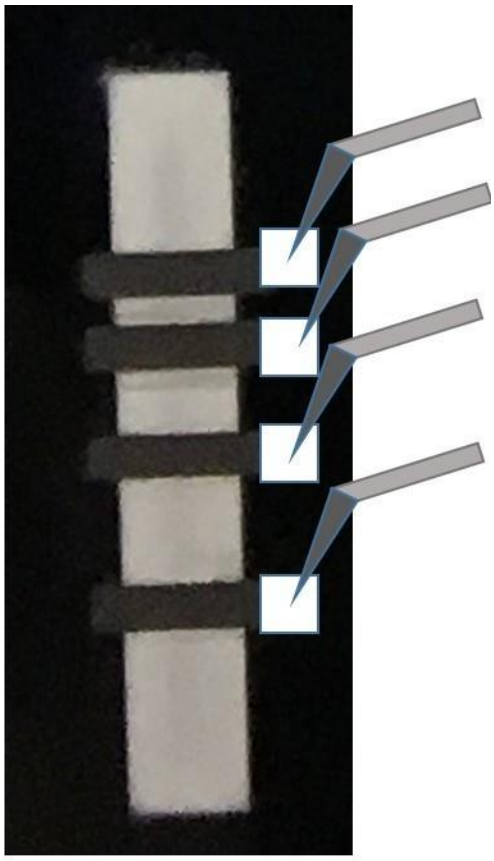

Figure 6.2: 5 mm graphene lines on h-BN/ SiO_2 substrate.

6.3 Capacitance analysis of graphene/h-BN inkjet printed coupled transmission lines

Variation of capacitance with frequency and with different separation distance for graphene electrodes on SiO_2 substrates is shown in Figure 6.3. The drop in capacitance was observed with increased separation distance from ~ 0.48 nF for 1 mm separation distance to ~ 0.40 nF for 3 mm separation distance at 1 kHz frequency. The drop in capacitance was also observed with an increase in frequency from 1 kHz to 1 MHz due to a decrease in a number of electrons getting trapped in interface states.

The variation in capacitance with the voltage at different frequencies and at 1 mm, 2 mm and 3 mm spacing for graphene electrodes on SiO_2 substrates is shown in Figure 6.4, Figure 6.5 and Figure 6.6 respectively. It can be observed that capacitance initially dropped with an increase in voltage which may be attributed to silver-graphene interface effect where silver is highly conducting and graphene is relatively less conducting thus creating the interface. The subsequent rise in capacitance can be due to the graphene/SiO_2 (dielectric) interface effect behaving like a metal-insulator junction. The drop in capacitance following that may be attributed to SiO_2 (dielectric)/ graphene interface and subsequent rise again may be the effect of formation of silver/graphene interface.

The variation of capacitance with frequency and with different separation distance for graphene electrodes on h-BN/ SiO_2 substrates is shown in Figure 6.7. It showed a similar trend as one obtained on only SiO_2 substrates but with diminished value of capacitance due to h-BN effect. The drop in capacitance was observed with increased separation distance from ~ 0.28 nF for 1 mm separation distance to ~ 0.24 nF for 3 mm separation distance at 1 kHz frequency. Change in capacitance with the voltage at different frequencies and at 1 mm, 2 mm and 3 mm spacing for graphene electrodes on h-BN/ SiO_2 substrates is shown in Figure 6.8, Figure 6.9 and Figure 6.10 respectively. They show a similar trend as one obtained on only SiO_2 substrates but the rise and drop in capacitance were significantly less as compared to the former which is attributed to strong h-BN dielectric presence.

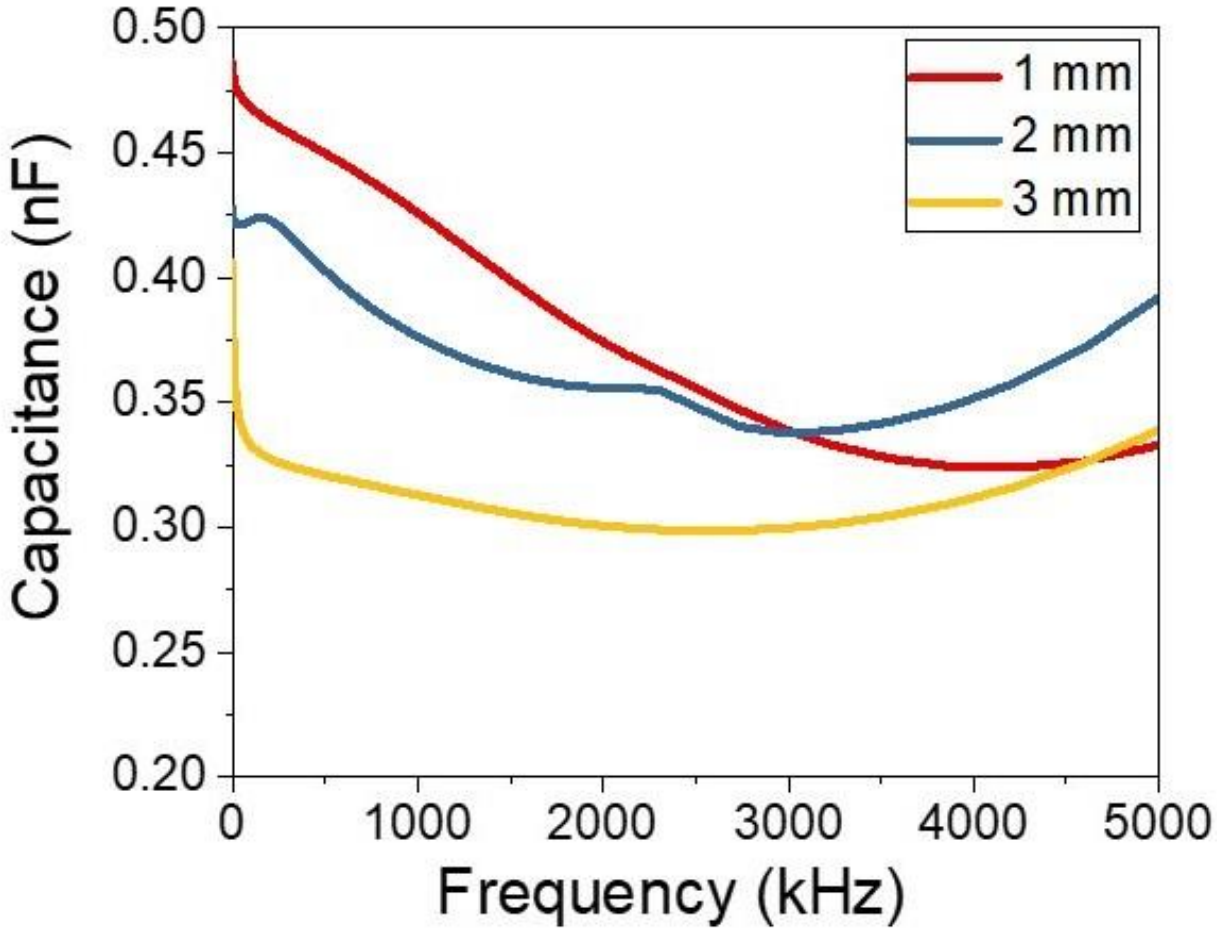

Figure 6.3: Variation of capacitance with frequency and line separation distance for graphene electrodes on SiO_2 substrates.

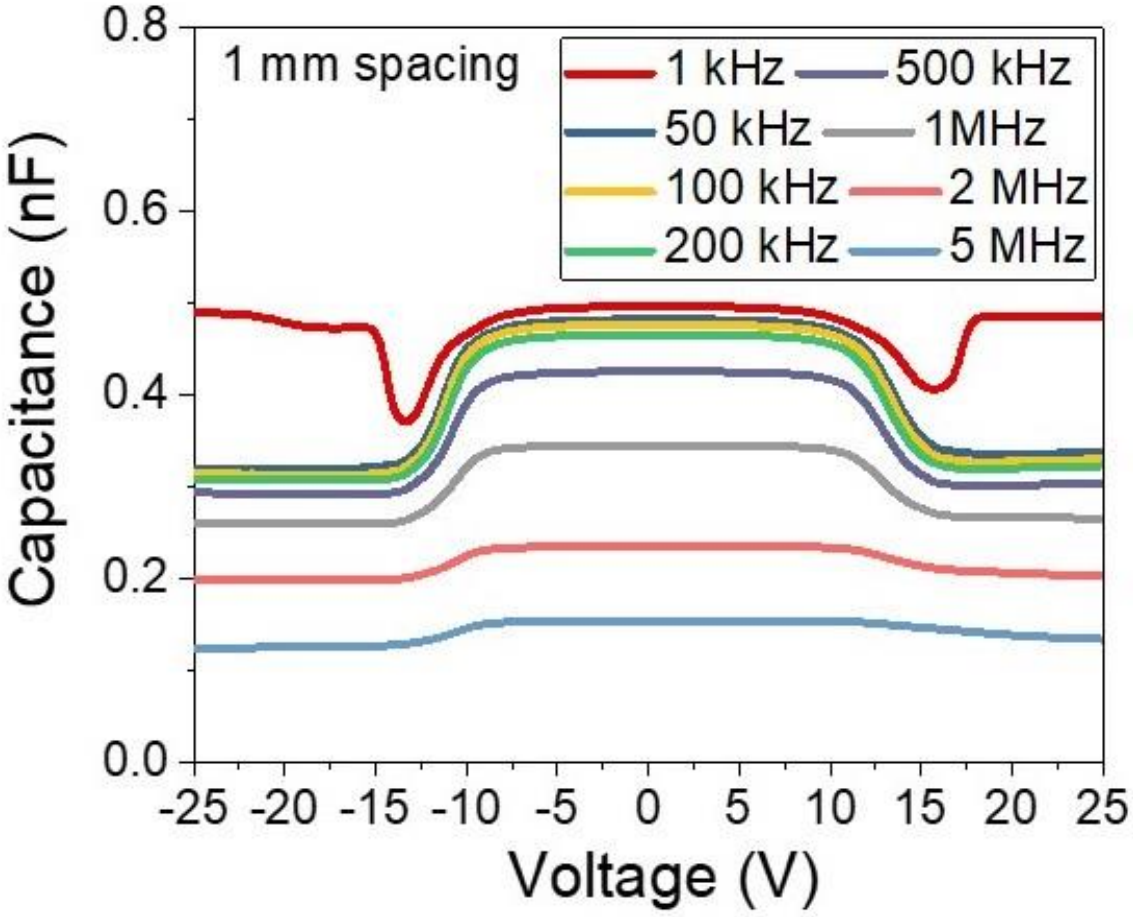

Figure 6.4: Variation of capacitance with voltage at different frequencies and 1 mm spacing for graphene electrodes on SiO_2 substrates.

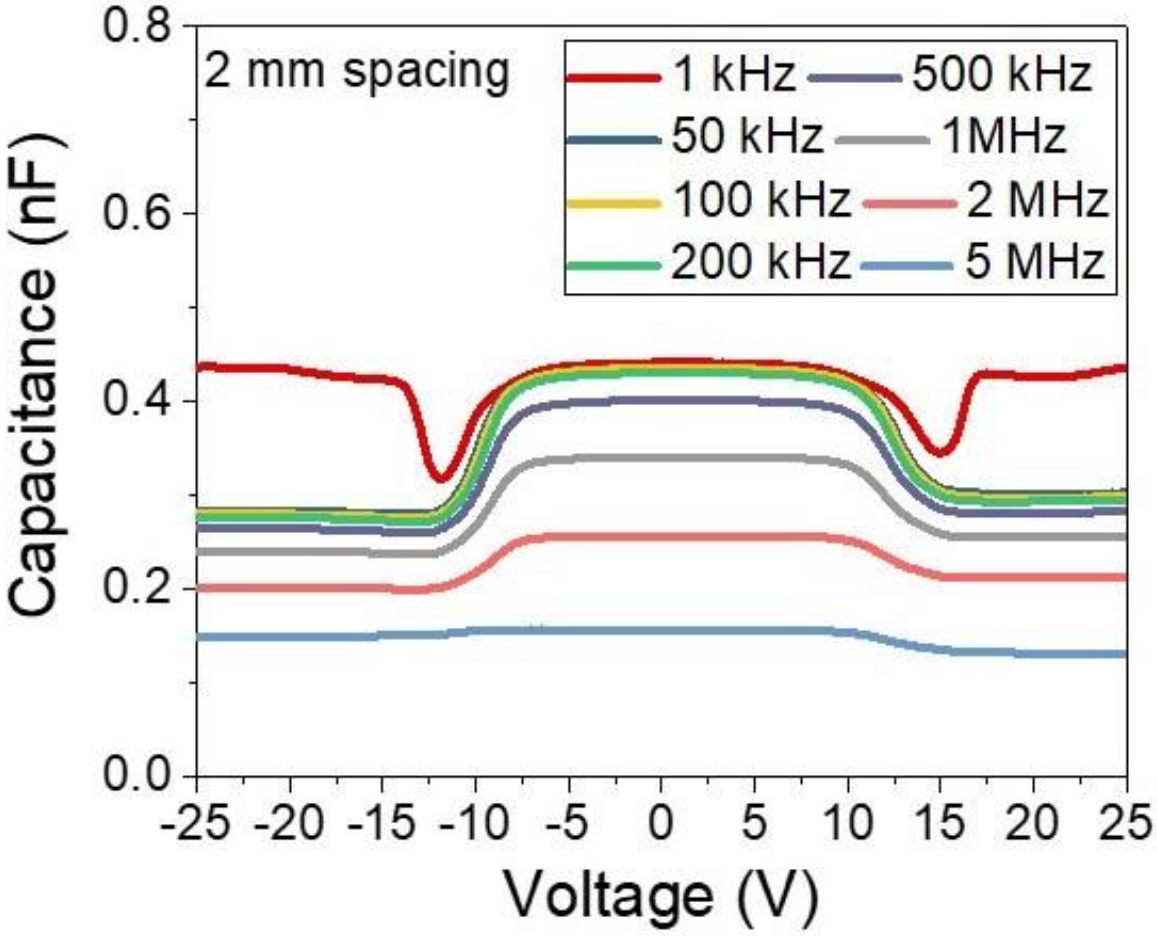

Figure 6.5: Variation of capacitance with voltage at different frequencies and 2 mm spacing for graphene electrodes on SiO_2 substrates.

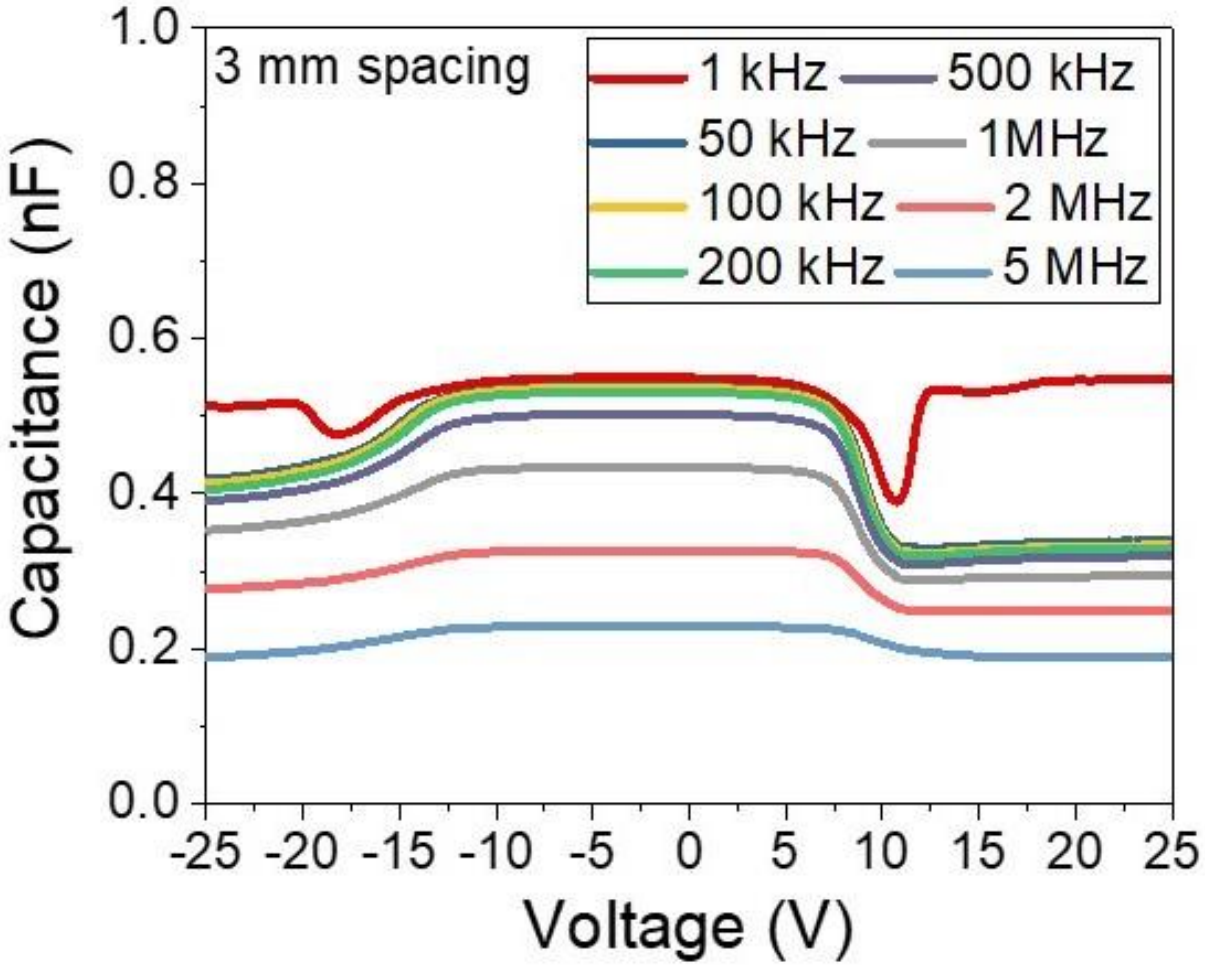

Figure 6.6: Variation of capacitance with voltage at different frequencies and 3 mm spacing for graphene electrodes on SiO_2 substrates.

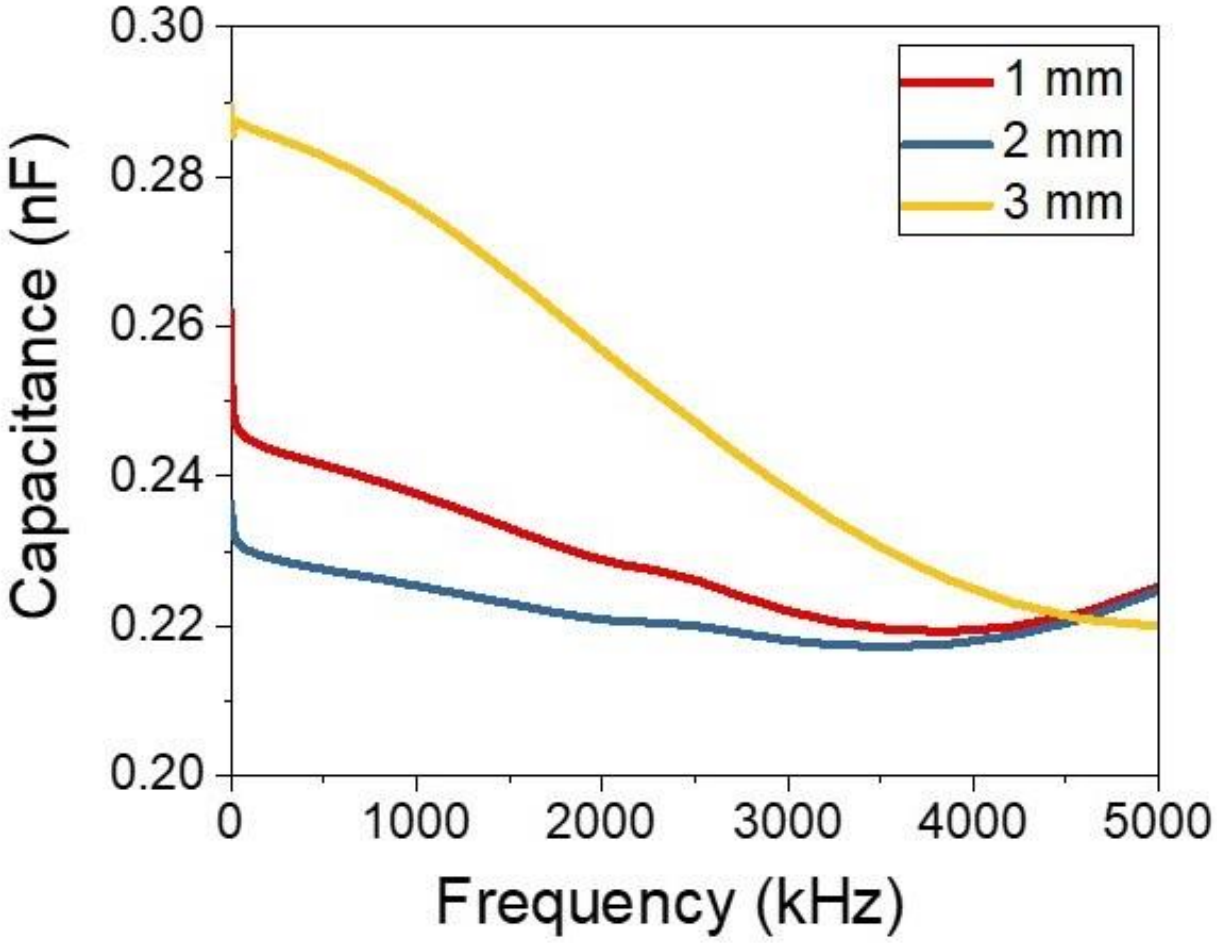

Figure 6.7: Variation of capacitance with frequency and line separation distance for graphene electrodes on h-BN/SiO_2 substrates.

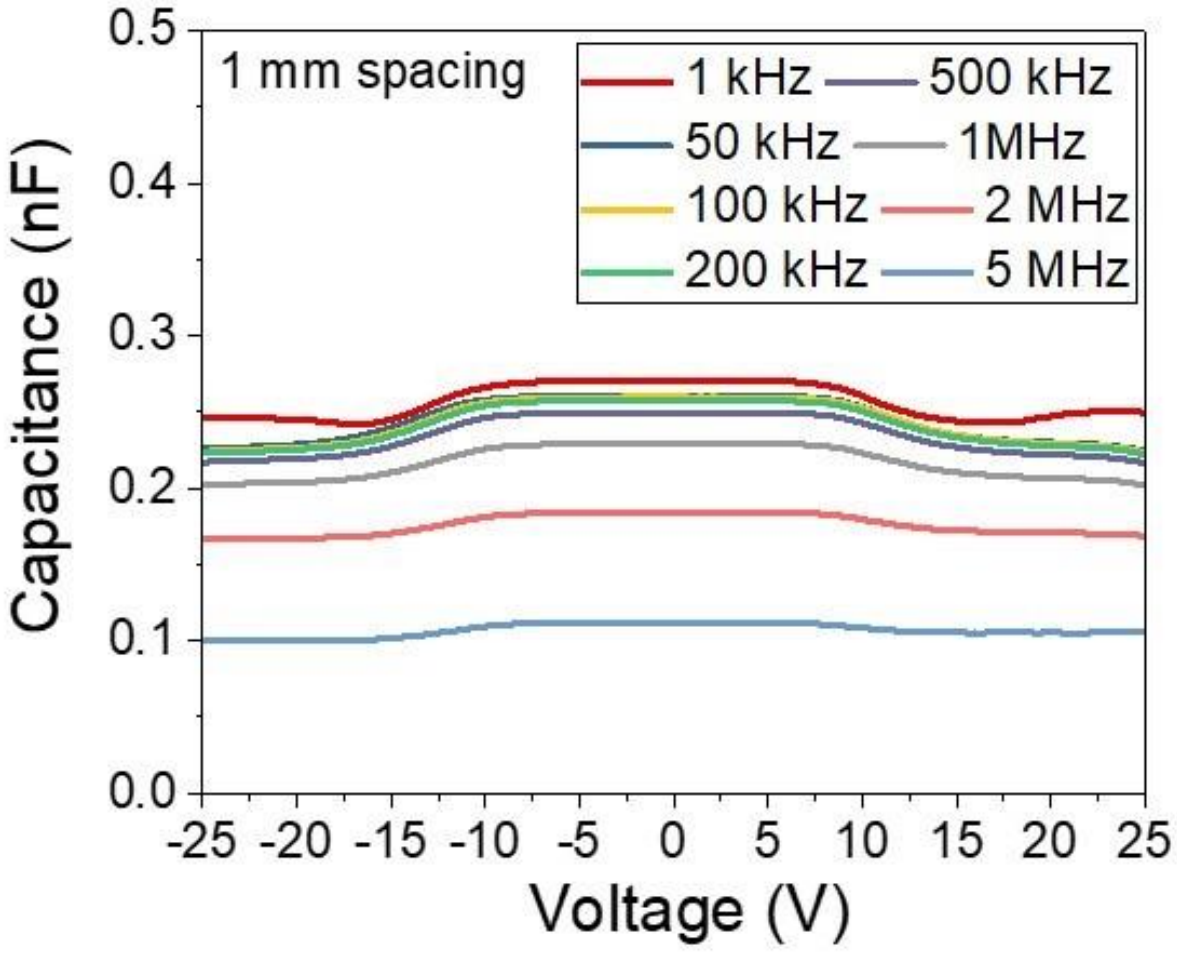

Figure 6.8: Variation of capacitance with the voltage at different frequencies and 1 mm spacing for graphene electrodes on h-BN/SiO_2 substrates.

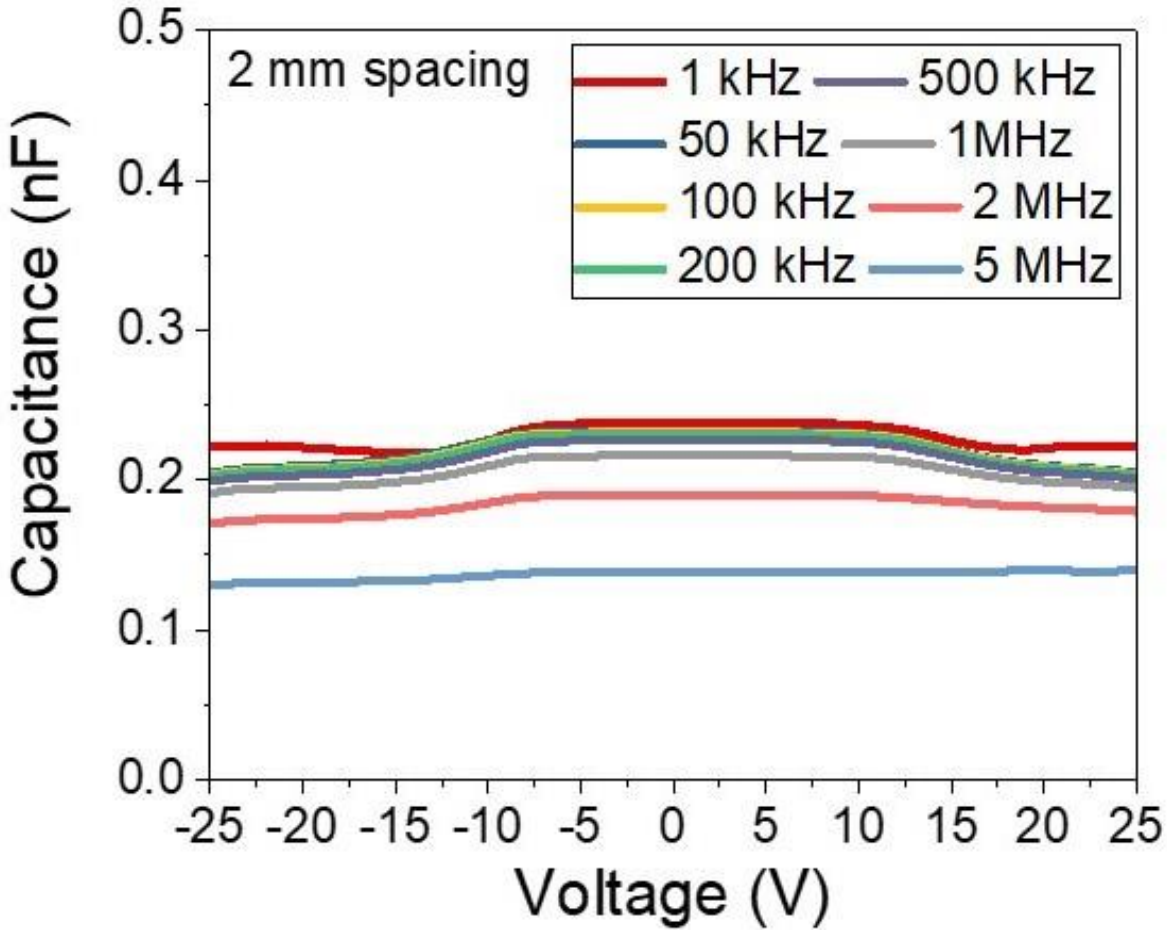

Figure 6.9: Variation of capacitance with the voltage at different frequencies and 2 mm spacing for graphene electrodes on h-BN/SiO_2 substrates.

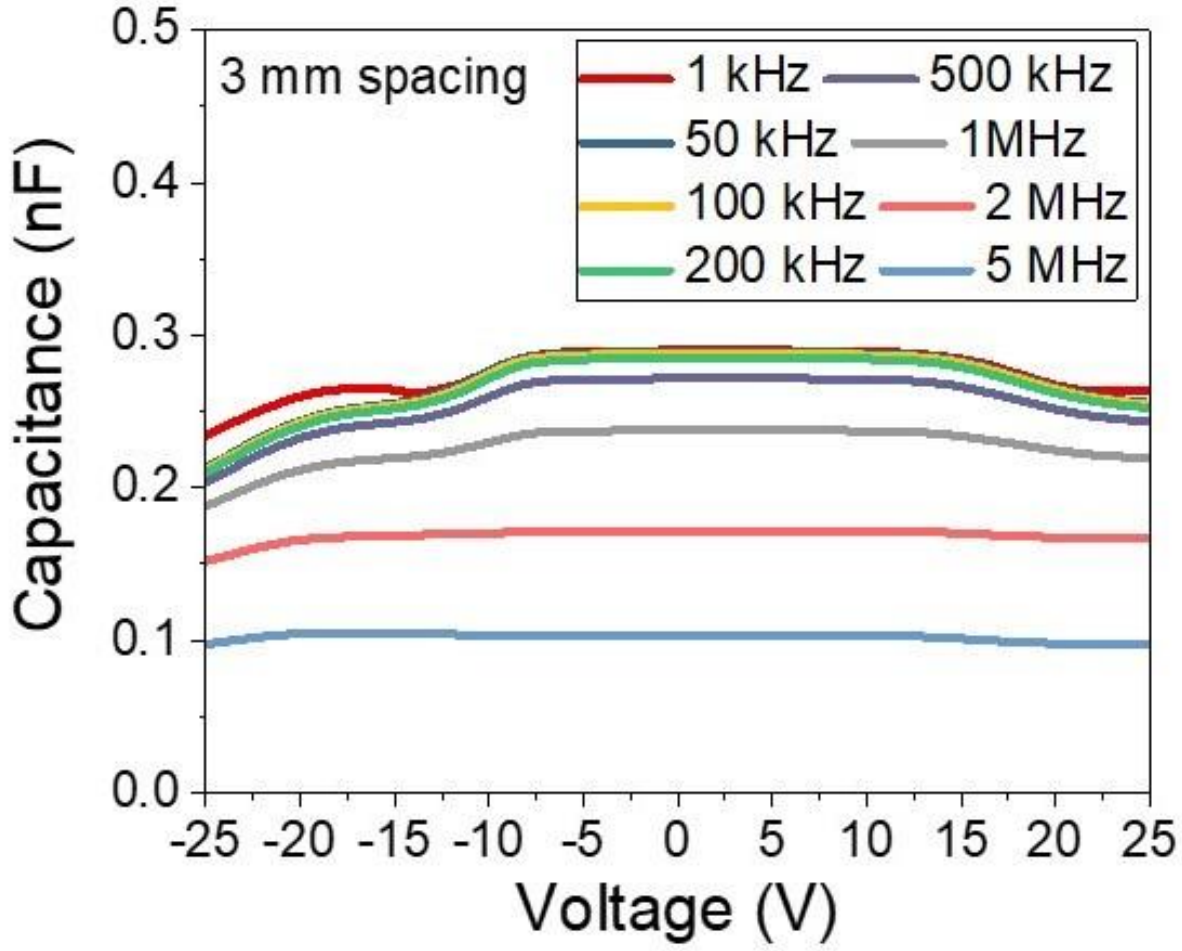

Figure 6.10: Variation of capacitance with the voltage at different frequencies and 3 mm spacing for graphene electrodes on h-BN/SiO_2 substrates.

Chapter 7: Conclusions

In summary, the viscoelastic stamping method for mechanical exfoliation appears to be a highly efficient method of mechanical exfoliation, as it leaves very little residue and yields larger platelets than the conventional scotch-tape mechanical exfoliation method. Mechanical exfoliation method in this work resulted in superior electrical properties (high current, high power, and low resistance) of HOPG platelets, as compared to previously reported work involving mechanical exfoliation. A very simple, yet highly efficient chemical exfoliation method is demonstrated for producing printable graphene inks with highly enhanced electrical properties. Scalability of the chemical exfoliation method was demonstrated while retaining similar or better electrical and optical properties than those produced by mechanical exfoliation. Both mechanical and chemical exfoliation was simple but highly efficient routes for producing graphene. The highly photoresponsive inkjet-printed graphene/WS_2 detector was demonstrated with faster decay and rise time.

High absorbance values were obtained for graphene/PEDOT: PSS inks indicating highly concentrated and dispersed graphene and PEDOT: PSS particles in NMP. Raman spectra confirmed the presence of both PEDOT: PSS and graphene in printed patterns. Graphene/PEDOT: PSS highly conductive patterns were successfully printed with good resolution using NMP as a solvent. High values of currents and low values of resistance were obtained which promotes inkjet printing as material-conserving and simple method for device fabrication. Scalability of inkjet printing process has also been demonstrated. This work will aid researchers in the organic electronics industry to make better conductive devices with graphene/PEDOT: PSS solution.

Magnetic stirring, shearing mixing, and horn-tip sonication methods have been explored using diverse and limiting conditions. Magnetic stirring gave the highest value of electrical conductivities but lack stability and uniformity over a period of time. Shear mixing gave lowest electrical values when compared to magnetic stirring and horn-tip sonication. The ink showed fewer defects but lacked stability. Horn-tip sonication offered electrical conductivities higher than obtained by shear mixing but lower than those obtained by magnetic stirring. However, horn-tip sonicated solutions were stable and did not show much precipitation with time. All inkjet-printed graphene/WS_2 based photodetector showed good responsivity in the range of 0.19 to 0.86 A/W, good detectivity in the range of 2.29 X 10^{12} $cmHz^{-1/2}W^{-1}$ to 10 X 10^{12} $cmHz^{-1/2}W^{-1}$ and faster decay and rise time of less than 50 ms. Capacitance-voltage measurements at different frequencies indicated that capacitance built up was highest (324.88 pF) for lowest frequency of 20 kHz and was almost negligible (2.81 pF) for highest frequency of 3 MHz.

Graphene/h-BN based capacitors were also fabricated and the effect of temperature, frequency and LED illumination on capacitance was studied using capacitance density-voltage measurements. The current density was lowest (0.072 $\mu A/mm^2$ at 40 V) for 30 number of printing passes due to thicker h-BN dielectric presence. Higher values of capacitance density up to ~ 24 $fF/\mu m^2$ at -25 V for 1kHz frequency were observed for a capacitor with 20 number of h-BN printing passes owing to the lower thickness and thus lower area. The capacitors showed good responsivity to temperature and LED illumination marking their potential as photosensitive devices.

The effect of silicon dioxide (SiO_2) and h-BN dielectric on graphene coupled transmission lines were studied using capacitance-voltage and capacitance- frequency measurements. The rise in capacitance can be due to the graphene/SiO_2 (dielectric) interface effect behaving like a metal-insulator junction. The drop in capacitance following that may be attributed to SiO_2 (dielectric)/ graphene interface. The capacitance values were significantly reduced during h-BN presence.

References

[1] K. S. Novoselov, A. K. Geim, S. V. Morozov, D. A. Jiang, Y. Zhang, S. V. Dubonos, I. V. Grigorieva, and A. A. Firsov, "Electric field effect in atomically thin carbon films," *Science,* vol. 306, no. 5696, pp. 666-669, 2004.

[2] K. S. Novoselov, D. Jiang, F. Schedin, T. J. Booth, V. V. Khotkevich, S. V. Morozov, and A. K. Geim, "Two-dimensional atomic crystals," *Proceedings of the National Academy of Sciences,* vol. 102, no. 30, pp. 10451-10453, 2005.

[3] A. B. Kaul, "Two-dimensional layered materials: Structure, properties, and prospects for device applications," *Journal of Materials Research,* vol. 29, no. 3, pp. 348-361, 2014.

[4] K-Y. Shin, J-Y. Hong, and J. Jang, "Flexible and transparent graphene films as acoustic actuator electrodes using inkjet printing," *Chemical Communications,* vol. 47, no. 30, pp. 8527-8529, 2011.

[5] Y. Xu, I. Hennig, D. Freyberg, A. J. Strudwick, M. G. Schwab, T. Weitz, and K. Chih-Pei Cha, "Inkjet-printed energy storage device using graphene/polyaniline inks," *Journal of Power Sources,* vol. 248, pp. 483-488, 2014.

[6] J. Li, F. Ye, S. Vaziri, M. Muhammed, M. C. Lemme, and M. Östling, "Efficient inkjet printing of graphene," *Advanced Materials,* vol. 25, no. 29, pp. 3985-3992, 2013.

[7] G. Fiori, F. Bonaccorso, G. Iannaccone, T. Palacios, D. Neumaier, A. Seabaugh, S. K. Banerjee, and L. Colombo, "Electronics based on two-dimensional materials," *Nature Nanotechnology,* vol. 9, no. 10, pp. 768, 2014.

[8] F. Schwierz, J. Pezoldt, and R. Granzner, "Two-dimensional materials and their prospects in transistor electronics," *Nanoscale,* vol. 7, no. 18, pp. 8261-8283, 2015.

[9] J. Azpeitia, G. Otero-Irurueta, I. Palacio, J. I. Martinez, N. R. del Árbol, G. Santoro and A. Gutiérrez, "High-quality PVD graphene growth by fullerene decomposition on Cu foils," *Carbon,* vol. 119, pp. 535-543, 2017.

[10] U. Narula, C. M. Tan and Chao Sung Lai, "Growth Mechanism for Low-Temperature PVD Graphene Synthesis on Copper Using Amorphous Carbon," *Scientific Reports,* vol. 7 pp. 44112, 2017.

[11] B. Liu, Y. Ma, A. Zhang, L. Chen, A. N. Abbas, Y. Liu, C. Shen, H. Wan and C. Zhou, "High-performance WSe2 field-effect transistors via controlled formation of in-plane heterojunctions," *ACS Nano,* vol. 10, no. 5, pp. 5153-5160, 2016.

[12] M. Sun, Q. Fang, D. Xie, Y. Sun, L. Qian, J. Xu and P. Xiao, "Heterostructured graphene quantum dot/WSe 2/Si photodetector with suppressed dark current and improved detectivity," *Nano Research,* vol. 11, no. 6, pp. 3233-3243, 2018.

[13] E. Serpini, A. Rota, A. Ballestrazzi, D. Marchetto, E. Gualtieri, and S. Valeri, "The role of humidity and oxygen on MoS2 thin films deposited by RF PVD magnetron sputtering," *Surface and Coatings Technology,* vol. 319, pp. 345-352, 2017.

[14] T. Stoica, M. Stoica, M. Duchamp, A. Tiedemann, S. Mantl, D. Grützmacher, D. Buca and B. E. Kardynał, "Vapor transport growth of MoS2 nucleated on SiO2 patterns and graphene flakes," *Nano Research,* vol. 9, no. 11, pp. 3504-3514, 2016.

[15] Y. Wang, Y. Zheng, X. Xu, E. Dubuisson, Q. Bao, J. Lu, and K. P. Loh, "Electrochemical delamination of CVD-grown graphene film: toward the recyclable use of copper catalyst," *ACS Nano* vol. 5, no. 12, pp. 9927-9933, 2011.

[16] M. Wang, S. K. Jang, W-J. Jang, M. Kim, S-Y. Park, S-W. Kim and S-J Kahng, "A Platform for Large-Scale Graphene Electronics–CVD Growth of Single-Layer Graphene on CVD-Grown Hexagonal Boron Nitride," *Advanced Materials,* vol. 25, no. 19, pp. 2746-2752, 2013.

[17] J. Xia, X. Huang, L-Z. Liu, M. Wang, L. Wang, B. Huang, D-D. Zhu, J-J. Li, C-Z. Gu and X-M. Meng, "CVD synthesis of large-area, highly crystalline MoSe2 atomic layers on diverse substrates and application to photodetectors," *Nanoscale* vol. 6, no. 15, pp. 8949-8955, 2014.

[18] L. Zhou, K. Xu, A. Zubair, A. D. Liao, W. Fang, F. Ouyang and Y-H Lee, "Large-area synthesis of high-quality uniform few-layer MoTe2," *Journal of the American Chemical Society,* vol. 137, no. 37, pp. 11892-11895, 2015.

[19] N. D. Boscher, C. J. Carmalt, and I. P. Parkin, "Atmospheric pressure chemical vapor deposition of NbSe2 thin films on glass," *European journal of inorganic chemistry,* vol. 2006, no. 6, pp. 1255-1259, 2006.

[20] H. Li, G. Lu, Y. Wang, Z. Yin, C. Cong, Q. He, L. Wang, F. Ding, T. Yu and H. Zhang, "Mechanical Exfoliation and Characterization of Single-and Few-Layer Nanosheets of WSe2, TaS2, and TaSe2," *Small* vol. 9, no. 11, pp. 1974-1981, 2013.

[21] M. Yi and Z. Shen, "A review on mechanical exfoliation for the scalable production of graphene," *Journal of Materials Chemistry A,* vol. 3, no. 22, pp. 11700-11715, 2015.

[22] A. Martinez, K. Fuse, and S. Yamashita, "Mechanical exfoliation of graphene for the passive mode-locking of fiber lasers," *Applied Physics Letters,* vol. 99, no. 12, pp. 121107, 2011.

[23] H. Liu, A. T. Neal, Z. Zhu, Z. Luo, X. Xu, D. Tománek and P. D. Ye, "Phosphorene: an unexplored 2D semiconductor with a high hole mobility," *ACS Nano,* vol. 8, no. 4, pp. 4033-4041, 2014.

[24] Y. Chen, G. Jiang, S. Chen, Z. Guo, X. Yu, C. Zhao and H. Zhang, "Mechanically exfoliated black phosphorus as a new saturable absorber for both Q-switching and mode-locking laser operation," *Optics Express,* vol. 23, no. 10, pp. 12823-12833, 2015.

[25] M. Michel, C. Biswas, and A. B. Kaul, "High-performance ink-jet printed graphene resistors formed with environmentally-friendly surfactant-free inks for extreme thermal environments," *Applied Materials Today,* vol. 6, pp. 16-21, 2017.

[26] D. Fadil, R. F. Hossain, G. A. Saenz, and A. B. Kaul, "On the chemically-assisted excitonic enhancement in environmentally-friendly solution dispersions of two-dimensional MoS2 and WS2," *Journal of Materials Chemistry C,* vol. 5, no. 22, pp. 5323-5333, 2017.

[27] M. Michel, C. Biswas, C. S. Tiwary, G. A. Saenz, R. F. Hossain, P. Ajayan and A. B. Kaul, "A thermally-invariant, additively manufactured, high-power graphene resistor for flexible electronics," *2D Materials,* vol. 4, no. 2, pp. 025076, 2017.

[28] A. Delgado, J. A. Catalan, H. Yamaguchi, C. N. Villarrubia, A. D. Mohite and A. B. Kaul, "Characterization of 2D MoS 2 and WS 2 Dispersed in Organic Solvents for Composite Applications," *MRS Advances,* vol. 1, no. 32, pp. 2303-2308, 2016.

[29] R. F. Hossain, I. G. Deaguero, T. Boland, and A. B. Kaul, "Biocompatible, large-format, inkjet printed heterostructure MoS 2-graphene photodetectors on conformable substrates," *npj 2D Materials and Applications,* vol. 1, no. 1, pp. 28, 2017.

[30] V. Nicolosi, M. Chhowalla, M. G. Kanatzidis, M. S. Strano and J. N. Coleman, "Liquid exfoliation of layered materials," *Science,* vol. 340, no. 6139, pp. 1226419, 2013.

[31] G. Eda, H. Yamaguchi, D. Voiry, T. Fujita, M. Chen and M. Chhowalla, "Photoluminescence from chemically exfoliated MoS2," *Nano Letters,* vol. 11, no. 12, pp. 5111-5116, 2011.

[32] G. F. Walker and W. G. Garrett, "Chemical exfoliation of vermiculite and the production of colloidal dispersions," *Science,* vol. 156, no. 3773, pp. 385-387, 1967.

[33] Y. Hernandez, V. Nicolosi, M. Lotya, F. M. Blighe, Z. Sun, S. De and I. T. McGovern, "High-yield production of graphene by liquid-phase exfoliation of graphite," *Nature Nanotechnology,* vol. 3, no. 9, pp. 563, 2008.

[34] M. Singh, H. M. Haverinen, P. Dhagat, and G. E. Jabbour, "Inkjet printing—process and its applications," *Advanced Materials,* vol. 22, no. 6, pp. 673-685, 2010.

[35] P. Calvert, "Inkjet printing for materials and devices," *Chemistry of materials,* vol. 13, no. 10, pp. 3299-3305, 2001.

[36] T. Boland, T. Xu, B. Damon and X. Cui, "Application of inkjet printing to tissue engineering," *Biotechnology Journal: Healthcare Nutrition Technology,* vol. 1, no. 9, pp. 910-917, 2006.

[37] B. Derby, "Inkjet printing of functional and structural materials: fluid property requirements, feature stability, and resolution," *Annual Review of Materials Research,* vol. 40, pp. 395-414, 2010.

[38] J. Perelaer, P. J. Smith, D. Mager, D. Soltman, S. K. Volkman, V. Subramanian, J. G. Korvink and U. S. Schubert, "Printed electronics: the challenges involved in printing devices, interconnects, and contacts based on inorganic materials," *Journal of Materials Chemistry,* vol. 20, no. 39, pp. 8446-8453, 2010.

[39] M. Michel, J. A. Desai, A. Delgado, C. Biswas and A. B. Kaul, "Optimization of fluid characteristics of 2D materials for inkjet printing," *MRS Advances,* vol. 1, no. 30, pp. 2199-2206, 2016.

[40] A. Capasso, A. E. D. R. Castillo, H. Sun, A. Ansaldo, V. Pellegrini, and F. Bonaccorso. "Ink-jet printing of graphene for flexible electronics: an environmentally-friendly approach," *Solid State Communications,* vol. 224, pp. 53-63, 2015.

[41] E. B. Secor, P. L. Prabhumirashi, K. Puntambekar, M. L. Geier and M. C. Hersam. "Inkjet printing of high conductivity, flexible graphene patterns," *The Journal of physical chemistry letters,* vol. 4, no. 8, pp. 1347-1351, 2013.

[42] L. T. Le, M. H. Ervin, H. Qiu, B. E. Fuchs and W. Y. Lee, "Graphene supercapacitor electrodes fabricated by inkjet printing and thermal reduction of graphene oxide," *Electrochemistry Communications,* vol. 13, no. 4, pp. 355-358, 2011.

[43] C-L. Lee, C-H. Chen and C-W. Chen, "Graphene nanosheets as ink particles for inkjet printing on a flexible board," *Chemical engineering journal,* vol. 230, pp. 296-302, 2013.

[44] R. Giardi, S. Porro, A. Chiolerio, E. Celasco and M. Sangermano, "Inkjet printed acrylic formulations based on UV-reduced graphene oxide nanocomposites," *Journal of Materials Science,* vol. 48, no. 3, pp. 1249-1255, 2013.

[45] M. Michel, J. A. Desai, C. Biswas, and A. B. Kaul, "Engineering chemically exfoliated dispersions of two-dimensional graphite and molybdenum disulfide for ink-jet printing," *Nanotechnology,* vol. 27, no. 48, pp. 485602, 2016.

[46] W. S. Leong, H. Gong, and J. T. L Thong, "Low-contact-resistance graphene devices with nickel-etched-graphene contacts" *ACS nano,* vol. 8, no. 1, pp. 994-1001, 2013.

[47] Q. Ran, M. Gao, X. Guan, Y. Wang and Z. Yu, "First-principles investigation on bonding formation and electronic structure of metal-graphene contacts," *Applied Physics Letters,* vol. 94, no. 10, pp. 103511, 2009.

[48] Y. M. Blanter and I. Martin, "Transport through normal-metal–graphene contacts," *Physical Review B,* vol. 76, no. 15, pp. 155433, 2007.

[49] S. Pang, H. N. Tsao, X. Feng, and K. Müllen, "Patterned graphene electrodes from solution-processed graphite oxide films for organic field-effect transistors," *Advanced Materials,* vol. 21, no. 34, pp. 3488-3491, 2009.

[50] J. Yang, E. Ziade, C. Maragliano, R. Crowder, X. Wang, M. Stefancich, M. Chiesa, A. K. Swan and A. J. Schmidt, "Thermal conductance imaging of graphene contacts," *Journal of Applied Physics,* vol. 116, no. 2, pp. 023515, 2014.

[51] D-H. Kang, M-S. Kim, J. Shim, J. Jeon, H-Y. Park, W-S. Jung, H-Y. Yu, C-H. Pang, S. Lee, and J-H. Park, "High-Performance Transition Metal Dichalcogenide Photodetectors Enhanced by Self-Assembled Monolayer Doping," *Advanced Functional Materials,* vol. 25, no. 27, pp. 4219-4227, 2015.

[52] J. A. Wilson and A. D. Yoffe, "The transition metal dichalcogenides discussion and interpretation of the observed optical, electrical and structural properties," *Advances in Physics,* vol. 18, no. 73, pp. 193-335, 1969.

[53] C. Ataca, H. Sahin, E. Akturk and S. Ciraci, "Mechanical and electronic properties of MoS2 nanoribbons and their defects," *The Journal of Physical Chemistry C,* vol. 115, no. 10, pp. 3934-3941, 2011.

[54] F. K. Perkins, A. L. Friedman, E. Cobas, P. M. Campbell, G. G. Jernigan and B. T. Jonker, "Chemical vapor sensing with monolayer MoS2," *Nano letters,* vol. 13, no. 2, pp. 668-673, 2013.

[55] Q. H. Wang, K. Kalantar-Zadeh, A. Kis, J. N. Coleman and Michael S. Strano, "Electronics and optoelectronics of two-dimensional transition metal dichalcogenides," *Nature nanotechnology,* vol. 7, no. 11, pp. 699, 2012.

[56] J. K. Ellis, M. J. Lucero, and G. E. Scuseria, "The indirect to direct band gap transition in multilayered MoS2 as predicted by screened hybrid density functional theory," *Applied Physics Letters,* vol. 99, no. 26, pp. 261908, 2011.

[57] S. Zhang, Z. Yan, Y. Li, Z. Chen and H. Zeng, "Atomically thin arsenene and antimonene: semimetal–semiconductor and indirect–direct band-gap transitions," *Angewandte Chemie,* vol. 127, no. 10, pp. 3155-3158, 2015.

[58] A. Kuc, N. Zibouche and T. Heine, "Influence of quantum confinement on the electronic structure of the transition metal sulfide TS2," *Physical Review B,* vol. 83, no. 24, pp. 245213, 2011.

[59] A. Kumar and P. K. Ahluwalia, "Electronic structure of transition metal dichalcogenides monolayers 1H-MX 2 (M= Mo, W; X= S, Se, Te) from ab-initio theory: new direct band gap semiconductors," *The European Physical Journal B,* vol. 85, no. 6, pp. 186, 2012.

[60] S. B. Desai, G. Seol, J. S. Kang, H. Fang, C. Battaglia, R. Kapadia, J. W. Ager, J. Guo and A. Javey, "Strain-induced indirect to direct bandgap transition in multilayer WSe2," *Nano letters,* vol. 14, no. 8, pp. 4592-4597, 2014.

[61] A. S. Pawbake, R. G. Waykar, D. J. Late and S. R. Jadkar, "Highly transparent wafer-scale synthesis of crystalline WS2 nanoparticle thin film for photodetector and humidity-sensing applications," *ACS applied materials & interfaces,* vol. 8, no. 5, pp. 3359-3365, 2016.

[62] C. Zhang, S. Wang, L. Yang, Y. Liu, T. Xu, Z. Ning, A. Zak, Z. Zhang, R. Tenne and Q. Chen, "High-performance photodetectors for visible and near-infrared lights based on individual WS2 nanotubes," *Applied physics letters,* vol. 100, no. 24, pp. 243101, 2012.

[63] N. Perea-López, A. L. Elías, A. Berkdemir, A. Castro-Beltran, H. R. Gutiérrez, S. Feng and R. Lv, "Photosensor device based on few-layered WS2 films," *Advanced Functional Materials,* vol. 23, no. 44, pp. 5511-5517, 2013.

[64] A. Jäger-Waldau, M. Ch Lux-Steiner and E. Bucher, "MoS2, MoSe2, WS2 and WSe2 thin films for photovoltaics," In *Solid State Phenomena,* vol. 37, pp. 479-484, 1994.

[65] C. Kuru, D. Choi, A. Kargar, C. H. Liu, S. Yavuz, C. Choi, S. Jin, and P. R. Bandaru, "High-performance flexible hydrogen sensor made of WS2 nanosheet–Pd nanoparticle composite film," *Nanotechnology,* vol. 27, no. 19, pp. 195501, 2016.

[66] G-H. Lee, Y-J. Yu, C. Lee, C. Dean, K. L. Shepard, P. Kim and J. Hone, "Electron tunneling through atomically flat and ultrathin hexagonal boron nitride," *Applied physics letters,* vol. 99, no. 24, pp. 243114, 2011.

[67] G. H. Lee, Y-J Yu, X. Cui, N. Petrone, C-H. Lee, M. S. Choi, and D-Y. Lee, "Flexible and transparent MoS2 field-effect transistors on hexagonal boron nitride-graphene heterostructures," *ACS nano,* vol. 7, no. 9, pp. 7931-7936, 2013.

[68] Z. Lin, A. Mcnamara, Y. Liu, K-S. Moon and C-P. Wong, "Exfoliated hexagonal boron nitride-based polymer nanocomposite with enhanced thermal conductivity for electronic encapsulation," *Composites Science and Technology,* vol. 90, pp. 123-128, 2014.

[69] L. Britnell, R. V. Gorbachev, R. Jalil, B. D. Belle, F. Schedin, M. I. Katsnelson and L. Eaves, "Electron tunneling through ultrathin boron nitride crystalline barriers," *Nano letters,* vol. 12, no. 3, pp. 1707-1710, 2012.

[70] K. K. Kim, A. Hsu, X. Jia, S. M. Kim, Y. Shi, M. Dresselhaus, T. Palacios and J. Kong, "Synthesis and characterization of hexagonal boron nitride film as a dielectric layer for graphene devices," *ACS nano,* vol. 6, no. 10, 8583-8590, 2012.

[71] G. Shi, Y. Hanlumyuang, Z. Liu, Y. Gong, W. Gao, B. Li and J. Kono, "Boron nitride–graphene nanocapacitor and the origins of anomalous size-dependent increase of capacitance" *Nano letters,* vol. 14, no. 4, pp. 1739-1744, 2014.

[72] C. Soldano, A. Mahmood, and E. Dujardin, "Production, properties and potential of graphene," *Carbon,* vol. 48, no. 8, pp. 2127-2150, 2010.

[73] A. Castellanos-Gomez, M. Buscema, R. Molenaar, V. Singh, L. Janssen, H. S. J. Van Der Zant and G. A. Steele. "Deterministic transfer of two-dimensional materials by all-dry viscoelastic stamping," *2D Materials,* vol. 1, no. 1, pp. 011002, 2014.

[74] D. Kim, S. Jeong, B. K. Park, and J. Moon. "Direct writing of silver conductive patterns: Improvement of film morphology and conductance by controlling solvent compositions," *Applied Physics Letters,* vol. 89, no. 26, pp. 264101, 2006.

[75] R. P. Vidano, D. B. Fischbach, L. J. Willis and T. M. Loehr, "Observation of Raman band shifting with excitation wavelength for carbons and graphites," *Solid State Communications,* vol. 39, no. 2, pp. 341-344, 1981.

[76] G. L. Cançado, A. Jorio, E. H. M. Ferreira, F. Stavale, C. A. Achete, R. B. Capaz, M. V. O. Moutinho, A. Lombardo, T. S. Kulmala and A. C. Ferrari. "Quantifying defects in graphene via Raman spectroscopy at different excitation energies," *Nano letters,* vol. 11, no. 8, pp. 3190-3196, 2011.

[77] A. Eckmann, A. Felten, A. Mishchenko, L. Britnell, R. Krupke, K. S. Novoselov and C. Casiraghi, "Probing the nature of defects in graphene by Raman spectroscopy," *Nano letters,* vol. 12, no. 8, 3925-3930, 2012.

[78] S. Tian, Y. Yang, Z. Liu, C. Wang, R. Pan, C. Gu and J. Li, "Temperature-dependent Raman investigation on suspended graphene: Contribution from thermal expansion coefficient mismatch between graphene and substrate," *Carbon,* vol. 104, pp. 27-32, 2016.

[79] W. Wang, Q. Peng, Y. Dai, Z. Qian and S. Liu, "Temperature dependence of Raman spectra of graphene on copper foil substrate," *Journal of Materials Science: Materials in Electronics,* vol. 27, no. 4, pp. 3888-3893, 2016.

[80] I. Calizo, A. A. Balandin, W. Bao, F. Miao and C. N. Lau, "Temperature dependence of the Raman spectra of graphene and graphene multilayers," *Nano letters,* vol. 7, no. 9, pp. 2645-2649, 2007.

[81] N. Hosoya, Y. Akaho, M. Inoue, S. Sahoo and M. Tachibana, "Temperature dependence of the Raman spectra of polycrystalline graphene grown by chemical vapor deposition," *Applied Physics Letters*, vol. 105, no. 2, pp. 023108, 2014.

[82] Y. Seekaew, S. Lokavee, D. Phokharatkul, A. Wisitsoraat, T. Kerdcharoen and C. Wongchoosuk, "Low-cost and flexible printed graphene–PEDOT: PSS gas sensor for ammonia detection," *Organic Electronics*, vol. 15, no. 11, pp. 2971-2981, 2014.

[83] D. Kong, L. T. Le, Y. Li, J. L. Zunino and W. Lee, "Temperature-dependent electrical properties of graphene inkjet-printed on flexible materials," *Langmuir*, vol. 28, no. 37, pp. 13467-13472, 2012.

[84] M. Lotya, Y. Hernandez, P. J. King, R. J. Smith, V. Nicolosi, L. S. Karlsson and F. M. Blighe, "Liquid phase production of graphene by exfoliation of graphite in surfactant/water solutions," *Journal of the American Chemical Society*, vol. 131, no. 10, pp. 3611-3620, 2009.

[85] Y. T. Liang and M. C. Hersam, "Highly concentrated graphene solutions via polymer enhanced solvent exfoliation and iterative solvent exchange," *Journal of the American Chemical Society*, vol. 132, no. 50, pp. 17661-17663, 2010.

[86] E. E. Tkalya, M. Ghislandi and C. E. Koning, "The use of surfactants for dispersing carbon nanotubes and graphene to make conductive nanocomposites," *Current Opinion in Colloid & Interface Science*, vol. 17, no. 4, pp. 225-232, 2012.

[87] W. Hong, Y. Xu, G. Lu, C. Li, and G. Shi, "Transparent graphene/PEDOT–PSS composite films as counter electrodes of dye-sensitized solar cells," *Electrochemistry Communications*, vol. 10, no. 10, pp. 1555-1558, 2008.

[88] Y. H. Kim, C. Sachse, M. L. Machala, C. May, L. Müller-Meskamp and K. Leo, "Highly conductive PEDOT: PSS electrode with optimized solvent and thermal post-treatment for ITO-free organic solar cells," *Advanced Functional Materials*, vol. 21, no. 6, pp. 1076-1081, 2011.

[89] Z. Liu, K. Parvez, R. Li, R. Dong, X. Feng and K. Müllen, "Transparent conductive electrodes from graphene/PEDOT: PSS hybrid inks for ultrathin organic photodetectors," *Advanced Materials*, vol. 27, no. 4, pp. 669-675, 2015.

[90] C. Karuwan, C. Sriprachuabwong, A. Wisitsoraat, D. Phokharatkul, P. Sritongkham and A. Tuantranont, "Inkjet-printed graphene-poly (3, 4-ethylenedioxythiophene): poly (styrene-sulfonate) modified on screen printed carbon electrode for electrochemical sensing of salbutamol," *Sensors and Actuators B: Chemical*, vol. 161, no. 1, pp. 549-555, 2012.

[91] C. Sriprachuabwong, C. Karuwan, A. Wisitsorrat, D. Phokharatkul, T. Lomas, P. Sritongkham and A. Tuantranont, "Inkjet-printed graphene-PEDOT: PSS modified screen printed carbon electrode for biochemical sensing," *Journal of Materials Chemistry*, vol. 22, no. 12, pp. 5478-5485, 2012.

[92] D. Yoo, J. Kim and J. H. Kim, "Direct synthesis of highly conductive poly (3, 4-ethylenedioxythiophene): poly (4-styrenesulfonate) (PEDOT: PSS)/graphene composites and their applications in energy harvesting systems," *Nano Research*, vol. 7, no. 5, pp. 717-730, 2014.

[93] S. Sakamoto, M. Okumura, Z. Zhao and Y. Furukawa, "Raman spectral changes of PEDOT–PSS in polymer light-emitting diodes upon operation," *Chemical physics letters,* vol. 412, no. 4, pp. 395-398, 200.

[94] M. Stavytska-Barba and A. M. Kelley, "Surface-enhanced Raman study of the interaction of PEDOT: PSS with plasmonically active nanoparticles," *The Journal of Physical Chemistry C,* vol. 114, no. 14, pp. 6822-6830, 2010.

[95] J. Ouyang, Q. Xu, C-W. Chu, Y. Yang, G. Li, and J. Shinar, "On the mechanism of conductivity enhancement in poly (3, 4-ethylenedioxythiophene): poly (styrene sulfonate) film through solvent treatment," *Polymer,* vol. 45, no. 25, pp. 8443-8450, 2004.

[96] M. Buscema, J. O. Island, D. J. Groenendijk, S. I. Blanter, G. A. Steele, H. S. J van der Zant, and A. Castellanos-Gomez, "Photocurrent generation with two-dimensional van der Waals semiconductors," *Chemical Society Reviews,* vol. 44, no. 11, pp. 3691-3718, 2015.

[97] H. Lin, N. J. Wu, F. Geiger, K. Xie and A. Ignatiev "A ferroelectric-superconducting photodetector," *Journal of applied physics,* vol. 80, no. 12, pp. 7130-7133, 1996.

[98] X. Gan, R-J. Shiue, Y. Gao, I. Meric, T. F. Heinz, K. Shepard, J. Hone, S. Assefa and D. Englund, "Chip-integrated ultrafast graphene photodetector with high responsivity," *Nature Photonics,* vol. 7, no. 11, pp. 883, 2013.

[99] H. Lin, N. J. Wu, F. Geiger, K. Xie and A. Ignatiev, "A ferroelectric-superconducting photodetector," *Journal of applied physics,* vol. 80, no. 12, pp. 7130-7133, 1996.

[100] L. Tang, S. E. Kocabas, S. Latif, A. K. Okyay, D-S. Ly-Gagnon, K. C. Saraswat, and D. A. B. Miller, "Nanometre-scale germanium photodetector enhanced by a near-infrared dipole antenna," *Nature Photonics,* vol. 2, no. 4, pp. 226, 2008.

[102] A. Rogalski, J. Antoszewski, and L. Faraone, "Third-generation infrared photodetector arrays," *Journal of applied physics,* vol. 105, no. 9, pp. 4, 2009.

[103] M. Furchi, A. Urich, A. Pospischil, G. Lilley, K. Unterrainer, H. Detz and P. Klang "Microcavity-integrated graphene photodetector," *Nano letters,* vol. 12, no. 6, pp. 2773-2777, 2012.

[104] C. S. Rout, P. D. Joshi, R. V. Kashid, D. S. Joag, M. A. More, A. J. Simbeck, M. Washington, S. K. Naya, and D. J. Late, "Superior field emission properties of layered WS 2-RGO nanocomposites," *Scientific reports,* vol. 3, pp. 3282, 2013.

[105] Y. Xue, Y. Zhang, Y. Liu, H. Liu, J. Song, J. Sophia and J. Liu, "Scalable production of a few-layer MoS2/WS2 vertical heterojunction array and its application for photodetectors," *Acs Nano,* vol. 10, no. 1, pp. 573-580, 2015.

[106] R. K. Jha and P. K. Guha, "Liquid exfoliated pristine WS2 nanosheets for ultrasensitive and highly stable chemiresistive humidity sensors," *Nanotechnology,* vol. 27, no. 47, pp. 475503, 2016.

[107] A. Berkdemir, H. R. Gutiérrez, A. R. Botello-Méndez, N. Perea-López, A. L. Elías, C-I. Chia, B. Wang, "Identification of individual and few layers of WS2 using Raman Spectroscopy," *Scientific Reports,* vol. 3, pp. 1755, 2013.

[108] M. Thripuranthaka, R. V. Kashid, C. S. Rout, and D. J. Late, "Temperature-dependent Raman spectroscopy of chemically derived few-layer MoS2 and WS2 nanosheets," *Applied Physics Letters*, vol. 104, no. 8, pp. 081911, 2014.

[109] H. Tan, Y. Fan, Y. Zhou, Q. Chen, W. Xu and J. H. Warner, "Ultrathin 2D photodetectors utilizing chemical vapor deposition grown WS2 with graphene electrodes," *ACS Nano*, vol. 10, no. 8, pp. 7866-7873, 2016.

[110] A. Allain, J. Kang, K. Banerjee and A. Kis, "Electrical contacts to two-dimensional semiconductors," *Nature Materials*, vol. 14, no. 12, pp. 1195, 2015.

[111] Zhang, Teng-Fei, Zhi-Peng Li, Jiu-Zhen Wang, Wei-Yu Kong, Guo-An Wu, Yu-Zhen Zheng, Yuan-Wei Zhao, En-Xu Yao, Nai-Xi Zhuang, and Lin-Bao Luo. "Broadband photodetector based on carbon nanotube thin film/single layer graphene Schottky junction." *Scientific Reports* 6 (2016): 38569.

[112] A. Zylbersztejn, “Trap depth and electron capture cross section determination by trap refilling experiments in Schottky diodes,” *Appl. Phys. Lett.*, vol. 33, no. 2, pp. 200–202, 1978.

[113] I. Hussain, M. Y. Soomro, N. Bano, O. Nur and M. Willander, "Interface trap characterization and electrical properties of Au-ZnO nanorod Schottky diodes by conductance and capacitance methods," *Journal of Applied Physics*, vol. 112, no. 6, pp. 064506, 2012.

[114] N. Adhikari, A. Bandyopadhyay and A. Kaul, "Nanoscale Characterization of WSe2 for Opto-electronics Applications," *MRS Advances*, vol. 2, no. 60, pp. 3715-3720, 2017.

[115] L. Peng, X. Peng, B. Liu, C. Wu, Y. Xie and G. Yu, "Ultrathin two-dimensional MnO2/graphene hybrid nanostructures for high-performance, flexible planar supercapacitors," *Nano Letters*, vol. 13, no. 5, pp. 2151-2157, 2013.

[116] R. Cárdenas, R. Peña, G. Asher, and J. Clare, "Power smoothing in wind generation systems using a sensorless vector controlled induction machine driving a flywheel," *IEEE transactions on energy conversion*, vol. 19, no. 1, pp. 206-216, 2004.

[117] A. Lahyani, P. Venet, G. Grellet, and P-J. Viverge, "Failure prediction of electrolytic capacitors during operation of a switchmode power supply," *IEEE Transactions on power electronics*, vol. 13, no. 6, pp. 1199-1207, 1998.

[118] T. C. Choi, R. T. Kaneshiro, R. W. Brodersen, P. R. Gray, W. B. Jett and M. Wilcox, "High-frequency CMOS switched-capacitor filters for communications application," *IEEE Journal of Solid-State Circuits*, vol. 18, no. 6, pp. 652-664, 1983.

[119] W. Zhuo, X. Li, S. Shekhar, S. H. K. Embabi, J. Pineda de Gyvez, D. J. Allstot and E. Sanchez-Sinencio, "A capacitor cross-coupled common-gate low-noise amplifier," *IEEE transactions on circuits and systems II: Express Briefs*, vol. 52, no. 12, pp. 875-879, 2005.

[120] J. Jevtic, "Ladder networks for capacitive decoupling in phased-array coils," In *Proceedings of the 9th Annual Meeting of ISMRM, Glasgow, Scotland*, vol. 17, 2001.

[121] J. Zmuidzinas, H. G. LeDuc, J. A. Stern, and S. R. Cypher, "Two-junction tuning circuits for submillimeter SIS mixers," *IEEE transactions on microwave theory and techniques*, vol. 42, no. 4, pp. 698-706, 1994.

[122] M. Bhushan and R. W. Newcomb, "Grounding of capacitors in integrated circuits, " *Electronics Letters,* vol. 3, no. 4, pp. 148-149, 1967.

[123] S. K. Jang, J. Youn, Y. J. Song and S. Lee, "Synthesis and characterization of hexagonal boron nitride as a gate dielectric," *Scientific Reports,* vol. 6, pp. 30449, 2016.

[124] N. Guo, J. Wei, Y. Jia, H. Sun, Y. Wang, K. Zhao and X. Shi, "Fabrication of large area hexagonal boron nitride thin films for bendable capacitors," *Nano Research,* vol. 6, no. 8, pp. 602-610, 2013.

[125] A. G. Kelly, D. Finn, A. Harvey, T. Hallam and J. N. Coleman, "All-printed capacitors from graphene-BN-graphene nanosheet heterostructures," *Applied Physics Letters,* vol. 109, no. 2, pp. 023107, 2016.

[126] C. Zhi, Y. Bando, C. Tang, H. Kuwahara and D. Golberg, "Large-scale fabrication of boron nitride nanosheets and their utilization in polymeric composites with improved thermal and mechanical properties," *Advanced Materials,* vol. 21, no. 28, pp. 2889-2893, 2009.

[127] L. Song, L. Ci, H. Lu, P. B. Sorokin, C. Jin, J. Ni and A. G. Kvashnin "Large-scale growth and characterization of atomic hexagonal boron nitride layers," *Nano Letters,* vol. 10, no. 8, pp. 3209-3215, 2010.

[128] G-X. Li, Y. Liu, B. Wang, X-M. Song, E. Li, and H. Yan, "Preparation of transparent BN films with the superhydrophobic surface," *Applied Surface Science,* vol. 254, no. 17, pp. 5299-5303, 2008.

[129] E. H. A. Dekempeneer, S. Kuypers, K. Vercammen, J. Meneve, J. Smeets, P. N. Gibson and W. Gissler, "Scratch-resistant transparent boron nitride films," *Surface and Coatings Technology,* vol. 100, pp. 45-48, 1998.

[130] S. Das, R. Gulotty, A. V. Sumant and A. Roelofs, "All two-dimensional, flexible, transparent, and thinnest thin film transistor," *Nano Letters,* vol. 14, no. 5, 2861-2866, 2014.

[131] L. H. Li and Y. Chen, "Atomically thin boron nitride: unique properties and applications," *Advanced Functional Materials,* vol. 26, no. 16, pp. 2594-2608, 2016.

[132] J. Wang, F. Ma and M. Sun, "Graphene, hexagonal boron nitride, and their heterostructures: properties and applications," *RSC Advances,* vol. 7, no. 27, pp. 16801-16822, 2017.

[133] T. Carey, S. Cacovich, G. Divitini, J. Ren, A. Mansouri, J. M. Kim, C. Wang, C. Ducati, R. Sordan and F. Torrisi, "Fully inkjet-printed two-dimensional material field-effect heterojunctions for wearable and textile electronics," *Nature Communications,* vol. 8, no. 1, pp. 1202, 2017.

[134] H. Zhou, J. Zhu, Z. Liu, Z. Yan, X. Fan, J. Lin and G. Wang, "High thermal conductivity of suspended few-layer hexagonal boron nitride sheets," *Nano Research,* vol. 7, no. 8, pp. 1232-1240, 2014.

[135] S. Anand, D. S. Kumar, R. J. Wu, and M. Chavali, "Graphene nanoribbon based terahertz antenna on a polyimide substrate," *Optik-International Journal for Light and Electron Optics,* vol. 125, no. 19, pp. 5546-5549, 2014.

[136] M. J. Jornet and I. F. Akyildiz, "Graphene-based nano-antennas for electromagnetic nano communication in the terahertz band," In *Antennas and Propagation (EuCAP), 2010 Proceedings of the Fourth European Conference on*, pp. 1-5, 2010.

[137] C. T. Phare, Y-H. D. Lee, J. Cardenas and M. Lipson "Graphene electro-optic modulator with 30 GHz bandwidth," *Nature Photonics*, vol. 9, no. 8, pp. 511, 2015.

Appendix I

Operating Procedure for Dimatix DMP 2800 Inkjet Printer

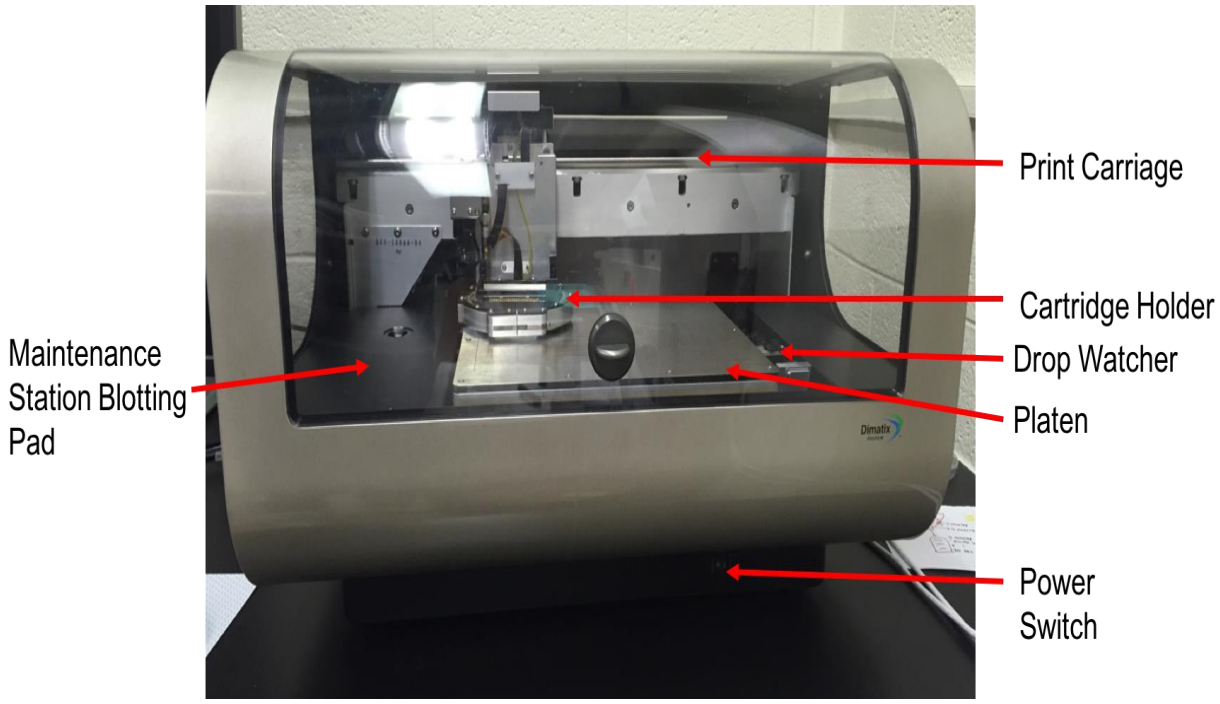

Figure 1: Dimatix DMP 2800 inkjet printer.

1. Turn on the computer and printer. Ensure the platen is obstacle free.
2. Keep the sample ready. It is also important to know the thickness of the sample on which printing needs to be done. The maximum thickness of the sample can be 25 mm. When using the fiducial camera, the system can print on a maximum substrate thickness of a 25 mm.
3. Double click on the “Dimatix Drop Manager” Icon.
4. Then follow instructions from the software.

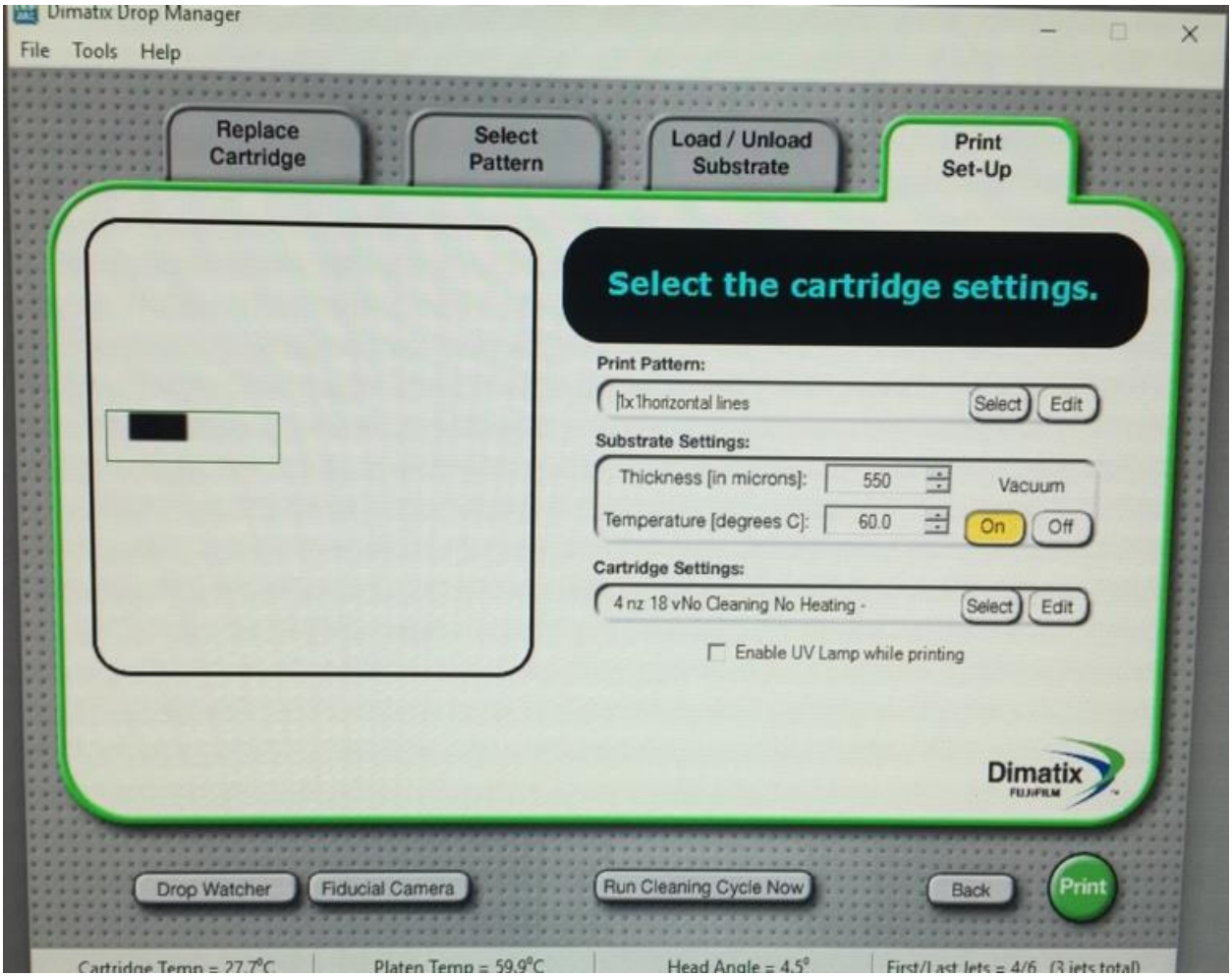

Figure 2: Software of Dimatix DMP 2800 inkjet printer.

5. Place the substrate or cartridge when the software prompts to do so.
6. While selecting patterns or cartridge settings, don't modify the originals. If there is a need to modify anything, make copies and name the new ones. The same can be done for waveforms and cartridge settings.
7. Please check with the superuser in order to modify printing patterns, waveforms, and cartridge settings. It is recommended to read the Dimatix manual before making any change.

8. With the pattern Editor one can modify the pattern and can also change drop spacing, a number of layers, pattern array, drop position array etc. There is a “Preview Drops” option here to finalize the pattern for printing.

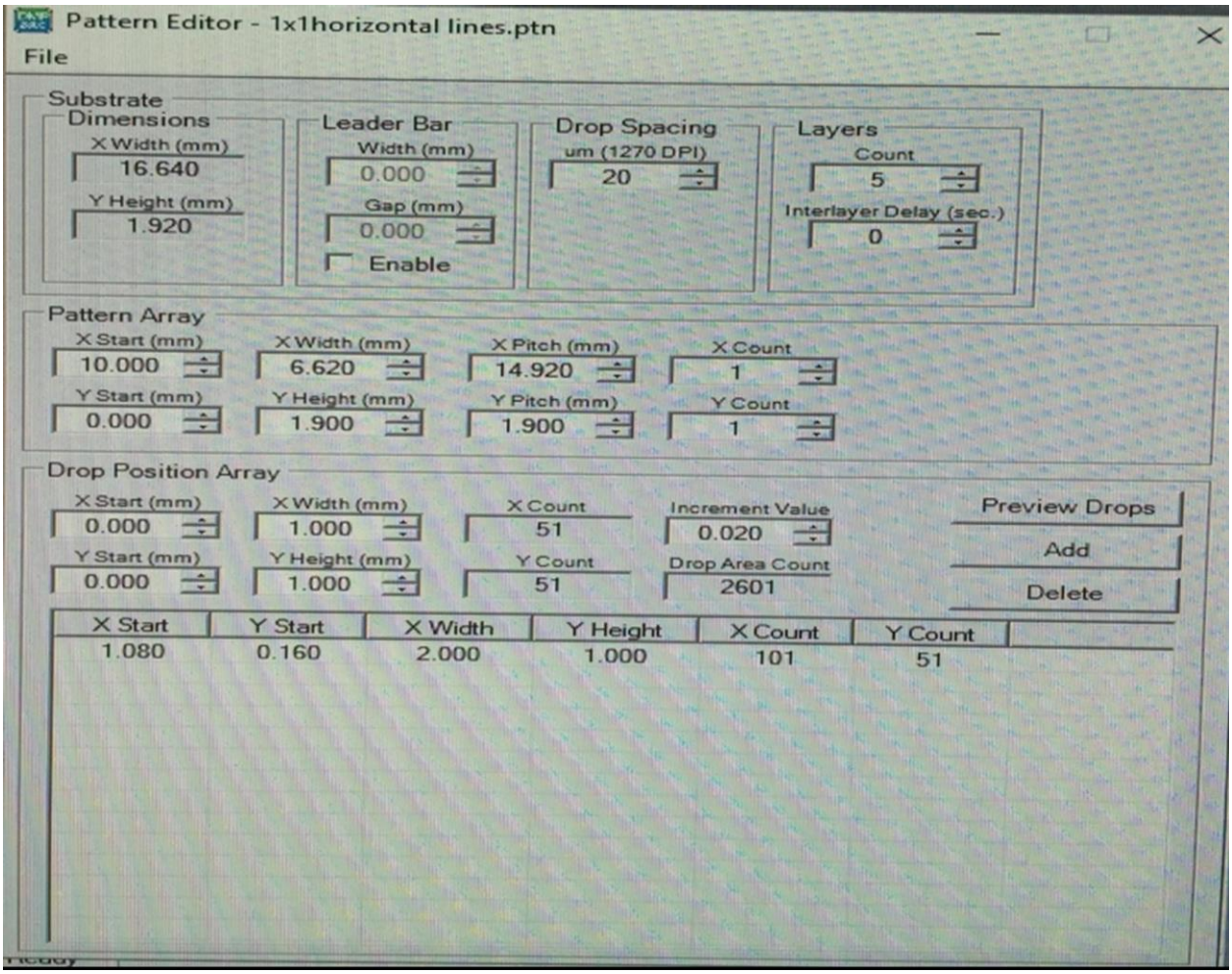

Figure 3: Pattern editor feature in Dimatix DMP 2800 inkjet printer.

9. With the Cartridge Setting one can adjust the waveform, a number of nozzles, cleaning cycle, jetting voltage, tickling frequency etc which may be very useful for inks with high and low viscosity.

10. By default, the temperature of the platen and cartridge should be off.
11. It is always a good idea to make sure the cartridge ejects drops by going to “Drop watcher” before printing. Here one can watch jetting of the drop, Cleaning cycle and display of the drop jetting. It is also possible to capture the movie of drop watch. This setting does not involve into the original printing settings.
12. Place the sample gently and turn on the vacuum.
13. If unsure about the position of the sample, use the “Fiducial camera” to align the sample.
14. After printing is done, turn off the vacuum. Remove the substrate first and then the cartridge by going to the directions on the main menu. Do not forget to turn down the temperature of the platen and cartridge if it is high. Make sure everything is clean.
15. Please check the cleaning pad before turning off the system. Located in the “Tools” pull-down menu on the DDM main screen is a feature called “Replace Cleaning Pad”. Cleaning pad can be replaced with a new one when it gets filled with fluid or clogged by fluid residue and does not effectively blot the nozzle surface of the cartridge, or while changing cartridge fluids and to avoid cross-contamination from contact with the previous material on the cleaning pad. Please see the super user for appropriate technique.
16. Be careful not to remove the cleaning pad by itself. This can damage the springs holding the receptacle which will then not position it correctly. Do not touch the top of the new maintenance pad with your fingers. Same instruction applies to the “Drop Watcher pad” also.
17. Turn off the printer first and then turn off the computer.

Vita

Jay was born in Karamsad, India. He eventually moved to Nagpur, India to obtain a degree of Bachelor of Technology (B.Tech) in the field of Metallurgical and Materials Engineering from Visvesvaraya National Institute of Technology Nagpur. His B.Tech project comprised of work on high cycle fatigue behavior of CFC laminates which are used as structural materials in aerospace industries. He investigated the cause and mechanism of fatigue failure in CFC laminates during that time frame. Around that time, he also got an internship at Bhabha Atomic Research Centre in Mumbai where he worked on time-temperature sensitization of 304LN stainless steel which aids in material selection and predicting material response in applications involving temperatures higher than 600 ^{o}C. After his graduation, he went to Indian Institute of Technology Kharagpur in Kharagpur, India to obtain his Master of Technology (M.Tech.) degree in Metallurgical and Materials Engineering during which he worked on the structural and mechanical characterization of electrodeposited and annealed nanocrystalline Ni-Fe alloys.

He then came to University of Texas at El Paso (UTEP) to pursue his Ph.D. in Materials Science and Engineering under the direction of Prof. Anupama B. Kaul. During this period, he explored and optimized various methods for two-dimensional (2-D), conducting, semiconducting and insulating inks and fabricated photodetectors, photosensitive capacitors and microstrip patch antenna using inkjet printing technology.

Contact Information: jaydesai28@hotmail.com

This thesis/dissertation was typed by Jay Amrish Desai.